UNIVERSITÀ DEGLI STUDI DI CAGLIARI
Facoltà di Scienze Matematiche, Fisiche e Naturali

MEASUREMENT OF STRANGE HADRON PRODUCTION RATIOS AND PERSPECTIVES FOR THE SEARCH OF $D^0 \to \mu^+\mu^-$ DECAY AT LHCB

FRANCESCO DETTORI

A thesis submitted for the degree of Doctor of Philosophy

December 2010

Supervisors: Dott. Walter Bonivento
Prof. Biagio Saitta

CONTENTS

PREFACE

Particle physics is remarkably well described by the Standard Model (SM) up to the energies probed so far [1]. However there are both experimental and theoretical motivations which point towards physics beyond the Standard Model.

From the experimental side few but important phenomena appear presently to deviate from the predictions of the SM. The existence of dark matter [2], non-interactig matter which constitues 80% of the mass of the Universe, is certainly one of the most striking. The origin of mass itself is difficult to be explained until the Higgs mechanism is experimentally proven. Moreover the nature of neutrinos, which are experimentally massive, is not consistent with SM hypothesis and is added *a posteriori* to it.

All of these problems appear to be related to particles mass, and also from the theoretical point of view, most of the problems of the Standard Model, often referred to *naturalness*, *hierarchy* and *fine-tuning*, depend essentially on the enormous distance between the SM typical energy scales and the Plank scale $M_P = (8\pi G_{Newton})^{-1/2} = 2.4 \cdot 10^{18}$ GeV, *i.e.* when the gravitational force becomes non negligible in particle interactions. These problems are essentially connected by how the various theory parameters vary with the energy scale. Since a parameter, *i.e.* the Higgs mass, varies *unnaturally* with the cut-off energy at which the theory is though to be valid, a *fine-tuning* of the parameters is needed in order not to have divergences; and if the SM is valid up to the Plank scale, then clearly there is a strange *hierarchy* between the scale of most physics (electroweak scale) and the one of gravitation.

These experimental and theoretical problems, which motivate the search for physics beyond the Standard Model, can be regarded as more fundamental and philosophical questions. Is it possible (and expectable) that exists one single theory to describe all possible interactions in the whole energy range? Is it realistic that this theory has a phenomena scale condensed in few orders of magnitude while decoupling other phenomena (*e.g.* gravity) to completely different scales and nothing else lies in between? Or is it instead more *natural* to expect unknown phenomena to be more deeply complex as the knowledge proceeds in an infinite deepening.

We do not try to give answers to these questions in this work since they are beyond the reach of present experimental and theoretical physics, but we keep them in mind to understand the limits of each *effective* theory, Standard Model included.

Also in the low energy regime problems with the Standard Model are present. Particle interactions within the Standard Model are described as gauge field theories, describing processes calculable with perturbative methods as far as the couplings are small. However strong interactions are described by couplings which increase at low energies, preventing the perturbative approach. Hence the low energy phenomena involved in particle production are far from being well described by the Standard Model.

High energy physics, and proton-proton scattering in particular, is therefore an important laboratory for the search for new phenomena and the comprehension of the known ones. The Large Hadron Collider (LHC) at CERN is presently providing proton-proton collisions at the highest energy ever reached on earth, with an energy in the center of mass of $\sqrt{s} = 7$ TeV, foreseen to be further increased in 2011. Besides having access to a new energy scale, thanks to the high luminosities reached, also very rare phenomena can be studied so that the LHC is one of the best machines to the study particle physics at present days.

The LHCb experiment is one of the main experiments taking data at LHC. It has been designed mainly for the study of b-hadrons physics, from precise measurements of CP violation to study of rare decays. The work during my Ph.D. started considering B^0 rare decays and the perspectives of the LHCb experiment for the search of new physics in these processes. Studies on the possible searches for the $B_s^0 \to \mu^+\mu^-$ decay were made but a more complete study was carried out on the radiative $B_s^0 \to \mu^+\mu^-\gamma$ decay and was recently summarised in an LHCb public note [3]. These studies performed on Monte Carlo simulations foresaw one year of data taking at the nominal LHC design conditions: pp collisions $\sqrt{s} = 14$ TeV with a luminosity $\mathcal{L} = 2 \cdot 10^{32}$ cm^{-2}s^{-1}. In parallel we started analysing also *charm* rare decays, and in particular the $D^0 \to \mu^+\mu^-$ decay.

In November 2008 the first protons started to circulate in the LHC; unfortunately after few days of commissioning an accident in one of the magnets caused a serious damage to the machine. This required almost one year of stop for fixing and commissioning. First proton-proton collisions were delivered by the LHC in December 2009, but in order not to risk further damages to

the machine, the 2010 data taking energy was set to $\sqrt{s} = 7$ TeV; modifications to the machine will be required before rising the energy up to the design values.

This delay is reflected in this thesis which could exploit less than one year of data taking and with low luminosity. Indeed the 2010 data taking run was ended by the LHCb experiment with $\mathcal{L}_{Int} = 37.7\ pb^{-1}$ of recorded integrated luminosity, mostly collected in September and October 2010.

With the first part of these data, taken with very loose trigger requirements, proton-proton collisions could be studied in an unbiased way.

This work is focused on the study of the production ratios of strange hadrons in proton-proton collisions, which give information on the non-perturbative phenomena involved in particle production and hadronisation, and on the transport of the initial state information, as the baryon number, to the final state particles. Moreover we consider a study of the polarisation of Λ particles produced at high energies, important for the comprehension of spin interactions in this regime.

On the other side we also report a preliminary study for searches of the rare decay of the charmed meson D^0 into two muons ($D^0 \to \mu^+\mu^-$), whose decay rate could be enhanced in new physics scenarios by several orders of magnitude with respect to Standard Model predictions.

The material in this thesis is organised as follows. In Chapter 1 we give a theoretical introduction on the strange hadrons production in proton-proton collisions and on their importance in high energy physics for the comprehension of strange quark production and hadronisation. A brief review of phenomenological models is given and predictions from Monte Carlo simulations are shown. The predictions of theoretical and phenomenological models on the polarisation of Λ baryons are subsequently described, with a focus on the ones of particular interest in high energy proton-proton collisions.

Afterwards we discuss in the same chapter the theoretical interest for rare charm decays and in particular for $D^0 \to \mu^+\mu^-$ searches. The Standard Model prediction and possible New Physics contributions are reviewed in order to present the importance of this process for the possible indirect discovery of new phenomena.

The work for this thesis was developed within the LHCb collaboration, the LHCb experiment and detector is therefore described in Chapter 2. A brief description of the various subdetectors is

given and the expected and measured performances are summarised.

In the second part of this work we describe the different measurements performed in pp collision data. In Chapter 3 we present a measurement of the production of V^0 particles in pp collisions both at $\sqrt{s} = 0.9$ TeV and 7 TeV. The analysis method is described and results for the $\bar{\Lambda}/\Lambda$ and $\bar{\Lambda}/K^0_S$ production ratios are shown. Close attention is put in the discussion of possible systematic uncertainties, in particular in relation with detector properties.

Following the same analysis of Λ particles, we also discuss a measurement of the Λ and $\bar{\Lambda}$ polarisation. The analysis details and preliminary results are presented in Chapter 4.

The studies for the search of the $D^0 \to \mu^+\mu^-$ decay are reported in Chapter 5. After discussing the developed analysis strategy, we consider some studies performed on Monte Carlo simulations of pp collisions at $\sqrt{s} = 10$ TeV, energy at which the protons where expected to collide in 2009 when this study was performed. While a complete study to measure the branching ratio or its upper limit is not yet completed, we present some preliminary studies on the background for this measurement as obtained in pp collisions at $\sqrt{s} = 7$ TeV and give qualitative estimates of prospects for the possible results.

For each of these measurements we give some final remarks on the respective chapter, while a general outlook of this thesis will be summarised in the Conclusions.

Part I

INTRODUCTION

1

THEORETICAL INTRODUCTION

Experiments at the LHC, colliding protons at high energies, have the potential to explore both the limitations of the Standard Model. On one side there is the non perturbative regime of the QCD, which, while is well established on a pure theoretical ground, it lacks of a good understanding of its phenomenology where the perturbative expansion is no longer applicable. LHC can then be exploited, owing to his copious number of soft events, to understand the phenomenology, tune the Monte Carlo generators and test different models. On the other side there are the limitations of the Standard Model on the high energy regime, in particular in very rare phenomena, where contribution of New Physics can be as important as the SM one revealing a brand new field of Particle Physics.

The rest of this chapter is organised as follows: first we will give a brief introduction on the general landscape of high energy proton-proton interactions (§1.1), to concentrate afterwards on *strange* quark production and hadronization (§1.2) and the predictions for meson to baryon production ratio, baryon asymmetry and polarisation; finally we will move on the other side of the SM and study charm rare decays which can be exploited to reveal hints of physics beyond the Standard Model.

1.1 HIGH ENERGY PROTON PROTON INTERACTIONS

Proton proton collisions are very complex interactions mainly phenomenologically described by current theories. Being the protons of a composed structure, the elementary interactions must be described in terms of partons, quark and gluons. In this section we give a description of how proton-proton collisions are thought to happen, dividing the whole process in different stages which are often described by complementary phenomenologies, lacking of a complete and coherent theoretical comprehension.

The following description is built in a roughly temporal order baring in mind that, being this type of interactions intrinsically of quantum-mechanical origin, this is just a convenient way to explain them rather than a real succession of separated events.

At the first stage there are the two incoming hadrons, protons in this case, which are brought to collision with a certain energy. As already said, they can be viewed as a collection of partons, of which the constituent quarks (uud) are only a probabilistic majority and not the only component.

The main interaction is then due to two partons, one from each side, which interact in one of the allowed modes of the Standard Model (or of the considered New Physics scenario), e.g. $ud \to ud$, $ug \to ug$, $u\bar{d} \to W^+$ etc. Obviously most of the collisions are elastic, diffractive or so soft to have only little physics interest. Interesting events, instead, usually start with a hard parton interaction which can yield either short-lived massive resonances ($W^\pm$, top, Higgs bosons, etc) or other (light) partons. The decays of massive resonances are usually considered to be included in the "hard" part of these interactions, as the quantum numbers are correlated and propagated to their final states. The other partons produced will give rise to hadrons, trough the hadronization process, which will be described later on.

As far as the the parton hard scattering is concerned, accelerated colour charges are involved so that it is natural to expect some (strong) bremsstrahlung radiation to be emitted. Usually this kind of process is referred to as *Initial State Radiation* (ISR) if coming from the incoming partons, or *Final State Radiation* (FSR) if from the outgoing partons. In order to understand the source of this radiation, rather than the bremsstrahlung picture, is more significant to look at it from another point of view. Consider the participants to the hard scattering, the harder it is the smaller is the considered space region and consequently time interval so that the partons must be (by the uncertainty principle) farther away far from their mass shell. However initial and final state partons must be on-shell so that the transition to off-shell is ascribable to the initial and final state radiations, which for this reason are often described as space-like and time-like showers respectively.

The FSR can be depicted as a succession of branchings from the outgoing parton which leads to the emission of softer and softer gluons until the typical energy of soft QCD is reached where this kind of description no longer holds. The ISR, instead, can be described as a specular process where the emitted gluons are harder and harder until the core of the hard scattering takes place. Clearly these gluons are virtual and they can be effectively *realised* into final state partons only at this level; if no hard scattering

occurred this virtual shower would be adsorbed by the same parton.

So far we have treated only one parton-parton interaction. However, being the protons built of a multitude of partons, more than one parton per side can take active part to the collision. Multi-parton Interactions are then usually considered in proton-proton interactions and are useful to explain the experimental data so far.

MPI is not to be confused with *pile-up* events, where more than one proton-proton interaction is involved; this case can be usually described by treating each of the proton-proton interactions independently.

At this point we are left with the partons created in the previous steps. The evolution of the partons from this stage to the final hadrons is the most difficult part to describe from the theoretical point of view, as it involves mainly soft quark and gluon interactions, which are very far from the perturbative regime of QCD. Hence models have to be introduced to explain this evolution in a phenomenological fashion rather than from first principles. A common idea of these models is to describe the confinement by a field which grows linearly with the distance of the partons and matches opposite colours between quark pairs and with gluons (considered simply as colour anti-colour pairs). Eventually this field can break, if the partons moving away have sufficient energy and the colour field is then screened by the formation of another quark pair. This sequence is repeated until the momentum of the outgoing partons is not enough to break this field and only quark pairs (or triplets) are present and constitute the final state hadrons. This process, called hadronization, is rather complicated and will be treated separately in more detail in §1.2, in particular concerning strange quarks. Clearly the distinction between final state interaction and hadronisation is rather subtle and relays mainly in the amount of transferred momentum per interaction.

The final stage of this type of events is represented by final state particles: while this is not really part of the proton-proton interaction all the experimental data are formed by the revelation of these (almost) stable particles. In particular, some of the hadrons formed in the hadronization process and most of the heavy particles produced in pp interactions (*e.g.* Z^0, τ etc) usually decay before encountering any particle detector and only their decay products are detected. Only electrons, photons, muons and some of the hadrons have a lifetime sufficiently long to reach some detectors, but this depends obviously on the principal decay

type (stable, electromagnetic, strong or weak) and on the Lorentz boost.

Being all the experimental data obtained at this level, it is easy to see that the experimental study of these processes will be done in the opposite direction. Experimentally unstable hadrons are reconstructed from the final state particles up those coming directly from the primary interaction; the hard processes can be inferred from a comparison of the predictions of different models on the final states with the experiment.

This introduction is important to understand that while the final states particles and the particles from which they have decayed can be studied in a very detailed way, having all the necessary information available, the partons from which they originate and their interactions can be studied only indirectly due to confinement, both in initial state interactions and inside final state hadrons.

1.2 STRANGE HADRONS PRODUCTION

Within this work we will be interested in strange quarks production. Since strange quarks are not valence quarks of initial state of proton-proton collisions they are very well suited to test quark production mechanism and hadronization. Contrary to heavier quarks (c, b, t) strange quarks can be produced both in the hard interactions and in the hadronization phase. Moreover their constituent mass is comparable with the scale at which the perturbative and non-perturbative regimes of the QCD are usually divided (Λ_{QCD}) so that strange quarks production explores the non-perturbative regime of QCD.

We will first consider the production of strange quarks from the point of view of perturbative QCD (§ 1.2.1) and then review some basic concepts of the production of strange quarks in hadronisation (§ 1.2.2).

As far as strangeness production is concerned, of interest for this work are the following observables, which will be used from the experimental point of view in § 3 and § 4:

- $\bar{\Lambda}/\Lambda$ production ratio[1], or Λ baryon production asymmetry, defined as

$$\bar{\Lambda}/\Lambda = \frac{\sigma(pp \to \bar{\Lambda}X)}{\sigma(pp \to \bar{\Lambda}X)} \tag{1.1}$$

1 For convenience we will indicate here and in the following the production ratios with the particle names ratios.

which is here defined just for the integrated cross-section but in practise is often referred to as ratio as a function of a particular variable and hence differential cross-sections are used.

- $\bar{\Lambda}/K^0_S$ production ratio, or baryon over meson suppression, analogously defined as

$$\bar{\Lambda}/K^0_S = \frac{\sigma(pp \to \bar{\Lambda}X)}{\sigma(pp \to K^0_S X)} \tag{1.2}$$

- Λ polarisation, or Λ spin asymmetry, which will be defined in detail in § 1.2.6.

The theoretical and Monte Carlo predictions for these observables will be presented in § 1.2.3, 1.2.4, 1.2.6 respectively.

1.2.1 *Strangeness production in pQCD*

Within the naive picture of pp interaction we have described above, the strange quark production can occur at various levels. In this section we analyse the production of strange quarks from the perturbative QCD point of view.

We consider the process

$$p + p \to \Lambda + X \tag{1.3}$$

as an example for strangeness production. If we restrict ourselves to the region of this reaction were the perturbative expansion of QCD is valid (*e.g.* $p_T > 1$ GeV/c) so that collinear factorisation [4] becomes applicable we can derive the cross-section of this process.

Here, we follow the derivation in Ref. [5] and write this cross-section as

$$\begin{aligned} d\sigma &= \frac{E_C d^3\sigma^{pp\to\Lambda X}}{d^3P_\Lambda} \\ &= \sum_{a,b,c,d} \int \frac{dx_a dx_b dz}{\pi z^2} f^p_a(x_a) f^p_b(x_b) \hat{s}\delta(\hat{s}+\hat{t}+\hat{u}) \times \\ &\quad \times \frac{d\hat{\sigma}^{ab\to cd}}{d\hat{t}}(x_a, x_b, z) D^\Lambda_c(z), \end{aligned} \tag{1.4}$$

which is written in terms of $\frac{d\hat{\sigma}^{ab\to cd}}{d\hat{t}}$, *i.e.* the cross-section of the subprocess $ab \to cd$ at the parton level; $f^p_{a,b}(x_{a,b})$ the parton distributions in the two protons with Bjorken variables $x_{a,b}$ and

D_c^{Λ} the fragmentation function for the parton c into the produced Λ with energy fraction z of the incoming quark c. In Eq. (1.4) we indicate with $\hat{s}, \hat{t}, \hat{u}$ the parton level Mandelstam variables.

As factorisation theorem states and is clearly understandable from Eq. (1.4) in this approach all the long-distance non-perturbative contribution to the production of a final-state hadron are *hidden* in the fragmentation function. Fragmentation functions can be extracted from experimental data, *e.g.* considering the same reaction of Eq. (1.3) but with e^+e^- in the initial state, but can also be parametrised in terms of the parton distribution functions [5]. In both cases the quark content of the fragmentation functions is thought it can be probed by the study of hadron production asymmetries [5, 6].

1.2.2 *Hadronization*

We refer to the hadronization process for the phase between the hard hadron interactions, where partons are essentially free, given the high energy involved, and the final state where the partons are confined within hadrons of typical 1 GeV mass scale.

As far as QCD is concerned the hadronization is a process intrinsically non perturbative since it deals with energies of a few GeV. Therefore at present only phenomenological models give a successful descriptions. In particular, the two approaches mostly used are: string fragmentation [7, 8] and cluster fragmentation [9].

1.2.2.1 *String fragmentation and the Lund model*

While non-perturbative QCD is not solved, a successful approach to this type of studies is lattice QCD, where the evolution of partons is simulated completely but in a discretised space-time. These studies suggested that confinement is produced by a colour dipole field extending between a pair of partons and the energy stored therein increases linearly with the separation (ignoring the short-distance Coulomb potential).

Starting from such a linear confinement, the string model [7, 8] is capable to describe the production of quark pairs. If one considers two already produced partons (*e.g.* in a hard process) which start to recede from each other, the linear dipole field can be depicted as a colour flux tube stretched between the quark and the anti-quark. This description considers a flux tube of a typical hadron transverse size (1 fm) and uniform along its length which

leads naturally to a linearly rising potential. Its dynamics can be described in a Lorentz covariant way considering a massless string with only the longitudinal degree of freedom. In particular, the amount of energy per unit length can be derived from hadron spectroscopy to be of the order $\kappa \approx 1\text{GeV/fm}$.

The assumption of a uniformity in the force field will also include the property that there are no concentrations of energy, transverse momentum or angular momentum along the field. The total energy stored in the string increases with the distance of the two quarks q and $\bar{q}$, this energy will be eventually enough to produce a second pair $q'\bar{q}'$, breaking the primary string.

Within such field massive $q\bar{q}$ pairs (of mass μ) cannot be produced in a single space-time point. Classically they must be produced at a distance $2l$ apart so that the field energy in between can be used for the mass production, so that

$$k \cdot 2l = 2\mu \tag{1.5}$$

Hence the process is intrinsically of quantum mechanical nature [8].

The generation of quark pairs from string breaking is described in the Lund model as a quantum-mechanical tunnelling process in a linear potential. Simple calculations show that the tunnelling probability is inversely proportional to the quark constituent masses:

$$|\mathcal{M}|^2 \propto e^{-(\pi\mu^2/\kappa)} \tag{1.6}$$

leading to the suppression of heavy quarks production; in particular the proportion between different quark flavours is

$$u : d : s : c \approx 1 : 1 : 0.3 : 10^{-11} \ . \tag{1.7}$$

Charm and heavier quarks are therefore not expected to be produced in hadronization even if they can take part in this process as the first quark pair, produced in the hard scattering.

After the first breaking the colour field will be stretched between the two colour singlets states $q\bar{q}'$ and $\bar{q}q'$. Each of these pairs can start a process of string break-up as the one described which can be repeated until each quark anti-quark pair has the mass of an hadron.

The process described shows the production of mesons; the production of baryons within this model is simply explained by replacing the production of a quark pair by the production of a di-quark pair in a colour triplet state [10]. The production of

baryons is then suppressed with respect to mesons simply by the larger mass of the di-quark pair compared to the quark pair.

A rather more complicated approach for baryon production with respect to this di-quark picture is called *pop corn* [11]. In this model di-quarks are never produced at once, but rather baryons appear from the production of different $q\bar{q}$ pairs. Assuming that the original $q\bar{q}$ pair is *red anti-red* coloured, *i.e.* $r\bar{r}$, the string stretched in between will usually generate $r\bar{r}$ quark pairs, but occasionally a *green anti-green* ($g\bar{g}$) quark pair can be generated. This new $q'\bar{q}'$ pair will not feel any net colour field and hence will not be able to gain energy (for the meson mass) from the field. However, the colour field between q' and $\bar{q}'$ will be $b\bar{b}$ on average so that a third quark pair ($q''\bar{q}''$ can be generated. In this way two baryons are produced. More complex generation patterns with also a meson in between are also possible. Moreover this *pop-corn* picture is not alternative to the di-quark previously described and the two can be often used as complementary.

1.2.2.2 *Cluster fragmentation*

An alternative way of explaining the hadronization process is referred to as cluster fragmentation [9].

The central idea is the formation, at the end of the perturbative phase of jet development, of colour singlet clusters of partons, which subsequently decay to hadrons. The dominant colour index structure can be represented in a planar form as depicted in Fig. 1 which starts from the partons already produced in the hard interaction.

It is assumed that a non-perturbative low q^2 enhancement of the splitting $g \to q\bar{q}$, which is relatively uncommon in the perturbative branching process, cause all the gluons to be split in quark pairs. Adjacent index pairs form colour singlet clusters represented by the blobs in Fig. 1 provided the two indices associated with each gluon are dynamically separated. Typically $q\bar{q}'$ colour singlets are formed from quarks coming from adjacent shower branches, therefore they tend to have small masses. In this model, a cluster is completely characterised by its total mass and flavour content while its internal structure is ignored. The decays of clusters are then treated like a two body decay of a resonance, taking into account, for the final states, just of the density of states, including spin degeneracy but ignoring spin correlations (phase space decay).

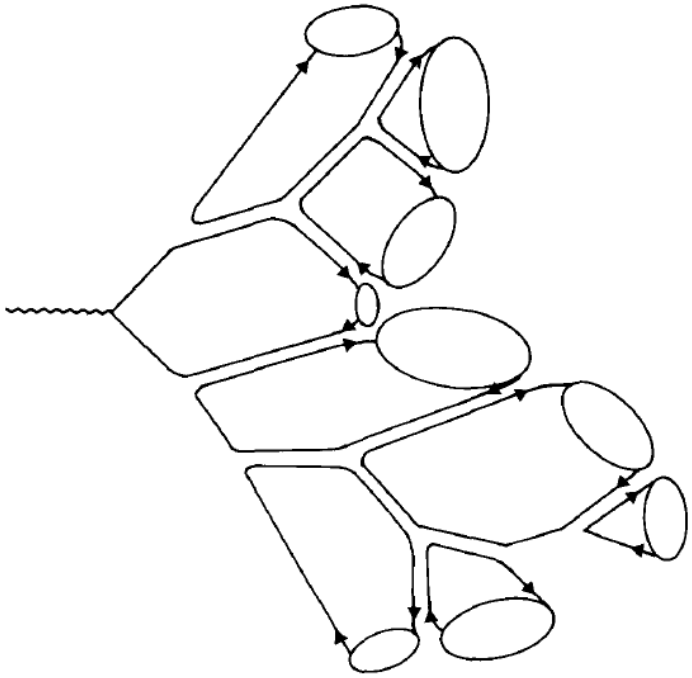

Figure 1.: Colour structure of an event as represented in the cluster fragmentation model. The *blobs* represent colour singlet clusters which are the basis of the hadronisation process described in the text.

Hence note that the dynamical suppression of strange particle or baryon production in cluster decay comes entirely from the resonance spectrum via the reduction of phase space for these channels.

This model gives a compact description of the whole hadronization process with few input parameters, however in order to explain the break-up of larger clusters it needs to incorporate some string-like concepts in order to explain the decay along the string direction.

1.2.2.3 *Strange particle production in hadronization*

Strange particle production offers good handles to understand the hadronization phenomena and hence the confinement phase of strong interactions.

The principal feature of strange quarks production is its suppression with respect to u and d type quarks. This suppression is related to the energy density in the colour field: within the

Lund model it is therefore useful to measure it as the "string" constant κ of Eq. (1.5). The "cluster" model explanation of this suppression is instead attributed directly to the available density of space in the cluster decay, which is of course diminished for an $s\bar{s}$ final state. The two explanations, are indeed very similar as they explain strange-quark suppression as a kinematic process rather than a dynamical property of strong interactions.

Moreover, the suppression of strange quarks give the possibility to explore the hadronization phase in a more direct way: while pions are produced copiously in high energy interactions, typically just one or two pairs of strange particles are present. Hence strangeness quantum number allows to label final state particles and explore their correlations: the distribution in the phase space of correlated strange hadrons gives a measurement of the momentum transfer in the confinement process.

The importance of strange particles in hadronization is also due to the fact that, while among the final state pions a large part can come from resonance decays (e.g. $\rho \to \pi\pi$), the secondary production of strange hadrons is less important, being due to higher mass quarks or to other (primary) strange hadrons.

The production of strange baryons is also an important subject since the hadronization into baryons is more delicate to include in the models mentioned. Finally the polarisation of strange baryons is a fundamental probe of the way strange quarks are joint to other quarks in the hadronization phase.

1.2.3 *Strange baryon production asymmetry*

In order to understand the production mechanism of strange particles it is often convenient to study production ratios rather than absolute cross-sections. This because either from the experimental and the theoretical point of view, the description of ratios is much more clean, cancelling out most of the common features.

The asymmetry between Λ and $\bar{\Lambda}$ production plays indeed a very important role in this field. At a very superficial level the production asymmetry in pp collisions can be easily understood: incoming particles are hadrons which carry much more partons than anti-partons so that the creation of a Λ particle requires just an s quark to be produced while the $\bar{\Lambda}$ requires an $\bar{u}$ and $\bar{d}$ besides the $\bar{s}$ quark. So if the strange quarks are mostly produced in $s\bar{s}$ pairs it is clear that an asymmetry must come from the energy needed to produce the other anti-quark needed in the $\bar{\Lambda}$ case and not in the Λ one. This naive picture is often referred to

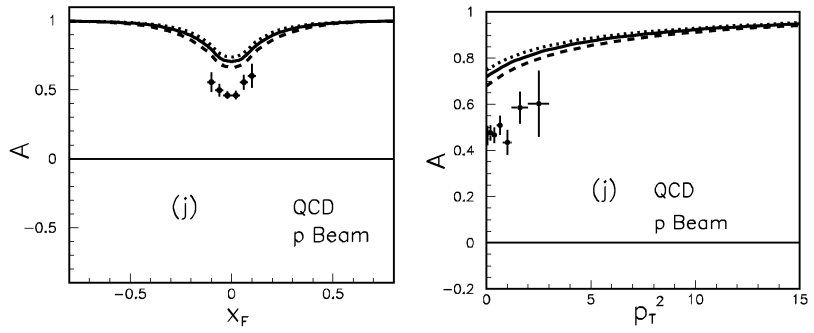

Figure 2.: $\bar{\Lambda}$ production asymmetry in proton proton collisions (left) as a function of the Feynman's x and (right) as a function of p_T^2 as obtained in perturbative QCD calculations of Ref. [5]. Theoretical predictions are compared with data from fixed target pp collisions from the E769 collaborations [12].

(especially when talking about heavier quarks) as *Leading Particle Effect*, where the final state particles keep trace (in a statistical manner) of the initial state hadrons.

From the QCD point of view [5], as described in § 1.2.1, the Λ production asymmetry is due to various factors. First of all the content of the initial state hadrons, through the parton distribution functions, is different for the $\bar{\Lambda}$ ($\bar{u}\bar{d}\bar{s}$) with respect to the Λ (uds). Secondly the fragmentation can be different and in particular for the $\bar{\Lambda}$, mostly sea quarks contributions must be advocated. Predictions for the Λ-$\bar{\Lambda}$ production asymmetry obtained with the model of Ref [5] are shown in Fig. 2 and compared with data from the E759 Collaboration taken by colliding a 250 GeV proton beam to a liquid hydrogen target [12]; note that the convention adopted for the asymmetry is different from the one of Eq. (1.1) which we will use experimentally, namely the asymmetry is defined as

$$A(x_F) = \frac{d^3\sigma/d^3p_\Lambda - d^3\sigma/d^3p_{\bar{\Lambda}}}{d^3\sigma/d^3p_\Lambda + d^3\sigma/d^3p_{\bar{\Lambda}}} \tag{1.8}$$

and an analogous formula holds for $A(p_T^2)$.

The two plots in Fig. 2 show that the asymmetry is more prominent in the high $|x_F|$ region, while at low x_F it is reduced.

1.2.3.1 *Baryon Number Transport*

A similar explanation to the *Leading Particle Effect* is often described in terms of *Baryon Number Transport*, *i.e.* the conservation

of the initial state information to the final state, with particular emphasis on the baryon number. This concept is more common in a rather different field in High Energy Physics, namely the high energy ion collisions. These reactions are thought to be the tool to discover a new state of matter called Quark Gluon Plasma, characterised by deconfined quarks and gluons and in this environment the strange quark production can be used as a probe.

Some authors suggest that anti-baryon to baryon production ratios in these collisions could help to distinguish between a hadron gas and a deconfined plasma of quarks and gluons [13]; we do not describe these processes since we will deal with proton-proton interactions, which however must be taken as a reference for the comparison with heavy ion collisions results.

We consider here only the concept of *Baryon Number Transport* over various rapidity units in order to measure how the $\bar{\Lambda}/\Lambda$ ratio can probe the mechanism of pp collisions.

The transport of the baryon number from the initial to the final state particles over various units of rapidity is often related to the *deceleration* of the incoming proton and has been subject of different theoretical approaches [14, 15, 16, 17, 18, 19]. Hence it is usually measured as a function of the rapidity difference:

$$\Delta y = y_{\text{beam}} - y_{\text{baryon}} \tag{1.9}$$

which in the $pp \to \Lambda X$ reaction is simply the difference in rapidity between the incoming proton and the outgoing Λ.

Within the Dual Parton Model [15] the Baryon Number is carried by the diquark and quark into which the incoming proton is split. The hadronisation of the diquark into the outgoing Λ (with the already explained mechanisms) transfers the baryon number to the latter. However this view is difficult to maintain when the difference in rapidity is various units; in this case in fact the incoming proton diquark should loose as a whole a considerable fraction of its momentum in the collision, which is rather difficult to justify.

Therefore different other models have been proposed; in particular according to Ref [14, 16, 20] the baryon number could be traced by a non-perturbative configuration of the gluon fields. Within this picture the classical baryon number association with the valence quark of a hadron would be just a prejudice, which could be simply shifted to the gluons that hold the hadron together (often called "string junction").

The authors of Ref. [20] suggest that this association is difficult to be studied by probing the structure of a baryon with hard interactions since these involve usually one parton at time. The right processes to be considered to understand this structure would be then the ones in which the baryon number flow is separated by the valence quark flow. The baryon production in the central rapidity region of pp and heavy ion collisions would be a suitable observable.

Quantitative predictions can made for the baryon production asymmetry in this kind of interactions by considering topological QCD expansion and Regge phenomenology which lead to a baryon number transport suppressed exponentially as a function of Δy:

$$\propto e^{-(\alpha_J - 1)\Delta y} \tag{1.10}$$

where α_J is a parameter of the considered Regge model.

Hence phenomenologically one would expect to find a sizable asymmetry at central rapidities depending on the value of α_J. If the string junction intercept is approximately correspondent to one meson exchange, $\alpha_J \approx 0$, so that the baryon transport up to high rapidity differences should decrease down to zero, correspondingly the baryon asymmetry should disappear (*i.e.* $\bar{\Lambda}/\Lambda \to 1$ for high Δy); on the contrary if as suggested by perturbative QCD $\alpha_J \approx 1$, the baryon transport will approach a certain finite value leading to a residual asymmetry also in the mid-rapidity region.

Within the LHCb experiment, as we will see in § 2, the mid-rapidity region is not accessible because of the forward acceptance of the detector, however in high energy collisions, large Δy intervals are still accessible due to the very high rapidities of the incoming protons compared with the produced Λ's. Therefore, the exponential shape of the baryon number transport versus Δy can still be studied as will be presented in § 3.

1.2.4 *Strange baryon to meson ratio*

A complementary information to the baryon asymmetry can be obtained through the baryon to meson production ratio which gives information on the differences in the hadronisation process into these particle types.

Different models explain the meson and the baryon hadronisation in different ways. A suppression of the baryons with respect to mesons is obviously present just for statistical reasons, because

of the need of one more (valence) quark, and kinematically due to the higher baryon masses (a lower tunnelling probability in the string model or a lower phase space in the cluster model). However, it is important to understand whether this explanations are compatible with experimental data.

Within heavy-ion collisions the strange baryon over meson production ratio is used to measure how the size of the colliding objects influences the hadronisation [21]. In this context data from pp collisions can be used as a benchmark besides being one of the data points.

1.2.5 *Monte Carlo predictions for strange particles production asymmetries*

Monte Carlo generators [22] simulate the very complex phenomena we have briefly summarised in § 1.1 with the help of (pseudo)-random numbers and phenomenological parametrizations of the unknown processes.

In the LHCb experiment in particular the PYTHIA [23] package is used to simulate proton proton collisions; we do not describe the implementation of this software and refer to the cited paper for any description.

Here we want just to summarise the current predictions for the $\bar{\Lambda}/\Lambda$ and $\bar{\Lambda}/K^0_S$ ratios as obtained with different parametrizations of PYTHIA. In particular we consider the so-called "Perugia" tunes [24, 25]. These settings of PYTHIA have been tuned using data mostly from LEP and Tevatron experiments, and extrapolated to the LHC energies. The following parameters and phenomena have been particularly tuned:

- Initial and final state radiation;
- Hadronisation;
- Underlying event;
- Beam remnants;
- Colour reconnections;
- Energy scaling.

for the parametrisation of which inside PYTHIA we refer to the PYTHIA user manual[23].

Some predictions for the $\bar{\Lambda}/\Lambda$ and $\bar{\Lambda}/K^0_S$ production ratios have been obtained with these tunes. In particular we show in Fig. 3

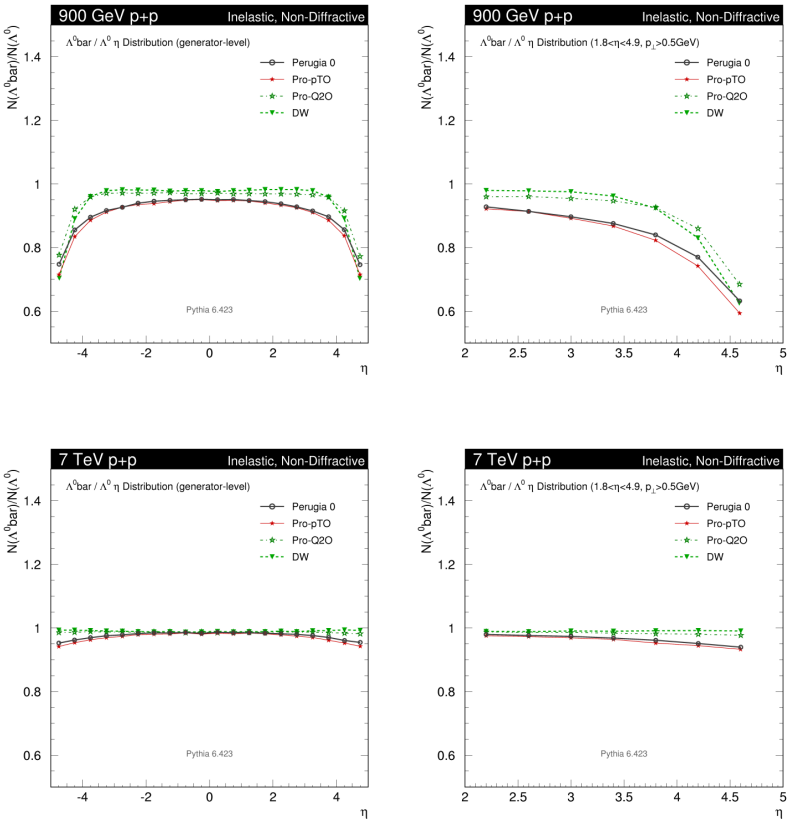

Figure 3.: Theoretical predictions for the $\bar{\Lambda}/\Lambda$ production ratio from Monte Carlo simulations as obtained using the PYTHIA package with different tunes [26].

the $\bar{\Lambda}/\Lambda$ production ratio as a function of the pseudorapidity (η) for both $\sqrt{s} = 0.9$ TeV and $\sqrt{s} = 7$ TeV center of mass energy. The plots on the right are zoomed in the region of interest of the LHCb experiment. Equivalent plots for the $\bar{\Lambda}/K^0_S$ ratio are shown in Fig. 4.

We do not try to give here a comparison between the predictions of theoretical models with respect to these Monte Carlo simulations. In fact these two approaches are complementary. On one side the theory is often disconnected from experimental considerations while on the other side the Monte Carlo approach is usually trying to reproduce the experimental results often forgetting some theoretical prejudices (*e.g.* colour reconnection).

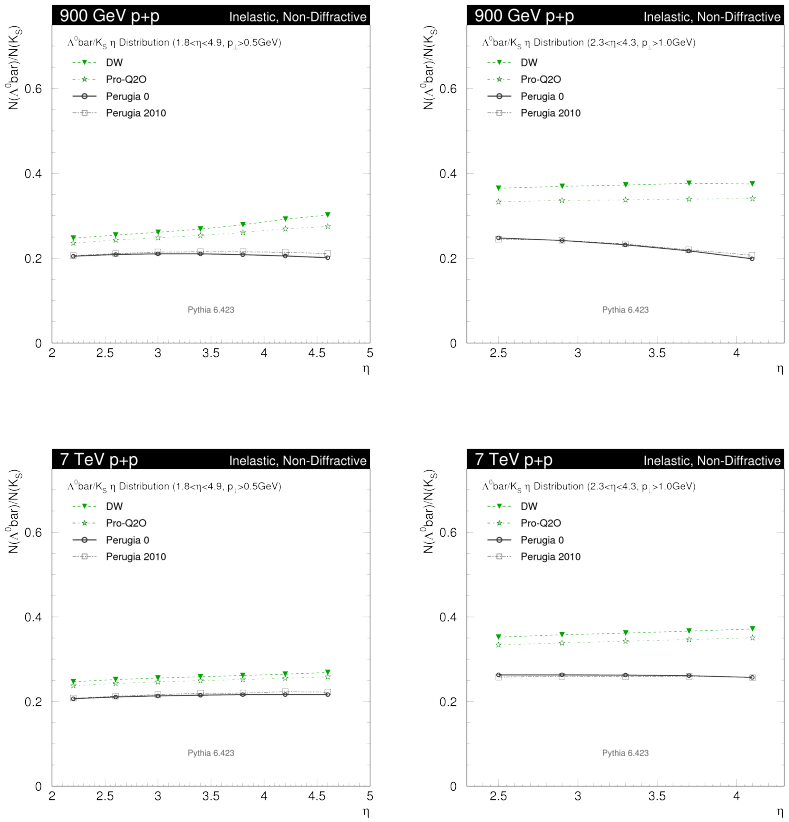

Figure 4.: Theoretical predictions for the $\bar{\Lambda}/K^0_S$ production ratio from Monte Carlo simulations as obtained using the PYTHIA package with different tunes [26].

1.2.6 Λ *polarisation*

The polarisation is the preference of a particle, in this case the Λ, to have the spin oriented along a particular axis. It can be defined, for Λ production in pp collisions as:

$$P = \frac{\sigma^{\uparrow} - \sigma^{\downarrow}}{\sigma^{\uparrow} + \sigma^{\downarrow}} \tag{1.11}$$

where $\sigma^{\uparrow} = \sigma(pp \to \Lambda^{\uparrow} X)$ is the cross-section for the production of a Λ with spin oriented upwards (with respect to the chosen axis) or downwards (for the superscript $\downarrow$).

Due to parity conservation in strong interactions only a transverse polarisation can arise in high energy hadron-hadron interactions and indeed transversely polarised Λ hyperons have been detected already long time ago in hadron-hadron collisions [27].

It is usually believed that hard scattering processes, as calculated in perturbative QCD, could not generate such spin effects; this is intuitively explainable as particle production at high energies involving a large number of final states should not have high coherent interference of amplitudes. In particular lowest order QCD predicts no polarisation for the Λ with high transverse momentum ($> 5 GeV/c$) [28].

Various models are then available in order to explain the observed data, each of which essentially attributes the polarisation to non perturbative effects either in the production or in the hadronization of the s quark from which the Λ originates.

A big amount of experimental data is available (for a comprehensive review, even if not up to date, cf. [27]) and show some common features:

- Primary Λ (not from other resonances decays) show a significant polarisation orthogonal to the production plane, *i.e.* parallel to the unit vector:

$$\hat{n} = \frac{\vec{p}_b \wedge \vec{p}_\Lambda}{|\vec{p}_b \wedge \vec{p}_\Lambda|} \tag{1.12}$$

  where $\vec{p}_b$ is the momentum of the incident beam. [2];

- The polarisation of Λ is found to be negative while no polarisation is usually observed for $\bar{\Lambda}$.

2 Some authors use the opposite convention, defining $\hat{n} = \frac{\vec{p}_\Lambda \wedge \vec{p}_b}{|\vec{p}_\Lambda \wedge \vec{p}_b|}$, which by property of the vector product leads to a minus sign on the final polarisation results.

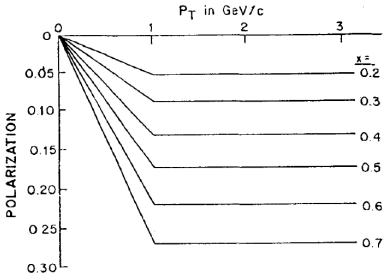

Figure 5.: Scheme of the measured Λ polarisation as a function of p_T for different x_F values [29].

- It is independent of the energy of the reaction ($\sqrt{s}$).
- Secondary Λ are usually not polarised.
- It depends strongly on the transverse momentum and in particular the absolute value rises linearly with p_T, for $p_T < 1$ GeV/c and the slope increases with x_F.
- For $p_T > 1$ GeV/c $|P_\Lambda|$ is independent of p_T and rises linearly with x_F.

Most of the data on Λ polarisation from pp collisions are consistent with a very schematic view presented in Fig. 5 from Ref. [29]. It shows the Λ polarisation for proton hadron interactions as a function of p_T for different x_F values. The figure is obtained from the compilation of many different experimental results but represents a reference scheme rather than a fit to them.

In the following will review some models which try to explain the theoretical origin of the polarisation. We will concentrate mainly on a semi-classical view and on a very modern approach, because we want to present the variety of models which are applicable to this phenomenon rather than furnish a comprehensive review. For completeness we will briefly summarise the main aspects of other models without going into details.

For reference, we describe in Appendix B the principles through which the polarisation can be measured by exploiting the $\Lambda \to p\pi^-$ final state angular distributions.

1.2.6.1 *Semi-classical model for the Λ polarisation*

A qualitative explanation and quantitative estimation of the production of polarised Λ in proton proton collision can be given starting from the Lund model for baryon production. The model

assumes that the Λ particle is produced from an $s\bar{s}$ quark pair produced by string breaking, as explained in §1.2.2, and a di-quark ud in a spin singlet state. In Ref. [30] the authors assume that the $(ud)_0$ di-quark comes from the spectators quarks of one of the colliding protons; however the following derivation is valid also for di-quarks produced in the hadronization process as far as they are spin singlets. It can be easily noticed that within this mechanism the spin of the outgoing Λ is completely determined by that of the s quark.

It is also assumed that in the breaking of the string the transverse momentum is conserved so that the two quarks are produced with opposite transverse momentum (k_T and $-k_T$). The transverse momentum of the Λ is then determined in part by the di-quark transverse momentum (q_T) but also by the s quark k_T. If the scattering angle is small enough these momenta sum up directly to give the transverse momentum of the Λ :

$$p_T \approx q_T + k_T \tag{1.13}$$

The condition of small scattering angles is satisfied if one studies the forward (or backward) region of proton-proton interactions; this is the case for the LHCb experiment as we will see in the next chapters.

The two quarks being massive they have to be produced at a certain distance from each other so that the energy stored in the field between them can be converted in their masses (cf. eq. (1.5)). Now it is easy to see that the quark pair will acquire in this way an angular momentum perpendicular to the plane given by the string axes and their transverse momentum. In order to conserve the angular momentum in the whole process the model hypothesises that the spin of the two quarks compensate this orbital angular momentum. Thus the polarisation of the Λ particle is merely due to the correlation between the quark transverse momentum and its spin.

Quantitatively, assuming as previously κ to be the energy density stored in the string and be the s and $\bar{s}$ quarks produced at a distance l with momenta $\vec{k}_T$ and $-\vec{k}_T$ respectively, energy conservation leads to the following relation

$$\kappa l = 2\sqrt{m_s^2 + k_T^2} \tag{1.14}$$

where m_s is the effective mass of the s quarks. The orbital angular momentum is then simply:

$$L = lk_T = 2k_T(m_s^2 + k_T^2)/\kappa \tag{1.15}$$

pointing along the orthogonal to the plane specified by the scattering (and string) direction and $\vec{k}_T$.

The angular momentum L is then compensated by the polarisation of the quarks P_q; this can be parametrised as:

$$P_q = L/(\beta + L) \tag{1.16}$$

where β is a convenient parameter to describe the degree of correlation. Note that different parametrisation can be used with some common features: rising about linearly with L for small L values and with a saturation at high transverse momentum.

In order to compute the shape of the Λ polarisation as a function of p_T one has to take into account the distributions of k_T and q_T. The s quark transverse momentum distribution as obtained from the tunnelling effect of the Lund model is usually of the form:

$$\frac{dP}{dk_T} \propto e^{-(k_T/\sigma_k)^2} \tag{1.17}$$

due to the exponential suppression of the tunnelling process. Assuming different forms for the distribution of q_T the final results can be computed and are shown in Fig 6. Note that contrary to our assumed notation, the figures show the polarisation referred to the axis $\vec{p}_\Lambda \wedge \vec{p}_{beam}$ and hence have the opposite sign (positive instead of negative).

1.2.6.2 Λ *polarisation from polarised fragmentation functions*

Since experimental data suggests that polarisation does not vanish at high transverse momentum ($p_T > 1GeV/c$ and up to $p_T \sim 4GeV/c$) factorisation theorem becomes applicable so that a better understanding can come from this region where detailed calculations are more feasible.

In this context it has been proposed that the polarisation of Λ particles can be studied using *polarising fragmentation functions* (cf. [32, 33] and references therein).

As an example, if one considers one of the possible processes which can contribute to the production of polarised Λ, *e.g.* $qg \to qg$ the cross-section can be written in the form:

$$\sigma \propto q(x_1) \otimes g(x_2) \otimes \sigma_{qg\to qg} \otimes D_{\Lambda/q}(z) \tag{1.18}$$

where $q(x_1)$ and $g(x_2)$ are the quark and gluon densities in the first and second proton respectively, $\sigma_{qg\to qg}$ is the cross-section for the bare involved partons, and $D_{\Lambda/q}(z)$ is the Λ fragmentation function.

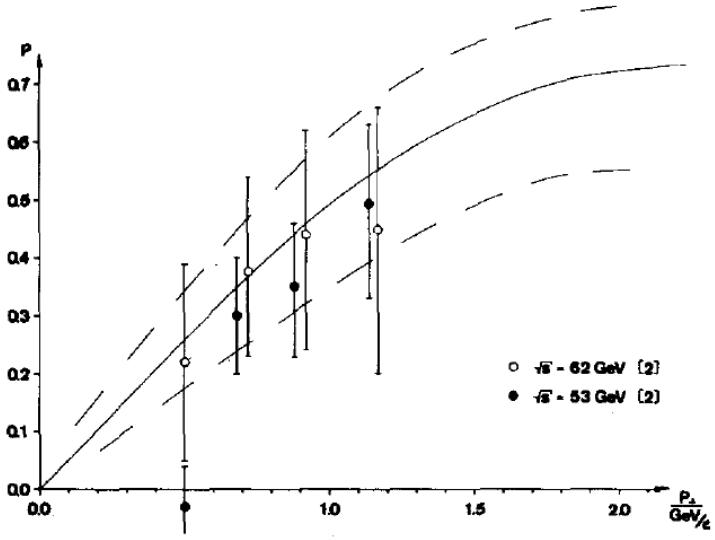

Figure 6.: The Λ polarisation (P) as a function of the transverse momentum. The different lines correspond to the central value and the limits of the predictions given with the Lund model in Ref.[30] while the experimental data points come from Ref [31]. The convention for the Λ polarisation is the opposite to the one adopted in this work.

A Λ polarisation can arise from Eq. (1.18) only from $D_{\Lambda/q}(z)$. At leading order it has to be symmetric by parity so that the polarisation must come from higher orders and should be suppressed as $\alpha_s m_q/\sqrt{s}$ [28]. However if a dependence on the spin and on k_T, the parton transverse momentum, is allowed in the fragmentation function a polarisation can be present also at the leading order. The so-called polarising fragmentation function $D_{1T}^{\perp}(k_T, z)$ is then introduced [34].

This approach is promising since at high energies the factorisation theorem allows to decouple the perturbative initial state from the non-perturbative fragmentation. The fragmentation functions have been extracted by fitting them to the existing data [32] with the restriction of $p_T > 1$ GeV/c to exclude the soft regime. Using these functions predictions of the polarisation can be made [32, 33, 35]. In figure 7 the predictions obtained in [32] are compared with data from [36] and good agreement is found.

A drawback is that in order for factorisation to hold, the final state must have high transverse momentum ($p_T > 1$GeV/c) and, in order for the polarisation to be sizable, also the longitudinal momentum must be large ($x_F \gtrsim 0.1$). These two conditions are

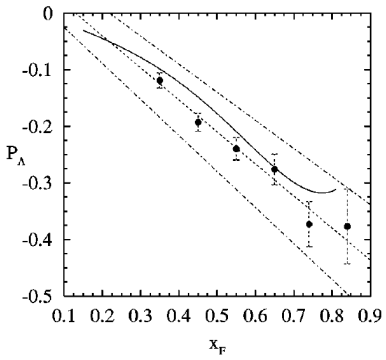

Figure 7.: Λ polarisation in unpolarised pp collisions as a function of x_F. The predictions of Ref [32] are compared with data from [36] and good agreement is found.

not always verified in high energy collisions; strange hadrons production in fact is often present in soft collisions so that the transverse momentum is usually very low. Moreover being the collisions in the center of mass system rarely particles have a considerable portion of the projectile energy.

However continuations of this work in different fields are giving promising predictions for the measurement of the Λ polarisation also at high energy colliders [35, 33, 37] In particular in [37] the authors suggest that at small x_F the polarisation can be measurable in the $pp \to \Lambda + \text{Jets} + X$ process. This reaction will be measurable at LHC in particular in the experiments which cover the low rapidity region.

As far as the LHCb experiment is concerned some other predictions show that the Λ polarisation can be very useful also in the forward region covered by this detector [38, 39]. The authors concentrate on $p - A$ reactions which at high energy should probe the gluon saturation scale. In particular the forward Λ production in these reactions is dominated by incoming quarks with high x which collide with high gluon density in the target. The pp collisions studied by the LHCb experiment can be taken as a reference but, being the involved energies so high, also a one of the possible $p - A$ reactions which could probe this phase. The authors of Ref [38] make very clear predictions of the way the polarisation should depend on the transverse momentum and on x_F. In particular $|P_\Lambda|$ should grow with p_T up to a certain maximum and then start decreasing. The position of this maximum is a measurement of the gluon saturation scale Q_s while its height (i.e. the maximum $|P_\Lambda|$ for a given reaction) depends on x_F. These

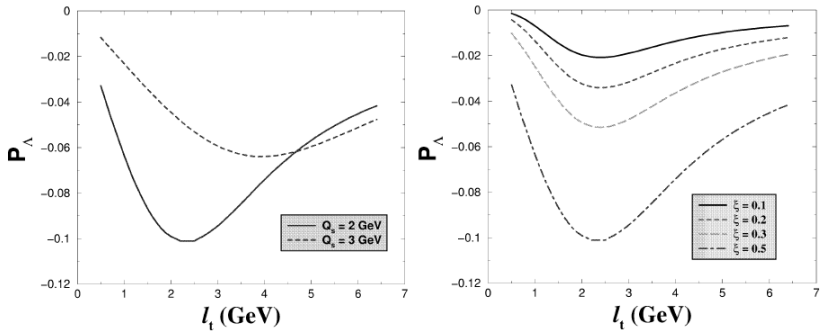

Figure 8.: Λ polarisation (P_Λ) as a function of the Λ transverse momentum (l_t) as predicted in Ref [38]. Left plots shows the Λ polarisation for two different gluon saturation scale Q_s values ($Q_s = 2, 3$ GeV) while the plot on the right shows P_Λ as a function of l_t at different x_F (denoted by ξ in this picture) values at a fixed $Q_s = 2$ GeV value.

two predictions are reported in Fig. 8 where i can be clearly seen that as the Q_s grows also the peak position in the P_Λ versus p_T moves to higher values. Fig. 8 right plot demonstrates that according to these predictions a non negligible polarisation can be seen also at very low x_F values (denoted by ξ in that picture) even if the height of the peak starts to be difficult to find due to the smoothness of the curve.

1.2.6.3 *Other models*

The models which we have described to understand the polarisation represent just the semi-classical beginning of this physical phenomenon explanation and one of the last attempts to explain it using QCD driven reasoning. However many different models during the past thirty years have tried to investigate the theoretical founding of the Λ polarisation. A review of this models can be found in Ref. [40] and a discussion on the theoretical basis of some of them is in Ref [41].

In the following we will briefly summarise the main ideas of this models, without going into details, in order to underline the variety of possible explanations for such a subtle phenomenon.

RECOMBINATION MODEL [42, 43] This semi-classical model attributes the Λ polarisation to a Thomas precession effect due to the acceleration of the s quark in the hadronisation process. While the qualitative behaviour of the polarisation

is correctly predicted, the experimental results of P_Λ as a function of x_F and p_T are not reproduced.

BERLIN MODEL [44, 45] The main idea is to relate the polarisation of hyperons to the left-right asymmetries observed in single -spin hadron-hadron collisions. In particular as the incoming spin is thought to move towards a preferred direction the outgoing hadron in these reactions, the polarisation is thought to come by the preferred direction to which the Λ is sent. Some quantitative predictions of the polarisation versus x_F appear to be in agreement with data but no p_T dependence is foreseen.

MILANO MODEL [46] The production of Λ particles is given in this model, besides direct production, by the decay of various baryon resonances produced off-shell. The model is able to reproduce the unpolarised cross-section for the production of hyperons in pp collisions but predicts a polarisation which decreases at high Λ p_T in contradiction with the experimental data.

SOFFER MODEL [47] relates the Λ polarisation in the $pp \to \Lambda X$ reaction to the one in the binary $\pi p \to K\Lambda$ process. However no dynamical source for this last polarisation is explained so that the problem of the polarisation origin is just moved to a different reaction. The model is able to predict roughly the p_T and x_F functionality while it cannot predict anti-hyperon production and polarisation being not due to low energy πp reactions.

We will not go into further details in the description of the theoretical interest of the Λ polarisation. Being a very complicated topic many different point of view contribute to uncovering its potential in understanding hadronisation and, in general, spin effects in unpolarised proton collisions.

However it is clear from this overview that despite the overwhelming amount of available data, no consensus is reached on its origin so that measurement of Λ polarisation at LHC could help in understanding the origin of this phenomenon.

1.3 RARE CHARM DECAYS

Among the searches for new physics beyond the Standard Model (SM), Flavour Physics plays a leading role in the indirect ones. In particular, the clearest place to look for deviation from the Standard Model predictions are processes which are forbidden or rare in it and instead can be allowed or enhanced in other physics scenarios.

Flavour changing neutral currents (FCNC) are forbidden at tree level in the Standard Model, so that the processes which happen just through them are sensitive as a test of the quantum structure of the theory.

Being allowed at loop level, FCNC usually mediate rare or very rare processes in the SM also because they suffer of suppression due to the Glashow-Iliopoulos-Maiani (GIM) cancellation. FCNC have been extensively studied in the *strange* and *beauty* sectors, *i.e.* primarily in processes which involve K and B mesons. In fact in the down-type quark sector the GIM suppression is less effective due to the presence of top-quarks running in the loops so that there is an effective decoupling with respect to the other diagrams, owing to the large t mass.

Within the *charm* sector FCNC are instead most effectively suppressed due to the absence of high mass down type quark. Therefore within the SM $D^0 - \bar{D}^0$ mixing and rare D decays have very small values. These processes then can receive contributions from new physics scenarios which can be up to several orders of magnitude larger than the SM ones.

Among these processes we have considered the $D^0 \to \mu^+\mu^-$ decay because of its clear signature from the experimental point of view, which can be detected in the LHCb experiment thanks to its high precision spectrometer, including the muon detectors, and the high statistics furnished by the LHC.

The current experimental limit for the branching ratio has been set by the Belle experiment and is [48]:

$$\mathcal{BR}(D^0 \to \mu^+\mu^-) < 1.4 \cdot 10^{-7} \tag{1.19}$$

at a 90% confidence level. As we shall see this is still very far from the SM branching ratio but is beginning to put constraints on the new physics parameters space.

In the following we will summarise the predictions of the SM for this channel and then we will briefly review the possible contributions of some new physics scenarios.

1.3.1 $D^0 \to \mu^+\mu^-$ *decay in the Standard Model*

Within the Standard Model two kinds of contributions to the $D^0 \to \mu^+\mu^-$ decay are present: the *short distance* contribution due to perturbatively calculable amplitudes and the *long-distance* contribution due to long-range propagation of intermediate hadronic states, of non-perturbative nature.

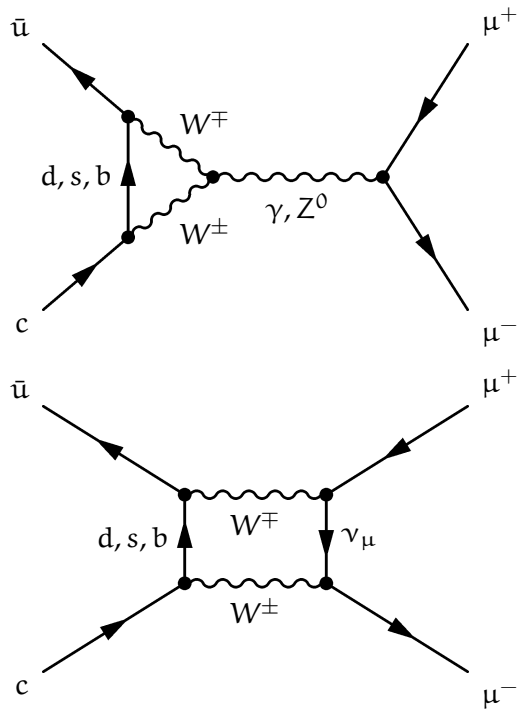

Figure 9.: Feynman diagrams of two possible Standard Model contributions to the FCNC $D^0 \to \mu^+\mu^-$ decay.

The short-distance contribution is at one loop in the standard model. Feynman diagrams of two possible contributions are shown in Fig. 9. These calculations are usually treated using an effective hamiltonian which has the W and b contributions integrated out as their respective thresholds are reached in the

renormalisation group evolution. The effective Hamiltonian is given by [49]:

$$\begin{aligned}\mathcal{H}_{\text{eff}} &= -\frac{4G_F}{\sqrt{2}}\left[\sum_{q=d,s,b} C_1^{(q)}(\mu)O_1^{(q)}(\mu) + C_2^{(q)}(\mu)O_2^{(q)}(\mu)\right. \\ &\quad \left. + \sum_{i=3}^{8} C_i(\mu)O_i(\mu)\right], \; m_b < \mu < M_W \\ \mathcal{H}_{\text{eff}} &= -\frac{4G_F}{\sqrt{2}}\left[\sum_{q=d,s} C_1^{(q)}(\mu)O_1^{(q)}(\mu) + C_2^{(q)}(\mu)O_2^{(q)}(\mu)\right. \\ &\quad \left. + \sum_{i=3}^{8} C_i'(\mu)O_i'(\mu)\right], \; \mu < m_b\,, \end{aligned} \tag{1.20}$$

with the O_i form a complete operator basis, and C_i are the corresponding Wilson coefficients. Here we do not give the explicit form of the operators, which can be easily found in the literature. The variable μ represents the renormalisation scale and the lower part of Eq. (1.20) indicates the condition in which the b quark has been integrated out. Within this approach the dependence on the Cabibbo-Kobayashi-Maskawa (CKM) matrix elements is contained in the Wilson coefficients.

The general form for the amplitude describing the $D^0(p) \to \mu^+(k_+, s_+)\mu^-(k_-, s_-)$ process is

$$\mathcal{M}_{D^0\to\mu^+\mu^-} = \bar{u}(k_-, s_-)\left[A_{D^0\mu^+\mu^-} + \gamma_5\, B_{D^0\mu^+\mu^-}\right] v(k_+, s_+) \tag{1.21}$$

and the associated decay rate is

$$\Gamma_{D^0\to\mu^+\mu^-} = \frac{M_D}{8\pi}\sqrt{1-4\frac{m_\mu^2}{M_D^2}}\left[|A_{D^0\mu^+\mu^-}|^2 + \left(1-4\frac{m_\mu^2}{M_D^2}\right)|B_{D^0\mu^+\mu^-}|^2\right]\,. \tag{1.22}$$

The $D^0 \to \mu^+\mu^-$ decay is given by the basic transition $c\bar{u} \to \mu^+\mu^-$. Following the derivation in Ref. [49] we can write the short distance contribution amplitude ($\mathcal{O}(\alpha_s)$ corrected) to this transition as:

$$B^{(s.d.)}_{D^0\mu^+\mu^-} \simeq \frac{G_F^2 M_W^2 f_D m_\mu}{\pi^2} F \tag{1.23}$$

where

$$F = \sum_{i=d,s,b} V_{ui}V_{ci}^*\left[\frac{x_i}{2} + \frac{\alpha_s}{4\pi}x_i\cdot\left(\ln^2 x_i + \frac{4+\pi^2}{3}\right)\right] \tag{1.24}$$

with $x_i = m_i^2/M_W^2$. While The amplitude $A_{D^0\mu^+\mu^-}$ vanishes due to the equations of motion. Note that the explicit dependence on muon mass in (1.23) in the decay amplitude makes the corresponding $D^0 \to e^+e^-$ even more suppressed with respect to the $D^0 \to \mu^+\mu^-$ case. This dependence reflects simply the helicity suppression of this kind of decay. This calculation lead to an overall short-distance contribution to the $D^0 \to \mu^+\mu^-$ decay which gives a branching ratio:

$$\mathcal{BR}^{s.d.}(D^0 \to \mu^+\mu^-) \simeq 10^{-18} \tag{1.25}$$

very far from being detectable by current and near future experiments.

However, within the SM also long distance contributions to the $D^0 \to \mu^+\mu^-$ decay are present. These are of two types: *single-particle* and *two-photon*.

The amplitude for the single-particle contribution can be written as

$$B^{(mix)}_{D^0\mu^+\mu^-} = \sum_{P_n} \langle P_n|\mathcal{H}_{wk}|D^0\rangle \, \frac{1}{M_D^2 - M_{P_n^2}} \, B_{P_n\mu^+\mu^-} \tag{1.26}$$

where $P_n = \pi^0, \eta, \eta'$ and $B_{P_n\mu^+\mu^-}$ is the corresponding amplitude for the $P_n \to \mu^+\mu^-$ process. The contribution of these processes to the $D^0 \to \mu^+\mu^-$ branching ratio is in total of the order of 10^{-18}.

The second contribution comes from the two-photon intermediate state which can be estimated to be:

$$\mathcal{BR}^{(\gamma\gamma)}(D^0 \to \mu^+\mu^-) \simeq 2.7 \times 10^{-5}\mathcal{BR}(D^0 \to \gamma\gamma)\,. \tag{1.27}$$

In fact, this is the largest contribution to the $D^0 \to \mu^+\mu^-$ branching ratio, being $\mathcal{BR}(D^0 \to \gamma\gamma) \gtrsim 10^{-8}$ so that the SM prediction for this breaching ratio is [49]:

$$\mathcal{BR}^{SM}(D^0 \to \mu^+\mu^-) \gtrsim 10^{-13} \tag{1.28}$$

Of course, this is still out of reach for the present experiments, but as we will see in the next section, new physics can contribute up to several orders of magnitude to this channel so that it represents a good testing ground for these models.

1.3.2 $D^0 \to \mu^+\mu^-$ *decay in New Physics scenarios*

Different new physics scenarios can give contributions to the $D^0 \to \mu^+\mu^-$ decay and some of them can be orders of magnitude larger than the SM one.

The introduction of new particles in such theories leads to the rise of tree level amplitudes or contributes to the loop level sector for this channel. However, each new particle can contribute also to different processes so that for every new theory the parameter space can be as tight as present measurements allow it to be.

Particularly, the rate at which the $D^0 \to \mu^+\mu^-$ decay happens can be strictly related to the level of $D^0 - \bar{D}^0$ mixing [50]. Hence the present measurement of $x_D = \Delta M_D/\Gamma_D$ leads to constraints on the $D^0 \to \mu^+\mu^-$ branching ratio as well.

The general form for the $D^0 \to \mu^+\mu^-$ rate reported in Eq. (1.22) is valid also for the new physics scenarios and the relative new particle contributions will be evident in the in the various Wilson coefficients contribution to A and B.

We will not report in detail the different models and the related calculations for our channel, but limit ourselves to review the basic concepts and results of the ones which could enhance significantly its branching ratio.

1.3.2.1 *Generic tree-level amplitudes*

The contribution of new particles mediating the $D^0 \to \mu^+\mu^-$ reaction can be analysed also in a more general fashion, considering generic possible new tree-level amplitudes.

SPIN 1 BOSON As far as a generic a spin 1 particle V with neutral flavour changing interactions is considered the $D^0 \to \mu^+\mu^-$ branching ratio can be written as[50]:

$$\mathcal{BR}^{(V)}_{D^0\to\mu^+\mu^-} = \frac{f_D^2 m_\mu^2 M_D}{32\pi M_V^4 \Gamma_D}\sqrt{1-\frac{4m_\mu^2}{M_D^2}}\left(g_{V1}-g_{V2}\right)^2\left(g'_{V1}-g'_{V2}\right)^2 \quad (1.29)$$

where g_{V1} (g_{V2}) and g'_{V1} (g'_{V2}) are the couplings with left-handed (right-handed) quarks and leptons respectively and M_V is the mass of the considered boson.

SPIN 0 BOSON On the other hand, if a spin-0 boson S is considered the branching ratio takes the form:

$$\mathcal{BR}^{(S)}_{D^0\to\mu^+\mu^-} = \frac{f_D^2 M_D^5}{128\pi m_c^2 M_S^4 \Gamma_D}\sqrt{1-\frac{4m_\mu^2}{M_D^2}}\left(g_{S1}-g_{S2}\right)^2 \times\left[\left(g'_{S1}+g'_{S2}\right)^2\left(1-\frac{4m_\mu^2}{M_D^2}\right)+\left(g'_{S1}-g'_{S2}\right)^2\right] \quad (1.30)$$

where g_{S1} and g'_{S2} are the quark couplings for left to right-handed quark anti-quark interactions and vice versa respectively,

while the primed quantities are referred to leptons. Now, if only scalar couplings are allowed ($g_{S1} = g'_{S2}$) the different contributions to the $D^0 \to \mu^+\mu^-$ cancel out exactly so that no contribution comes from this tree-level amplitudes and loops must be considered.

1.3.2.2 *Supersymmetry with R-parity violation*

Supersymmetric theories associate to SM particles a "partner" assuming a symmetry between boson and fermions is present but broken at the energy scales typically probed by present experiments.

Supersymmetric particles, not observed so far, can contribute to SM processes and hence enhance rare decays as the $D^0 \to \mu^+\mu^-$ studied here. Considering the simplest extension of the SM, the Minimal Supersymmetric Standard Model, or MSSM, it has been shown that no sizable contribution come from this model to the $D^0 \to \mu^+\mu^-$ branching ratio[50].

Within Supersymmetric models, the R-parity conservation prohibits the violation of the lepton and baryon numbers conservation. However different symmetries can be advocated to prevent such violations without an explicit R parity conservation. If one considers R-parity violating ($\not{R}_p$) models there can be terms which allow tree-level contributions to the $D^0 \to \mu^+\mu^-$. In terms of the couplings given by these contributions the $D^0 \to \mu^+\mu^-$ branching ratio can be written as:

$$\mathcal{BR}^{\not{R}_p}_{D^0\to\mu^+\mu^-} = \frac{f_D^2\, m_\mu^2\, M_D}{\Gamma_D}\left[1-\frac{4m_\mu^2}{M_D^2}\right]^{1/2}\frac{\left(\tilde{\lambda}'_{22k}\tilde{\lambda}'_{21k}\right)^2}{128\pi m^4_{\tilde{d}_k}} \quad (1.31)$$

where λ'_{ijk} stand for the coupling that in this model weights the transition between the i-generation lepton, j-generation up-type quark and j-generation down-type quark (or the corresponding super partners).

Different rare D decays (but also some rare K decay) can impose constraints on the coupling parameters. In particular exploiting bounds from the $D \to \rho\mu^+\mu^-$ and $D \to \rho\pi^+\pi^-$ decays [51] the branching ratio can be written as[52]:

$$\mathcal{BR}^{\not{R}_p}_{D^0\to\mu^+\mu^-} < 3.5\cdot 10^{-7}\left(\frac{\tilde{\lambda}'_{22k}\tilde{\lambda}'_{21k}}{0.004}\right)^2 \quad (1.32)$$

with a clear dependence on the size of the involved couplings.

Conversely, relating the $D^0 \to \mu^+\mu^-$ branching ratio to the $D^0 - \bar{D}^0$ mixing, other authors [50], make the following prediction:

$$\mathcal{BR}^{\not{R}_p}_{D^0\to\mu^+\mu^-} \simeq 4.8\times10^{-7} x_D \left(\frac{300\ \text{GeV}}{m_{\tilde{d}_k}}\right)^2 \leqslant 4.8\times10^{-9}\left(\frac{300\ \text{GeV}}{m_{\tilde{d}_k}}\right)^2 . \tag{1.33}$$

with inverse proportionality on the mass of the supersymmetric partner of the down-type quarks.

As it can be seen the, depending on the parameters of the $\not{R}_p$ supersymmetry, the $D^0 \to \mu^+\mu^-$ branching ratio can be enhanced of several orders of magnitude so that it could be discovered at LHC or, in case of no signal, tight bounds on these parameters could be put.

We do not specify these kind of interactions, while we described separately the (loop-level) NP contribution from R-parity violating Supersymmetry since it gives the largest contribution and then is the most promising.

Moreover we must say that various other charm rare decays are also sensitive, even more than $D^0 \to \mu^+\mu^-$, to New Physics, but we restricted our analysis to this decay since it is the one that we chose for our experimental search, being the cleaner thanks to its simple di-muon signature.

Finally, from this brief review we would like to conclude that the $D^0 \to \mu^+\mu^-$ is a promising tool for the search of new physics beyond the Standard Model.

2

THE LHCB EXPERIMENT AND DETECTOR

The LHCb experiment [53] is dedicated to flavour physics studies at the Large Hadron Collider (LHC) [54] at CERN. In particular precision measurements of CP violation and rare decays in *beauty* and *charmed* hadrons will be performed for indirect searches of new physics beyond the Standard Model.

In order to accomplish such delicate measurements LHCb has been designed with some important characteristics. A flexible and yet robust trigger, described in §2.4, is needed to select many different final states in hadronic environment. The detection of short lived resonances and lifetime measurements require optimal vertex resolution, while good momentum and consequently invariant mass resolution help to reduce combinatorial background. Finally particle identification is a critical issue for final states distinction. In addition to muons and electrons and neutrals which are identified by means of muon chambers and calorimeters respectively, also charged hadrons (π, K, p) have to be distinguished through RICH detectors.

In the following the LHCb detector will be described in detail as well as its commissioning and performances.

2.1 DETECTOR DESIGN

The LHCb detector has the structure typical of a single arm spectrometer and covers the forward region of proton-proton interactions from 10 mrad to 300 (250) mrad in the bending (non bending) plane.

This peculiar geometry has been designed to detect the decay products of b and $\bar{b}$-hadrons, which are produced in the same forward (and backward) region at the typical LHC energies ($\sqrt{s} > 1$ TeV). For the same reasons, the LHCb detector is also well suited for c-hadrons studies.

The LHCb detector is placed in Intersection Point 8 of LHC, which formerly hosted the DELPHI experiment at LEP. In order to exploit the entire cavern length without further civil engineering work, the proton-proton interaction point of LHC has been displaced by 11.25 m from the centre to the side of the cavern.

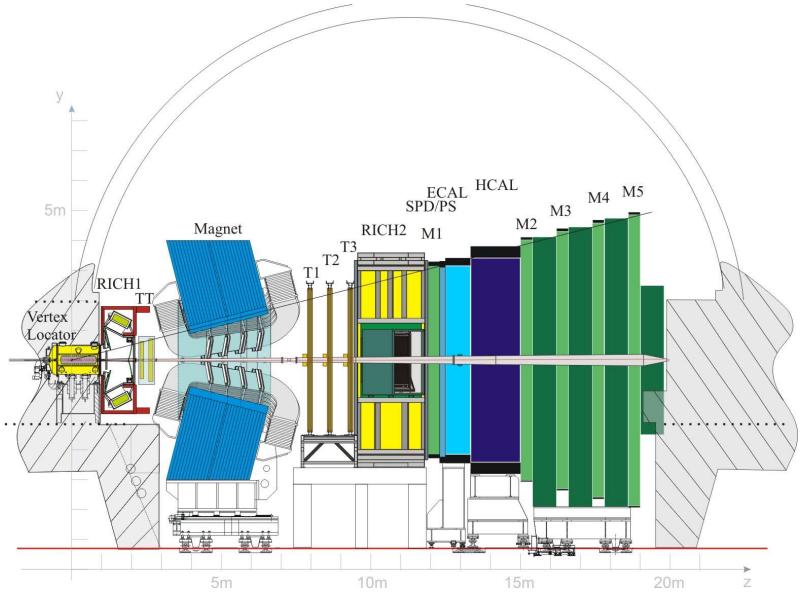

Figure 10.: Layout of the LHCb detector as seen in a vertical projection.

The detector layout is shown in Fig.10. A right-handed coordinate system is defined with the z axis along the beam direction and the y axis along the vertical.

Most of the LHCb sub-detectors are built in two separable halves which can be moved out horizontally for maintainance.

In order to minimise the interactions of particles with the detector inactive material, which would lower the detection efficiency and degrade the momentum resolution, special care has been put to reduce the detector material budged. After travelling about 10 m in the LHCb detector a particle, from the VELO to the entrance of RICH2, has traversed about 60% of a radiation length and 20% of an absorption length [55].

In the following all the sub-detectors will be described in detail.

2.2 TRACKING

The LHCb tracking system is composed of the Vertex Locator (VELO) and four tracking stations: the Tracker Turicensis (TT) upstream of the dipole magnet and the T1-T3 trackers downstream of the magnet. VELO, TT and the inner part of T1-T3, called Inner Tracker (IT), use silicon microstrip detectors, while the outer part of T1-T3 employs straw-tubes.

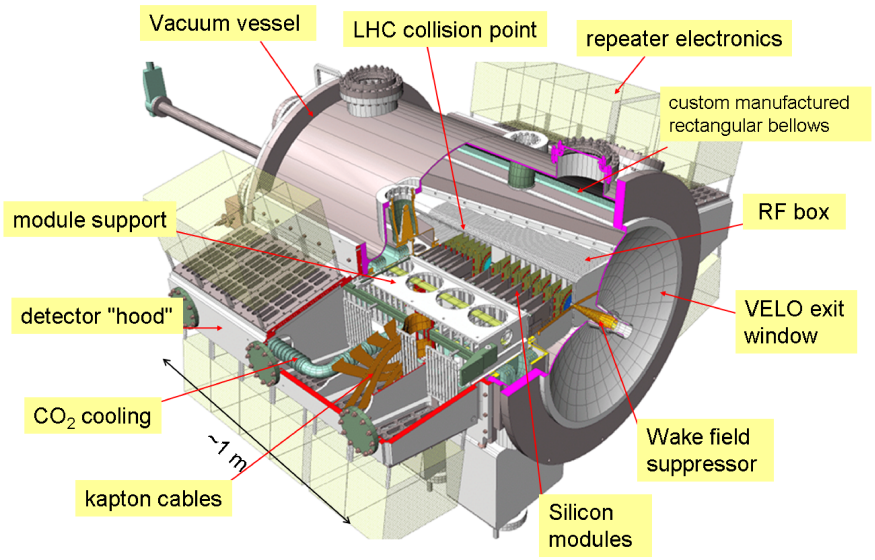

Figure 11.: Full layout of the Vertex Locator. The sensor modules are positioned in the very inner region, very close (8 mm) to the beams and share the same primary vacuum.

2.2.1 *Vertex Locator*

The VErtex LOcator (VELO)[56] is used to measure precisely the trajectories of particles very close to the proton-proton interaction point: this ensures an excellent resolution on vertex positions which enables to separate the secondary vertices due to b and c hadrons decays from the primary vertex (proton-proton interaction).

The VELO is built as a series of planar silicon detector modules, parallel to the vertical (x-y) plane, which measure the radial (r) and azimuthal (ϕ) coordinates of particles.

The VELO sensors are arranged along the beam direction and placed at a radial distance of only 8 mm from the beam. This does not allow a safe LHC beam injection, therefore the two halves of the VELO can be moved apart whenever needed, allowing a safe beam injection and ramping, besides giving access for maintainance purposes.

All the VELO detectors are inside a vessel which is maintained under the same ultra high vacuum as the machine (beam vacuum or primary); however sensors are held inside two boxes under a

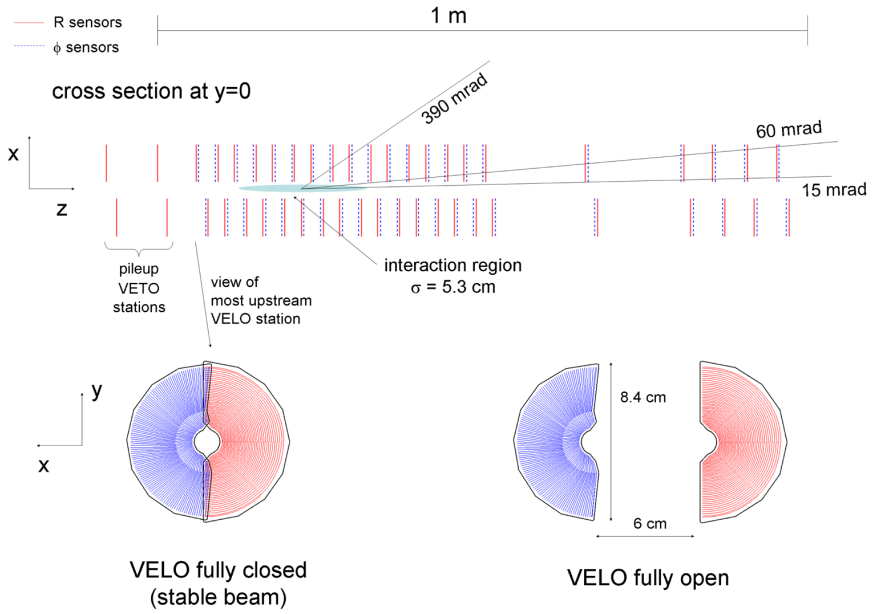

Figure 12.: Design of the VELO sensors positions in the xz plane (top) for the fully closed position and in the xy plane for the fully closed (left bottom) and open (right bottom) positions.

secondary (lower) vacuum. The walls of the boxes on the beam side are called RF foils, specially designed to prevent Radio-Frequency pickup of the VELO sensors from the LHC beams.

Two sensor planes, called *pile-up veto system*, whose function will be described in section 2.4.1.3, are placed upstream of the VELO.

The VELO is built of r- and ϕ-sensors to measure the radial and azimuthal variables respectively. Both types of sensor are constructed with the same technology, namely of silicon microstrips diodes 300 µm thick. Readout for both sensor types is placed at the outer radius.

The layout of both the sensors types is shown in Fig. 13. The microstrips of the r-sensor are concentric semi-circles, with their centres coinciding with the nominal LHC beam position. Each strip is divided in four segments 45° wide, this ensures a lower occupancy per readout channel and lower strip capacitance. The strip pitch increases linearly from a minimum of 40 µm to a maximum of 101.6 µm, at the outer radius of 41.9 mm. This variable pitch design makes the various hits of a track contribute with equal weight to the impact parameter precision.

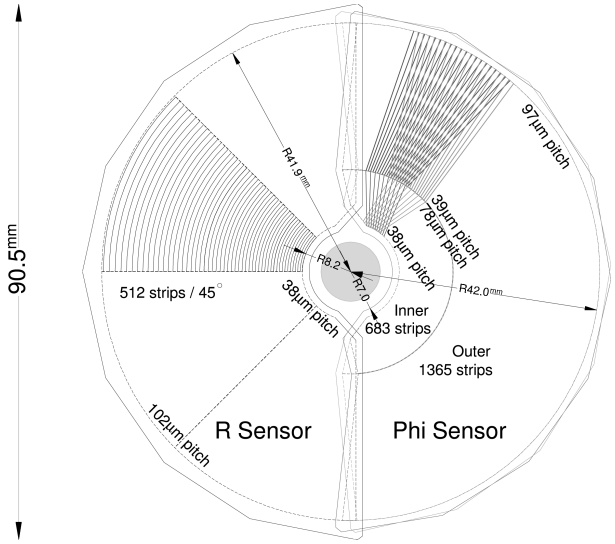

Figure 13.: Scheme of the r (left half) and ϕ (right half) VELO sensor types. For the ϕ sensors the strips of two adjacent modules, with different bendings, are shown.

The ϕ-sensors measure the azymuthal angle which form a cylindrical coordinate system together with r and z. This sensors are not simply made by radially disposed strips because this design would lead to unacceptably high occupancies of the strips due to a large area in the outer part. Therefore they are instead divided in two regions at a radius of 17.25 mm as is visible in Fig. 13. The inner part is made of sensor with pitch increasing radially from 39.3 μm to 78.3 μm, while the outer starts from a pitch of 39.3 μm ending at 97 μm. Moreover strips are skewed with respect to the radial direction of 20° (10°) for the inner (outer) region; adjacent ϕ-sensors have opposite skew which improves the rejection of ghost hits thanks to the stereo view.

Different systems play an important role in a delicate detector such the VELO. For safety reasons, the two halves of the VELO have to be moved out from the nominal position during beam injection and ramping. Moreover, the position of the sensors has to be optimised, even on a fill by fill basis, to have their centres coinciding with the beam. Hence, a very precise movement system have been designed for the VELO, which can set the position of the two halves with an accuracy of about 10 μm.

The RF-boxes which contain the VELO sensors, are very thin to minimise the material budged, but are exposed on one side to the LHC machine Ultra High Vacuum (10^{-8}mbar). For this reason a

vacuum system has been put in place in order to maintain also their inner region under vacuum, with a residual pressure of the order of 10^{-4}mbar limited by detectors and cables outgassing.

Finally, in order to limit radiation damages to the silicon sensors, they should be maintained in operation at a temperature below -5°C. This cooling is achieved with a cooling system which uses two-phase CO_2.

The VELO detector design was optimised to minimise the amount of material traversed by particles, while still providing a good geometrical acceptance. Each of the tracks originating from the interaction point, and inside LHCb acceptance (*i.e.* pseudorapidity $1.6 < \eta < 4.9$), pass through at least three modules. Detailed simulations have calculated the amount of material traversed by each of this tracks which in average is 17.5% of a radiation length, with the largest contribution coming from the RF-foil.

The individual strip resolution has been determined from test beam measurements and is clearly a strong function of the strip pitch. The best raw resolution is 7 μm.

2.2.2 *Silicon Tracker*

The Silicon Tracker (ST) is a project common to both the Tracker Turicensis (TT)[57] and the Inner Tracker (IT) [58] detectors. Indeed they have are very similar, using silicon microstrips with a strip pitch of 200 μm. The TT is placed upstream of the dipole magnet, while the IT is the inner part of the three tracking stations (T1-T3) placed downstream of the magnet.

Each of the four ST stations is composed by four detector layers with the so called *x-u-v-x* arrangement of strips directions: first and fourth layers have vertical strips, while *u-v* have layers with strips rotated by $\pm 5°$. This layout is designed in order to have the best hit resolution in the x direction (along the bending plane), without loosing the stereo view of the tracks.

2.2.2.1 *Tracker Turicensis*

The TT detector is composed of four sensors which are housed in module electrically and thermally insulated. The volume is maintained at a working temperature of 5°C. The four sensors are divided in two pairs separated by 27 cm along the beam axis to allow a better pattern recognition.

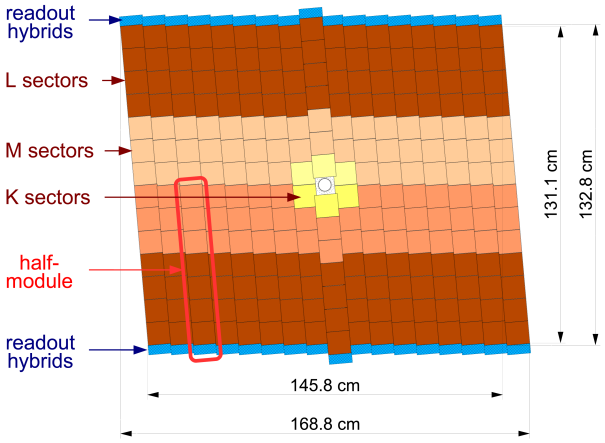

Figure 14.: Layout of one of the TT layers. The different readout sectors are shown with different shadings.

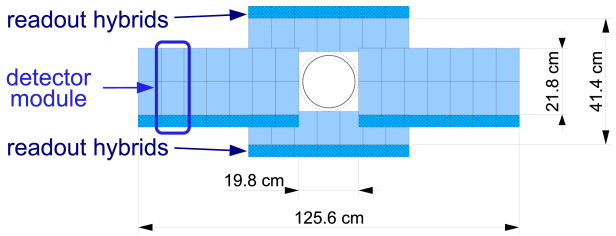

Figure 15.: Layout of one of the IT layers. The different modules placed just around the beam-pipe are shown.

The layout of one of the layers is shown in Fig. 14. It consists of different modules put side by side. Each single module covers half of LHCb acceptance in height. The different modules are slightly staggered in order to be overlapped by a few millimetres; this prevents acceptance gaps and helps the relative alignment between modules.

Each of the modules is made of seven silicon sensors placed in row. The silicon sensors are 500 µm thick and each of them is composed of 512 silicon strips with a pitch of 183 µm.

2.2.2.2 *Inner Tracker*

Each of the three IT stations is composed of four detector boxes disposed around the beam-pipe in a cross shape as shown in Fig. 15. The IT detector boxes, like the TT ones, are maintained at a temperature of 5°C.

Each detector box contains 4 layers of detectors, in the already described *x-u-v-x* configuration. Each of the layers consists of 7

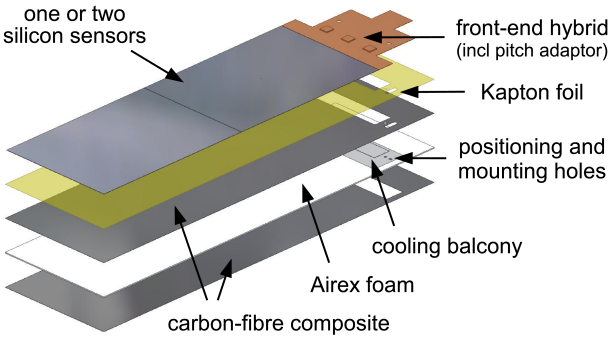

Figure 16.: Exploded view of a two-sensor module of the IT.

sensors modules. Adjacent modules are staggered in z by few millimetres and overlap in x by 3 mm to avoid acceptance gaps and facilitate the relative alignment of the modules.

Each detector module consists of one (above and below the beam pipe) or two silicon sensors plus a front-end readout hybrid; an exploded view of a two-sensor module is shown in Fig. 16. Each of the sensors is almost identical in design to the ones of the TT. They are single sided p^+-on-n sensors, carrying 384 silicon strips with a strip pitch of 198 µm.

2.2.2.3 *Performance*

Extensive measurements were made to validate the expected performances of the Silicon Detector. Signal-to-noise ratio was found in agreement with the expectations around 12:1. The corresponding total detection efficiency was found to be above 99.8%.

The spatial resolution was also measured and found to be 50 µm in agreement with the design specifications.

From detailed simulations the strip occupancy was found to be between 3.5% and 0.35% for the TT, depending on the proximity to the beam axis, while for the IT the occupancy is between 2.5% and 0.5%.

A careful analysis of the material budget has been also performed. For the TT, where most of the dead material (supports, cooling etc.) is located outside the LHCb acceptance, the material present is equivalent to 0.04 X_0 half of which is due to the active detectors. For the IT however the dead material is inside LHCb acceptance, hence the material budged is less uniform and corresponds to about 0.035 X_0 but has peaks of 0.3 X_0 where cooling rods are present.

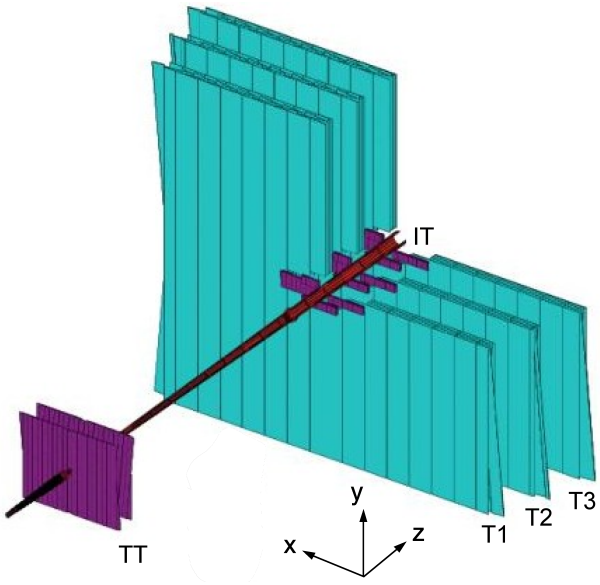

Figure 17.: Overall layout of the Outer Tracker (light blue) shown together with the TT, IT and beam-pipe

2.2.3 *Outer Tracker*

The Outer Tracker (OT)[59] is a drift-time detector which measures the position of charged particles over the whole LHCb acceptance, with the exception of the very inner area which is covered by the already described Inner Tracker.

This detector is made of gas filled drift tubes with a inner diameter of 4.9 mm. The straw tubes are arranged in gas tight modules. The used gas mixture is composed of Argon (70%) and CO_2 (30%) continuously flushed and purified in a closed loop. Detector modules are grouped in three stations (T1-T3) (Fig. 17) each of which has four layers arranged in the already described *x-u-v-x* stereo configurations, with the first and fourth layers with straw-tubes along the vertical direction, for a better measurement of the x directions in which tracks are bent, and the middle layers rotated by $\pm 5^\circ$ with respect to the vertical.

The different stations are divided in modules. The layout of one module is shown in Fig. 18: it is made of two staggered layers of drift tubes, which are read from the outer side of the module.

2.2.3.1 *Material budget*

All detector services and supports for the OT could be allocated outside the LHCb acceptance, so that the total material budget is

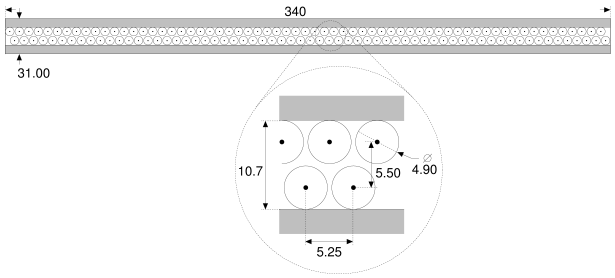

Figure 18.: Cross-section design of one of the OT modules. A zoom on the different strawtubes dimensions and positions is shown.

dominated by the active part of the detector, and is equivalent to 3.2% of X_0 per station and 9.6% of X_0 in total.

2.2.3.2 *Performance*

Tests with an electron beam were performed to asses the performances of the OT. Track finding efficiencies larger than 99% were found and position resolutions below 200 μm. Noise level was found to be very low, corresponding to 1 kHz per channel, corresponding to an average channel occupancy of $7.5 \cdot 10^{-3}$%. Moreover the crosstalk, or probability to find a coherent hit in neighbouring channels, was found to be lower than 5%.

2.2.4 *Magnet*

In order to measure charged particles momentum, trajectories have to be bended by the presence of a magnetic field. In LHCb this is ensured by a warm dipole magnet [60] placed between the first (TT) and the second group (T1-T3) of tracking stations. It has an angular coverage for the full LHCb acceptance, i.e. ±250 mrad in the vertical (non-bending) plane and ±300 mrad in the horizontal (bending) plane. While aiming at high magnetic field between the tracking stations, the magnet had to produced a very low residual field in the RICH1 detector (less than 2 mT) and the design is influenced by this constraint.

The magnet is composed of two identical coils which are disposed symmetrically with respect to the horizontal plane, and with an angular opening which follows LHCb acceptance; in Fig. 19 a schematic layout is shown. Each coil is conical with respect to its axis, and saddle shaped; it is composed of fifteen layers, grouped in five triplets, of Al–99.7 hollow conductor. Plates

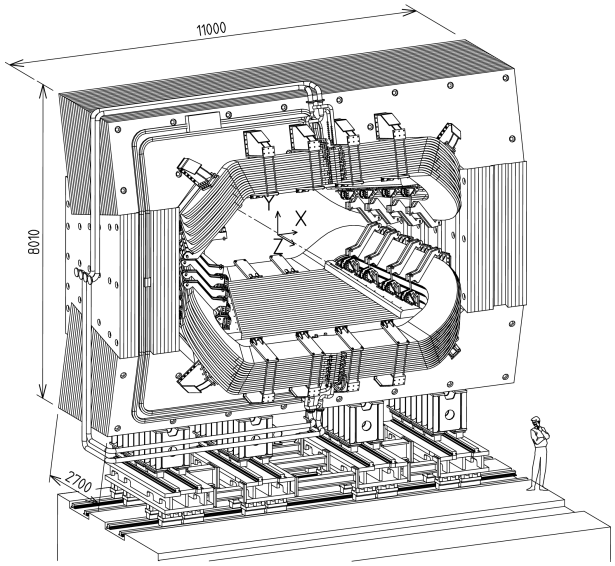

Figure 19.: Layout of the LHCb dipole magnet. In this figure the interaction point lies behind the magnet.

of laminated low carbon steel were used to form the magnet yoke which surrounds the coils.

2.2.4.1 *Field mapping*

The integrated magnetic field has to be known with a precision of about 10^{-4} in order to achieve the required momentum resolution on charged particles.

Extensive campaigns of field mapping were performed after the magnet installation, from the interaction point to the RICH2, along about 9 meters. Both field polarities were tested; in fact their knowledge is very important for systematics checks since the magnetic field approximately divides opposite charged particles to the different halves of the detectors. Using data from both field polarities helps understanding the detector and reducing residual acceptance asymmetries.

Hall probes, which could measure the 3 coordinates of the magnetic field, were used as field sensors, after being calibrated to a precision of 10^{-4}. Measurements were compared to magnetic field calculations obtained with TOSCA (Vector Field TM). The precision achieved for the field measurement has been of $4 \cdot 10^{-4}$. The main component, B_y, is shown in Fig. 20 for both polarities and is compared to the calculation results. An excellent agreement is reached.

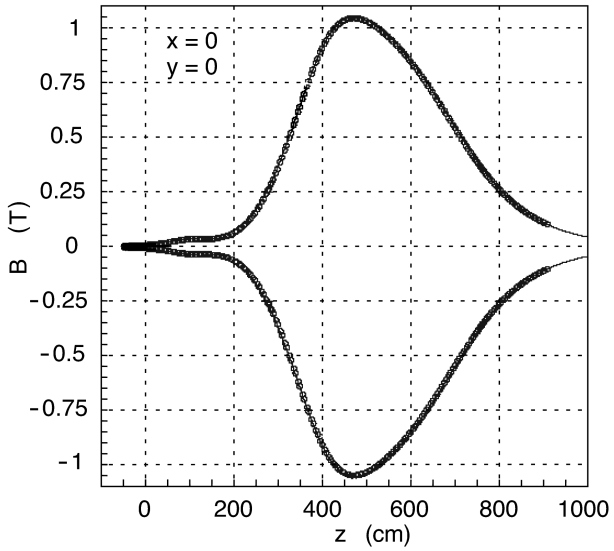

Figure 20.: Magnetic field along the z axis as mapped (points) and from theoretical predictions (continuous line).

A total integrated magnetic field of $\int Bdl \simeq 4\ T \cdot m$ is seen by a particle travelling the LHCb detector, and in particular $\int Bdl = 3.615\ T \cdot m$ is the value downstream of the TT stations.

2.3 PARTICLE IDENTIFICATION

Particle identification (PID) is a crucial requirement for the LHCb experiment. In particular in order to reconstruct the hadronic b decays is very important to be able to distinguish kaons from pions. Moreover calorimetry is fundamental in order to measure particles energy and for neutral hadrons and photons detection. Finally muon identification is of primary importance for leptonic decays analysis. In this section the different LHCb detectors designed for particle identification are presented: Ring Imaging Cherenkov detectors (RICH1 and RICH2) in §2.3.1, Hadronic and Electromagnetic calorimeters (ECAL and HCAL) in §2.3.2 and muon detectors in §2.3.3.

2.3.1 *RICH*

Two Ring Imaging Cherenkov (RICH) [61] detectors are present in LHCb to cover the full particles momentum range. RICH1, placed upstream of the magnet, covers the low momentum range ($\sim 1-60$ GeV/c) using areogel and C_4F_{10} as radiators. RICH2 placed

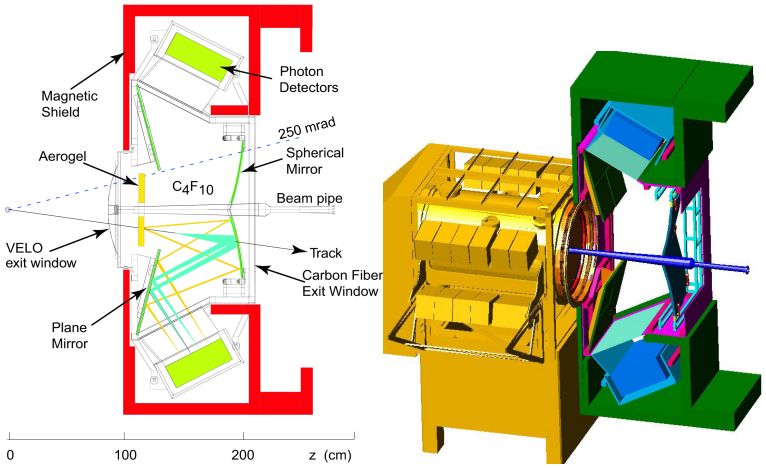

(a) (b)

Figure 21.: Layout of the RICH1 detector projected in the (y, z) plane (a) and a 3D model together with the VELO(b)

downstream of the magnet, covers the high momentum range (from ~ 15 GeV/c to beyond 100 GeV/c) using CF_4 as radiator. Both RICH detectors use a combination of flat and spherical mirrors in order to focus the Cherenkov light to photo-detectors placed outside the acceptance. The two RICH are described in detail in the following.

2.3.1.1 *RICH1*

The RICH1 detector is located upstream of the LHCb magnet between the VELO and the TT. It contains areogel and C_4F_{10} gas radiators, providing a sensitivity for identification of particles with momentum between ~ 1 and 60 GeV/c. RICH1 covers the full LHCb angular acceptance from ±25 mrad to 300 (250) mrad in the horizontal (vertical) plane. A scheme of the RICH1 layout is shown in Fig. 21.

When particles travel trough the radiators, Cherenkov photons are emitted along the whole path. The reconstruction of the Cherenkov emission angle is then affected by an error on the exact emission point. The parameters of the optical system have been optimised in designing a RICH in order to minimise this error, achieving a signal emission error of 0.67 mrad negligible with respect to other sources. Spherical mirrors are tilted with respect to vertical in order to send the light to the flat mirrors placed outside the angular acceptance. Being along the trajectory of particles, spherical mirrors had to be designed with low material

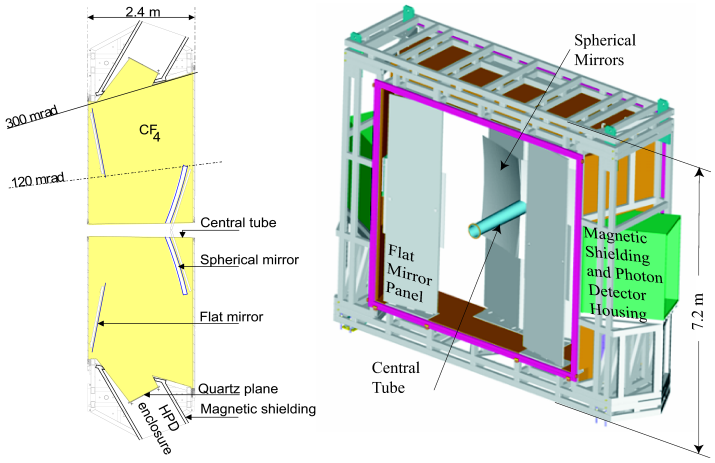

(a) (b)

Figure 22.: Layout of the RICH2 detector in the (x, z) plane (a) and a 3D model of it (b).

budget: carbon fibre reinforced polymer was used instead of glass mirrors, corresponding, in total, to 1.5% X_0. Thanks to a careful design, imperfections on the mirrors geometry give negligible contribution to the angle precision. Flat mirrors, placed in two planes below and above the beam-line, outside acceptance, are made of Simax glass; they contribute with an error < 0.2 mrad to the final precision.

The RICH1 (and RICH2) detector utilise Hybrid Photon Detectors (HPDs) to measure the emitted Cherenkov photons. In an HPD a photon hits the photocatode emitting an electron which is accelerated by a high voltage and guided to the sensitive surface, a silicon detector. These HPDs are divided in pixels so that the position of the incident photon can be measured. Dedicated HPDs were developed for LHCb; tests showed a quantum efficiency well above the specification minimum of 20% and a dark count rate of 5 kHz/cm^2, 10^3 times less than average expected occupancy. Magnetic fields produce deviation in the path of photo-electrons inside HPDs so that the detected image results distorted: HPDs operate properly at a maximum magnetic field of 3 mT. Hence, being near the LHCb dipole, they had to be shielded from the residual magnetic field, and are thus allocated in magnetic shield boxes.

2.3.1.2 *RICH2*

The RICH2 detector is located downstream of the tracking stations and before the first muon station (M1). It contains a CF_4 radiator, with sensitivity for identification of particles with momentum larger than 15 GeV/c up to well above 100 GeV/c. It has a reduced angular acceptance from 15 mrad to 120 (100) mrad in the horizontal (vertical) plane.

A schematic layout of RICH2 is shown in Fig. 22. Unlike the RICH1, RICH2 is developed horizontally, with photo-detectors allocated on the left and right of the beam-line. With a careful design the overall material budget, including the active radiator, is about 0.15 X_0.

The emission-point error has to be kept as small as possible: as for RICH1, an optimisation of the mirror parameters has minimised this error. The limiting factor on the angle precision is the chromatic dispersion of the radiator and corresponds to an uncertainty of 0.42 mrad. Due to a large surface to be covered spherical and flat mirrors are divided in smaller elements in RICH2: the spherical mirrors surfaces is obtained with hexagonal mirror elements, while the flat mirrors are composed of rectangular elements. The mirrors have been installed and aligned with a final precision of the order of 100 μm.

The same HPDs as for RICH1 were used in RICH2 and analogous considerations hold for their shielding.

2.3.1.3 *Performance*

Detailed studies both at test beam and with Monte Carlo simulations were made in order to assess the RICH performances. A RICH prototype, with its associated electronics, was tested with N_2 as radiator. on a 10 GeV/c pion beam at the CERN-PS. The distribution of reconstructed Cherenkov angles was found in good agreement with the simulations and the angle resolution was measured to be 1.66 ± 0.03 mrad.

A full description of the two RICH detectors have been implemented trough GEANT4 package in the LHCb simulations. The mean number of photo-electrons for particles travelling the RICH detectors was determined to be 6.7 for aerogel, 30.3 for C_4F_{10} and 21.9 for CF_4, while the single angular resolution were 2.6 mrad, 1.5 mrad and 0.7 for aerogel, C_4F_{10} and CF_4 respectively.

The final effect of this performances on the particle identification will be discussed in § 2.5.3.4.

2.3.2 *Calorimeter system*

The LHCb calorimeter system, besides providing energy measurements, plays a fundamental role in the first level of the trigger selecting high transverse energy (E_T) particles.

The overall design of the Calorimeter system is classical: an Electromagnetic Calorimeter (ECAL), to detect electrons and photons, is followed by an Hadronic Calorimeter (HCAL) for charged and neutral hadrons.

In order to select electrons from the high charged pions background, a pre-shower (PS) has been built before the electromagnetic calorimeter. Moreover, a scintillator pad detector is installed before the PS in order to select charged particles and reject background to electrons coming from high E_T π^0.

All the calorimeter subsystems follow the same working principle: light is produced by particles by scintillation and is subsequently read by photomultipliers after having been conducted through wavelength-shifting fibres (WLS).

For an optimal energy resolution on electromagnetic showers, they have to be fully contained on the ECAL, which has been designed to be 25 radiation lengths. On the contrary, for triggering on hadrons, such a good energy resolution is not needed so that HCAL is only 5.6 interaction lengths (minimising the occupied space).

The whole calorimeter system is segmented in the (x, y) plane; the segmentation increases in dimension for different sections moving away from the beam-pipe. In particular the SPD/PS and ECAL are segmented in three sections and with scaling widths in a projective design. HCAL is segmented in only two sections with larger sizes. A picture of this segmentation scheme is given in Fig. 23.

2.3.2.1 *The scintillator pad and pre-shower detector*

The SPD/PS detector is composed by two planes of scintillator pads of high granularity (12032 channels in total) with a 15 mm thick lead converter in between. The pre-shower lead converter corresponds to 2.5 X_0. As already said, the two detector planes are divided in three regions with different cell width in order to match the charged particles multiplicity which decreases with the distance from the beam-line. The cell size is slightly different for the two planes in order to accomplish the desired projectivity.

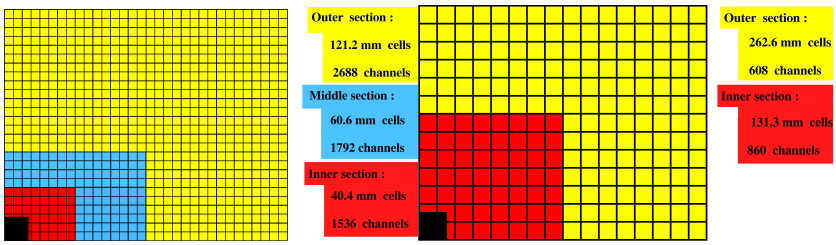

Figure 23.: A scheme of the segmentation of the calorimeter system in the vertical (x, y) plane. The ECAL segmentation, valid also for SPD/PS detectors, is shown on the left, while the right plot is for HCAL only.

The cell design is very simple: a pad of scintillator plastic is equipped with WLS fibres coiled and placed in a ring groove milled in it; both ends of the WLS fibre are read. Light, produced by a ionising particle in the scintillator is driven by the WLS to the detector exit were other (clear) fibres guide it to the PMTs. In order to be able to read the single fibres, the SPS/PS detector has been equipped with multianode photomultiplier tubes (MAPMT). In particular the two fibre lines coming from a single pad are read by a single MAPMT pixel.

The performances of the SPS/PS modules for e to π separation were assessed in test beam studies at the CERN SPS with electrons and pions with momentum between 10 and 50 GeV/c. Pions rejection always above 99.5 % was achieved with electron retention between 91% and 97% depending on the particle momentum. Photon to electron separation at the trigger level is achieved through the SPD information, however some processes can contribute to a photon background to the electrons. Apart from photon conversion before the SPD, two other background sources are present and have been studied with photons with momentum between 20 and 50 GeV/c:

- photon interactions in the SPD which can produce charged particles, for which measurements have shown a misidentification probability of about 0.8%;
- *back splash* interactions due to particles coming back from PS or ECAL electromagnetic showers, for which the measured probability is around 1%.

All these effects are integrated and in agreement with the prediction of the LHCb Monte Carlo generator simulations.

2.3.2.2 *Electromagnetic calorimeter*

The LHCb Electromagnetic calorimeter, ECAL, is designed with the classical shashlik technology: a sampling calorimeter is built alternating scintillator and lead pads with a readout based on plastic WLS fibres. While this technique has a modest energy resolution (if compared with other calorimeter types) fast time response, radiation resistance and reliability due to large past experiences are reached.

ECAL outer dimension follows LHCb projectivity, while the inner angular acceptance is limited at 25 mrad for both directions because of the high radiation doses at smaller angles. The three regions in which the calorimeter is divided are called inner, middle and outer, with increasing cell sizes.

Each cell of the calorimeter hosts a detector module which is the base unit of the detector. Each module is composed of alternated layers of 2 mm thick lead as converter and 4 mm thick scintillator tiles which are covered by 120 μm thick white reflecting paper. Each module corresponds to 25 X_0 in depth and a Moliere radius of 3.5 cm.

The scintillator pads are made of polystyrene with 0.25% PTP and 0.01% POPOP dopants. A light yield fluctuation of 2.5% RMS is reached among the different pads. Each of the lead and scintillator pads holds precisely positioned holes which host the WLS fibres bended in order to traverse each module twice. A light yield variation of 1.6% is reached by reading the fibres. Standard phototubes are used to read the light coming from the bunch of fibres of the modules: one, four and nine phototubes are used to read inner, middle and outer region modules respectively.

2.3.2.3 *Hadron calorimeter*

The hadron calorimeter (HCAL) of LHCb is a sampling calorimeter, build up of iron tiles as radiator and scintillating tiles as active material. As it can be seen in Fig. 24 the disposition of the different tiles is parallel to the beam axis and hence to the particle flow. The longitudinal length of the iron tiles correspond to the hadron λ_I in steel. WLS fibres are used to collect the scintillation light and drive it to the photomultipliers.

The HCAL is designed segmented in two regions, inner and outer, with different cell sizes (131.3 mm for the inner and the double for the outer region). The active tiles are made of polystyrene as the base plastic and PTP and POPOP as dopants, and wrapped in white reflecting paper. The WLS fibres are inserted at the edges

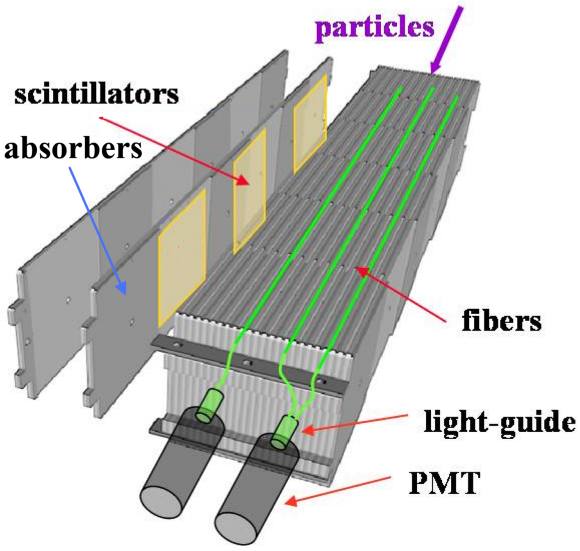

Figure 24.: Layout of a typical HCAL module cell. The structure divided in scintillator and absorber pads can be seen on the left.

of the tiles, and each of them collects light from three scintillating tiles along the direction of the development of the hadronic shower. Since the light degrades while propagating through the fibre, the optical contact is progressively reduced along the shower direction so that all the tiles contribute equally to the collected light. All the fibres from one cell are read by the same photomultiplier which is in optical contact with them through a small light mixer. As for ECAL, also for HCAL photomultipliers were shielded from the magnetic field by enclosing them with a MuMetal layer.

A special feature of HCAL is to have a device for self-calibration: a ^{137}Cs gamma source (with 10mCi of activity) can be transported in front of each module thanks to a computer controlled driving system. HCAL is then calibrated by measuring the PMT anode current while moving the gamma source to scan each module. Moreover by comparing the anode currents obtained at test beams, an absolute calibration to particles energy can be made, which can also help to cross-check the ECAL calibration.

2.3.3 *Muon system*

Muon detection and identification is fundamental i LHCb both for triggering and for reconstruction of many different physics channels either for CP violation and for rare b-hadron decays.

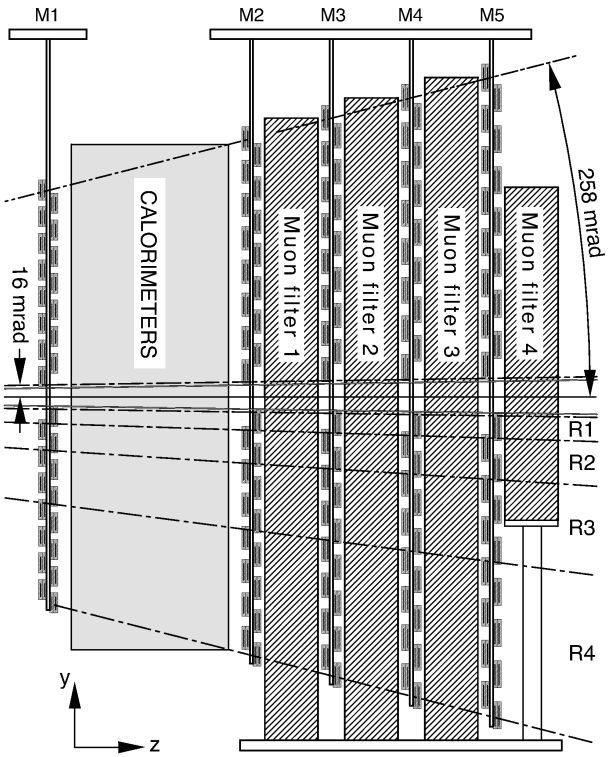

Figure 25.: Schematic view of the full MUON system.

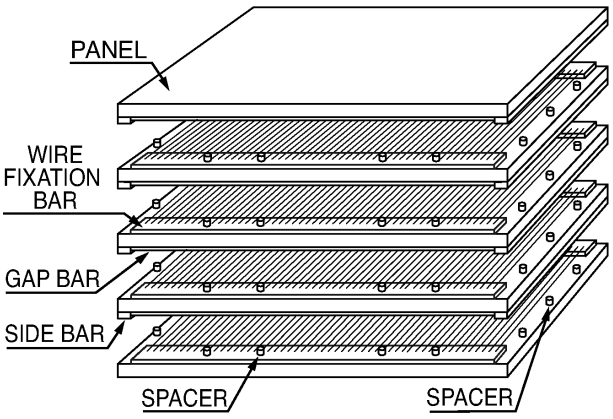

Figure 26.: Exploded view of one MWPC.

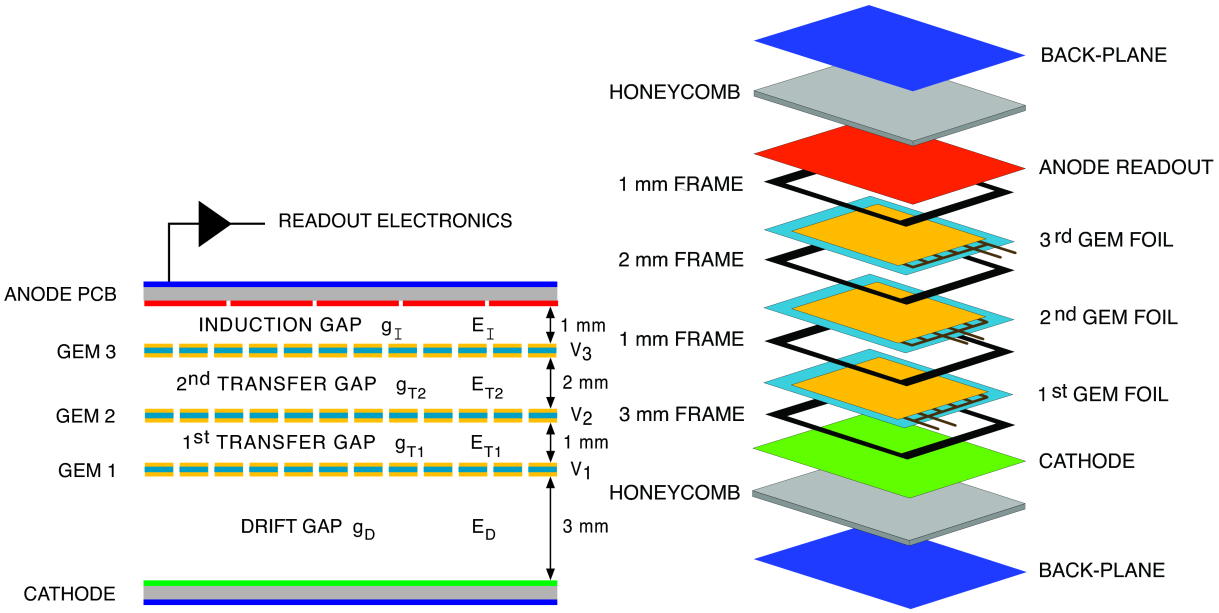

Figure 27.: Schematic view of one triple GEM detector.

The LHCb muon system is composed of five stations with angular acceptance from 20 (16) mrad to 306 (258) mrad in the bending (non bending) plane. The first station (M1) is placed upstream of the calorimeters while the other four (M2-M5) are placed downstream and intervealed by iron absorbers 80 cm thick. The total absorption length is about 20 λ_I if the calorimeters are taken into account, thus muons with at least 6 GeV/c of momentum can traverse all the 5 chambers.

The first three stations (M1-M3) have high spatial resolution in order to ensure a good transverse momentum reconstruction for triggering purposes, while M4 and M5, with limited spatial resolution are mainly used for identification of penetrating particles.

Each muon station is divided in four regions (R1-R4) with scaling dimension and granularity, doubling at each step: the same particle flux is thus expected in each region.

Multi-wire proportional chambers were chosen as detector technology for the entire muon system with the exception of the very inner region of the first station (M1R1) where, due the to high particle rate, triple-GEM detectors are used. In order to achieve an efficiency exceeding 95% in a 25 ns time window, a fast gas mixture and optimised charge collection geometry were studied for both technologies. In order to ensure high efficiency

each of the M2-M5 detector chambers is built with four gas gaps connected in OR; M1 MWPCs have just two gaps because of material budged minimisation, while M1R1 uses two superimposed triple-GEM chambers connected in OR.

Different readout technologies have been chosen for the various stations and regions by dividing the chambers in *logical pads* which define the spatial resolution of one hit. Logical pads may be different from physical pads segmentation either for cathode and for anode readouts. Most of the chambers are read through the different cathode segments; R4 chambers which don't need a high spatial resolution are read from group of wires which constitute the physical pad; R1-R2 of M2 and M3 use a mixed readout in order to achieve the higher resolution needed therein; finally M1R1 (triple-GEM) chambers use anode pads readout. A total of 122112 physical channels is present in the muon system connected in OR to form 25920 logical channels; by the combination of the logical channels 55296 logical pads are used in the muon tracking.

Each of the M2-M5 (M1) MWPCs is made of four (two) gas filled gaps where the anode wires are located intervealed by the cathode layers as shown in Fig. 26 while the external layers are grounded and act as electrical shield. The gas mixture is $Ar : CO_2 : CF_4$ (40 : 55 : 5) which provides a gain $G \simeq 10^5$ at a voltage of 2600-2700 V. Severe quality controls were performed in the MWPCs building process: the final wire pitch distribution has an r.m.s. of 16 μm and the maximum accepted noise rate was 1kHz per front-end channel, which has a no effect for the trigger.

As previously said, the innermost region of M1 is equipped with triple-GEM detectors which can be used in the high particle flux rate which is foreseen for this region at LHC (500 kHz/cm²). Each of these chambers has an active area of $20 \times 24\text{cm}^2$ and is built of two triple-GEM detectors superimposed and connected in OR. A triple-GEM detector consists of three gas electron multiplier foils (GEM) placed in a gas-filled gap between an anode and a cathode layers. Electrons, produced by a traversing ionising particle, are drifted and accelerated and pass through the GEM foils where are multiplied. After the last GEM foil the electron avalanche moves toward the anode inducing a current signal in its pads. A gas mixture of $Ar : CO_2 : CF_4$ (40 : 15 : 40) has been chosen allowing a time resolution better than 3 ns.

Extensive tests were performed on the muon chambers both in test beams and with cosmic rays. Measurements have shown that the desired high efficiency is reached by the MWPCs working with 4 gaps in OR; moreover tests with only 3 gaps in OR prove

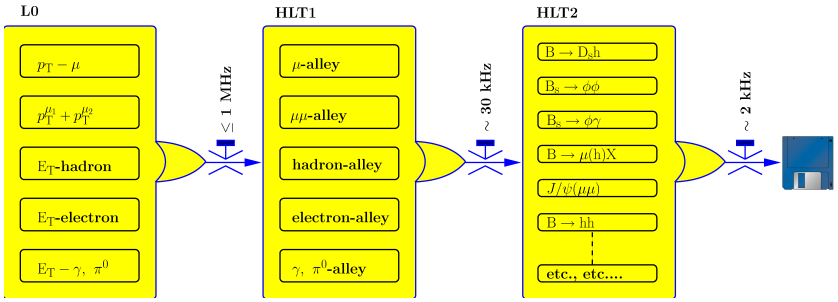

Figure 28.: Schematic data flow through the LHCb trigger system.

that a high efficiency can be maintained even in case one of the gaps is no more usable, providing robustness to the whole system. Similar tests performed on GEM detectors have shown a very high efficiency for the two layers operated in OR but also, increasing the detector gain, for single layers.

2.4 TRIGGER

The LHCb detector is designed to operate at an average luminosity of $2 \cdot 10^{32} cm^{-2} s^{-1}$, reduced with respect to the LHC nominal one ($\sim 10^{34} cm^{-2} s^{-1}$). In this conditions the average frequency of visible interactions is 10 MHz which, in order to be recorded on tape, has to be reduced to about 2 kHz. This reduction is achieved by means of two trigger levels: a Level-0 trigger (L0) and an High Level Trigger (HLT). A scheme of the data flow through the trigger system is shown in Fig.28. The L0, implemented with custom made electronics, reduces the event rate from 40 MHz to 1 MHz imposing constraints on the highest E_T hadron, electron and photon and the two highest p_T muons; global event cuts in order to reject multiple interactions and on the number of tracks are also applied. The HLT reduces further the rate from 1 MHz to 2 KHz using full event information in algorithms that run in a processor farm; after having confirmed the L0 decision, it further selects by requiring high p_T and impact parameter tracks and finally reconstructing inclusive and exclusive final states

The L0 and HLT triggers are describe in detail in the following sections.

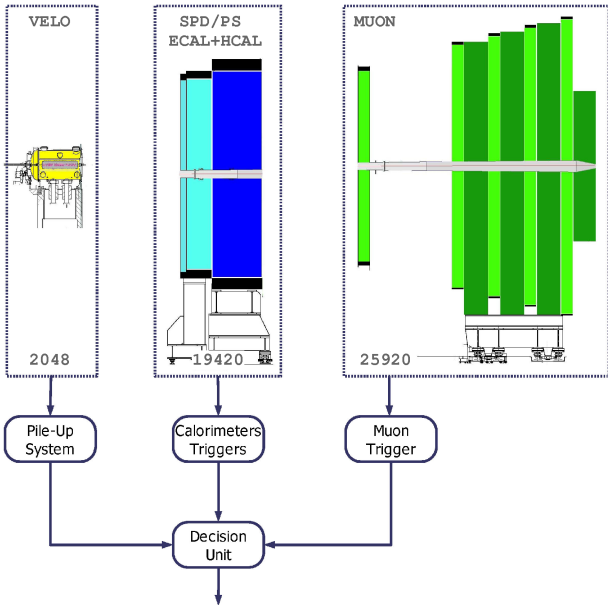

Figure 29.: Schematic view of the L0 information flow, which from the relevant subdetectors goes to the final decision unit through the three L0 trigger types.

2.4.1 *L0 Trigger*

The L0 trigger is subdivided in three main components: the muon L0 trigger, the calorimeter L0 trigger and the pile-up system; each of these component receives information from the detectors with same name. The collected information is sent to the L0 decision unit (L0-DU) which takes the final decision.

As far as the LHC nominal conditions are concerned (pp interactions at $\sqrt{s} = 14$ TeV and luminosity $\mathcal{L} = 2 \times 10^{32} cm^{-2} s^{-1}$) the typical L0 trigger threshold are: at least one HCAL cluster with $E_T > 3.5$ GeV (hadrons), an ECAL cluster with $E_T > 2.5$ GeV (electrons, photons, π^0) or a muon trigger given by one muon with $p_T > 1.2$ GeV or two muons with $p_T^1 + p_T^2 > 1$ GeV.

2.4.1.1 *L0 calorimeter trigger*

The calorimeter trigger looks for high transverse energy (E_T) particles exploiting the information from the whole calorimeter system. Electrons, photons, neutral and charged hadrons are selected from 2×2 cells clusters in SPD, PS, ECAL and HCAL. The cluster dimension is enough to contain the whole shower from a particle but not too large in order to avoid two particle showers to be summed.

L0 candidates are formed from the above information and selected in three stages.

1. Front-end cards of ECAL and HCAL manage 32 cells and select the highest 2×2 cluster.
2. ECAL is then merged with PS and SPD hits identifying the type of candidate: electron, photon or π^0.
3. Finally the highest E_T candidate is selected and the total E_T in HCAL, used to reject events without a visible interaction, and SPD multiplicity are computed.

In order to minimise the processing time, for each event, just the candidate with highest E_T is kept at each stage.

2.4.1.2 *L0 muon trigger*

The L0 muon trigger exploits tracks reconstructed from hits in the muon system. The muon system alone allows a $\sim 20\%$ resolution on the transverse momentum (p_T) of the muons.

The muon trigger is composed of four processors which analyse the 4 sectors of the muon system (corresponding to the four quadrants of the vertical (x, y) plane). The track finding starts using logical pads hits to reconstruct the first and second highest p_T muons. Seeds for the track finding are given by hits in the M3 station; for each seed hits are searched in the other muon stations along a straight line which joins the M3 hit and the interaction point. A Field-Of-Interest (FOI) region is defined in each station; the dimension of the FOI depends on the spatial resolution of the stations. If one hit is found in each of the M2-M5 stations a muon candidate is formed and, extrapolating to the M1 station the hit closest to the extrapolation is chosen. The track find is very simplified by the muon system geometry: being the whole design projective with respect to the interaction point a one (two) to one correspondence is present between logical pads in M2 and M3 and logical pads in M4 and M5 (M1).

The position of a track in the first two stations allows the measurement of the p_T and finally the candidate with highest p_T is selected and sent to the Decision Unit.

2.4.1.3 *L0 pile-up*

The pile-up system is dedicated to the rejection of events with multiple visible interactions. It exploits two sensor modules simi-

lar to the ones of the VELO and placed upstream of it in order to reconstruct the primary vertices positions.

The two sensor planes (A and B) are composed of two VELO r-sensors (See §2.2.1); the measured radii for each traversing track can be simply related to the interaction point position: if $k = r_B/r_A$ then

$$z_{PV} = \frac{kz_A - z_B}{k-1} \tag{2.1}$$

is the z position of the primary vertex from which the particle is originated. By combining all the z_{PV} measurements from hit combinations an histogram is derived which should show only one peak for single interaction and more than one peak for multiple-interactions. If by masking the highest found peak a second peak is found, with some requirements on its height, the event is vetoed and hence rejected by L0.

2.4.2 *High Level Trigger*

The High Level Trigger (HLT) is made of a C++ algorithm which runs on up to 2000 CPUs of the Event Filter Farm (EFF). These algorithms have access to the complete event information coming from the detector; unfortunately due to the high incoming event rate (1 MHz) just part of this information can be exploited according to the available CPU power. Being completely software based the HLT is completely flexible and can be changed at any moment to vary with beam conditions, energy and luminosity, and physics requirements.

The HLT is subdivided in two stages, HLT1 and HLT2. HLT1 has to confirm the L0 decision and to further reduce the rate at a level where the full patter recognition can be performed, i.e. 30 kHz; at this rate the HLT2 exploit the whole event information in order to reconstruct and select inclusive and exclusive final states.

2.4.2.1 *HLT1*

The HLT1 is divided in so-called "alleys", one for each L0 trigger line. L0 objects, calorimeter clusters and muon tracks, are then passed to the HLT1 together with the full event information. Different algorithms are used for the L0 confirmation:

- L0 $\rightarrow$T: reconstructs hits in the L0 object trajectory (or trajectory hypothesis for calorimeter clusters) starting from seeds

in the T stations and requires both a space and momentum match;

- L0 →VELO: starting from 2D tracks in the VELO using just r-sensors, after a χ^2 requirement with respect to the L0 object, 3D tracks and PV are reconstructed and tracks are matched to the L0 object;
- VELO→T: above-mentioned VELO tracks are propagated to T stations and matched as the L0 →T algorithm;
- T→VELO: analogous to the L0 →VELO but starting from a seed in the T stations.

Each of the HLT1 alleys employs a sequence of these algorithms in order to reduce the rate. As an example the muon alley tries to match L0 muon candidates using first the L0 →T algorithm to match the track and then the T→VELO, imposing a constraint on the minimum impact parameter of the muon with respect to the primary vertex.

2.4.2.2 *HLT2*

At the HLT1 output rate, the HLT2 is able to perform the full event reconstruction in the same way as in the offline analysis, with the exception of the track fitting which is not performed with a Kalman filter in this case. Common resonances are formed with loose requirements (e.g. $\phi \to K^+K^-$ or $J/\psi \to \mu^+\mu^-$) which are subsequently used by different lines.

The HLT2 final step requires cuts similar to an offline analysis reconstructing completely some exclusive final states (e.g. $B \to J/\psi\phi$) or inclusively (e.g. $B \to \phi X$). The output of the HLT2 is the logical OR of all the inclusive and exclusive selections and corresponds to a final rate of 2kHz which is stored on tape for offline analysis.

2.5 LHCB COMMISSIONING AND PERFORMANCES

The commissioning of LHCb [62] started in 2007 with tests of each of the subdetectors separately. Safety systems and hardware control and monitoring were initially tested. Hardware checks were then performed including power cables (high and low voltage), signal and trigger cables; exploiting calibration pulses, mapping and connectivity were tested in order to identify dead or noisy

detector channels and a first time alignment was done on the subdetectors.

After this first step the LHCb detector was commissioned as a whole to be ready to take data for the foreseen LHC start date of September 2008. The system control, which exploits PVSS SCADA to control processes and Finite State Machines for state and commands, was already taken from one console by a small shift crew. The detector readout was commissioned at 100 kHz limited by the network and event filter farm and a data storage at 2 kHz was already exploited.

2.5.1 *Commissioning with cosmic rays events*

The LHCb detector is not well suited for the detection of cosmic rays, which arrive mainly in vertical direction; nevertheless, even if at low rate (less than 1 Hz), about 10^6 events have been collected and used in order to understand the detectors behaviour.

Cosmic rays data have been useful for various tasks. The basic blocks of the trigger have been tested and commissioned successfully. A first spatial alignment and coarse time synchronisation have been executed on bigger subdetectors.

The subdetector which took more advantage from the cosmic rays data taking has been, for obvious reasons, the MUON system [63]. About 250000 tracks were reconstructed with a standalone MUON tracking and a first space and time alignment were performed. Moreover MUON detectors performances such as cluster size, time resolution and detection efficiency were estimated from these data. In particular the efficiency resulted at the level of 99%, with exact values depending on the considered station and region.

2.5.2 *Commissioning with beam induced events*

During summer 2008 beam injection tests were performed. The beam was dumped on a beam-stopper (TED) 300 m behind LHCb and 8 (12) mrad horizontally (vertically) displaced from the LHCb beam axis. A high particle density was produced in these dumps ($10/\text{cm}^2$ of particle flux on the beam dump axis, $0.1/\text{cm}^2$ on the VELO) and detected by LHCb. Even if TED particles came from the *wrong* direction (*i.e.* MUON first) and were not centred, the produced tracks helped in aligning the detectors, especially the smaller ones, in space and time.

On September 10th 2008 new beam tests were performed, with the beam injected upstream the LHCb detector and circulating, for about 30 minutes, in the *right* direction for LHCb (i.e. VELO first). Many clean beam-gas interaction events and some *splash* events, with beam hitting the collimator, were recorded. During these tests control and DAQ systems showed a very good response and the consecutive trigger reading was exploited.

2.5.3 *Commissioning and performances with beams*

After the LHC incident of September 2008, the data taking with proton-proton collisions started again in 2009 at $\sqrt{s} = 0.9$ TeV and finally in 2010 at $\sqrt{s} = 7$ TeV. Data taking helped to fully commission the detector and the data acquisition system.

In the following some of the present performances of the LHCb detector will be shown as obtained exploiting either the data from 2010 pp collisions or test beams data.

2.5.3.1 *Vertex Locator*

As already said at $\sqrt{s} = 7$ TeV the two halves of the Vertex Locator can be safely positioned, in stable beam conditions, in their nominal fully closed position. In this situation the nominal performance of the VELO can be fully exploited.

In order to understand the vertex resolution with real data the following procedure was adopted: inside each event the tracks were splitted in two samples (either randomly or in detector regions) and one primary vertex for each sample was fitted. Then the difference of the two positions is a measurement of the resolution; results obtained with this method are shown in Fig. 30 as a function of the number of tracks used to fit the vertex. Similarly the impact parameter (IP) with respect to the primary vertex resolutions can be measured. In Fig. 31 the IP resolution as a function of the inverse of the transverse momentum is shown as obtained from 2010 data and compared to MC simulations. These resolutions are linear functions of the transverse momentum and for 2010 data are $\sigma_x(\mathrm{IP}) = 16.2 + 24.6/p_T$ μm and $\sigma_x(\mathrm{IP}) = 16.2 + 24.6/p_T$ μm in in the x and y directions respectively. While the real data have a worse resolution with respect to simulations, they are always improving thanks to new alignments and better descriptions of the real detector which clearly refine as the data-taking proceeds.

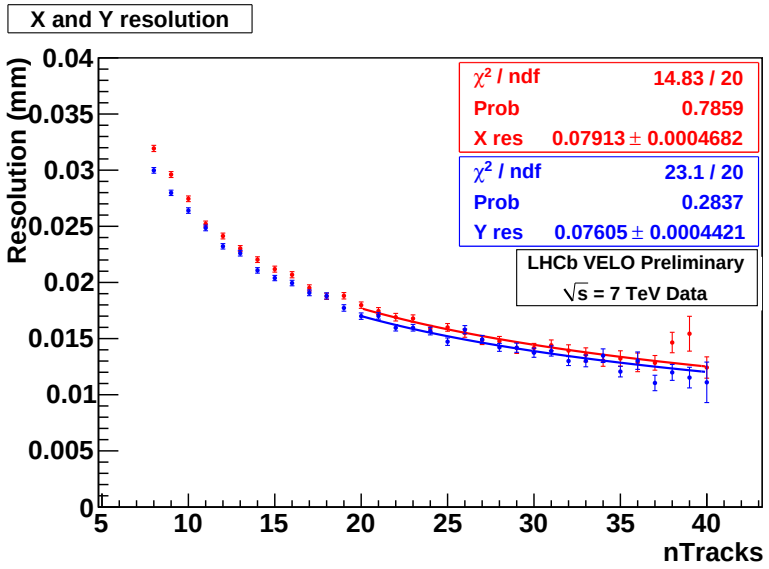

Figure 30.: Primary vertex resolutions as obtained from measurements in pp collisions at $\sqrt{s} = 7$ TeV shown as a function of the number of tracks used to fit the vertex position. The red and blue points are the resolution in the x and y direction respectively.

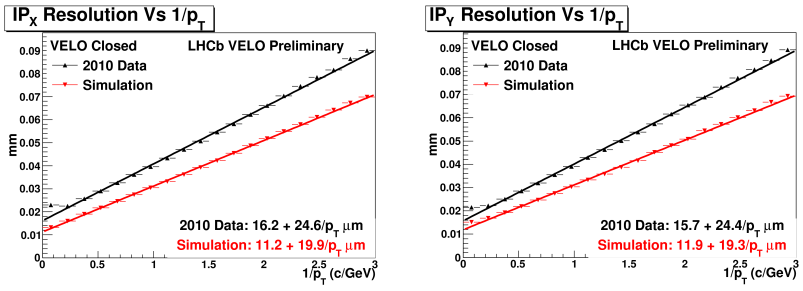

Figure 31.: Resolutions on the impact parameter of particles with respect to the PV as obtained from measurements in pp collisions at $\sqrt{s} = 7$ TeV. The resolutions are shown, as a function of the inverse of the transverse momentum of the particle, on the left for the x direction and on the right for the y. Data results (in black) are compared with simulations (in red).

2.5.3.2 *Tracking*

Tracks in LHCb are reconstructed with hits coming from the full tracker (VELO, TT, IT and OT). The reconstruction algorithm fits the trajectories taking into account magnetic field and multiple scattering. All the tracks with sufficient detector hits are reconstructed and, depending on their trajectories and, consequently, on the detector which traverse, the following tracks types can be defined and their schematic view can be seen in figure 32:

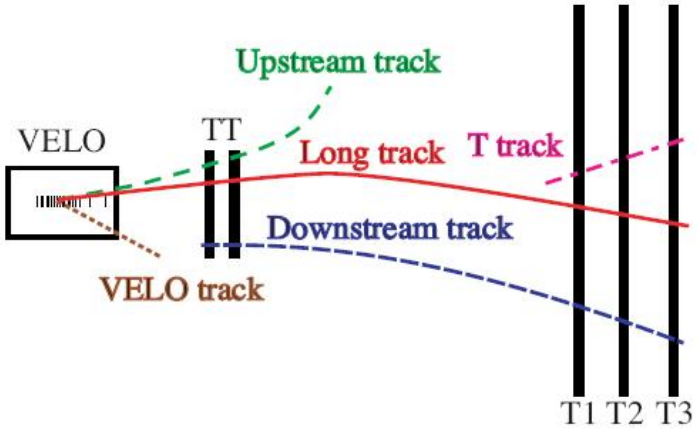

Figure 32.: Scheme of the different LHCb track types.

LONG TRACKS traverse the full tracking system from the VELO to the T stations and thus have the most precise momentum measurement.

UPSTREAM TRACKS traverse only the VELO and TT stations and, being in general lower momentum tracks, are bent out of the detector acceptance by the magnetic field.

DOWNSTREAM TRACKS traverse only the TT and T stations. Usually are due to decay products of long lived resonances which decay after the VELO.

VELO TRACKS are measured in the VELO only and are typically large angle or backward tracks, useful for the primary vertex reconstruction.

T TRACKS are only measured in the T stations. They are typically produced in secondary interactions, but are useful for the matching with photong rings in RICH2.

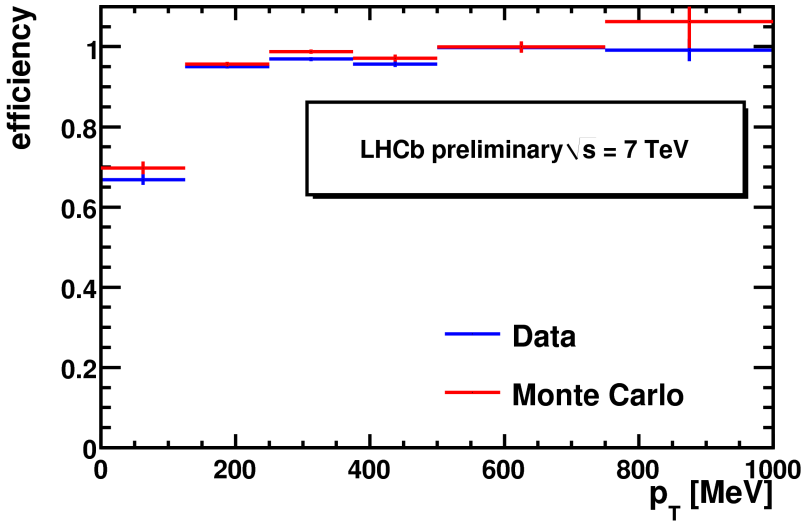

Figure 33.: Tracking efficiency for *long* tracks as a function of the transverse momentum. The values refer to TT and T1-T3 overall efficiency.

The track reconstruction starts so called track *seeds*, *i.e.* track segments in the VELO and in the T stations. These segments are propageted through the magnetic field giving trajectories which are fitted exploting all the available hits with a Kalman filter, traking into accound multiple scattergina and energy loss. The χ^2 of this fit gives a measurement of the quality of the tracks.

The tracking system performances have been measured exploiting the copious number of K^0_S produced in typical minimum bias proton proton collisions.

Given its large lifetime, a good purity on this signal can be reached without requiring two fully reconstructed tracks. If one considers combinations of one *long* track and one track formed by a track segment in the VELO extrapolated to match a hit in the calorimeter, the rest of the tracking system (TT and T1-T3) can be tested in an unbiased way. The tracking efficiency can then simply measured as the fraction of VELO-Calo tracks which are also reconstructed as *long* tracks.

The result of this measurement can be seen, as a function of the transverse momentum, in Fig. 33. The values obtained in this way are just overall efficiencies for the TT and T1-T3 tracking system. VELO efficiency is not considered being used as basis for the sample.

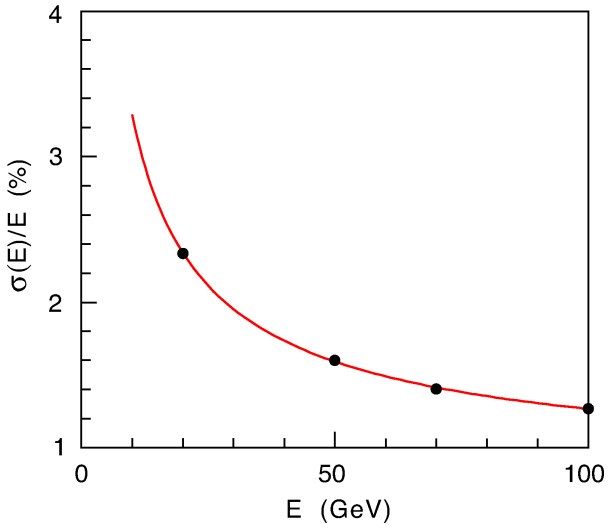

Figure 34.: Energy resolution for the ECAL as measured with electrons.

2.5.3.3 *Energy measurement*

Energy resolution and response uniformity of ECAL modules was studied at test beam. A certain non-uniformity is expected due to various reasons: imperfect reflection from tile edges and a dependence of the amount of collected light with the distance from a WLS fibre. Tests with minimum ionising particles compared with Monte Carlo simulations show and reproduce this local non-uniformity while global non-uniformity was found to be negligible. Electromagnetic showers from electrons and photons reduce considerably this non-uniformities because of obvious statistical compensation. The module response with 50 GeV/c electrons is uniform within 0.8%. The energy resolution determined from test beams has been parametrised as $\sigma_E/E = a/\sqrt{E} \oplus b \oplus c/E$ where a, b and c represent the stochastic, constant and noise terms respectively. Test beam result in a measured stochastic term $8.5\% < a < 9.5\%$ and constant term $b \sim 0.8\%$ which reaches and overcome the design resolution $\sigma_E/E = 10\%/\sqrt{E} \oplus 1\%$.

HCAL performances were studied at the CERN SPS test beam. First of all the dependence of the response versus the angle with respect to the beam was measured in the 0°- 15°range and found a uniformity well within ±3%. Owing to the limited space available the overall length of HCAL is equivalent to $5.6\lambda_I$ (plus $1.2\lambda_I$ of the ECAL) and the active to passive material ratio is 0.18 which matches the loose energy resolution requirement for this detector. The energy response have been studied with pions test

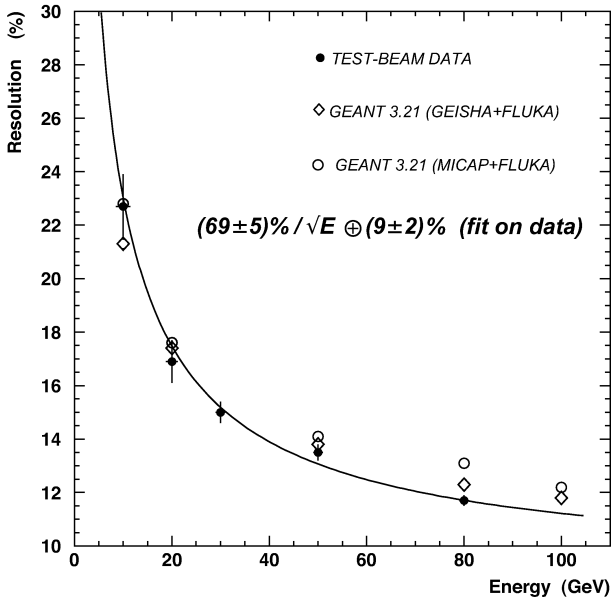

Figure 35.: Energy resolution for the HCAL as obtained from measurements with 50 GeV pions. The fit to the data measures the resolution as quoted in the text.

beam. The low energy tail due to the shower leakage doesn't affect the rejection power to the low E_T minimum bias events even if it causes some inefficiency for high E_T events. The energy resolution has been studied by fitting, for different energies, the HCAL response with a gaussian. The fit to the data, shown in Fig. 35, gives $\sigma_E/E = (69 \pm 5)\%/\sqrt{E} \oplus (9 \pm 2)\%E$ (with E in GeV).

2.5.3.4 *Particle identification*

Particle identification with the RICH system is performed as follows.

The fundamental algorithm is based on a likelihood approach which combines information from the various detectors in order to calculate a probability for a given particle hypothesis.

Each pixel pattern in the in the RICH photodetectors is matched to a track. The likelihood is constructed considering the effective Cherenkov radiation emission angle for a given track-RICH combination The likelihood is then calculated for the different particle hypothesis.

The output of this algorithm gives the best hypothesis for each track as the massimum of the likelihood in the different hypothesis (often expressed as log-Likelihood differences rather than Likelihood ratios).

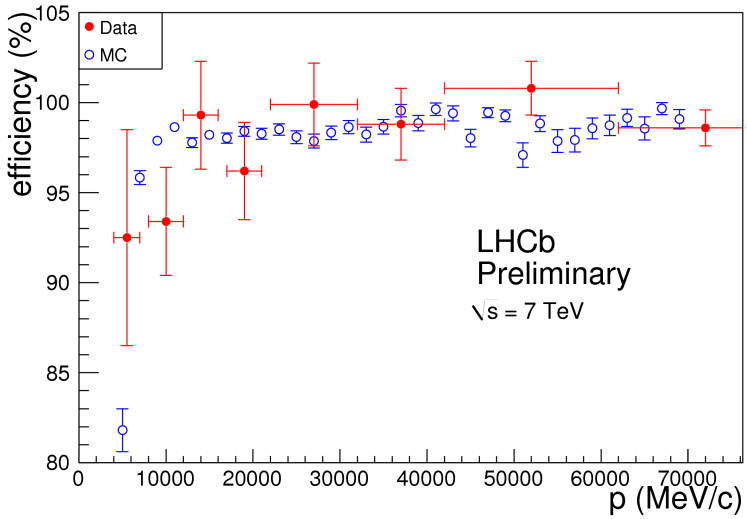

Figure 36.: Muon identification efficiency as measured from data taken in pp collisions at $\sqrt{s} = 7$ TeV. Data points (red) are compared to MC simulations (blue).

Muons are instead identified by extrapolating reconstructed tracks with $p > 3$ GeV/c into the muon stations. Hits are searched within fields of interest (FOI) around the extrapolation point of the track in each muon station, parameterized as a function of momenta for each station and region. A track is considered as a muon candidate when a minimum number of stations (2-4 depending on momentum) have hits in their corresponding FOI.

Moreover a combined identification can be build considering further information as the slopes in the muon system and the main tracker, and the average track-to-hit distance for the various hits associated to the track. Then for each track the difference in log-likelihood between the muon hypothesis and pion hypothesis is determined, and summed with the values from the RICH and calorimeter systems.

Muon identification has been tested on real data using the $J/\psi \to \mu^+\mu^-$ decay. One of the two muons is required to fully reconstructed by the tracking system and the muon system while for the second muon no requirement is made on the MUON system information. In this manner the efficiency of the muon identification can be measured directly on pp collisions. In Fig. 36 the results of the muon identification measurement are shown as a function of the muon momentum and compared with MC simulations with which they are consistent.

Part II

EXPERIMENTAL WORK

3

MEASUREMENT OF V^0 PRODUCTION RATIOS

The study of the V^0 particles is important to understand the physics of the strange quark production and of the hadronization phase in high energy pp collisions (Cf.§ 1.2).

In this chapter we present measurements performed within the LHCb experiment of two main observables, the $\bar{\Lambda}/\Lambda$ production ratio, which is a measurement of the strange baryon production asymmetry, and the $\bar{\Lambda}/K^0_S$ production ratio, measurement of the baryon to meson suppression.

The $\bar{\Lambda}/\Lambda$ production ratio is defined as:

$$\frac{\bar{\Lambda}}{\Lambda} = \frac{\sigma(pp \to \bar{\Lambda}X)}{\sigma(pp \to \Lambda X)} \tag{3.1}$$

where X is used to denote the inclusive nature of the cross-section and includes any final state accompanying the Λ particles. Similarly the $\bar{\Lambda}/K^0_S$ ratio is defined as

$$\frac{\bar{\Lambda}}{K^0_S} = \frac{\sigma(pp \to \bar{\Lambda}X)}{\sigma(pp \to K^0_S X)} \quad . \tag{3.2}$$

For the two ratios we consider only particles produced at the primary vertex either directly or from strong or electromagnetic decays of particles produced therein; more details on this distinction will be given in §3.1.

The measurement of production ratios, rather than production cross-sections, besides being cleaner from the theoretical point of view, is also simpler experimentally. Some common factors to be taken into account in the cross-section cancel out when dealing with ratios. In particular the luminosity can be simplified exactly and most of the efficiencies cancel out approximately, simplifying the final analysis.

The measurements of the two production ratios have been done in parallel, with common data samples and analysis and therefore will be presented together in this chapter.

Common data samples (§3.2) have been used both for data and Monte Carlo simulations, and they have been analysed in parallel. A common selection, described in §3.3, has been developed for all V^0 particles, and raw event yields have been extracted from invariant mass distributions both for data and MC simulations.

The data raw event yields (§3.5.2) have been corrected for the efficiency obtained from MC (§3.6) so that the final event yields have been obtained. Then the two production ratios have been measured in bins of transverse momentum, p_T, and rapidity, y, and the results will be presented in §3.7.

While the measurement is apparently simple, it needs a clear knowledge of the detector so that great attention has been put in the evaluation of possible systematics, described in §3.8.

3.1 PROMPT AND SECONDARY V^0

As explained in the introduction, to understand the real mechanism of V^0 production we intend to study the prompt component. We consider as prompt all the particles produced directly at the primary vertex (PV) or coming from strong or electromagnetic decays of other particles produced in the PV. The theoretical reason for the inclusion of the latter component is that the s quark of the V^0, in these decays, in not altered and comes directly from the PV. A secondary but very important reason, is that these events are usually experimentally indistinguishable from the V^0 directly from PV; in fact being able to distinguish them would require the detection of very soft photons or slow charged particles for which the efficiency would be very low, if not vanishing.

In order to understand the composition in terms of V^0 of typical pp collisions we have looked at Monte Carlo simulated minimum bias events. Most of these events (at high energies) contain at least one V^0 particle. In particular, in minimum bias events at $\sqrt{s} = 7$ TeV a K^0_S is present in about 71% of the cases and a Λ in about 60%, the two percentages decrease to 50% and 35% respectively for K^0_S and Λ in collisions at $\sqrt{s} = 0.9$ TeV. These numbers are derived from generator level Monte Carlo simulations without propagation in the detector and are referred to the entire solid angle, not to the LHCb acceptance. If one considers a full simulation the numbers might change due to V^0 produced in particle interactions with material or absorbed therein.

As mentioned before, the V^0 particles can come from other resonances decays, in particular in Tables 1 and 2 are listed the various fractions of V^0 coming from the PV or from other particles decays as obtained from MC simulations at generator level at $\sqrt{s} = 0.9$ TeV and $\sqrt{s} = 7$ TeV respectively.

In Tables 4, 3 are listed all the possible sources of V^0 particles as obtained from MC events with full detector simulation; the

reported origin particles can be either the head of the decay chain or particles which interacted with detector material and produced a V^0. At generator level about half of the Λ and $\sim 60\%$ of the K^0_S come from the PV and the rest is mainly due to various K^* resonances for the K^0_S and to Σ and Ξ particles for the Λ so that the prompt fraction of the V^0 particles is at the level of 97% or more. After full detector simulation the percentages do not change much, but many more sources of V^0 particles are present, mainly due to V^0 re-scattering or other particles interactions in the material.

3.2 DATA SAMPLES AND RUNNING CONDITIONS

The data samples used in these analysis were collected by the LHCb detector in pp collisions at LHC during 2010. Samples at two different energies were recorded respectively at $\sqrt{s} = 0.9$ TeV and 7 TeV.

3.2.1 *Data at $\sqrt{s} = 0.9$ TeV*

During the end of 2009 proton beams were delivered by the LHC at 450 GeV per beam so that the first collision tests were made at $\sqrt{s} = 0.9$ TeV. This energy corresponds to the injection energy of the proton beams from the SPS. Different analyses were started considering data taken at this energy among which also the V^0 production ratios analyses. Since data were found interesting but the statistics was very low a special run at $\sqrt{s} = 0.9$ TeV was requested once the luminosity increased and was delivered on May 2nd and 3rd 2010. Integrated luminosities of 148 and 163 μb^{-1} were recorder with LHCb magnetic field polarity *up* and *down* respectively, for a total of 311 μb^{-1}.

The collisions have been recorded by LHCb which was running in nominal conditions with the exception of the VELO. In these conditions both the crossing angle and size of the beams are larger than those at nominal higher energies beams, for which the detector has been designed. For these reasons, to avoid damages in the VELO, its two halves were kept 10 mm away from the nominal closed position (semi-open position), reducing the azimuthal acceptance of the detector.

The trigger during this data taking was in the so-called "micro-bias" configuration. This is a sort of minimum bias trigger which requires just one track in the VELO detector (a 2 dimensional

Table 1.: Head of decay chain for V^0 particles in minimum bias events at $\sqrt{s} = 0.9$ TeV, as obtained from MC simulations at generator level. Charge conjugate modes are always implied. Standard PDG ID [64] are listed for reference.

Head	PDG ID (abs.)	Fraction (%)	Fraction on non-PV (%)	V^0 prompt
PV	0	60.5 ± 0.5		Yes
$a_2^0(1320)$	115	0.4 ± 0.1	1.2 ± 0.2	Yes
$a_2^{\pm}(1320)$	215	0.7 ± 0.1	2.0 ± 0.2	Yes
$f_2(1270)$	225	0.3 ± 0.1	0.9 ± 0.1	Yes
$K^{*0}(892)$	313	8.9 ± 0.3	24.1 ± 0.7	Yes
$K_2^{*0}(1430)$	315	1.5 ± 0.1	4.0 ± 0.3	Yes
$K^{*+}(892)$	323	18.9 ± 0.4	51.2 ± 0.8	Yes
$K_2^{*+}(1430)$	325	2.3 ± 0.1	6.1 ± 0.4	Yes
$\phi(1020)$	333	2.8 ± 0.2	7.6 ± 0.4	Yes
$f_2'(1525)$	335	0.4 ± 0.1	1.2 ± 0.2	Yes
$D^{*\pm}(2010)$	413	0.1 ± 0.0	0.3 ± 0.1	No
D^0	421	0.2 ± 0.0	0.4 ± 0.1	No
$D^{*0}(2010)$	423	0.1 ± 0.0	0.4 ± 0.1	No
Others		2.7 ± 0.1	0.1 ± 0.1	

(a) Head of decay chain for K_S^0

Head	PDG ID (abs.)	Fraction (%)	Fraction on non-PV (%)	V^0 prompt
PV	0	42.0 ± 0.6		Yes
$\Sigma^{*\mp}$	3114	8.0 ± 0.4	13.8 ± 0.6	Yes
Σ^0	3212	18.1 ± 0.5	31.2 ± 0.8	Yes
Σ^{*0}	3214	9.1 ± 0.4	15.7 ± 0.6	Yes
$\Sigma^{*\pm}$	3224	10.6 ± 0.4	18.3 ± 0.7	Yes
$\Xi^{\mp}$	3312	4.2 ± 0.3	7.3 ± 0.4	Yes
$\Xi^{**\mp}$	3314	1.3 ± 0.1	2.2 ± 0.3	Yes
Ξ^0	3322	5.1 ± 0.3	8.7 ± 0.5	Yes
Ξ^{*0}	3324	1.3 ± 0.2	2.3 ± 0.3	Yes
$\Omega^{\mp}$	3334	0.1 ± 0.0	0.2 ± 0.1	No
$\Lambda_c^{\pm}$	4122	0.2 ± 0.1	0.3 ± 0.1	No
Others		< 0.1	< 0.1	

(b) Head of decay chain for Λ

Table 2.: Head of decay chain for V^0 particles in minimum bias events at $\sqrt{s} = 7$ TeV, as obtained from MC simulations at generator level. Charge conjugate modes are always implied. Standard PDG ID [64] are listed for reference.

Head	PDG ID (abs.)	Fraction (%)	Fraction on non-PV (%)	V^0 prompt
PV	0	58.2 ± 0.1		Yes
$a_2^0(1320)$	115	0.4 ± 0.1	1.2 ± 0.0	Yes
$a_2^{\pm}(1320)$	215	0.9 ± 0.1	2.2 ± 0.1	Yes
$f_2(1270)$	225	0.4 ± 0.1	1.1 ± 0.1	Yes
$K^{*0}(892)$	313	9.2 ± 0.1	23.9 ± 0.1	Yes
$K_2^{*0}(1430)$	315	1.7 ± 0.1	4.5 ± 0.1	Yes
$K^{*+}(892)$	323	18.8 ± 0.1	48.7 ± 0.1	Yes
$K_2^{*+}(1430)$	325	2.4 ± 0.1	6.2 ± 0.1	Yes
$\phi(1020)$	333	2.9 ± 0.1	7.4 ± 0.1	Yes
$f_2'(1525)$	335	0.5 ± 0.1	1.4 ± 0.1	Yes
$D^{\pm}$	411	0.2 ± 0.1	0.5 ± 0.1	No
$D^{*\pm}(2010)$	413	0.2 ± 0.1	0.6 ± 0.1	No
D^0	421	0.3 ± 0.1	0.8 ± 0.1	No
$D^{*0}(2010)$	423	0.2 ± 0.1	0.4 ± 0.1	No
Others		3.2 ± 0.1	0.1 ± 0.1	

(a) Head of decay chain for K_S^0

Head	PDG ID (abs.)	Fraction (%)	Fraction on non-PV (%)	V^0 prompt
PV	0	40.4 ± 0.1		Yes
Σ^{*-}	3114	8.8 ± 0.1	14.8 ± 0.1	Yes
Σ^0	3212	17.4 ± 0.1	29.3 ± 0.1	Yes
Σ^{*0}	3214	9.3 ± 0.1	15.6 ± 0.1	Yes
Σ^{*+}	3224	10.8 ± 0.1	18.1 ± 0.1	Yes
$\Xi^{\pm}$	3312	4.8 ± 0.1	8.1 ± 0.1	Yes
$\Xi^{*\mp}$	3314	1.3 ± 0.1	2.2 ± 0.1	Yes
Ξ^0	3322	5.0 ± 0.1	8.5 ± 0.1	Yes
Ξ^{*0}	3324	1.4 ± 0.1	2.3 ± 0.1	Yes
$\Omega^{\pm}$	3334	0.1 ± 0.1	0.2 ± 0.1	No
$\Lambda_c^{\pm}$	4122	0.2 ± 0.1	0.4 ± 0.1	No
Others		< 0.1	< 0.1	

(b) Head of decay chain for Λ

Table 3.: Origin of K^0_S in minimum bias events at $\sqrt{s} = 0.9$ TeV, as obtained from MC simulations with full detector simulation. Origin means either head of decay chain or particle that interacted with material and originated a K^0_S. Charge conjugate modes are always implied.

Origin particle	PDG ID (abs.)	Fraction (%)	Fraction on non-PV (%)
PV	0	54.7	
$\rho^0(770)$	113	0.5	1.1
$a_2^0(1320)$	115	0.4	1.0
K^0_L	130	0.2	0.4
$\pi^\pm$	211	0.9	1.9
$\rho^0(770)$	213	0.5	1.0
$a_2^\pm(1320)$	215	0.9	2.0
$\omega(782)$	223	0.3	0.6
$f_2(1270)$	225	0.4	1.0
$K^*(892)0$	313	8.9	19.6
$K_2^{*0}(1430)$	315	1.4	3.2
$K^\pm$	321	2.9	6.5
$K^{*\pm}(892)$	323	17.2	38.0
$K_2^{*\pm}(1430)$	325	2.0	4.5
$\phi(1020)$	333	2.6	5.8
$f_2'(1525)$	335	0.5	1.0
$D^\pm$	411	0.1	0.2
$D^{*\pm}(2010)$	413	0.1	0.3
D^0	421	0.2	0.3
$D^{*0}(2010)$	423	0.1	0.2
$\Delta^\pm$	1114	0.1	0.3
n	2112	0.5	1.0
Δ^0	2114	0.2	0.4
p	2212	0.5	1.1
$\Delta^\pm$	2214	0.2	0.4
$\Sigma^{*\pm}$	2224	0.3	0.7
Λ	3122	0.1	0.3
Others		2.7	0.1

Table 4.: Origin of Λ in minimum bias events at $\sqrt{s} = 0.9$ TeV, as obtained from MC simulations with full detector simulation. Origin means either head of decay chain or particle that interacted with material and originated a Λ V^0. Charge conjugate modes are always implied.

Origin particle	PDG ID (abs.)	Fraction (%)	Fraction on non-PV (%)
PV	0	29.7	
$\rho^0(770)$	113	0.7	1.0
$a_2^0(1320)$	115	0.1	0.2
K_L^0	130	1.2	1.6
$\pi^\pm$	211	1.4	2.0
$\rho^\pm(770)$	213	0.6	0.9
$a_2^\pm(1320)$	215	0.2	0.3
$\omega(782)$	223	0.4	0.6
$f_2(1270)$	225	0.2	0.2
K^0	311	6.0	8.5
$K^*(892)0$	313	2.8	3.9
$K_2^{*0}(1430)$	315	0.3	0.4
$K^\pm$	321	8.5	12.1
$K^{*\pm}(892)$	323	2.2	3.1
$K_2^{*\pm}(1430)$	325	0.2	0.4
$\phi(1020)$	333	0.7	1.0
$f_2'(1525)$	335	0.1	0.1
$\Delta^\pm$	1114	0.2	0.3
n	2112	0.7	1.0
Δ^0	2114	0.2	0.3
p	2212	0.8	1.1
$\Delta^\pm$	2214	0.3	0.4
$\Delta^{++(--)}$	2224	0.4	0.6
$\Sigma^{*\pm}$	3114	5.7	8.2
Λ	3122	0.4	0.5
Σ^0	3212	12.0	17.1
Σ^{*0}	3214	6.5	9.3
$\Sigma^{*\pm}$	3224	8.0	11.5
$\Xi^\pm$	3312	3.0	4.3
$\Xi^{*\pm}$	3314	0.8	1.1
Ξ^0	3322	3.2	4.6
Ξ^{*0}	3324	0.9	1.3
$\Omega^\pm$	3334	0.1	0.1
others		0.6	< 0.1

Table 5.: Summary of the datasets used in this work. The analysed integrated luminosity is shown for real data while the number of events is shown for Monte Carlo simulations; numbers for different field polarities are shown separately.

	Field down	Field up
Data at $\sqrt{s} = 0.9$ TeV	163 μb^{-1}	148 μb^{-1}
Data at $\sqrt{s} = 7$ TeV	597 μb^{-1}	1193 μb^{-1}
MC at $\sqrt{s} = 0.9$ TeV	73 M	73 M
MC at $\sqrt{s} = 7$ TeV	69 M	60 M

rz track) or in the TT stations. This trigger results in $\sim$ 100% efficiency for the channels we considered in this work.

3.2.2 *Data at $\sqrt{s} = 7$ TeV*

The second dataset used for this analysis was recorded by LHCb at the energy $\sqrt{s} = 7$ TeV. LHCb started recording data in these conditions on April 1st 2010 and they have been kept for the whole year 2010. The LHCb detector was in its nominal conditions, including the VELO which at these energies can run in its closed position.

The data used for this analysis has a visible interaction rate much smaller than 1, *i.e.* there is essentially no pile up. Also these data have been recorded using the "micro-bias" trigger and corresponds to integrated luminosities of 1193 and 597 μb^{-1} for the field up and down configurations respectively.

3.2.3 *Monte Carlo samples*

The LHCb collaboration has produced simulated Monte Carlo (MC) events data sets which reproduce closely the conditions of real data taking.

Minimum bias MC events have been used for this analysis. In particular 73 M events for each magnetic field polarity have been generated at $\sqrt{s} = 0.9$ TeV. The detector was simulated with the VELO semi-open position already described in order to match real data conditions. The $\sqrt{s} = 7$ TeV sample is composed of 60 and 69 M events for the field up and down configurations respectively and has the VELO in its nominal fully closed position.

Furthermore some MC samples were also generated in order to compare the data with various PYTHIA [23] tunings. In particular the so called "Perugia-0", tuned on LEP and Tevatron data, and the "Perugia NOCR", with extreme description of Baryon number transport without color reconnection, tunings [25] were used to generate MC samples at both energies since these are considered here "standard-candles". These samples were simply generated without full detector simulation since they are used only to understand the Monte Carlo predictions for our observables with different tunings.

Being V^0 hadrons copiously present in minimum bias events only this type was considered in the MC for the estimation of LHCb performances both for the signal properties and for background contamination.

3.3 V^0 SELECTION

Events at high energy proton-proton collisions are quite complex; within the LHCb acceptance hundreds of tracks are reconstructed per event: in particular distributions of the number of reconstructed tracks per event in pp collisions at $\sqrt{s} = 0.9$ TeV and 7 TeV are shown in Fig. 37 (a) and (b) respectively. Nevertheless, the selection of V^0 particles is rather simple. Owing to the V^0 large proper times (Λ $c\tau = 7.89$ cm, K^0_S $c\tau = 2.6842$ cm) and boosts their decay vertices are usually some distance away from the primary vertex so that many handles allow to separate real V^0 from combinatorial background. Simple requirements on the impact parameter of the decay products with respect to the primary vertex are usually enough to discard the large number of particles from the primary vertex. We have developed a simple analysis for these decays aiming mainly at having pure samples without biasing our observables.

In order to select V^0 candidates, pairs of oppositely charged tracks are selected. In this analysis only long tracks have been used, which require hits in every tracking detector helping to understand detector effects and control the systematic uncertainties. Given the lifetimes for the considered V^0 particles, a large fraction of them decays out of the VELO so that their reconstruction can be done only using *downstream* tracks which do not require any hit in this detector. However the momentum (and hence the mass) resolution is worse for downstream tracks, so that we have preferred to avoid using them.

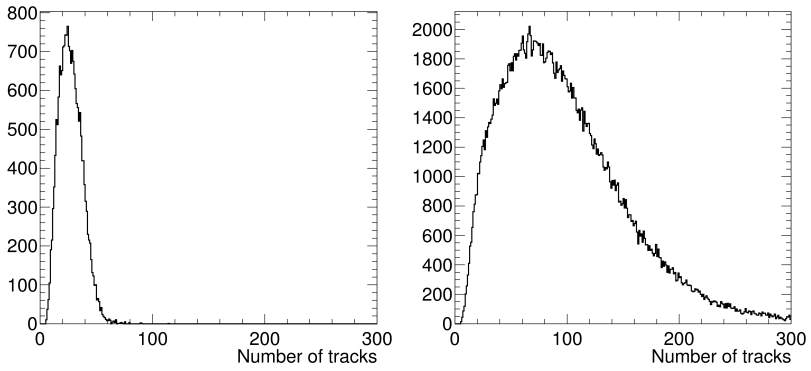

(a) (b)

Figure 37.: Distributions of the number of tracks reconstructed in LHCb per event in pp data at (a) $\sqrt{s} = 0.9$ TeV and (b) $\sqrt{s} = 7$ TeV in LHCb.

Each track is required to have the χ^2 per degree of freedom of the track fit less than 9. This cut, being very loose, has been chosen just as a quality cut to select clean tracks and reject *ghost* tracks.

The two tracks are combined to form a common vertex which is then fitted. A quality cut on the χ^2/dof of the fit was chosen considering the signal to background ratio and the value was found to be optimal around 9. This cut is quite loose however the combinatorial background is efficiently removed by the kinematic selection so that we have chosen this value in order not to diminish the signal efficiency.

Within this selection we do not use particle identification in order to distinguish between pions and protons since, as seen later, it is not needed to have pure signals. Therefore we consider all of the tracks either as pions or protons assigning the correspondent mass hypothesis when needed.

3.3.1 *Kinematic selection*

The final selection is performed exploiting the kinematics of the decay. In order to avoid any bias on our measurements and to reduce the uncertainty contribution coming from efficiencies, any cut on the transverse momentum either of the V^0 or of its decay products has been avoided, also because not really needed to select pure samples.

The variable which holds most of the information in this type of events is the impact parameter (IP) relative to the primary vertex. While the V^0 particle, being directly produced at the primary vertex, must have a small impact parameter relative to the PV, the decay products must be displaced from it. Moreover given the V^0 proper time the large lever arm ensures that even for small decay angles the IP of the decay products would be large.

In order to combine the information of the three impact parameters (V^0 and its decay products) the following variable was defined:

$$\nu = \log(IP_1) + \log(IP_2) - \log(IP_{V^0}) = \log(\frac{IP_1 \cdot IP_2}{IP_{V^0} \cdot [1\ mm]}) \quad (3.3)$$

this combination can be thought as a Fisher discriminant [65] for the logarithms of the impact parameters. In the following will be presented a study which compares the ν variable with other widely used discriminant methods.

3.3.1.1 *Comparison of ν discriminant variable with different multivariate methods*

In order to assess the performances of the ν variable, it was compared to other commonly used multivariate methods. We exploited a tool for multivariate techniques, called TMVA [66], widely used, especially in the high energy physics community. It allows the study of different multivariate methods for data mining purposes; we refer to its user guide for a detailed mathematical treatment of the different multivariate methods [67].

As input samples for these studies we have used a loosely preselected sample of minimum bias events from MC simulations at $\sqrt{s} = 0.9$ TeV. K^0_S candidates were built as previously described and divided in two samples:

- signal sample, composed of MC truth matched K^0_S candidates;
- combinatorial background sample, composed of all the other random combinations.

Then the three input variables (IP_1, IP_2, IP_{V^0}) were combined using the following methods:

- ν variable[1]

1 Because of the way TMVA requires its input, the implementation of the ν variable has been done via the "FDA" method (Function Discriminant Analysis) which allows the user to define the desired function of the input variables.

- Likelihood
- Fisher discriminant
- Standard cuts
- Neural network

since we will describe these methods in detail in §5.1.5, we do not repeat here their treatment.

The different methods were trained and tested using the above-mentioned samples, which were divided (randomly) in two halves each in order to separate the training from the testing sample; two independent samples are in fact needed in order not to bias the estimate of the performances.

The methods were then rated according to their results on the testing sample in terms of signal efficiency and background rejection. In Fig. 38 we show the background versus the signal efficiency. It can be seen that the ν variable outperforms most of the methods with the exception of the Neural network (MLP). The ν variable is in particular more efficient at a given background rejection than standard cuts and (linear) fisher discriminant showing that some non-linearity and correlation in the combination of the input variables is present. It is at the same level of the likelihood and worse than the neural network but significantly simpler than these methods.

A second test was performed using as input variables directly the logarithms of the impact parameters. In this way the Fisher discriminant should be almost equal to the ν, for the set of parameters (1,1,-1). The already described steps were made and the final results are shown in the Fig. 38 bottom plot. Again ν is better than standard cuts, at the same level of the likelihood and worse than the neural network. The comparison with the Fisher discriminant shows that ν is still better. The reason of this behaviour may be found in the way the Fisher discriminant is optimised: this method tries in fact to find the best axis in the variables space to separate the two populations, however this optimisation is exact only for gaussian distributed variables while it can be sub-optimal in case of different distributions or in presence of non-linear correlations. In this sense the ν variable appears to be better suited to the problem under consideration.

While the performance of the likelihood and of the neural network were equal or better than ν, we preferred to continue using this variable since the study of systematics due to our

knowledge of IP distributions in data is much simpler in this case than in more complex methods.

3.3.2 *Misidentification background and Armenteros-Podolanski analysis*

As already stated no particle identification method was used in this analysis. No mis-identification background is expected in V^0 events excepted from crossover misidentification of Λ to K^0_S and vice-versa. If we assign to the proton from the Λ decay the pion mass the reconstructed $\pi\pi$ mode could lie in the K^0_S invariant mass region, and the opposite happens if one of the two K^0_S pions is labelled as a proton. A particle identification cut would safely remove this background, but at the price of lowering signal efficiencies and, more important, introducing higher uncertainties on the efficiency since the performance of a RICH detector is more complex to understand than that of the tracking system.

In the following we present some studies which show the particle identification properties and background after our selection in order to prove that our crossover background is quite small so that no concern comes from this issue.

A classical way to analyse V^0 events when particle identification is not present, or one prefer not to use it, is the Armenteros-Podolanski analysis [68]. It can be shown that a certain identification of the decay products can be achieved just by exploiting the kinematic properties of the decay. In particular there is an elliptic relation between p_T^-, the transverse momentum of the negatively charged particle [2] with respect to the V^0 momentum, and the longitudinal momentum asymmetry defined as:

$$\alpha = \frac{p_L^+ - p_L^-}{p_L^+ + p_L^-} \tag{3.4}$$

where $p_L^\pm$ is the longitudinal momentum with respect to the V^0 of the decay products. Particles with different masses or different decay products produce different ellipsis so that they can be easily distinguished.

In Fig. 39 we show what we would expect from perfectly pure V^0 samples: this figure is obtained from MC truth matched V^0 particles from simulations at $\sqrt{s} = 7$ TeV. The three ellipses can be

2 This is just a convention, an analogous relation can be derived for the positively charged particle.

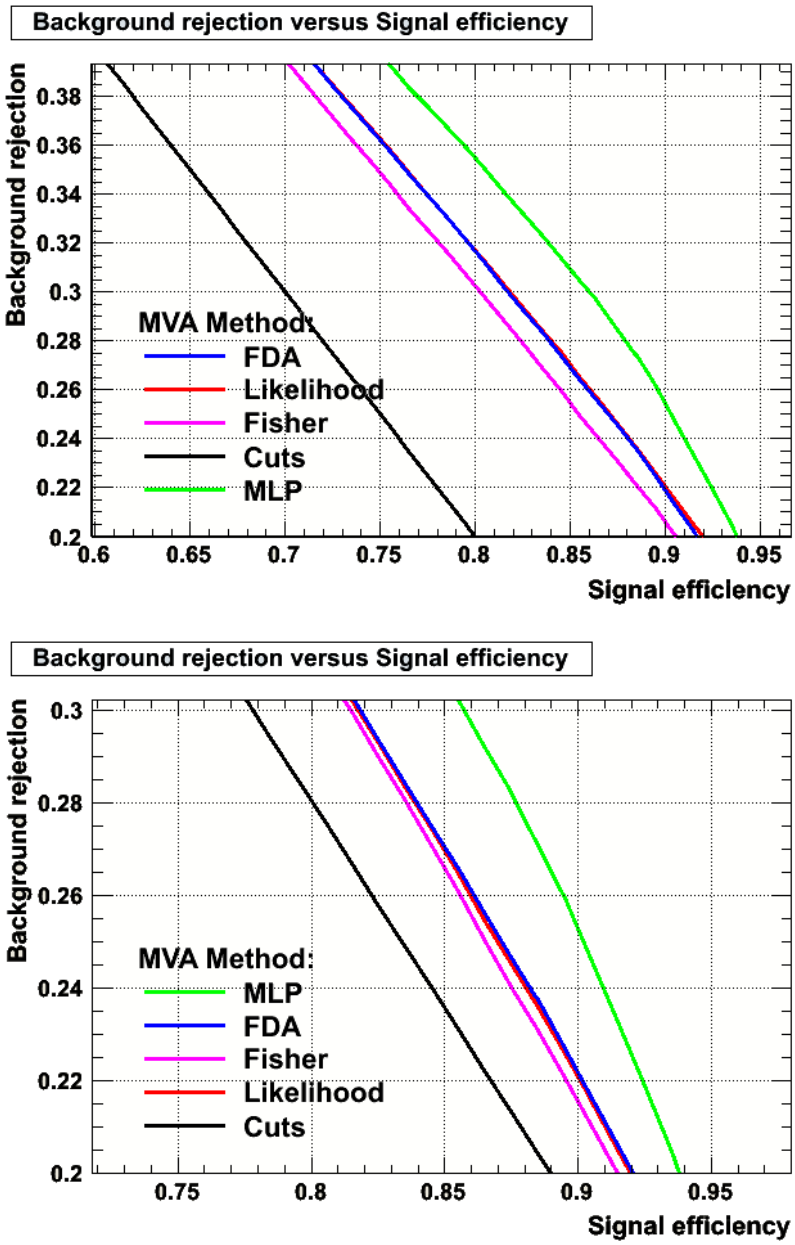

Figure 38.: Background efficiency versus signal efficiency, for different multivariate methods studied for the rejection of combinatorial background in V^0 selection. A zoom in the high signal efficiency region is shown. Top plots shows methods output with impact parameters as input while in the bottom plot the methods had $\log(IP)$ as input. The ν variable is denoted as "FDA" in these plots.

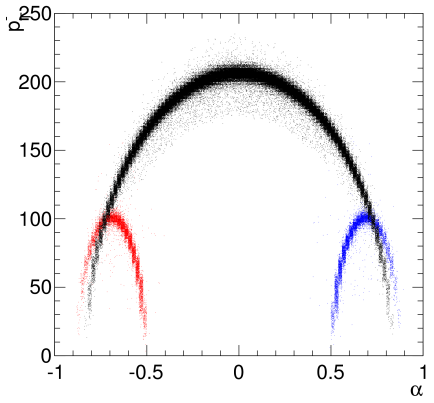

Figure 39.: Armenteros-Podolanski plot for Monte Carlo associated events. The black ellipse arch is composed of $K^0_S \to \pi^+\pi^-$ events, while the red and blue ellipses represent $\bar{\Lambda} \to \bar{p}\pi^+$ and $\Lambda \to p\pi^-$ events respectively. The MC simulations are of pp collisions at $\sqrt{s} = 7$ TeV.

seen to be very precisely separated apart from two crossing points of the K^0_S with the $\bar{\Lambda}$ and Λ ellipses. In this two points the two decay scheme hypothesis coincide kinematically so that cannot be distinguished using only the Armenteros-Podolanski information. However if one uses the two different decay products hypotheses one can calculate the invariant masses of the decaying particle. Often only one of the two decay hypotheses lies in the correct signal region so that the crossing misidentification is small.

In Fig. 40 the Armenteros-Podolanski plot for selected V^0 candidates in Monte Carlo and data events in the large invariant mass region are shown. The different signals can be distinguished very brightly and the overlap between K^0_S and Λ's is very little. When considering only an invariant mass region of plus or minus three standard deviations for the three signals and after sideband subtraction the same events are shown in Fig. 41 for MC events (top plots) and data ones (bottom plots); as it can be seen the signal is very pure already after the kinematic selection.

In order to remove the misidentification background of Λ in the K^0_S invariant mass region a cut has been applied requiring that the $p\pi^-$ and $\bar{p}\pi^+$ combinations had an invariant mass in the $\pi\pi$ hypothesis different of $4.5 \text{MeV}/c^2$ from the K^0_S nominal mass. This cut appears in Fig. 41 as a small deficit of events in the Λ and $\bar{\Lambda}$ plots in the region where the K^0_S ellipse would have crossed the Λ ones. After applying this cut the contamination

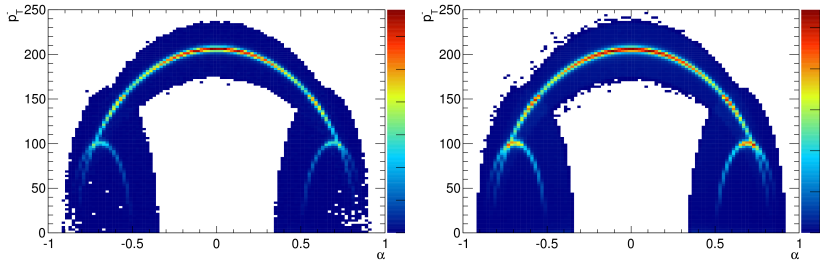

Figure 40.: Armenteros-Podolanski plot after pre-selection for (left) MC and (right) data events at $\sqrt{s} = 7$ TeV with field down.

of K^0_S to the Λ and $\bar{\Lambda}$ samples is reduced to less than 0.5%. An analogous cut was foreseen for the opposite condition of Λ and $\bar{\Lambda}$ contamination to the K^0_S sample; however this cut was not applied since this contamination was already at a negligible level.

3.3.3 *Boost to the centre of mass*

Due to the presence of the LHCb magnetic field the proton beams are subjected to a deviation of about 2 mrad at $\sqrt{s} = 0.9$ TeV and 0.3 mrad at 7 TeV. In order to compensate for this deviation the incoming beams arrive in the LHCb interaction point with a certain angle symmetric and opposite for each beam with respect to the LHCb laboratory frame z axis. This angle lies in the (x, z) plane, orthogonal to the magnetic field.

Therefore, the pp collisions rest frame is not exactly coincident with the laboratory frame and hence, in order to compute the variables in the correct centre of mass frame a Lorentz transformation have to be applied to all the considered particles. The transformation consists mainly in a boost along the x direction in opposite directions for opposite field configurations. Moreover, the system has to be rotated in order to make the z direction coincident with the incoming beam direction.

In the following when we use variables such as momentum, rapidity etc, we consider them as computed in this proton-proton centre of mass system, if not otherwise specified.

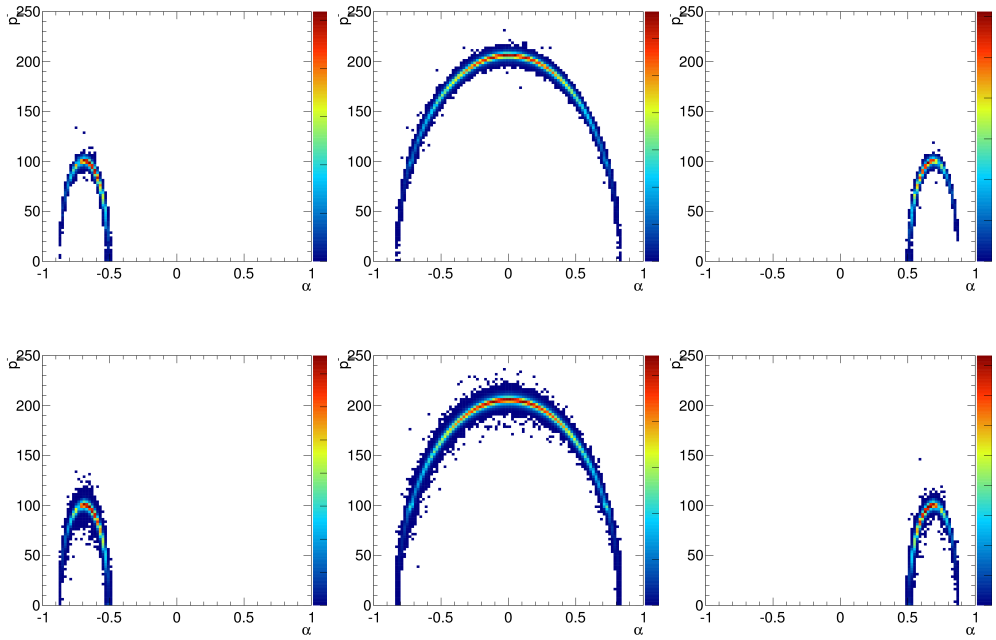

Figure 41.: Armenteros-Podolanski plots for (top) MC and (bottom) data events at $\sqrt{s} = 7$ TeV with field down after sideband subtraction and $\pi\pi$ invariant mass cut. From left to right $\bar{\Lambda}$, K^0_S and Λ events are shown respectively.

3.4 PROPERTIES OF THE SELECTED V^0

From the selected samples we can extract the properties of the V^0 particles. This is very useful in order to compare real data with MC simulations to understand if the latter reproduce the reality and can be used to estimate efficiencies and other corrections to be applied to the data.

In this paragraph we compare the uncorrected distributions for some variables of data and MC. The Monte Carlo distributions are obtained from selected events, following the same procedure applied to the data. We do not require any information coming from MC truth so that the distributions should be an unbiased estimate for the properties of the data.

All the distributions are shown after background subtraction performed statistically. For each distribution two histograms are obtained one for the mass window of the V^0 particle and the other for the sidebands region. The background is removed from the former distribution by subtracting the latter with a scaling factor proportional to the ratio of the two considered invariant mass intervals. This technique is similar to the sideband subtraction adopted for signal extraction (cf. 3.5), in particular it exploits the property of the combinatorial background to be a linearly distributed along the invariant mass.

In Fig. 42 and 43 the momentum distributions of the Λ and K^0_S are shown respectively. The data and MC distributions are compared in these plots; the MC distributions have been normalised to the number of entries in the corresponding data histograms. This would be applied from now on whenever we compare data and MC distributions, unless otherwise specified. It can be seen that the distributions for MC and data are different, the latter having a larger average in each sample. Since both MC and data are analysed in parallel, the difference in the spectra must rely on a physics difference between the simulations and the real data. The origins of these differences can be different and their discussion is beyond the scope of this work; here we consider the MC only as a way to understand our detector efficiencies. This feature is propagated to the different distributions which are correlated with the momentum, p_T and x_F in particular.

In Fig. 44 and 45 the rapidity (y) distributions of the Λ and K^0_S respectively are shown. The two figures show plots for the samples at the two different energies and at both field configurations. The data and MC distributions are not very different but clearly do not agree in some bins. In particular the data has an higher

average in every plot. This reflects the higher momentum of the data with respect to the Monte Carlo. This same effect is even more visible in the transverse momentum distributions which are shown in figures 46 and 47 for Λ and K^0_S respectively. The p_T spectra are clearly different for data and MC showing that the real data correspond to harder V^0 particles at both energies. As will be explained in 3.6.1.1 this spectrum difference can cause a bias when correcting the data for the efficiencies calculated from MC, so that a reweighting technique, there described, has been used.

Another interesting variable is the Feynman x, or x_F, which is usually defined in the experimental context as

$$x_F = \frac{2p_L}{\sqrt{s}} \tag{3.5}$$

where p_L is the longitudinal momentum for the considered particle in the laboratory frame. The distribution of x_F for Λ and K^0_S as obtained in data and MC samples are shown in Fig. 48 and 49. In addition of the consideration that the spectrum is again different for data and MC, another important conclusion can be drawn: we observe that the average x_F for the considered samples is $\langle x_F \rangle \sim 0.04$ and $\langle x_F \rangle \sim 0.003$ for $\sqrt{s} = 0.9$ TeV and $\sqrt{s} = 7$ TeV respectively so that, even if our detector is forward, with the study of V^0 we are actually probing the *central* region of pp interactions. This property will be particularly important when analysing the Λ polarisation.

Finally we show in Fig. 50, 51 and 52 the distributions of the azimuthal angle ϕ for Λ, $\bar{\Lambda}$ and K^0_S respectively. It can be noticed that the MC reproduces quite well the distributions of the data. In particular at $\sqrt{s} = 0.9$ TeV it can be seen both in MC and data distributions the effect on the acceptance of the VELO open position which cause a loss of events at $\phi = \pm\pi/2$. From the comparison in these three figures of the left side plots, referred to field down configuration, and right side plots, for field up, it can be noticed that the acceptance for Λ decays is not invariant for the field change. In particular while with the field down the Λ combinations accumulate around $\phi = 0$, with field up they move to $\phi = \pm\pi$. The situation is reversed for the $\bar{\Lambda}$ combinations. This effect is not present in the K^0_S combinations suggesting that the reasons have to be found in the asymmetry of the Λ and $\bar{\Lambda}$ decay. The detection and reconstruction efficiency for protons and pions is certainly not the same leading to asymmetries in the reconstructed phase space. No concern comes from this since the

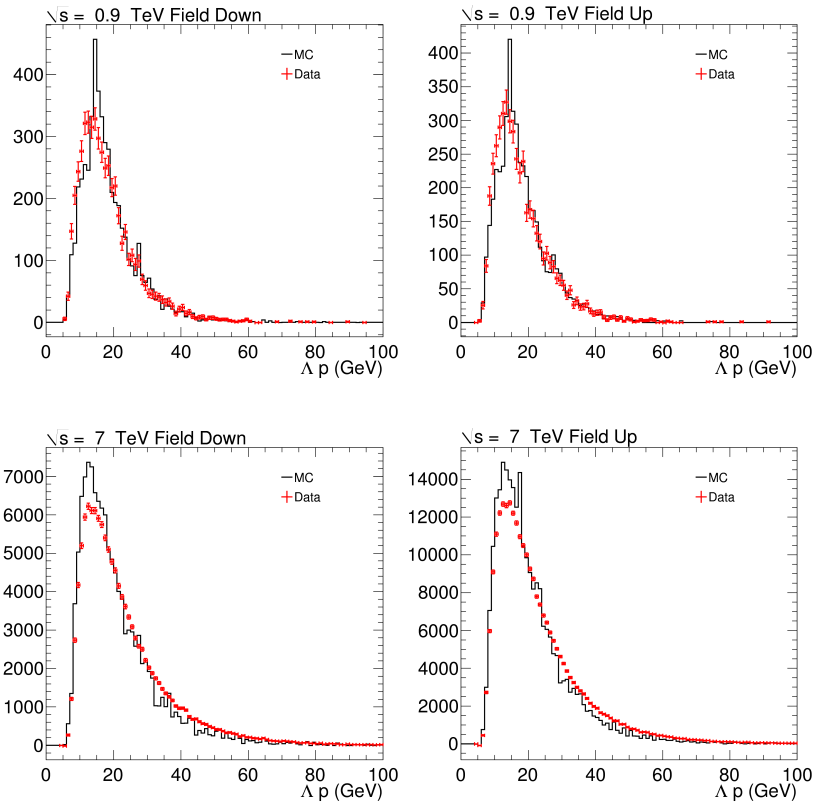

Figure 42.: Distributions of the Λ and $\bar{\Lambda}$ momentum for MC (black line) and data (red error bars) at $\sqrt{s} = 0.9$ TeV (top) and at 7 TeV (bottom). The left side plots are for the field down configuration while the right side ones for the field up.

distributions are well reproduced by the MC. Anyhow studies on the possible systematic uncertainties given by this variable were conducted and will be resumed in §3.8.6.1.

3.5 SIGNAL EXTRACTION

In order to extract the number of selected V^0 in our samples, we need to identify the invariant mass region which we consider as signal and the ones which we use to estimate our background (sidebands).

In Fig. 53 and 54 we show the invariant mass distributions for selected V^0 candidates as obtained analysing the pp collisions data at $\sqrt{s} = 0.9$ TeV and 7 TeV. The distributions are fitted with

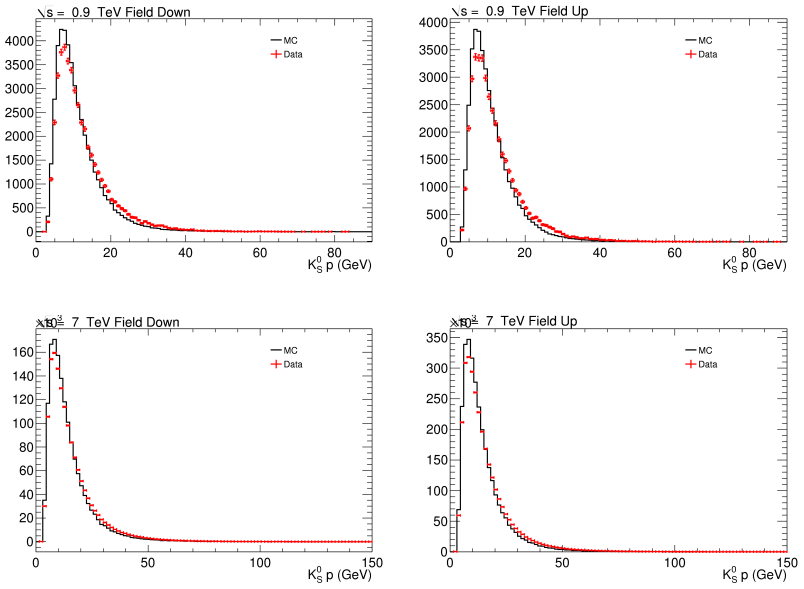

Figure 43.: Distributions of the K^0_S momentum for MC (black line) and data (red error bars) at $\sqrt{s} = 0.9$ TeV (top) and at 7 TeV (bottom). The left side plots are for the field down configuration while the right side ones for the field up.

a gaussian signal function plus a linear function to reproduce the combinatorial background.

The estimated invariant mass resolutions are $\sigma_\Lambda \simeq 1.3$ MeV/c² for Λ and $\bar{\Lambda}$ candidates and $\sigma_{K^0_S} \simeq 4.1$ MeV/c² for K^0_S candidates. We do not report more precise measurements of the resolutions since an exact estimate of their values is beyond the scope of the present work.

We have used the approximate values of the resolutions $\sigma_\Lambda = 1.5$ MeV/c² and $\sigma_{K^0_S} = 4.5$ MeV/c² in order to set the invariant mass signal region and sidebands. If σ_{V^0} is the approximate resolution for the considered V^0 species, we define as "signal" what is inside $\pm 3\sigma_{V^0}$ with respect to the nominal [69] value of the V^0 mass. Conversely, we define sidebands two regions on the left and right of the signal region. These regions have been set $10\sigma_\Lambda$ and $10\sigma_{K^0_S}$ in width for the $\bar{\Lambda}/\ \Lambda$ and for the K^0_S respectively. The values of the signal and sidebands region are summarised in Table 6.

Following this division, the extraction of the number of events from the invariant mass distributions has been obtained through sideband subtraction. This simple technique computes the num-

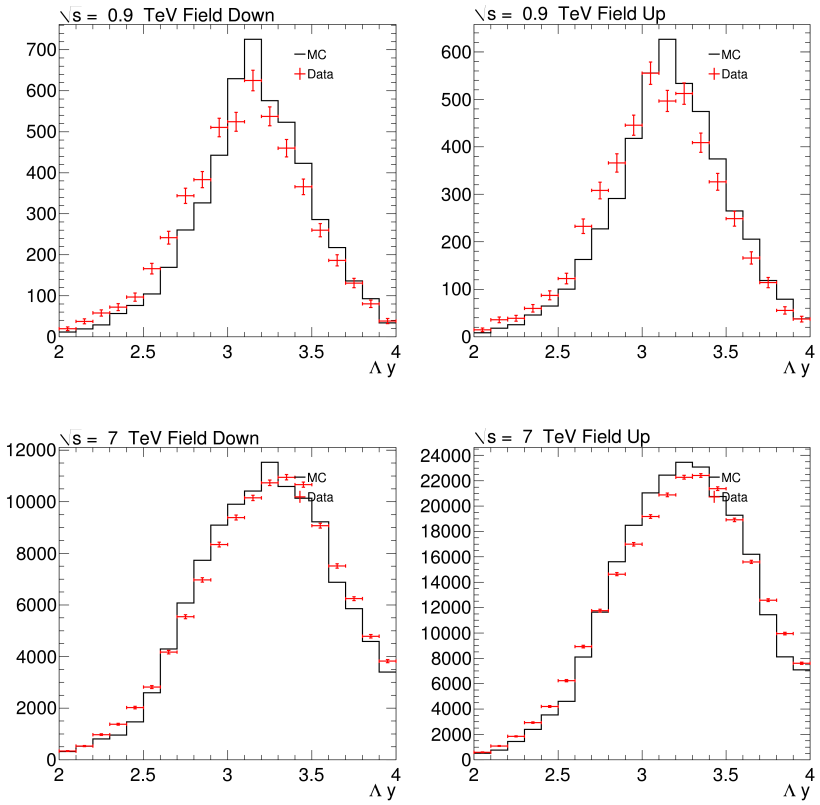

Figure 44.: Distributions of the Λ and $\bar{\Lambda}$ rapidity for MC (black line) and data (red error bars) at $\sqrt{s} = 0.9$ TeV (top) and at 7 TeV (bottom). The left side plots are for the field down configuration while the right side ones for the field up.

Table 6.: Summary of the signal and sidebands invariant mass regions for the different V^0 species. Values are reported as a function of the approximate experimental resolutions, σ_Λ and $\sigma_{K^0_S}$, and the nominal masses [69], m_Λ and $m_{K^0_S}$, of the respective candidates. Numerical values are in MeV/c^2.

Sample	Signal region	Left sideband	Right sideband
Λ and $\bar{\Lambda}$	$m_\Lambda \pm 3\sigma_\Lambda$	$[1080, 1080 + 15\sigma_\Lambda]$	$[1150 - 15\sigma_\Lambda, 1150]$
K^0_S	$m_{K^0_S} \pm 3\sigma_{K^0_S}$	$[447.6, 447.6 + 4\sigma_{K^0_S}]$	$[547.6 - 4\sigma_{K^0_S}, 547.6]$

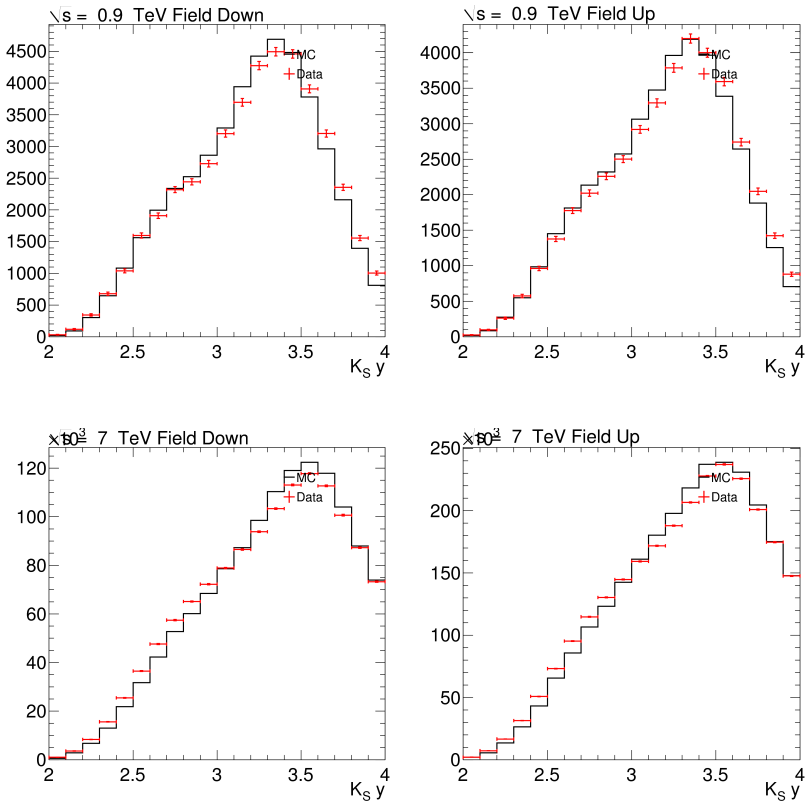

Figure 45.: Distributions of the K^0_S rapidity for MC (black line) and data (red error bars) at $\sqrt{s} = 0.9$ TeV (top) and at 7 TeV (bottom). The left side plots are for the field down configuration while the right side ones for the field up.

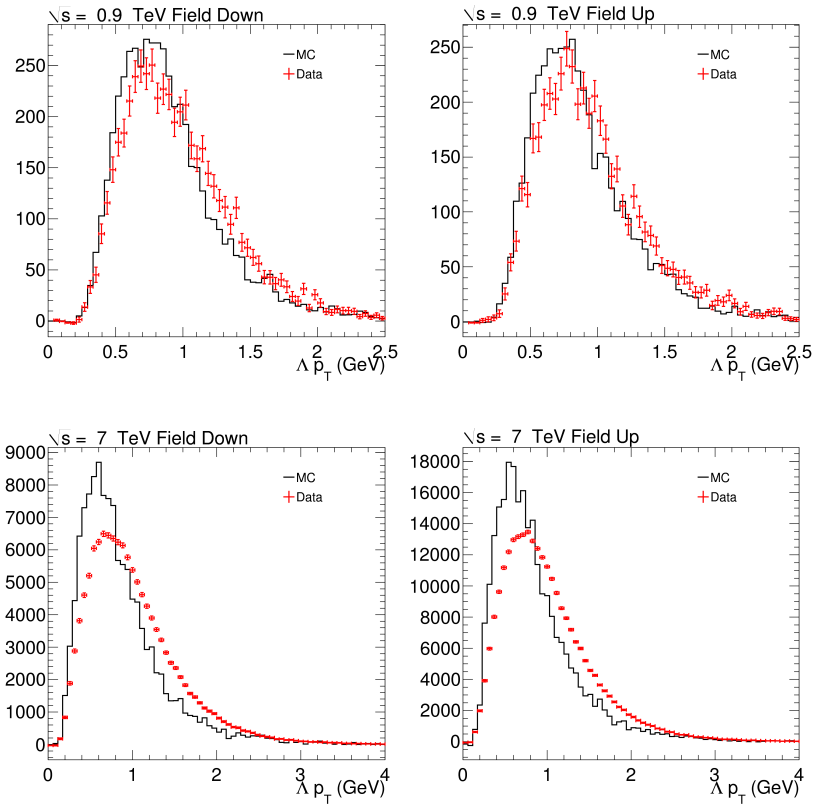

Figure 46.: Distributions of the Λ and $\bar{\Lambda}$ p_T for MC (black line) and data (red error bars) at $\sqrt{s} = 0.9$ TeV (top) and at 7 TeV (bottom). The left side plots are for the field down configuration while the right side ones for the field up.

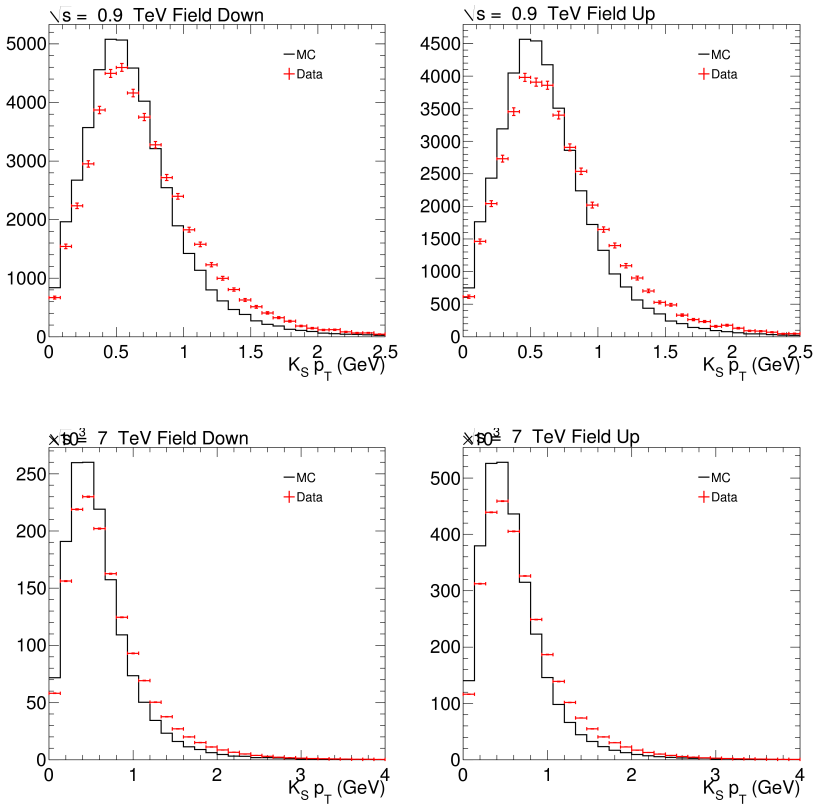

Figure 47.: Distributions of the K^0_S p_T for MC (black line) and data (red error bars) at $\sqrt{s} = 0.9$ TeV (top) and at 7 TeV (bottom). The left side plots are for the field down configuration while the right side ones for the field up.

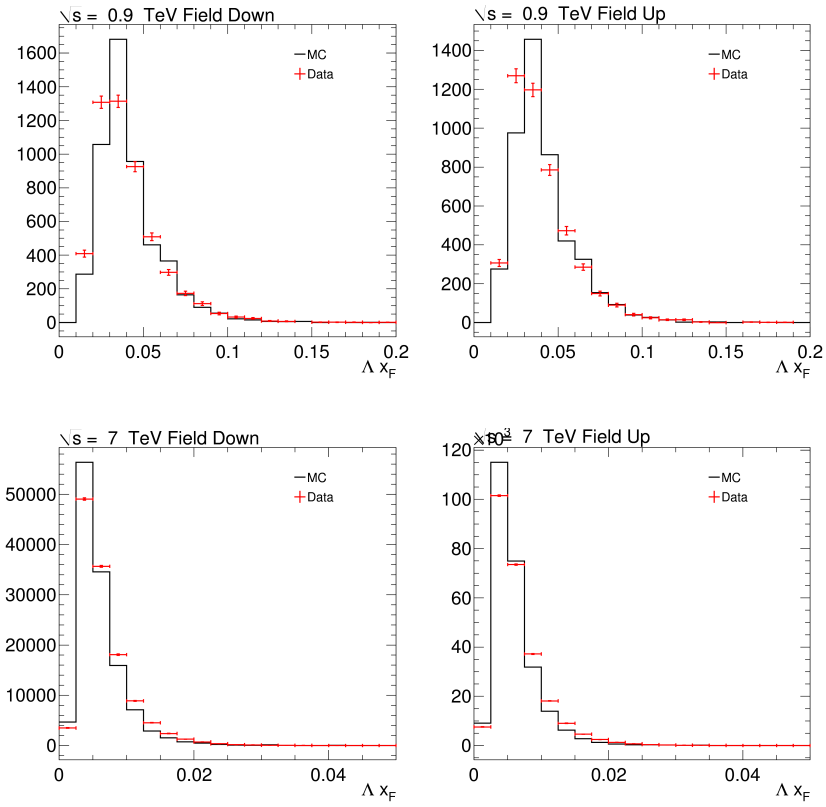

Figure 48.: Distributions of the Λ and $\bar{\Lambda}$ x_F for MC (black line) and data (red error bars) at $\sqrt{s} = 0.9$ TeV (top) and at 7 TeV (bottom). The left side plots are for the field down configuration while the right side ones for the field up.

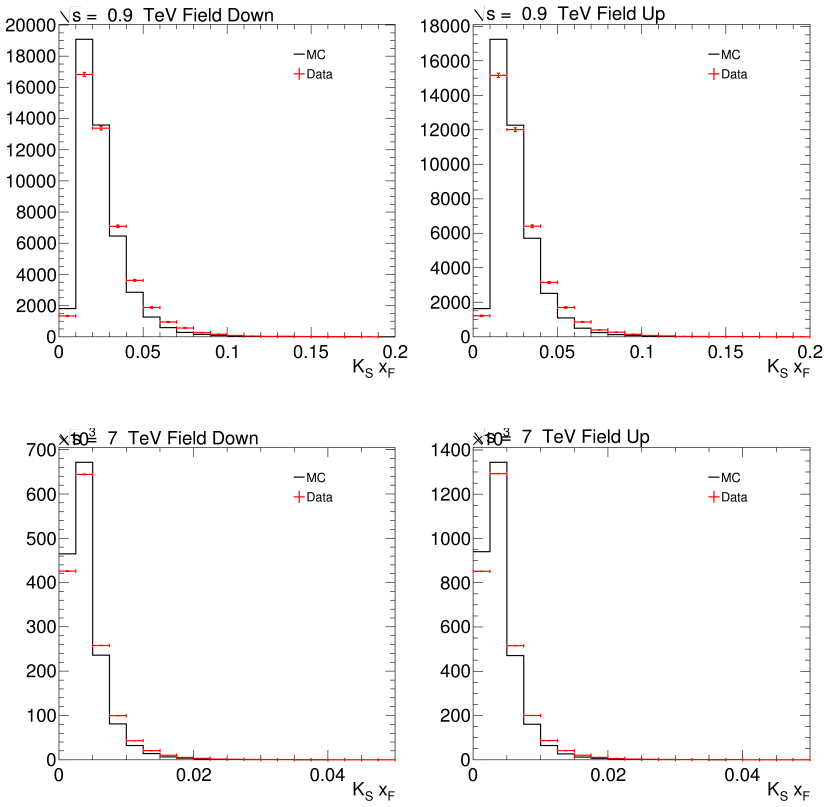

Figure 49.: Distributions of the K^0_S x_F for MC (black line) and data (red error bars) at $\sqrt{s} = 0.9$ TeV (top) and at 7 TeV (bottom). The left side plots are for the field down configuration while the right side ones for the field up.

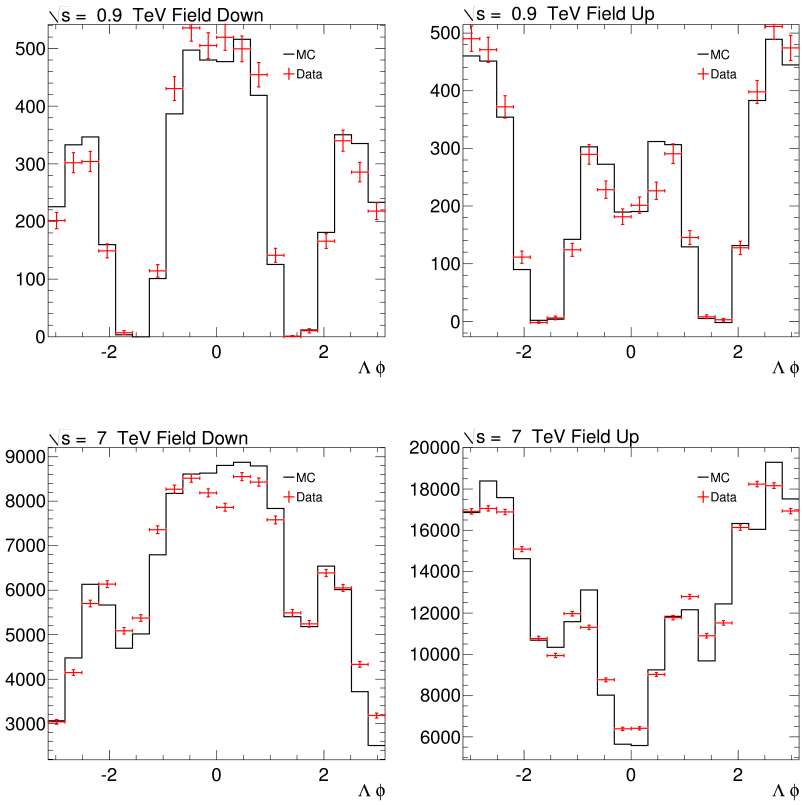

Figure 50.: Distributions of the Λ azimuthal angle ϕ for MC (black line) and data (red error bars) at $\sqrt{s} = 0.9$ TeV (top) and at 7 TeV (bottom). The left side plots are for the field down configuration while the right side ones for the field up.

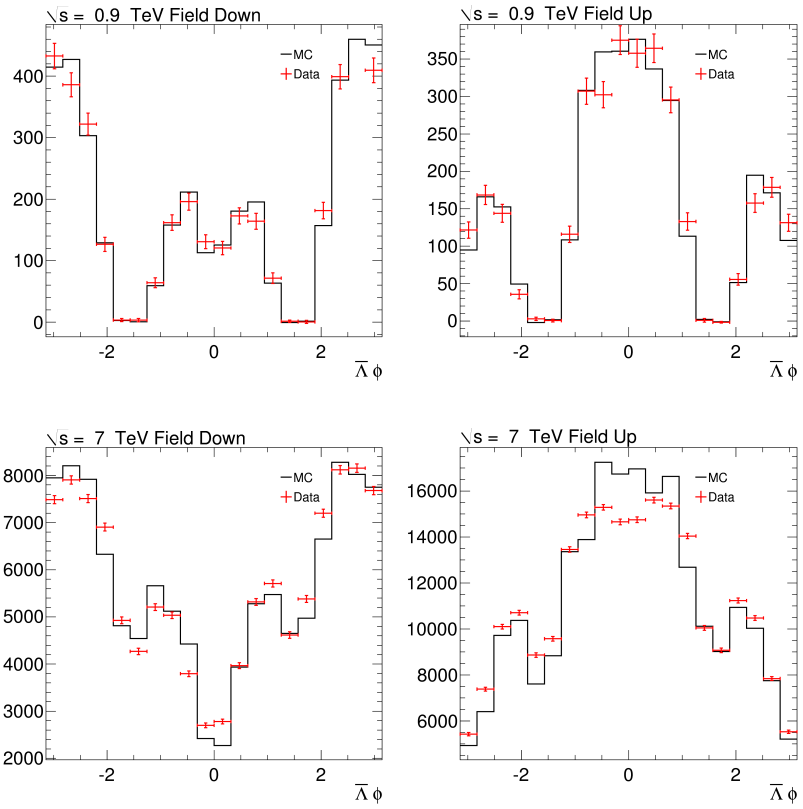

Figure 51.: Distributions of the $\bar{\Lambda}$ azimuthal angle ϕ for MC (black line) and data (red error bars) at $\sqrt{s} = 0.9$ TeV (top) and at 7 TeV (bottom). The left side plots are for the field down configuration while the right side ones for the field up.

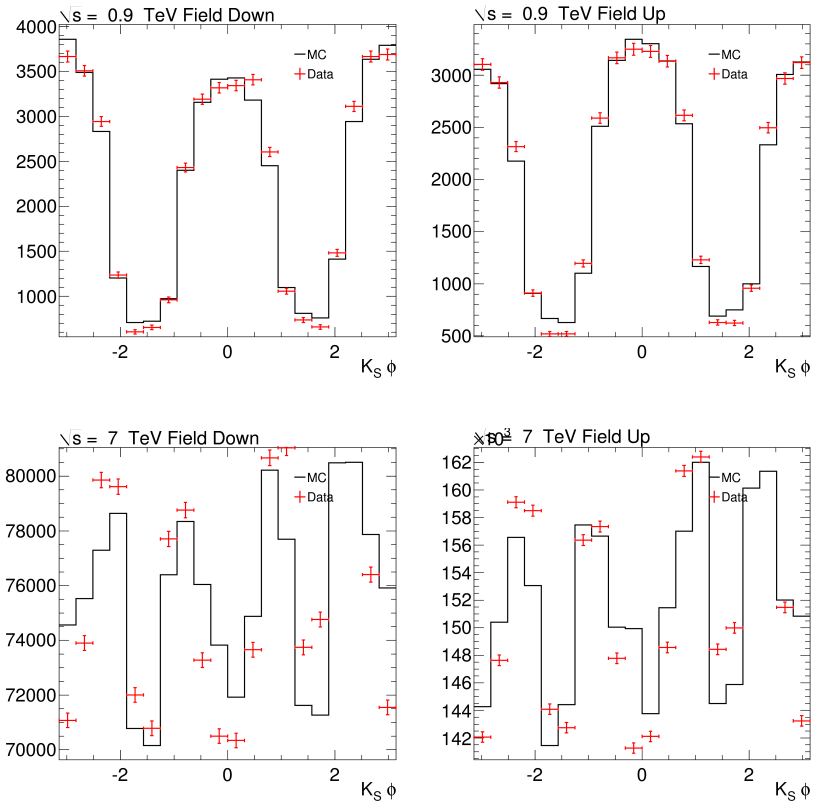

Figure 52.: Distributions of the K^0_S azimuthal angle ϕ for MC (black line) and data (red error bars) at $\sqrt{s} = 0.9$ TeV (top) and at 7 TeV (bottom). The left side plots are for the field down configuration while the right side ones for the field up.

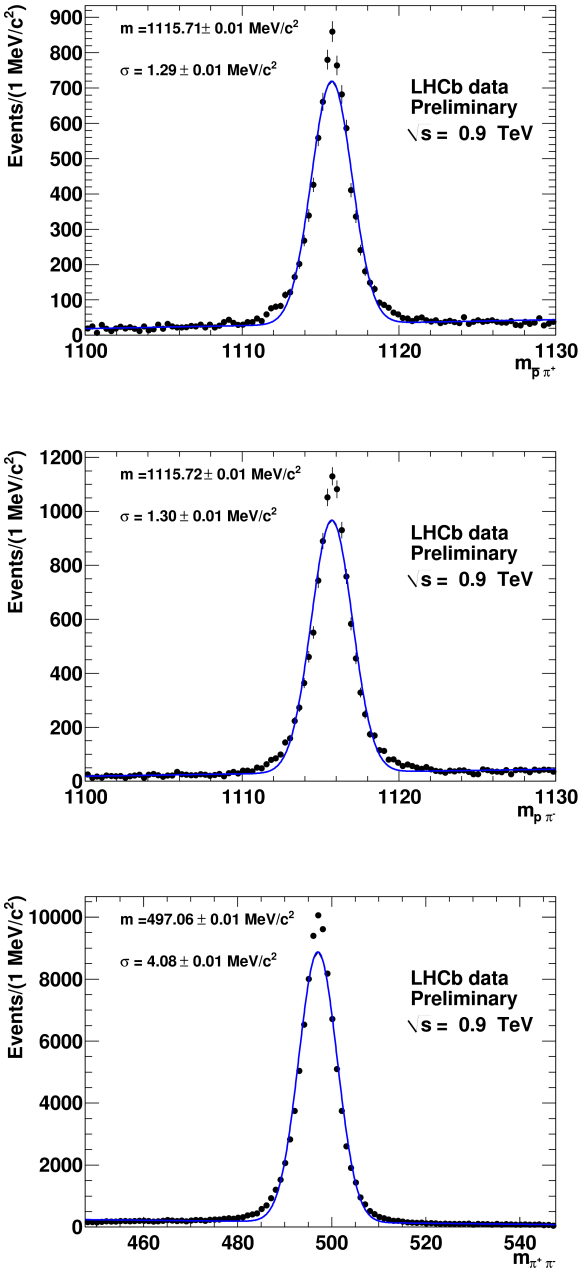

Figure 53.: Invariant mass distributions for selected V^0 candidates in pp collisions at $\sqrt{s} = 0.9$ TeV. From top to bottom the $\bar{\Lambda} \to \bar{p}\pi^+$, $\Lambda \to p\pi^-$ and $K^0_S \to \pi^+\pi^-$ combinations are shown.

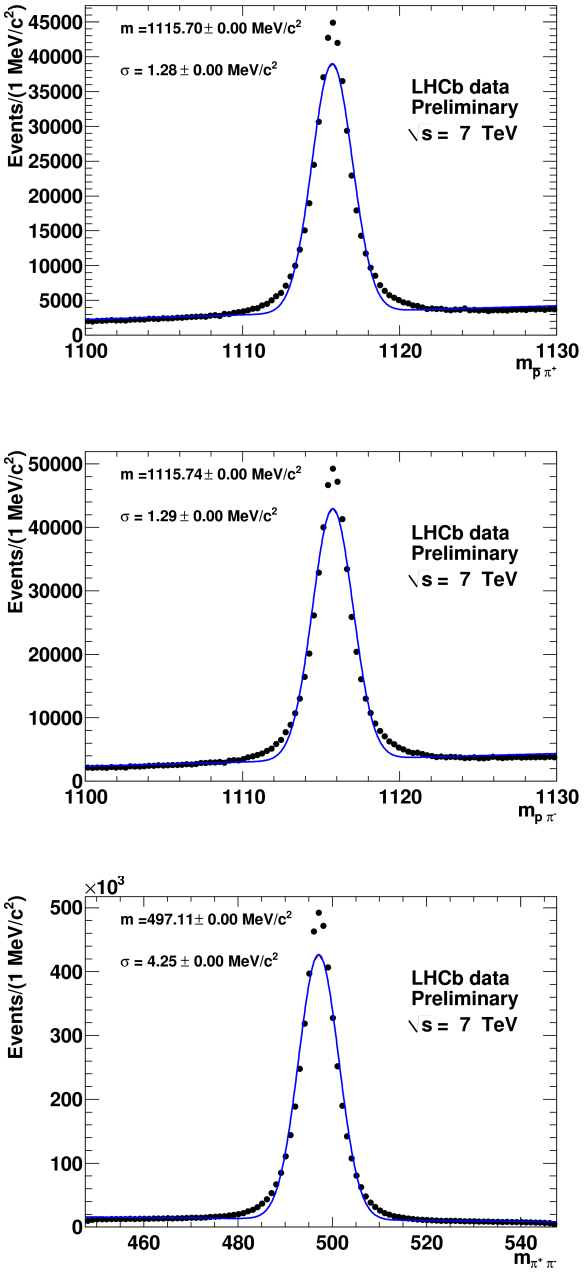

Figure 54.: Invariant mass distributions for selected V^0 candidates in pp collisions at $\sqrt{s} = 7$ TeV. From top to bottom the $\bar{\Lambda} \to \bar{p}\pi^+$, $\Lambda \to p\pi^-$ and $K^0_S \to \pi^+\pi^-$ combinations are shown.

ber of signal events by statistically subtracting the combinatorial background in the invariant mass region from an estimate obtained with the sidebands, namely:

$$N_{sig} = N_{mw} - N_{sb}/\rho \tag{3.6}$$

where N_{sig} is the extracted number of signal events from N_{mw} events in the signal mass window minus N_{sb} of the sidebands regions weighted by ρ which is the ratio between the widths of the signal mass windows and sidebands. This technique is analytically exact if the background is distributed linearly as a function of the invariant mass, as we expect for combinatorial background.

3.5.1 *Choice of variables and binning*

Most of the theoretical works on the V^0 production consider pseudo-rapidity and transverse momentum as relevant variables. However we prefer to use p_T and rapidity instead of pseudo-rapidity. In fact rapidity transforms by translation in Lorentz boosts which helps to compare results at different energies; in particular, as we have seen, we want to understand the behaviour of the $\bar{\Lambda}/\Lambda$ ratio as a function of Δy.

In order to have sufficient statistics in the considered bins, the following binning division were chosen. In rapidity we consider constant 0.5 wide bins from $y = 2.0$ to $y = 4.0$ for $\sqrt{s} = 0.9$ TeV plus one additional bin ($4.0 < y < 4.5$) at $\sqrt{s} = 7$ TeV. In transverse momentum we divided the range in non-constant bins of about the same statistics, using the following intervals, in MeV/c: $[150(250), 500, 650, 800, 1000, 1200, 2500]$ for the $\sqrt{s} = 7$ TeV ($\sqrt{s} = 0.9$ TeV) sample.

3.5.2 *Raw yields*

We have extracted the number of V^0 candidates in the considered kinematic regions for the two data samples of pp collisions at $\sqrt{s} = 0.9$ TeV and 7 TeV. As already said for each energy the samples taken with different magnetic field are analysed separately and consequently the results are reported in different tables.

In Table 7 we report the integrated number of the different V^0 species as obtained from data. The numbers are not efficiency corrected.

The raw yields in transverse momentum and rapidity bins have been also obtained. Since this is a long list of tables, being one

Table 7.: Number of background subtracted V^0 as obtained from the different data samples analyses. The numbers are not corrected for efficiency.

Sample	$\bar{\Lambda}$	Λ	K^0_S
$\sqrt{s} = 0.9$ TeV field down	4104	5435	48658
$\sqrt{s} = 0.9$ TeV field up	7563	10321	91988
$\sqrt{s} = 7$ TeV field down	135084	144611	1552920
$\sqrt{s} = 7$ TeV field up	263132	298709	3114803

for each V^0 species, energy and field, we have decided to report them all in Appendix A. The tables show the raw yields in p_T and y bins but also the yields integrated in the considered p_T range in y bins.

Most of the bins have sufficient statistics, however in the very low p_T and low rapidity region some of the samples have not enough events because in these regions the efficiency is very low.

3.6 EFFICIENCY CORRECTION

In order to obtain the production yield for V^0 particles, the raw event yields, obtained from signal extraction, have to be corrected for the efficiency.

The efficiency has been measured exploiting MC simulations and computed as:

$$\varepsilon_{MC} = \frac{N^{sel}_{MC}(\text{prompt, non–diffractive})}{N^{gen}_{MC}(\text{prompt, non–diffractive})} \tag{3.7}$$

where $N^{sel\ (gen)}_{MC}$ is the number of selected (generated) Monte Carlo events for each considered bin. For the calculation of the efficiency we consider just prompt V^0 particles, as previously defined. Moreover we do not consider the diffractive component. Thus, we do not make any attempt for correcting neither the non-prompt nor the possible diffractive contributions through efficiency, however we give an estimate of their contribution and possible effect on the final measurement in the systematics uncertainties calculation, in §3.8.2 and 3.8.3 respectively.

The number of selected Monte Carlo events is estracted by analysing full MC simulations in the very same way as the real data, following reconstruction, selection and signal extraction.

Hence the efficiency of Eq. (3.7) is inclusive of acceptance, reconstruction and selection efficiencies. Moreover the denominator is defined as the total number of V^0 generated and therefore the efficiency takes into account those particles which decay via other channels or which interact with the detector material before decaying.

The efficiencies for every sample and for each V^0 species are reported in tables from 47 to 58 of Appendix A.

3.6.1 *Calibration of the p_T scale*

As already stated, there is a significant difference between the V^0 transverse momentum distribution of data and MC. From the theoretical point of view this can be due to many reasons, which could reflect the poor description of our MC with respect to reality. However in this context we are using Monte Carlo simulations just as a convenient way to understand the efficiency of our detector with respect to V^0 selection. In this respect the underlying initial state physics differences are not important and we shall concentrate instead on the influence of this spectrum difference on the efficiency estimation.

Clearly the reconstruction and selection efficiencies are function of the transverse momentum. If the p_T distribution is not the same for data and MC, the correction with an efficiency integrated in transverse momentum would bias the results. In terms of the LHCb detector p_T and y are almost a measurement of the zone of the detector which detected the V^0 particles decay products. This is not exact for two reasons:

- the V^0 decay products do not share exactly the same portion of phase space of the V^0;
- a third independent coordinate is present, the azimuthal angle ϕ, which could influence the efficiency.

While the influence of the latter will be discussed as a systematic uncertainty in §3.8.6.1, the effect of the former should not give a large contribution since the correlation between the phase space of the V^0 and of its decay products is the same for data and MC.

Therefore it is reasonable to assume that, while the overall function of the efficiency with respect to p_T can be different, its first derivative have to be the same, i.e.:

$$\frac{\partial \varepsilon_{\text{Data}}(p_T)}{\partial p_T} = \frac{\partial \varepsilon_{\text{MC}}(p_T)}{\partial p_T} \tag{3.8}$$

where $\varepsilon(p_T)$ is the efficiency either averaged on the other variables or in a given bin of an other variable (e.g. in a given y bin). This assumption is rather weak and is based just on the conviction that the detector simulation represents quite well its real behaviour.

In principle a rather safe estimate of the efficiency would be already given when calculating the results in bins of p_T; however when integrating the results this contribute with statistical errors for each bin. Hence we have decided to calculate the estimate of the efficiency from MC simulations after re-weighting their p_T spectrum in order to match the one obtained in the data.

Even if a only a small difference is present in the y distribution for data and MC, it has been decided to re-weight both variables distributions simultaneously in order to avoid artifacts in the non-reweighted distribution.

3.6.1.1 *Re-weighting technique*

The re-weighting of the p_T and y spectrum is done as follows. First we estimate the background subtracted bidimensional p_T-y distributions for data and MC, as shown in Fig. 46 and 47. Secondly we normalise these distributions so that can be treated as probability distribution functions: $f^{data}(p_T, y)$ and $f^{MC}(p_T, y)$ for data and MC respectively. Then we divide the distribution of the data with the one of the MC:

$$w(p_T, y) = \frac{f^{data}(p_T, y)}{f^{MC}(p_T, y)} \tag{3.9}$$

which gives us the desired weight function. Since we obtain $w(p_T, y)$ as the ratio of two histograms in order to have a continuous function we interpolate it with a polynomial function. This procedure of course does not increase artificially the information content of the function but permits a smoother usage. After that we can use $w(p_T, y)$ to weight the MC events.

Note that in order not to bias the efficiency estimation the re-weighting has to be applied both to reconstructed and generated MC events, i.e. to the numerator and to the denominator of the efficiency.

The re-weighting procedure has been applied separately to Λ and K^0_S particles, while a common function has been used for Λ and $\bar{\Lambda}$.

The possible systematic errors connected with this procedure will be discussed in §3.8.4.

3.6.2 *Corrected yields*

By applying the efficiency correction to the raw yields we have obtained the corrected production yields for the different V^0 species. We report these results in Appendix A: Tables from 59 to 70 show the results for the different V^0 species at $\sqrt{s} = 0.9$ TeV and 7 TeV for both the magnetic fields.

3.7 RESULTS

In this section we present the results of our analysis for the $\bar{\Lambda}/\Lambda$ and $\bar{\Lambda}/K^0_S$ production ratios.

3.7.1 $\bar{\Lambda}/\Lambda$ *ratio*

The $\bar{\Lambda}/\Lambda$ ratio obtained in bins of rapidity and transverse momentum from the corrected yields calculated in §3.6.2 is reported in Table 71 and 72 of Appendix A for $\sqrt{s} = 0.9$ TeV with field down and field up respectively. Since the two results are in agreement they have been averaged for the final results which are reported in Table 8. The p_T integrated results are also shown for the $\sqrt{s} = 0.9$ TeV sample in Fig. 55; the plot on the left shows the results for field down and field up samples which are compared using only statistical errors. The plot on the right side of Fig 55 shows the final results for the $\bar{\Lambda}/\Lambda$ ratio as a function of rapidity; it includes statistical and systematics errors summed in quadrature. The results are compared with different Monte Carlo samples: one is the standard PYTHIA tune for the LHCb MC, the second the Perugia-0 tune and the third the Perugia-NOCR tune [24, 25] presented in 1.2.5. As it can be seen the data obtained in our analysis are not consistent with the predictions of the two Monte Carlo simulations for the LHCb MC and Perugia-0 tunes while they are in agreement with the Perugia-NOCR sample. In Figure 56 we show the $\bar{\Lambda}/\Lambda$ ratio as a function of the transverse momentum of the baryons: the ratio is shown for the two different field configurations in (a) and averaged in (b). It can be seen that this observable is independent of p_T. This is confirmed by the plot in Fig. 57 where the $\bar{\Lambda}$ ratio is shown as a function of the rapidity for different p_T ranges which give results in agreement with each other.

Analogous results have been obtained for the $\sqrt{s} = 7$ TeV analysis. The final results for the $\bar{\Lambda}/\Lambda$ ratio in bins of p_T and y are shown in Tables 73 and 74 of Appendix A separately for field down and up respectively and averaged in Table 9 together with the p_T integrated values. In Figure 58 we report the p_T integrated results as a function of the rapidity for the LHCb data as obtained in this analysis and for the three mentioned Monte Carlo samples (LHCb MC, Perugia-0 tune and Perugia-NOCR tune [24, 25]).

The $\bar{\Lambda}/\Lambda$ ratio is very close to 1 at $\sqrt{s} = 7$ TeV and the various MC prediction are all consistent with the experimental results. The decreasing trend as a function of rapidity is better reproduced

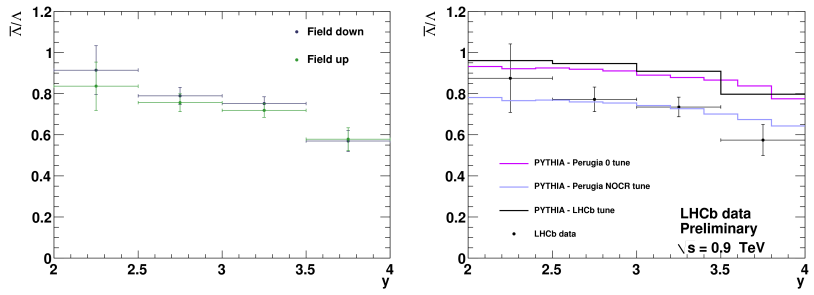

(a) (b)

Figure 55.: The $\bar{\Lambda}/\Lambda$ ratio as a function of rapidity as measured in pp collisions at $\sqrt{s} = 0.9$ TeV in LHCb: (a) the comparison of results obtained at the two polarities of the LHCb magnetic field; (b) the final results, obtained averaging the two fields values, compared with the LHCb standard Monte Carlo and Monte Carlo predictions which use the Perugia-0 and Perugia-NOCR PYTHIA tunes[24, 25].

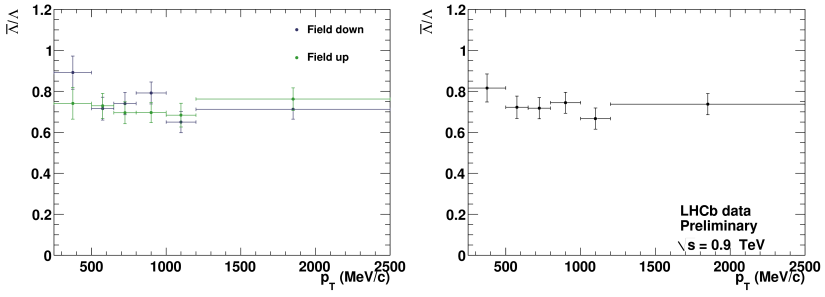

(a) (b)

Figure 56.: The $\bar{\Lambda}/\Lambda$ ratio as a function of p_T as measured in pp collisions at $\sqrt{s} = 0.9$ TeV in LHCb: (a) the comparison of results obtained at the two polarities of the LHCb magnetic field; (b) the final results, obtained averaging the two fields values.

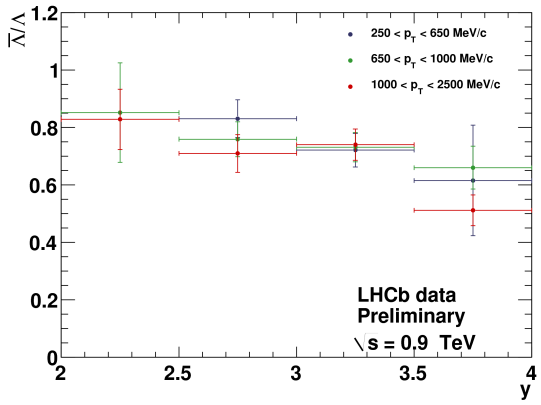

Figure 57.: The $\bar{\Lambda}/\Lambda$ ratio as a function of rapidity for different p_T ranges as measured in pp collisions at $\sqrt{s} = 0.9$ TeV in LHCb.

by the Perugia-NOCR sample, confirming that this tune is best suited in order to describe the baryon number transport.

In Figure 59 we show the $\bar{\Lambda}/\Lambda$ ratio as a function of p_T (integrated over rapidity). As noticed for the $\sqrt{s} = 0.9$ TeV sample, also at 7 TeV this production ratio is not a function of transverse momentum. Again, this is confirmed by the different $\bar{\Lambda}/\Lambda$ ratios trends as a function of rapidity for different p_T ranges, shown in Fig. 60, which are consistent with each other.

As we have anticipated in §1.2.3 the same results can be shown as a function of Δy, the difference between the rapidity of the incoming proton and the one of the outgoing Λ, defined as:

$$\Delta y = y_{beam} - y_{\Lambda} \quad . \tag{3.10}$$

This variable allows us to compare results taken at different energies and in different rapidity ranges. In Fig. 61 (a) the results of our analysis at $\sqrt{s} = 0.9$ TeV and $\sqrt{s} = 7$ TeV are shown together with one data point from the STAR experiment at RHIC [70]. As it can be seen our results are continuous as a function of Δy, they are in agreement with each other in the Δy range in which overlap and are consistent with the STAR data point. In Fig. 61 (b) we reproduce the same plot comparing these experimental results with different MC predictions obtained using the Perugia-0 and Perugia NOCR tunes of PYTHIA. Results appear more consistent with the Perugia NOCR tune for small Δy and with Perugia-0 tune for larger rapidity differences, suggesting that none of the two tunes is able to reproduce this trend in the whole range. The

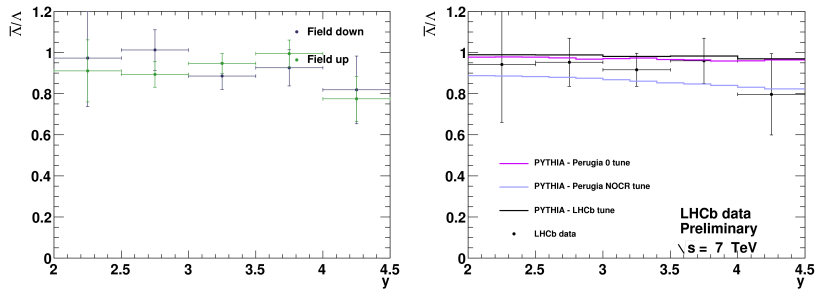

(a) (b)

Figure 58.: The $\bar{\Lambda}/\Lambda$ ratio as a function of rapidity as measured in pp collisions at $\sqrt{s} = 7$ TeV in LHCb: (a) the comparison of results obtained at the two polarities of the LHCb magnetic field; (b) the final results, obtained averaging the two fields values, compared with the LHCb standard Monte Carlo and Monte Carlo predictions which use the Perugia-0 and Perugia-NOCR PYTHIA tunes[24, 25].

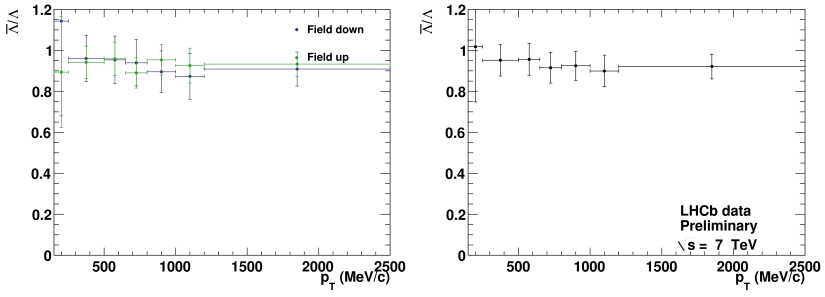

(a) (b)

Figure 59.: The $\bar{\Lambda}/\Lambda$ ratio as a function of p_T as measured in pp collisions at $\sqrt{s} = 7$ TeV in LHCb: (a) the comparison of results obtained at the two polarities of the LHCb magnetic field; (b) the final results, obtained averaging the two fields values.

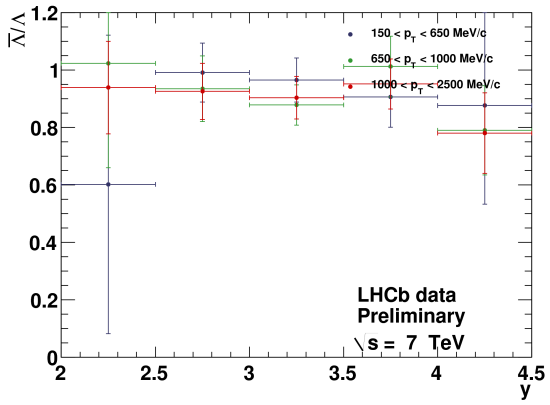

Figure 60.: The $\bar{\Lambda}/\Lambda$ ratio as a function of rapidity for different p_T ranges as measured in pp collisions at $\sqrt{s} = 7$ TeV in LHCb.

non perfect description of this phenomenon by MC tunes is also confirmed by the fact that the same MC tune at fixed Δy but different energies do not predict the same value. However our experimental uncertainties in the high Δy range do not allow to discriminate between the two models.

3.7.2 $\bar{\Lambda}/K^0_S$ *ratio*

Following the same procedure of the $\bar{\Lambda}/\Lambda$ ratio, results on the $\bar{\Lambda}/K^0_S$ ratio have been also obtained. The values of the $\bar{\Lambda}/K^0_S$ ratio in bins of p_T and rapidity are shown in Table 10 for the $\sqrt{s} = 0.9$ TeV data analysis.

The $\bar{\Lambda}/K^0_S$ values as a function of rapidity, integrated in p_T, are also shown in Fig. 62 and are compared with Monte Carlo predictions from a standard tune LHCb Monte Carlo, and from the Perugia-0 and Perugia NOCR Pythia tunes [24, 25]. The $\bar{\Lambda}/K^0_S$ ratio slightly decreases as a function of rapidity, as predicted by MC simulations, but the central value is not consistent with the predictions, which are close to each other.

In Fig. 63 we show instead the $\bar{\Lambda}/K^0_S$ ratio as a function of the transverse momentum comparing the different field results in (a) and reporting the average in (b). Moreover we show in Fig. 64 the $\bar{\Lambda}/K^0_S$ results as a function of rapidity for different p_T ranges. Both plots show that $\bar{\Lambda}/K^0_S$ ratio increases as a function of p_T indicating that the suppression of the baryons in hadronisation is less important in harder collisions.

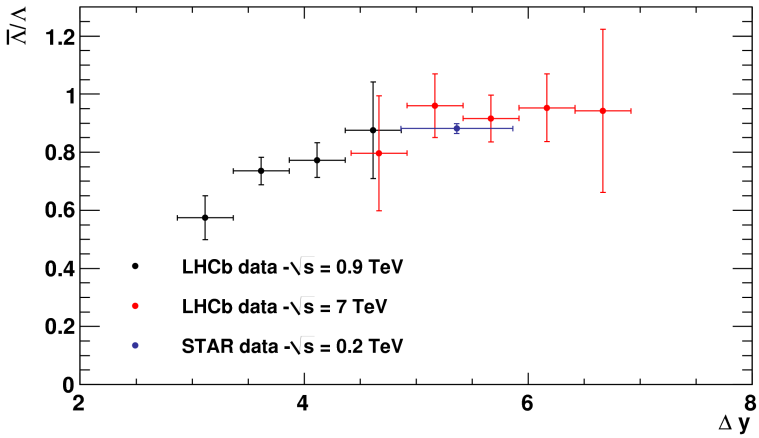

(a)

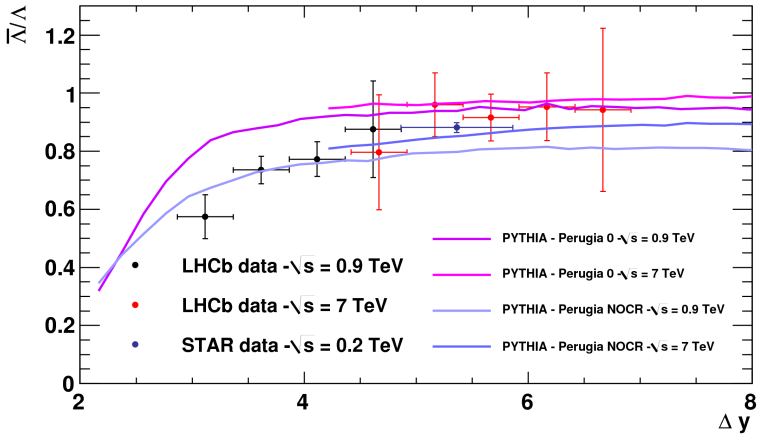

(b)

Figure 61.: $\bar{\Lambda}$ ratio as a function of Δy as obtained from pp collisions in LHCb at $\sqrt{s} = 0.9$ TeV and $\sqrt{s} = 7$ TeV. Results are compared from one data point from the STAR experiment at RHIC [70]. In (b) we also show the comparison with Monte Carlo predictions obtained with the Perugia-0 and Perugia-NOCR Pythia tunes [24, 25] at the two different energies.

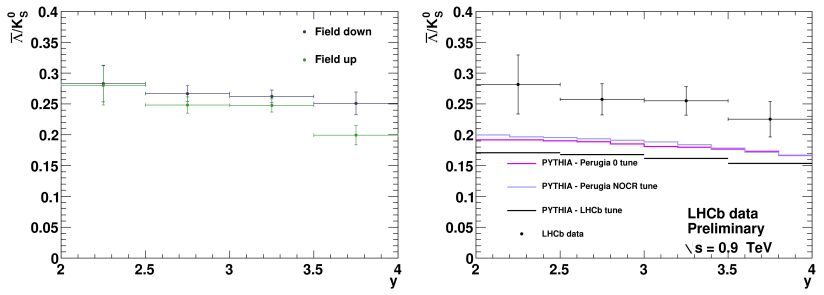

(a) (b)

Figure 62.: The $\bar{\Lambda}/K^0_S$ ratio as a function of rapidity as measured in pp collisions at $\sqrt{s} = 0.9$ TeV in LHCb: (a) the comparison of results obtained at the two polarities of the LHCb magnetic field; (b) the final results, obtained averaging the two fields values, compared with the LHCb standard Monte Carlo and Monte Carlo predictions which use the Perugia-0 and Perugia-NOCR PYTHIA tunes[24, 25].

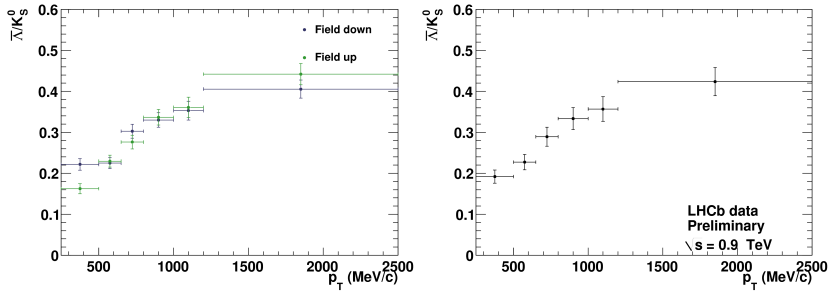

(a) (b)

Figure 63.: The $\bar{\Lambda}/K^0_S$ ratio as a function of p_T as measured in pp collisions at $\sqrt{s} = 0.9$ TeV in LHCb: (a) the comparison of results obtained at the two polarities of the LHCb magnetic field; (b) the final results, obtained averaging the two fields values.

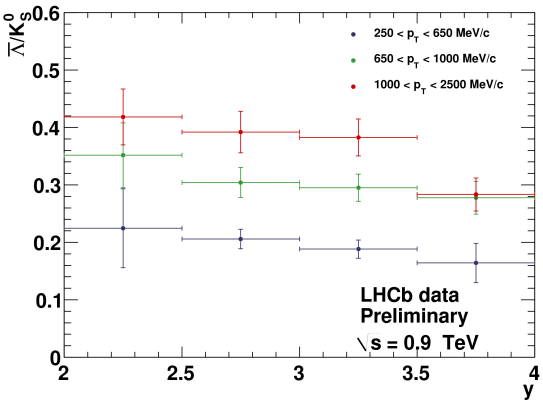

Figure 64.: The $\bar{\Lambda}/K^0_S$ ratio as a function of rapidity for different p_T ranges as measured in pp collisions at $\sqrt{s} = 0.9$ TeV in LHCb.

Finally we report the $\bar{\Lambda}/K^0_S$ results at $\sqrt{s} = 7$ TeV in Table 11 in bins of p_T and rapidity. The p_T integrated results are the last row of this table and are shown in Fig. 65. Therein they are compared with Monte Carlo predictions from the standard LHCb MC Pythia tune, and from the Perugia-0 and Perugia NOCR tunes. At this collision energy, the $\bar{\Lambda}/K^0_S$ ratio is almost flat as a function of rapidity and the trend of the data is reproduced by the various MC samples which however do not agree with the mean value, which is around 0.25 in the data and 0.2 in the MC predictions. The discrepancy is not large if compared with experimental uncertainties, but only two data points are consistent with predictions. Data seem to indicate that both at $\sqrt{s} = 0.9$ TeV and 7 TeV the suppression of hadronisation into baryons with respect to mesons is less effective than predicted. In Fig. 67 we show the same plot, $\bar{\Lambda}/K^0_S$ ratio as a function of rapidity, for different transverse momentum ranges. Moreover the trend of $\bar{\Lambda}/K^0_S$ ratio versus p_T for pp collisions at $\sqrt{s} = 7$ TeV is reported in Fig. 66. Again we see that the $\bar{\Lambda}/K^0_S$ ratio is a strong function of transverse momentum and we can conclude, as for the $\sqrt{s} = 0.9$ TeV sample, that the suppression of baryons in hadronisation is less effective when the energy transfer in the collision is larger. This indicates, as suggested by the different phenomenological models, that the suppression is mainly due to kinematic factors which open a smaller phase space to the creation of a diquark with respect to a single quark in hadronisation.

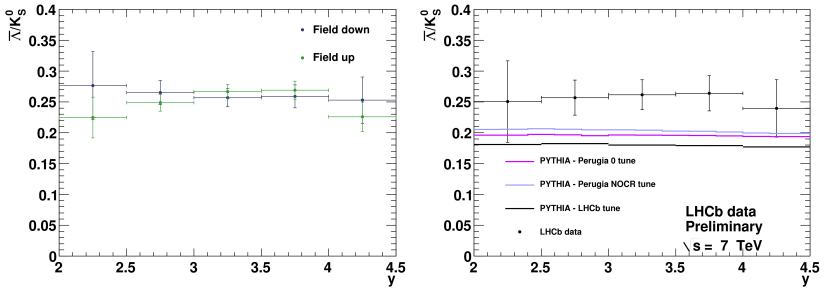

(a) (b)

Figure 65.: The $\bar{\Lambda}/K^0_S$ ratio as a function of rapidity as measured in pp collisions at $\sqrt{s} = 7$ TeV in LHCb: (a) the comparison of results obtained at the two polarities of the LHCb magnetic field; (b) the final results, obtained averaging the two fields values, compared with the LHCb standard Monte Carlo and Monte Carlo predictions which use the Perugia-0 and Perugia-NOCR PYTHIA tunes[24, 25].

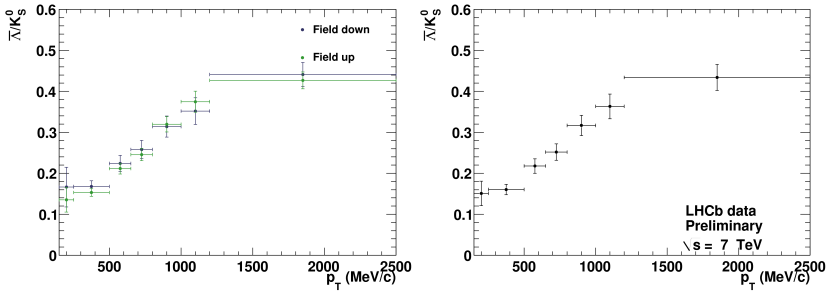

(a) (b)

Figure 66.: The $\bar{\Lambda}/K^0_S$ ratio as a function of p_T as measured in pp collisions at $\sqrt{s} = 7$ TeV in LHCb: (a) the comparison of results obtained at the two polarities of the LHCb magnetic field; (b) the final results, obtained averaging the two fields values.

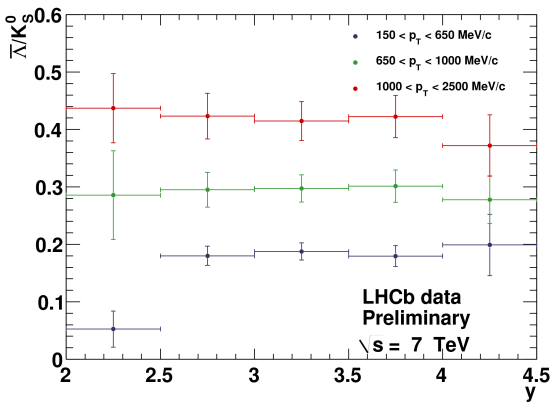

Figure 67.: The $\bar{\Lambda}/K^0_S$ ratio as a function of rapidity for different p_T ranges as measured in pp collisions at $\sqrt{s} = 7$ TeV in LHCb.

Table 8.: $\bar{\Lambda}/\Lambda$ ratio in y and p_T bins, for events at $\sqrt{s} = 0.9$ TeV.

	$2.0 < y < 2.5$	$2.5 < y < 3.0$	$3.0 < y < 3.5$	$3.5 < y < 4.0$	$2.0 < y < 4.0$
$250 < p_T < 500$	$1.48 \pm 1.50 \pm 0.07$	$0.91 \pm 0.08 \pm 0.04$	$0.77 \pm 0.09 \pm 0.04$	$0.21 \pm 0.27 \pm 0.01$	$0.82 \pm 0.06 \pm 0.04$
$500 < p_T < 650$	$2.15 \pm 0.94 \pm 0.10$	$0.77 \pm 0.07 \pm 0.04$	$0.70 \pm 0.06 \pm 0.03$	$0.67 \pm 0.22 \pm 0.04$	$0.72 \pm 0.04 \pm 0.04$
$650 < p_T < 800$	$0.78 \pm 0.24 \pm 0.04$	$0.77 \pm 0.07 \pm 0.04$	$0.69 \pm 0.05 \pm 0.04$	$0.73 \pm 0.13 \pm 0.03$	$0.72 \pm 0.04 \pm 0.04$
$800 < p_T < 1000$	$0.96 \pm 0.25 \pm 0.06$	$0.75 \pm 0.07 \pm 0.04$	$0.77 \pm 0.05 \pm 0.04$	$0.63 \pm 0.08 \pm 0.03$	$0.74 \pm 0.04 \pm 0.04$
$1000 < p_T < 1200$	$0.74 \pm 0.17 \pm 0.03$	$0.78 \pm 0.09 \pm 0.04$	$0.68 \pm 0.06 \pm 0.03$	$0.46 \pm 0.07 \pm 0.02$	$0.67 \pm 0.04 \pm 0.03$
$1200 < p_T < 2500$	$0.87 \pm 0.12 \pm 0.04$	$0.66 \pm 0.07 \pm 0.03$	$0.79 \pm 0.06 \pm 0.04$	$0.56 \pm 0.07 \pm 0.03$	$0.74 \pm 0.04 \pm 0.04$
p_T integrated	$0.88 \pm 0.17 \pm 0.00$	$0.77 \pm 0.06 \pm 0.00$	$0.74 \pm 0.05 \pm 0.00$	$0.57 \pm 0.08 \pm 0.00$	

Table 9.: $\bar{\Lambda}/\Lambda$ ratio in y and p_T bins, for events at $\sqrt{s} = 7$ TeV.

	$2.0 < y < 2.5$	$2.5 < y < 3.0$	$3.0 < y < 3.5$	$3.5 < y < 4.0$	$4.0 < y < 4.5$	$2.0 < y < 4.5$
$150 < p_T < 250$	-	$1.54 \pm 0.83 \pm 0.06$	$0.91 \pm 0.29 \pm 0.03$	$0.45 \pm 0.57 \pm 0.02$	-	$1.02 \pm 0.27 \pm 0.04$
$250 < p_T < 500$	-	$0.94 \pm 0.13 \pm 0.03$	$0.96 \pm 0.10 \pm 0.03$	$0.97 \pm 0.16 \pm 0.03$	$0.37 \pm 0.51 \pm 0.02$	$0.95 \pm 0.07 \pm 0.03$
$500 < p_T < 650$	$0.60 \pm 0.52 \pm 0.02$	$1.02 \pm 0.15 \pm 0.04$	$0.98 \pm 0.11 \pm 0.03$	$0.86 \pm 0.13 \pm 0.03$	$0.94 \pm 0.38 \pm 0.03$	$0.96 \pm 0.07 \pm 0.03$
$650 < p_T < 800$	$1.07 \pm 0.72 \pm 0.04$	$0.88 \pm 0.15 \pm 0.03$	$0.86 \pm 0.09 \pm 0.03$	$1.06 \pm 0.16 \pm 0.04$	$0.87 \pm 0.25 \pm 0.03$	$0.92 \pm 0.07 \pm 0.03$
$800 < p_T < 1000$	$1.01 \pm 0.42 \pm 0.04$	$1.00 \pm 0.16 \pm 0.03$	$0.89 \pm 0.09 \pm 0.03$	$0.97 \pm 0.13 \pm 0.03$	$0.74 \pm 0.20 \pm 0.03$	$0.92 \pm 0.06 \pm 0.03$
$1000 < p_T < 1200$	$0.96 \pm 0.35 \pm 0.03$	$0.90 \pm 0.17 \pm 0.03$	$0.93 \pm 0.11 \pm 0.03$	$0.92 \pm 0.13 \pm 0.03$	$0.74 \pm 0.24 \pm 0.03$	$0.90 \pm 0.07 \pm 0.03$
$1200 < p_T < 2500$	$0.94 \pm 0.18 \pm 0.03$	$0.94 \pm 0.11 \pm 0.03$	$0.89 \pm 0.08 \pm 0.03$	$0.97 \pm 0.10 \pm 0.03$	$0.80 \pm 0.17 \pm 0.03$	$0.92 \pm 0.05 \pm 0.03$
p_T integrated	$0.94 \pm 0.28 \pm 0.00$	$0.95 \pm 0.12 \pm 0.00$	$0.92 \pm 0.08 \pm 0.00$	$0.96 \pm 0.11 \pm 0.00$	$0.80 \pm 0.20 \pm 0.00$	

Table 10.: $\bar{\Lambda}/K^0_S$ ratio in y and p_T bins, for events at $\sqrt{s} = 0.9$ TeV.

	$2.0 < y < 2.5$	$2.5 < y < 3.0$	$3.0 < y < 3.5$	$3.5 < y < 4.0$	$2.0 < y < 4.0$
$250 < p_T < 500$	$0.10 \pm 0.08 \pm 0.01$	$0.19 \pm 0.01 \pm 0.01$	$0.18 \pm 0.01 \pm 0.01$	$0.11 \pm 0.08 \pm 0.01$	$0.19 \pm 0.01 \pm 0.01$
$500 < p_T < 650$	$0.29 \pm 0.09 \pm 0.02$	$0.24 \pm 0.02 \pm 0.02$	$0.21 \pm 0.01 \pm 0.01$	$0.19 \pm 0.04 \pm 0.01$	$0.23 \pm 0.01 \pm 0.02$
$650 < p_T < 800$	$0.32 \pm 0.08 \pm 0.02$	$0.29 \pm 0.02 \pm 0.02$	$0.27 \pm 0.02 \pm 0.02$	$0.28 \pm 0.03 \pm 0.02$	$0.29 \pm 0.01 \pm 0.02$
$800 < p_T < 1000$	$0.39 \pm 0.07 \pm 0.03$	$0.33 \pm 0.02 \pm 0.02$	$0.32 \pm 0.02 \pm 0.02$	$0.29 \pm 0.03 \pm 0.02$	$0.33 \pm 0.01 \pm 0.02$
$1000 < p_T < 1200$	$0.31 \pm 0.05 \pm 0.02$	$0.36 \pm 0.03 \pm 0.02$	$0.36 \pm 0.02 \pm 0.03$	$0.26 \pm 0.03 \pm 0.02$	$0.36 \pm 0.02 \pm 0.02$
$1200 < p_T < 2500$	$0.49 \pm 0.05 \pm 0.03$	$0.42 \pm 0.03 \pm 0.03$	$0.40 \pm 0.02 \pm 0.03$	$0.30 \pm 0.03 \pm 0.02$	$0.42 \pm 0.02 \pm 0.03$
p_T integrated	$0.28 \pm 0.04 \pm 0.02$	$0.26 \pm 0.02 \pm 0.02$	$0.25 \pm 0.02 \pm 0.02$	$0.23 \pm 0.02 \pm 0.02$	

Table 11.: $\bar{\Lambda}/K^0_S$ ratio in y and p_T bins, for events at $\sqrt{s} = 7$ TeV.

	$2.0 < y < 2.5$	$2.5 < y < 3.0$	$3.0 < y < 3.5$	$3.5 < y < 4.0$	$4.0 < y < 4.5$	$2.0 <$
$150 < p_T < 250$	-	$0.17 \pm 0.06 \pm 0.01$	$0.18 \pm 0.04 \pm 0.01$	$0.10 \pm 0.09 \pm 0.01$	$0.13 \pm 0.57 \pm 0.01$	0.15
$250 < p_T < 500$	-	$0.16 \pm 0.02 \pm 0.01$	$0.17 \pm 0.01 \pm 0.01$	$0.19 \pm 0.02 \pm 0.01$	$0.18 \pm 0.13 \pm 0.01$	0.16
$500 < p_T < 650$	$0.07 \pm 0.04 \pm 0.00$	$0.24 \pm 0.03 \pm 0.01$	$0.24 \pm 0.02 \pm 0.01$	$0.21 \pm 0.02 \pm 0.01$	$0.26 \pm 0.07 \pm 0.02$	0.22
$650 < p_T < 800$	$0.23 \pm 0.12 \pm 0.01$	$0.25 \pm 0.03 \pm 0.01$	$0.27 \pm 0.02 \pm 0.02$	$0.28 \pm 0.03 \pm 0.02$	$0.25 \pm 0.05 \pm 0.01$	0.25
$800 < p_T < 1000$	$0.33 \pm 0.10 \pm 0.02$	$0.35 \pm 0.04 \pm 0.02$	$0.33 \pm 0.02 \pm 0.02$	$0.32 \pm 0.03 \pm 0.02$	$0.31 \pm 0.06 \pm 0.02$	0.32
$1000 < p_T < 1200$	$0.44 \pm 0.11 \pm 0.03$	$0.37 \pm 0.05 \pm 0.02$	$0.39 \pm 0.03 \pm 0.02$	$0.36 \pm 0.04 \pm 0.02$	$0.36 \pm 0.08 \pm 0.02$	0.36
$1200 < p_T < 2500$	$0.45 \pm 0.06 \pm 0.03$	$0.45 \pm 0.04 \pm 0.03$	$0.43 \pm 0.03 \pm 0.03$	$0.46 \pm 0.04 \pm 0.03$	$0.38 \pm 0.06 \pm 0.02$	0.43
p_T integrated	$0.25 \pm 0.06 \pm 0.02$	$0.26 \pm 0.02 \pm 0.02$	$0.26 \pm 0.02 \pm 0.02$	$0.26 \pm 0.02 \pm 0.02$	$0.24 \pm 0.04 \pm 0.01$	

3.8 SYSTEMATIC UNCERTAINTIES

After discussing the final results, we concentrate now in the possible systematic uncertainties which can influence the measurement of the two production ratios. These uncertainties were already included in the final results previously shown.

3.8.1 *Stability of the results with respect to the selection cuts*

The influence of the V^0 selection on our observables has been assessed by considering a not pre-selected sample of the data and MC simulations. Without a preselection the level of combinatorial background is huge so that in order to keep our samples manageable we had to use a small fraction of the original samples.

We have analysed these samples in order to extract the distributions of the ν variable for the different V^0 species in the two samples. We have then computed the $\bar{\Lambda}/\Lambda$ and $\bar{\Lambda}/K^0_S$ ratios as a function of ν for data and MC. We do not expect the single ratios to be independent from ν since, for example, the impact parameters of a K^0_S decay product can be different for a given kinematic region to the ones of the Λ decay products. However we do expect that, if no systematic uncertainty is present, this dependence is the same for data and MC. Therefore we have computed the ratio of the data over MC $\bar{\Lambda}/\Lambda$ and $\bar{\Lambda}/K^0_S$ ratios. This ratio was then fitted with a constant line and the χ^2/dof of the fit has been considered as a measurement of the consistency with this hypothesis.

The results of this procedure are shown in Fig. 68 where the data over MC ratio of the $\bar{\Lambda}/\Lambda$ and $\bar{\Lambda}/K^0_S$ observables is shown. For each distribution a constant line fit is shown together with its χ^2/dof and the relative probability. While the $\bar{\Lambda}/\Lambda$ probability is very good, the one for the $\bar{\Lambda}/K^0_S$ ratio is quite small, nevertheless it is enough to say that both distributions are consistent with the null hypothesis. Therefore we do not assign any systematic error for this contribution.

3.8.2 *Non-prompt contribution in selected events*

Since our efficiency correction does not take into account the possible non-prompt component present in V^0 selected from pp collision data, we need to estimate whether and how much this affects our final results on production ratios.

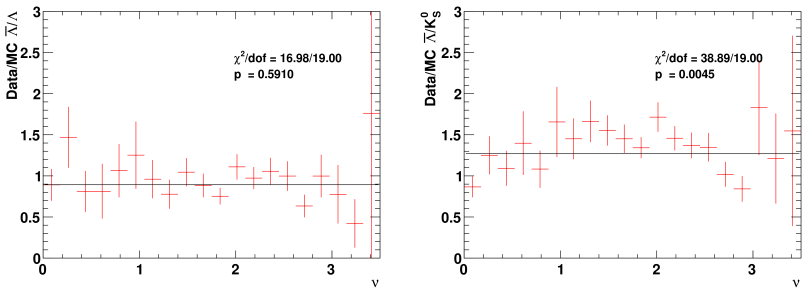

Figure 68.: Data over MC ratio of the (left) $\bar{\Lambda}/\Lambda$ and (right) $\bar{\Lambda}/K^0_S$ observables as a function of ν as obtained from not preselected samples.

In order to size this effect we have computed the relative variation on the final results obtained by including non-prompt events in the Monte Carlo efficiency.

We have obtained an average relative variation on the final results of 0.01 and 0.02 for the $\bar{\Lambda}/\Lambda$ and $\bar{\Lambda}/K^0_S$ ratios respectively.

3.8.3 *Diffractive events contribution*

As illustrated for the non-prompt contribution, also the presence of diffractive events in the data sample can influence our measurements.

Therefore we have measured this effect by the difference obtained in the final results by including or not the diffractive events in the Monte Carlo calculation of the efficiency.

We have obtained an average relative variation on the final results of 0.01 and 0.02 for the $\bar{\Lambda}/\Lambda$ and $\bar{\Lambda}/K^0_S$ ratios respectively.

3.8.4 *Uncertainties in the re-weighting of the p_T-y MC spectrum*

The procedure illustrated in 3.6.1.1, in order to calibrate the transverse momentum and rapidity distributions of the Monte Carlo samples, is certainly a source of uncertainty for the final results.

In order to assess the level of this uncertainty we have measured the variation on the efficiency by varying the function used to re-weight this spectrum. In particular we have considered a variation of the binning of the histograms used to interpolate the weighting function between 15 and 25 per variable, *i.e.* ± 5 around the value, 20, used in the analysis procedure. Furthermore we

have considered a variation in the number of parameters considered in the spline used to reweight the MC spectrum. We have considered variations between a 3-order to a 5-order polynomial.

Overall the variations for both parameters that we have observed are at the level of 1% on the final results. Therefore we assign a conservative systematic error of the same amount due to this procedure.

3.8.5 *Influence of the Λ transverse polarisation to the production ratios.*

As we have seen in the introduction and will study in detail in chapter 4, Λ particles produced in pp collisions can be transversely polarised, *i.e.* have a spin asymmetry along the orthogonal to the production plane. For the convention used and the details on the reference systems we refer to the mentioned chapter.

In order to study the effect that a Λ transverse polarisation could rise on the V^0 production ratios we computed the variation of the rations for a maximum change in the polarisation, i.e. from $P = -1$ to $P = +1$. The effect on the V^0 ratios of the polarisation can come from a modification of the acceptance [3] for the Λ as a function of the P.

The distribution of the Λ events as a function of $\cos\vartheta$ can be parametrised as:

$$\frac{dN}{d\cos\vartheta} = \mathcal{A}(\cos\vartheta)(1 - \alpha P\cos\vartheta) \equiv f(\cos\vartheta, P) \tag{3.11}$$

where $\mathcal{A}(\cos\vartheta)$ is the acceptance as a function of $\cos\vartheta$ for unpolarized events and the second factor is just the distribution of $\cos\vartheta$ for polarised Λ events, with P being the polarisation level and α the asymmetry parameter [69] (Cf. Appendix B for a detailed calculation).

We parametrise the unpolarized acceptance with a forth order polynomial as follows

$$\mathcal{A}(\cos\vartheta) = a(1 + b\cos\vartheta + c\cos^2\vartheta + d\cos^3\vartheta + e\cos^4\vartheta) \tag{3.12}$$

where $a, \ldots, e$ are the parameters of the different terms. In order to derive the acceptance parameters we consider the distribution of $\cos\vartheta$ for Monte Carlo simulated events. These events have no polarisation so that Eq. (3.11) becomes (3.12) and the fit to the distribution of $\cos\vartheta$ gives us $\mathcal{A}(\cos\vartheta)$.

3 In this case with *acceptance* we mean the cumulative effect of geometric acceptance, reconstruction and selection.

Looking at the distributions of the MC simulated Λ events in Fig. 69 the parametrisation appear to be justified.

The number of reconstructed and selected Λ is now simply the integral of equation (3.11); the influence of the polarisation on this value can be simply estimated by computing this integral for different P values. In particular we consider the maximum possible variation which is given by the difference between the integral with extreme values $P = \pm 1$, viz.:

$$\Delta_\Lambda = \frac{\int_{-1}^{1} f(\cos\vartheta, P = +1)\,d(\cos\vartheta) - \int_{-1}^{1} f(\cos\vartheta, P = -1)\,d(\cos\vartheta)}{\int_{-1}^{1} f(\cos\vartheta, P = +1)\,d(\cos\vartheta) + \int_{-1}^{1} f(\cos\vartheta, P = -1)\,d(\cos\vartheta)} \tag{3.13}$$

where Δ_Λ is a measurement of the percentage variation of the Λ measured yields for a maximum variation (or maximum ignorance) of the polarisation. The expression in eq. (3.13) can be analytically solved given our polynomial form for $\mathcal{A}$ and, after a little algebra, leads to:

$$\Delta_\Lambda = \alpha \frac{5b + 3d}{15 + 5c + 3e} \tag{3.14}$$

which gives the variation of the yields in terms of the parameters of $\mathcal{A}$. It has to be noticed the presence of α, the asymmetry parameter, in eq.(3.14), which tells us that the variation is on opposite directions for Λ and $\bar{\Lambda}$; this would be a very dangerous problem, giving a bias for the production ratio measurement for polarised Λ if the overall variation was not very small, as is indeed the case.

In Fig 69 is shown the distribution of $\cos\vartheta$ for $\bar{\Lambda}$ and Λ from reconstructed and selected MC simulated events at $\sqrt{s} = 0.9$ TeV with field down. The black lines are the fit of the function $\mathcal{A}$ to the distributions; the parameters of these fits are reported in Table 12 together with the calculation of the values of Δ_Λ for Λ and $\bar{\Lambda}$. Finally the values of the relative variation for the $\bar{\Lambda}/\Lambda$ and $\bar{\Lambda}/K^0_S$ ratios are reported which are both consistent with no error. The same procedure has been applied to $\sqrt{s} = 0.9$ TeV events with field up and to $\sqrt{s} = 7$ TeV events with field down and up: the results are shown in figures 70, 71 and 72 and in tables 13, 14, 15 respectively. Each data sample gives results compatible with no systematic error on the ratios coming from the uncertainty on the polarisation of the Λ baryons and anti-baryons.

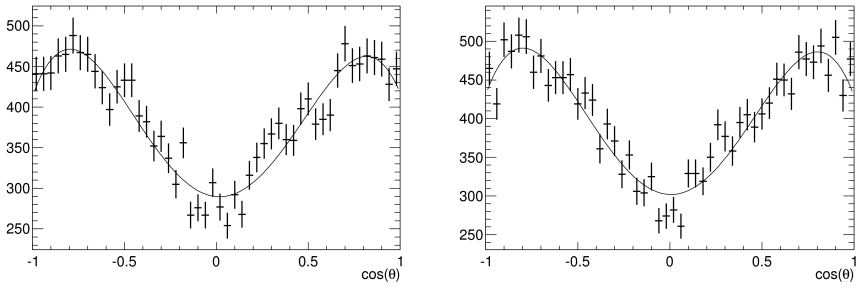

(a) $\bar{\Lambda}$ (b) Λ

Figure 69.: Distribution of $\cos\vartheta$ for (left) $\bar{\Lambda}$ and (right) Λ from reconstructed and selected MC simulated events at $\sqrt{s} = 0.9$ TeV with field down. The line is the fit of $\mathcal{A}$ to the distribution.

Table 12.: Systematic uncertainty on the $\bar{\Lambda}/\Lambda$ and $\bar{\Lambda}/K^0_S$ ratios coming from the polarisation angle acceptance for $\sqrt{s} = 0.9$ TeV field down events. The parameter values of the fit of $\mathcal{A}$ (Eq. (3.12)) to Monte Carlo events are shown. The last 3 rows show the Δ_Λ value and the systematic relative uncertainties for the two ratios.

Parameter	$\bar{\Lambda}$	Λ
a	292.389 ± 4.705	304.837 ± 4.805
b	-0.064 ± 0.042	-0.025 ± 0.041
c	1.894 ± 0.135	1.937 ± 0.133
d	0.069 ± 0.065	0.026 ± 0.064
e	-1.457 ± 0.143	-1.517 ± 0.140
Δ	0.004 ± 0.009	-0.002 ± 0.009
$\sigma(\bar{\Lambda}/\Lambda)$	0.005 ± 0.013	
$\sigma(\bar{\Lambda}/K^0_S)$	0.007 ± 0.018	

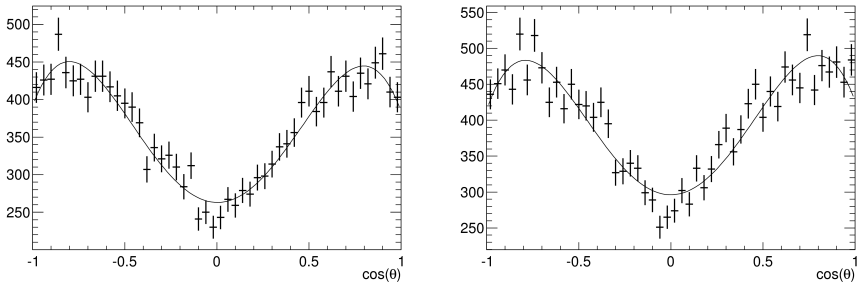

(a) $\bar{\Lambda}$ (b) Λ

Figure 70.: Distribution of $\cos\vartheta$ for (left) $\bar{\Lambda}$ and (right) Λ from reconstructed and selected MC simulated events at $\sqrt{s} = 0.9$ TeV with field up. The line is the fit of $\mathcal{A}$ to the distribution.

Table 13.: Systematic uncertainty on the $\bar{\Lambda}/\Lambda$ and $\bar{\Lambda}/K^0_S$ ratios coming from the polarisation angle acceptance for $\sqrt{s} = 0.9$ TeV field up events. The parameter values of the fit of $\mathcal{A}$ (Eq. (3.12)) to Monte Carlo events are shown. The last 3 rows show the Δ_Λ value and the systematic relative uncertainties for the two ratios.

Parameter	$\bar{\Lambda}$	Λ
a	265.684 ± 4.505	299.492 ± 4.783
b	-0.017 ± 0.045	-0.003 ± 0.042
c	2.177 ± 0.147	2.033 ± 0.137
d	0.007 ± 0.069	0.021 ± 0.065
e	-1.690 ± 0.155	-1.619 ± 0.146
Δ	0.002 ± 0.009	0.001 ± 0.009
$\sigma(\bar{\Lambda}/\Lambda)$	0.000 ± 0.013	
$\sigma(\bar{\Lambda}/K^0_S)$	0.004 ± 0.019	

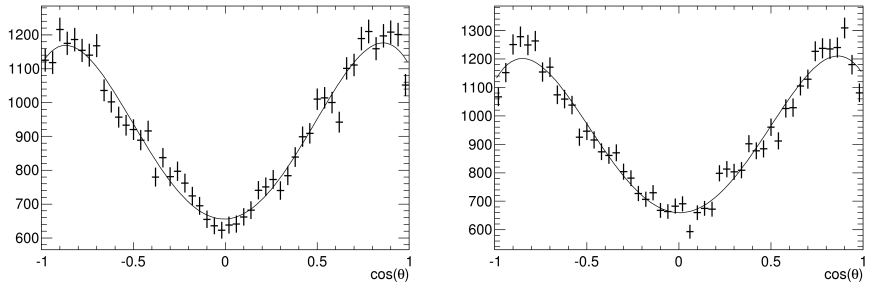

(a) $\bar{\Lambda}$ (b) Λ

Figure 71.: Distribution of $\cos\vartheta$ for (left) $\bar{\Lambda}$ and (right) Λ from reconstructed and selected MC simulated events at $\sqrt{s} = 7$ TeV with field down. The line is the fit of $\mathcal{A}$ to the distribution.

Table 14.: Systematic uncertainty on the $\bar{\Lambda}/\Lambda$ and $\bar{\Lambda}/K^0_S$ ratios coming from the polarisation angle acceptance for $\sqrt{s} = 7$ TeV field down events. The parameter values of the fit of $\mathcal{A}$ (Eq. (3.12)) to Monte Carlo events are shown. The last 3 rows show the Δ_Λ value and the systematic relative uncertainties for the two ratios.

Parameter	$\bar{\Lambda}$	Λ
a	663.449 ± 7.175	666.554 ± 7.239
b	0.037 ± 0.028	-0.021 ± 0.028
c	2.119 ± 0.094	2.276 ± 0.096
d	-0.045 ± 0.044	0.041 ± 0.044
e	-1.423 ± 0.097	-1.555 ± 0.099
Δ	-0.002 ± 0.006	0.001 ± 0.006
$\sigma(\bar{\Lambda}/\Lambda)$	-0.002 ± 0.008	
$\sigma(\bar{\Lambda}/K^0_S)$	-0.003 ± 0.012	

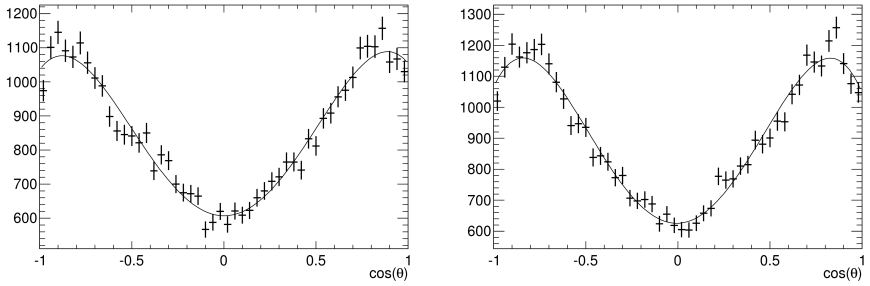

(a) $\bar{\Lambda}$ (b) Λ

Figure 72.: Distribution of $\cos\vartheta$ for (left) $\bar{\Lambda}$ and (right) Λ from reconstructed and selected MC simulated events at $\sqrt{s} = 7$ TeV with field up. The line is the fit of $\mathcal{A}$ to the distribution.

Table 15.: Systematic uncertainty on the $\bar{\Lambda}/\Lambda$ and $\bar{\Lambda}/K^0_S$ ratios coming from the polarisation angle acceptance for $\sqrt{s} = 7$ TeV field up events. The parameter values of the fit of $\mathcal{A}$ (Eq. (3.12)) to Monte Carlo events are shown. The last 3 rows show the Δ_Λ value and the systematic relative uncertainties.

Parameter	$\bar{\Lambda}$	Λ
a	612.673 ± 6.872	633.814 ± 7.081
b	-0.007 ± 0.021	0.030 ± 0.029
c	2.029 ± 0.094	2.457 ± 0.100
d	0.022 ± 0.036	-0.045 ± 0.046
e	-1.310 ± 0.099	-1.771 ± 0.104
Δ	-0.001 ± 0.005	0.000 ± 0.006
$\sigma(\bar{\Lambda}/\Lambda)$	-0.001 ± 0.007	
$\sigma(\bar{\Lambda}/K^0_S)$	-0.002 ± 0.009	

3.8.6 *Effects of possible detector asymmetries*

The LHCb detector is divided in two approximately symmetric halves (for details cf. Chapter 2). The magnetic field given by the dipole magnet bends in opposite directions tracks with opposite charge so that negatively charged particles are preferably detected from one half while positively charged ones from the other side. Obviously, inverting the magnetic field polarity switches the bending so that asymmetries can be easily crosschecked.

These possible asymmetries have been evaluated in this work both by checking the acceptance of the detector as a function of ϕ and by looking at possible differences between so called "cowboys" and "sailors" types of track pairs.

3.8.6.1 ϕ *angular acceptance effects*

Since the signal yield estimation for the measurement of the $\bar{\Lambda}/\Lambda$ and $\bar{\Lambda}/K^0_S$ ratios has been done in bins of rapidity and transverse momentum, the only possible source of a systematic uncertainty coming from acceptance effects can reside in the ϕ coordinate (the azimuthal angle) which is the only kinematic variable independent of the other two.

If the ϕ acceptance description in the Monte Carlo simulations is not correctly reproducing the data, residual asymmetries can affect the final ratios.

In order to estimate these effects we compare the ϕ distributions for Λ and K^0_S particles as estracted from background subtracted signal and MC events. In Fig. 50 and 52 the distributions of data and MC for Λ and K^0_S respectively are compared; it can be seen that the MC reproduces well the shape of the data distribution but in some bins some discrepancy appears. The lack of events at $\phi \approx \pm\pi/2$ for the $\sqrt{s} = 0.9$ TeV sample is simply due to the VELO-open configuration for this energy which reduces the acceptance for long tracks in those regions.

The effect of these discrepancies can be seen in detail in the left side plots of figures 73, 74, 75 and 76 where the $\bar{\Lambda}/\Lambda$ and $\bar{\Lambda}/K^0_S$ ratios are shown as a function of ϕ for different fields and different energies. The common feature of these plots is that a clear pattern can be seen, mapping some detector asymmetry which suppresses the ratio at $\phi = \pm\pi$ and enhance it at $\phi = 0$ for field down events (vice versa for field up). As we already noticed, in fact, considering field down events, these differences can be traced both in a suppression of $\bar{\Lambda}$ and in an enhancement of Λ

yields at $\phi = 0$; while at $\phi = \pm\pi$ the situation is the opposite. Hence the difference is to be searched not in an efficiency for one specific particle but rather in a specific asymmetry which makes the detector prefer one particle to another depending on the ϕ region.

In the right hand side plots of figures 73, 74, 75 and 76 are shown instead the ratios of the $\bar{\Lambda}/\Lambda$ and $\bar{\Lambda}/K^0_S$ distribution as a function of ϕ for data divided by MC.[4] In these plots the common feature due to the natural inefficiencies of our detector cancel out and just some features remain. These features could be source systematic uncertainties for our measurements. However if one compares field up and field down events, the effect is the opposite so that this asymmetry do not represent a significant problem for our analysis. In fact, in Fig. 77 we show the distributions of $\bar{\Lambda}/\Lambda$ and $\bar{\Lambda}/K^0_S$ ratio as a function of ϕ averaging field down and field up events. The asymmetries tend to disappear making us confident that they do not affect our physics results. In particular, considering these distributions as flat we calculate a χ^2 variable comparing the different points to the average value. As the results are well compatible with the hypothesis of a flat distribution we do not assign a systematic error for this contribution.

3.8.6.2 *Cowboys and sailors*

Historically the V^0 particles were divided in two groups according to the shape that they showed in bubble chamber pictures. Pairs of tracks bended in such a way to approach each other after V^0 decay vertex were usually called "cowboys", while pairs bended oppositely to move away from each other were called "sailors" (or "marines"), both names being due to their shape recalling the stereotyped vision of the legs of cowboys and sailors. A schematic view of the two track pairs types is shown in Fig. 78.

Within LHCb the distinction between cowboys and sailors corresponds (approximately) to the difference between a V^0 candidate with a positive track on the right half and a negative track on the left and the opposite case. Obviously cowboy and sailor V^0 switch with the field polarity. The exactly opposite cases correspond to having the decay plane exactly in the (x, z) plane. In general a decay will be in a generic plane with angle ξ with respect to the y axis (the field axis) and the distinction between

4 Note that data and MC distributions are here not normalised to each other so that their ratio is not necessarily 1, but rather the ratio of the mean values of the observables.

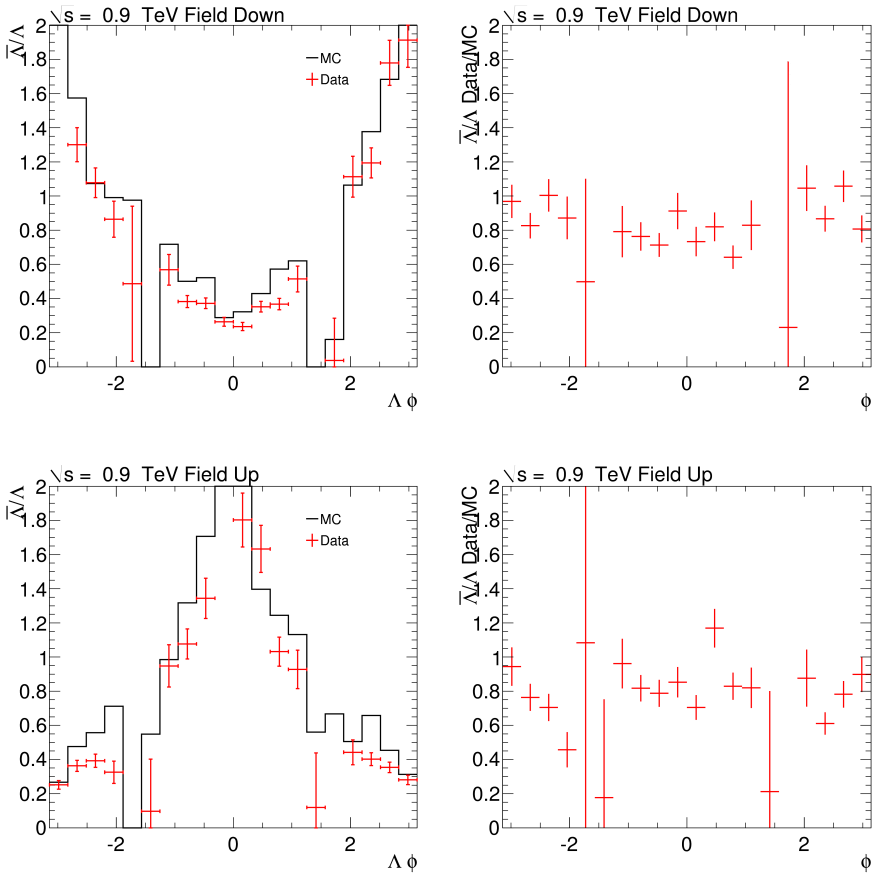

Figure 73.: The left hand side plots show the distributions of the $\bar{\Lambda}/\Lambda$ ratio as a function of ϕ at $\sqrt{s} = 0.9$ TeV for (top) field down and (bottom) field up configurations for data (red error bars) and MC (black line). The right hand side plots show the ratio of the same data distribution divided by correspondent MC distribution.

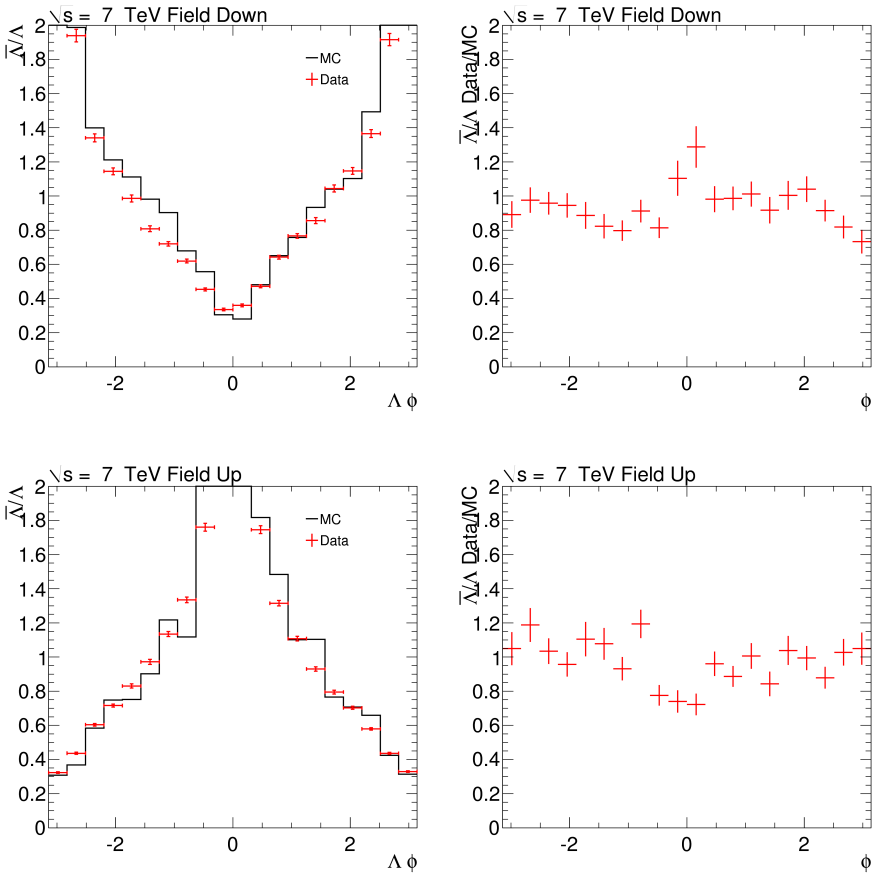

Figure 74.: The left hand side plots show the distributions of the $\bar{\Lambda}/\Lambda$ ratio as a function of ϕ at $\sqrt{s} = 7$ TeV for (top) field down and (bottom) field up configurations for data (red error bars) and MC (black line). The right hand side plots show the ratio of the same data distribution divided by correspondent MC distribution.

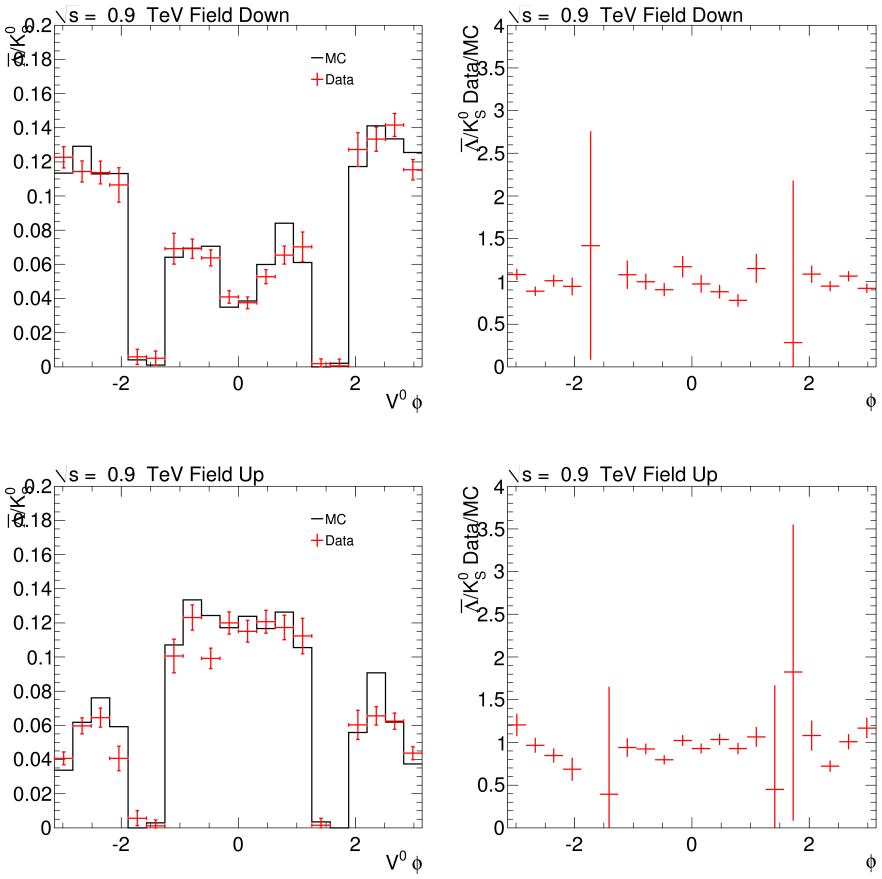

Figure 75.: The left hand side plots show the distributions of the $\bar{\Lambda}/K^0_S$ ratio as a function of ϕ at $\sqrt{s} = 0.9$ TeV for (top) field down and (bottom) field up configurations for data (red error bars) and MC (black line). The right hand side plots show the ratio of the same data distribution divided by correspondent MC distribution.

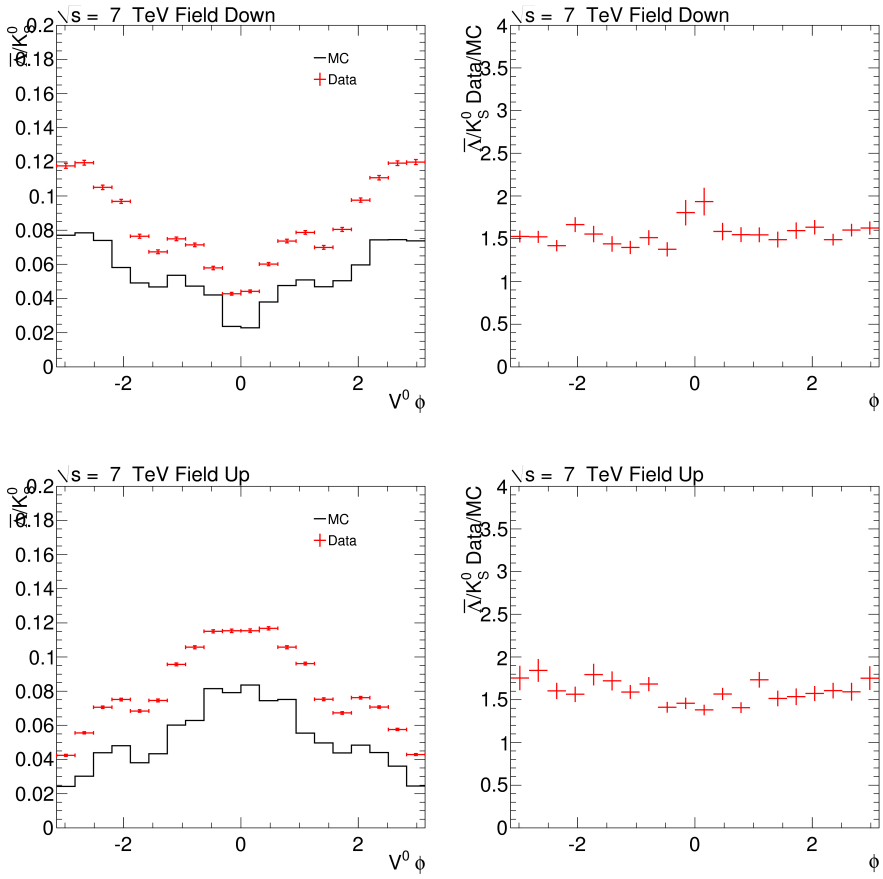

Figure 76.: The left hand side plots show the distributions of the $\bar{\Lambda}/K^0_S$ ratio as a function of ϕ at $\sqrt{s} = 7$ TeV for (top) field down and (bottom) field up configurations for data (red error bars) and MC (black line). The right hand side plots show the ratio of the same data distribution divided by correspondent MC distribution.

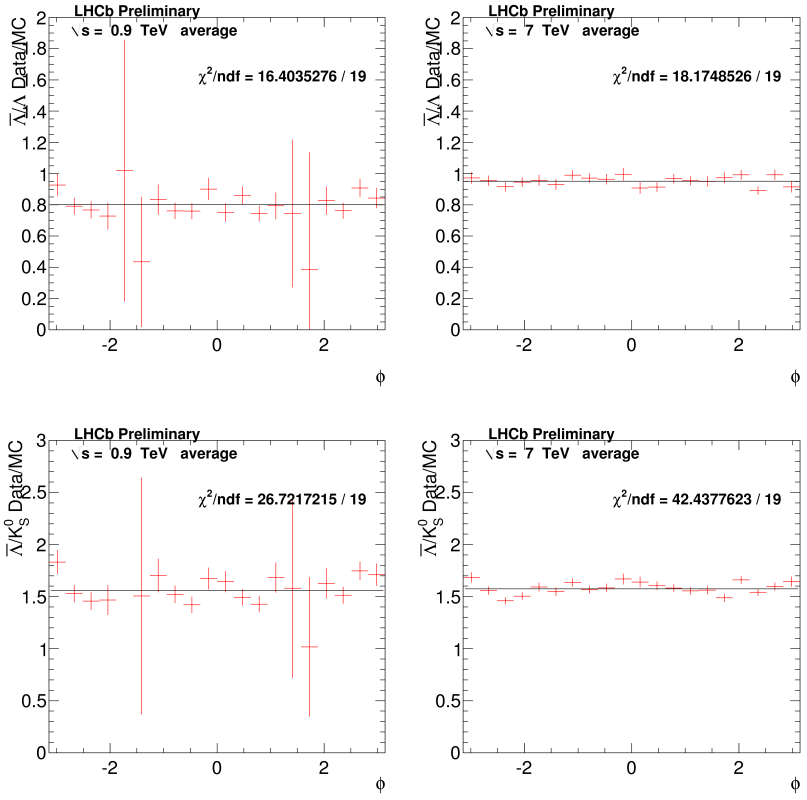

Figure 77.: Distributions of the V^0 production ratios as a function of ϕ; the data over MC ratios as obtained averaging field up and field down events are shown for (top) the $\bar{\Lambda}/\Lambda$ ratio and (bottom) the $\bar{\Lambda}/K^0_S$ ratio.

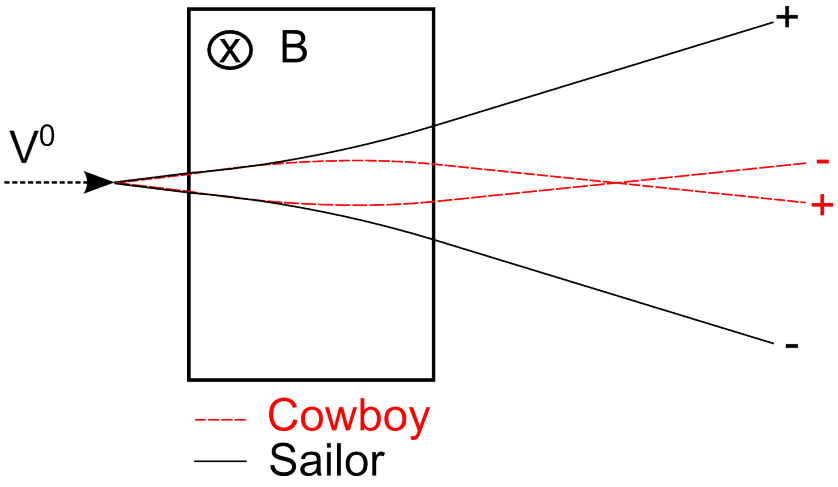

Figure 78.: Scheme of the "cowboy" and "sailor" tracks pairs definition. The red dashed lines represent the tracks in the "cowboy" configuration, the continuous black lines the "sailor" one. B is the magnetic field directed perpendicularly to the paper and entering into it.

cowboys and sailors will be a smooth function of ξ. In Fig. 79 we show a schematic view of the definition of the angle ξ.

As far as our measurement of $\bar{\Lambda}/\Lambda$ is concerned, the difference between cowboys and sailors could be propagated to a slight difference in the efficiencies for Λ and $\bar{\Lambda}$. This could be due to a difference in the efficiency for protons and anti-protons which, taken one field polarity and a given ξ, would be bended in opposite directions; the same reasoning holds for pions.

In order to assess a possible systematic effect arising from this distinction, we studied the $\bar{\Lambda}/\Lambda$ ratio for cowboys and sailors as a function of ξ. If the ratio would be different for different track pairs types and the yield of Λ and $\bar{\Lambda}$ were not even in the two species a systematic effect would arise biasing the results toward the most numerous sample.

In Fig. 80 we show the distributions of the ξ variable for the different V^0 species in data and MC at $\sqrt{s} = 7$ TeV for field up and down.

In Fig. 81 we show the distributions for the $\bar{\Lambda}/\Lambda$ and $\bar{\Lambda}/K^0_S$ ratios as a function of ξ for $\sqrt{s} = 7$ TeV data and MC samples with field down. On the left we show the distributions separately for data and MC while on the right we show their ratios. The plots show that no sizable effect can come from this variable. In particular we performed a fit to understand the difference between the data over MC ratio distribution and a perfectly flat

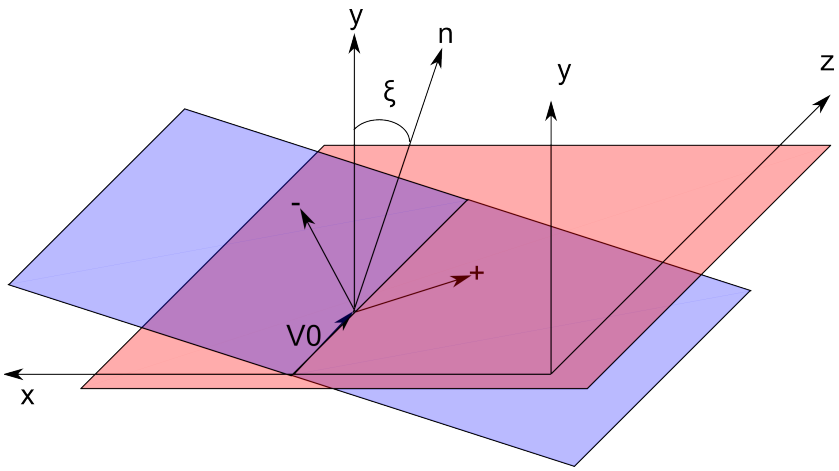

Figure 79.: Definition of the angle ξ, for the "cowboys" - "sailors" distinction.

distribution and the χ^2/dof are reported in the plots. As it can be seen the distributions are consistent with the hypothesis of being flat. We have repeated these tests for each of the samples and we have found the same consistency. We do not report for brevity all of the plots.

3.8.7 *Material interactions*

Material interactions can influence our measurements in two ways:

1. V^0 particles produced in the PV can interact with the detector active and inactive material being absorbed before decaying so that they cannot be detected.

2. Interactions of other particles with material can create secondarily produced V^0 particles which would dilute our measurement (*e.g.* $K^- p \to \Lambda n$).

Both effect modify the number of detected V^0 particles in our analysis. The second effect is partially included in the non-prompt contribution which we have already analysed. Moreover secondarily produced V^0 particles are effectively rejected by the cut on the ν variable since they can have a sizable impact parameter with respect to the primary vertex.

The influence of the two effect is further reduced by the requirement of long tracks in our analysis; in fact long tracks are due to V^0 particles decaying within the VELO detector so that

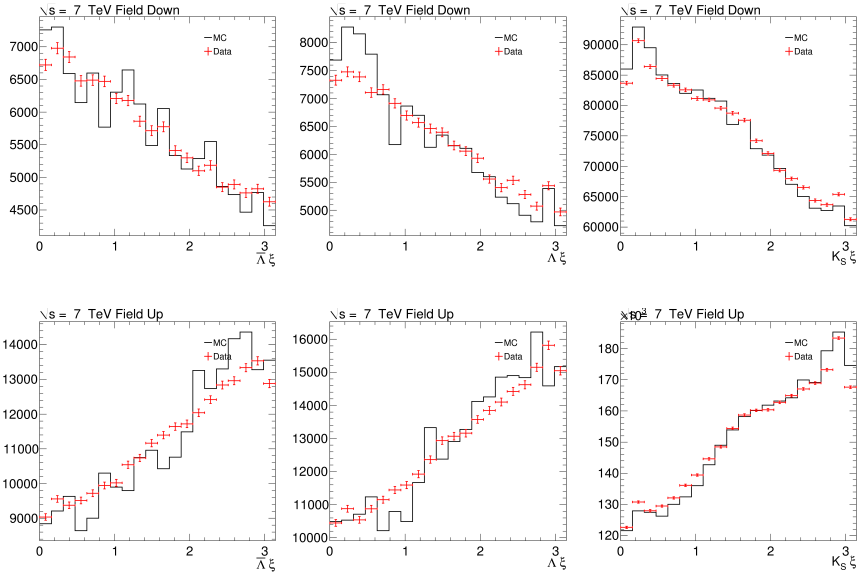

Figure 80.: Distribution of the ξ variable for the different V^0 species in pp collisions at $\sqrt{s} = 7$ TeV for (top) field up and (bottom) field down events.

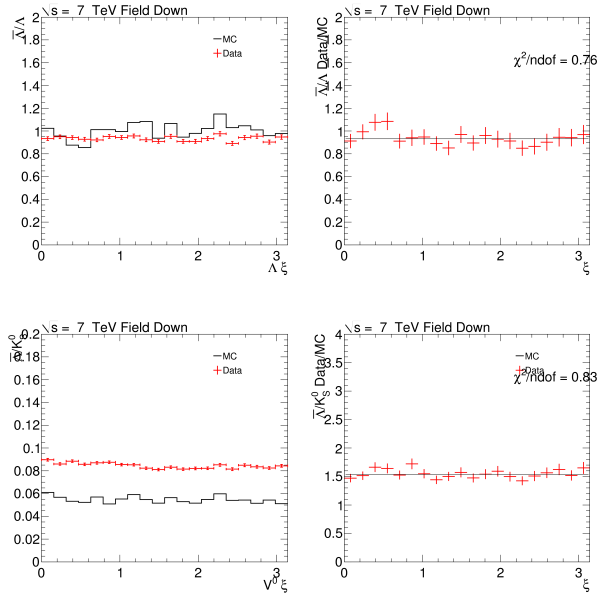

Figure 81.: Distribution of the V^0 production ratios as a function of ξ. Data and MC distributions are shown separately on the left for (top) the $\bar{\Lambda}/\Lambda$ ratio and (bottom) the $\bar{\Lambda}/K^0_S$ ratio; the data over MC ratio is shown on the right together with the fit for a constant line. The sample used for these plot is at $\sqrt{s} = 7$ TeV with field down.

the material traversed by each V^0 particle is at most equal to some part of the VELO.

We have studied the influence of material interactions on our measurements considering the variation of the V^0 production ratios as a function of the traversed material. In particular, we have divided our samples according to the distance travelled in the radial coordinate by the V^0 particle in two bins: $r < 5$ mm (almost no material traversed) and $r > 5$ mm (RF foil and sensor material traversed Cf.§2.2.1).

We expect some variation between the first and the second bin but as far as this is reproduced by the Monte Carlo it is corrected within the data when dividing by the efficiency. Hence, we have computed the $\bar{\Lambda}/\Lambda$ and $\bar{\Lambda}/K^0_S$ ratios in these two bins for Monte Carlo and data samples. We have subsequently divided the data by the MC histograms in order to have the relative variation.

The results of this procedure applied to the $\sqrt{s} = 0.9$ TeV and $\sqrt{s} = 7$ TeV field down events are shown in Fig. 82 and 83 for the $\bar{\Lambda}/\Lambda$ and $\bar{\Lambda}/K^0_S$ ratios respectively, where we show the ratio of the data and MC distributions. As it can be seen, there is a certain difference in these ratios between the first and the second bin. We consider this as an effect due to a non perfect description of the detector material in the MC simulations. Numerically the effect is diminished by the fact the most ($\sim 75\%$) of the statistics is concentrated in the first bin, *i.e.* for the V^0 that do not encounter any material before decaying.

By the comparison of the first and second bin we can estimate the size of this effect and the relative contribution to the systematic uncertainty on our measurements. For the $\bar{\Lambda}/\Lambda$ ratio the only sample in which the two bins are not consistent within the errors is the $\sqrt{s} = 0.9$ TeV field down. While this makes us suspect that this effect, being sizable in just one sample, may be due to statistical fluctuations, we prefer to assign a systematic uncertainty to all the samples. The final systematic uncertainties in percentage are reported in Table 16 for the different samples.

3.8.8 *Summary of the systematic uncertainties*

We report in Tables 17 and 18 the summary for the different systematic uncertainties considered in this work on the $\bar{\Lambda}/\Lambda$ and $\bar{\Lambda}/K^0_S$ ratios respectively. The total value obtained by adding the different contributions in quadrature has been used for the final results.

Table 16.: Summary of the systematic uncertainties due to the material interactions.

Sample	$\sigma(\bar{\Lambda}/\Lambda)$	$\sigma(\bar{\Lambda}/K^0_S)$
$\sqrt{s} = 0.9$ TeV field up	0.5%	1.5%
$\sqrt{s} = 0.9$ TeV field down	2.5%	3.2%
$\sqrt{s} = 7$ TeV field up	0.25%	0.3%
$\sqrt{s} = 7$ TeV field down	0.5%	0.6%

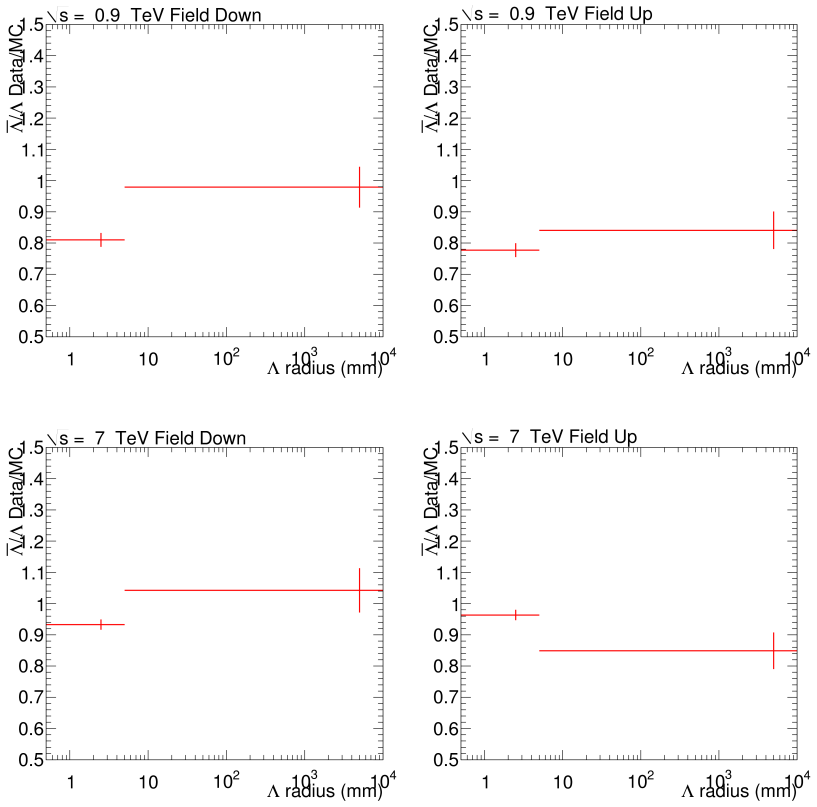

Figure 82.: Distributions of the $\bar{\Lambda}/\Lambda$ ratio in different bins of r, the radial distance travelled by the V^0 particle, for (top) the $\sqrt{s} = 0.9$ TeV and (bottom) the $\sqrt{s} = 7$ TeV sample. Data over MC distributions are shown.

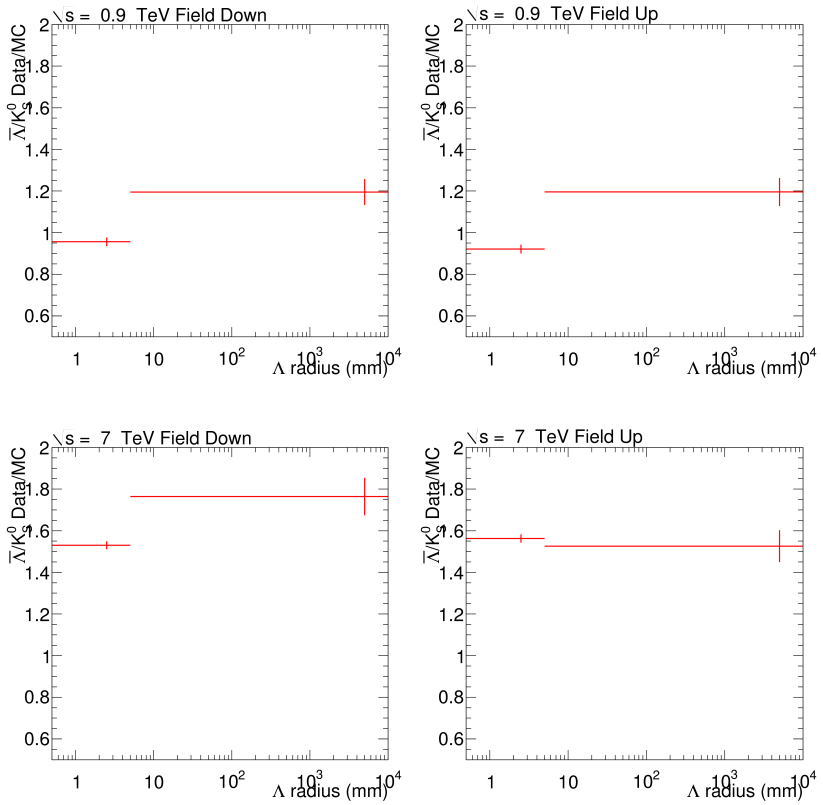

Figure 83.: Distributions of the $\bar{\Lambda}/K^0_S$ ratio in different bins of r, the radial distance travelled by the V^0 particle, for (top) the $\sqrt{s} = 0.9$ TeV and (bottom) the $\sqrt{s} = 7$ TeV sample. Data over MC distributions are shown.

Table 17.: Summary of the systematic uncertainties on the $\bar{\Lambda}/\Lambda$ production ratio.

Effect	$\sigma(\bar{\Lambda}/\Lambda)$			
	$\sqrt{s} = 0.9$ TeV		$\sqrt{s} = 7$ TeV	
	field down	field up	field down	field up
Selection cuts variation	-	-	-	-
Λ transverse polarisation	-	-	-	-
Non-prompt contribution	1%	1%	1%	1%
Diffractive contribution	1%	1%	1%	1%
p_T calibration	1%	1%	1%	1%
ϕ acceptance	-	-	-	-
Cowboys and sailors effect	-	-	-	-
Material interactions	0.5%	2.5%	0.25%	0.5%
Total	1.8%	3%	1.7%	1.8%

Table 18.: Summary of the systematic uncertainties on the $\bar{\Lambda}/K^0_S$ production ratio.

Effect	$\sigma(\bar{\Lambda}/K^0_S)$			
	$\sqrt{s} = 0.9$ TeV		$\sqrt{s} = 7$ TeV	
	field down	field up	field down	field up
Selection cuts variation	-	-	-	-
Λ transverse polarisation	-	-	-	-
Non-prompt contribution	2%	2%	2%	2%
Diffractive contribution	2%	2%	2%	2%
p_T calibration	1%	1%	1%	1%
ϕ acceptance	-	-	-	-
Cowboys and sailors effect	-	-	-	-
Material interactions	0.5%	2.5%	0.25%	0.5%
Total	3%	3.9%	3%	3%

4

MEASUREMENT OF THE Λ AND $\bar{\Lambda}$ TRANSVERSE POLARISATION

In this chapter we present a measurement of the polarisation of Λ particles produced in high energy pp collisions as obtained with data taken by the LHCb experiment.

4.1 CONVENTION

The Λ polarisation, as described in the theoretical introduction, is an asymmetry in the spin orientation of these baryons as produced in a particular reaction, in this case proton-proton collisions. It can be measured exploiting the self-analysing parity violating $\Lambda \to p\pi^-$ decay. Once a reference axis has been considered the polarisation is measured from the angular distribution of the proton (or pion) with respect to that axis.

As already explained from theoretical considerations (for symmetry reasons) and from experimental data, no polarisation is allowed within the production plane, while transverse polarisation, *i.e.* orthogonal to the production plane, is permitted.

In Fig. 84 is reported a scheme of the used reference system. The production plane is given by the beam axis (which corresponds, after beam crossing correction, to the z axis of the LHCb reference frame) and by the Λ momentum direction at production. The Λ rest frame is then orientated such that the z axis is directed in the Λ momentum direction (which is also the axis of the boost to the center of mass) and the y axis is:

$$\hat{y} = \frac{\vec{p}_b \wedge \vec{p}_\Lambda}{|\vec{p}_b \wedge \vec{p}_\Lambda|} \tag{4.1}$$

while the x completes this right-handed Cartesian system. The angle ϑ to be measured is then given by the one formed by the proton (boosted to the Λ rest frame) and the y axis.

The distribution of ϑ for polarised Λ is:

$$\frac{dN}{d\cos\vartheta} = \mathcal{A}(\cos\vartheta)(1 - \alpha P \cos\vartheta) \equiv f(\cos\vartheta, P) \tag{4.2}$$

where P is the polarisation, $\mathcal{A}$ is the instrumental acceptance (including reconstruction and selection efficiency) and α is the asymmetry parameter[69] (for a detailed calculation see Appendix B).

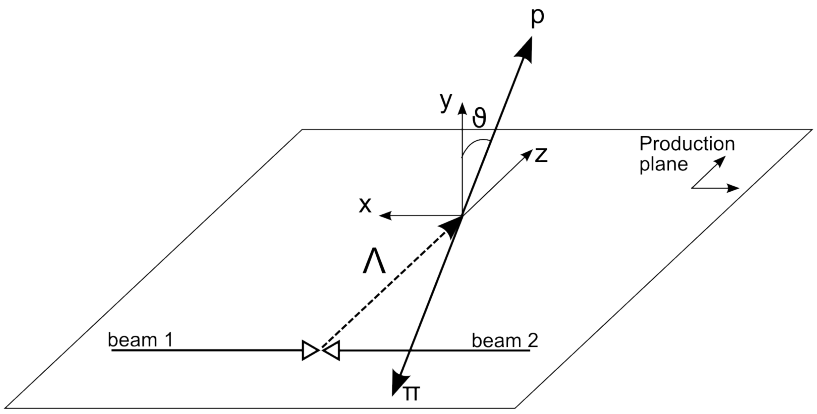

Figure 84.: Schematic view of the reference systems for the measurement of the Λ polarisation. The production plane is located by the vector product of the beam one direction and the produced Λ momentum. The Λ center of mass frame is directed so that the z and x directions belong to the production plane, while the orthogonal y is used to define the ϑ polarisation angle.

The extraction of the polarisation value, once the distribution has been corrected for the acceptance, is then simply done by fitting a linear function of $\cos\vartheta$.

Obviously the other two direction cosines could also be measured, but often, and we adopt this convention, it is preferable to measure the angles in the production plane. These angles will be denoted by χ and ζ, for the angles in the production plane with respect to the x and z axis respectively.

4.2 Λ SELECTION

For the polarisation measurement we have considered the selected Λ as obtained in the measurement of the V^0 production ratios. Hence for the used samples and selection details cf. § 3.2 and § 3.3 respectively.

Here we want to underline the effect that this selection might have on the measurement of the polarisation. The only used selection cut which could affect the distribution of the proton angle is clearly the cut on the ν variable. In fact, the χ^2 of the track fit and the χ^2 of the vertex fit cannot be dependent on ϑ.

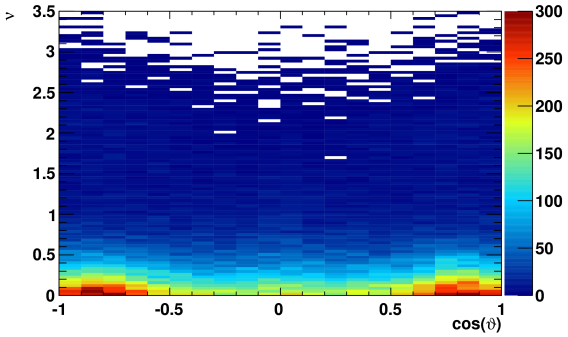

Figure 85.: Distribution of the ν discrimination variable against the cosine of the polarisation angle ϑ for Λ combinations in pp collision data events. Distribution is statistically background subtracted.

The ν variable selects, for the same V^0 impact parameter, combinations with protons and pions with large impact parameters. Geometrically this corresponds to cutting part of the combinations with $\vartheta = \pi/2$, i.e. lying in the production plane, and in particular the ones with $\zeta = 0, \pi$. This effect can be seen in Fig. 85 which shows the distribution of the ν variable against the cosine of ϑ for Λ particles in pp collision data. This plot has been obtained by studying a sub-sample of the considered data, selected without any cut on the ν variable.

However, while this cut can modify the distribution of the proton ϑ by cutting events at $\pi/2$, the slope of the distribution cannot be biased because this cut is symmetric with respect to ϑ.

A bias could arise instead in the measurement of the ζ distribution. In this case the ν cut would reject more combinations at $\zeta = 0$ (proton *forward*) than at $\zeta = \pi$ (pion *forward*). In fact this two values of the ζ angle indicate which of the two particles is directed parallel and which anti-parallel to the Λ momentum in the lab frame. But the pion in the Λ decay has usually a smaller momentum than the pion, and hence, when the it is directed backwards has a smaller probability to be detected than the proton (due to the possibility that the magnet bend out the low momentum charged particles before they reach the T1-T3 trackers). Nevertheless we have decided to keep this selection for our helicity measurements because first of all we want to be sensitive to the transverse polarisation rather than the longitudinal one and second because this kind of instrumental bias is almost unavoidable in our experiments and depends only marginally on

the ν variable, but more on the forward projective nature of the detector configuration.

4.3 EXTRACTION OF ϑ DISTRIBUTIONS AND CORRECTION FOR EFFICIENCY

After the selection, one can extract from the Λ candidates the distribution of ϑ. Before doing this, as stated in § 3.3.3, we have to correct for the beam crossing angle, by boosting the Λ and its decay products in the CM system and rotating the system such that the beam axis direction be coincident with the z axis. After that we calculate the relevant quantities in the Λ rest frame as depicted in Fig. 84.

In particular, for convenience, rather than considering the angle ϑ itself we consider directly its cosine; in this case the proton angular distribution is just a line which, if normalised, would have the polarisation as its slope.

The distributions then can be simply made in constant bins of $\cos\vartheta$ to be fitted in order to extract the parameters.

Even if our particular selection should not bias, as we have see, the $\cos\vartheta$, various detector effect could change the shape of this distribution. Now, in order to understand if a polarisation is present we have not only to fit the distribution in order to obtain the P value but also to compare the distribution with the *null* hypothesis, i.e. compare it with a constant distribution. For this reason, we decided to correct the ϑ in the data with the efficiency as calculated from MC simulations. In particular the efficiency should be defined as:

$$\varepsilon_{MC}(\vartheta) = \frac{f^{sel}_{MC}(\vartheta)}{f^{gen}_{MC}(\vartheta)} \tag{4.3}$$

indicating with f the distribution of ϑ for the given MC sample, generated (gen) or reconstructed and selected (sel). However the distribution for the MC generated sample (*i.e.* before reconstruction and selection) is perfectly flat and with no polarisation, that is $f^{gen}_{MC}(\vartheta) \equiv 1$. Hence, apart from an overall normalisation, the efficiency with which we should correct the data distributions is just the selected MC distribution and we can safely ignore the generated MC distribution, avoiding in this way also the statistical error contribution coming from an additional histogram. Since our parametrisation of the ϑ distribution contains already an overall normalisation of which we shouldn't concern, we will not normalise anyhow our data corrected distribution.

Table 19.: Values of the χ^2/dof and the relative probability for the hypothesis of flat distributions of corrected $\cos\vartheta$ for the different V^0 species.

	χ^2/d.o.f.	$p(\chi^2)$
$\bar{\Lambda}$	32.49/19	0.027
Λ	37.95/19	0.006
K^0_S	189.66/19	-

In order to obtain the $\cos\vartheta$ distribution for signal events we have to subtract the background contribution, for which we use the simple sideband subtraction already described (Cf. § 3.5).

The distributions for pp collisions data and MC samples at $\sqrt{s} = 0.9$ TeV are shown in Fig. 86 (left side) for $\bar{\Lambda}$, Λ and K^0_S candidates. The MC distribution is normalised to the one of the data. As it can be seen the reconstruction and selection cause a distortion of the Monte Carlo distribution shape. This distortion is clearly very similar to the one in the data sample. As already said the Monte Carlo distribution in these plots represent the efficiency with which we have to correct the data. In the right side of Fig. 86 we show the data $\cos\vartheta$ distribution divided by the MC one. While the Λ and $\bar{\Lambda}$ distributions seems to be properly corrected for efficiency while the K^0_S distribution is not. In particular, while the shape of K^0_S data and MC distributions appear to be the same, the parabolic values are clearly different as it is shown by the ratio distribution.

We have fit the data over MC distribution ratios with constant lines in order to accept or reject the null hypothesis of no polarisation. The χ^2 divided by the degrees of freedom are reported in the plots and in Table 19 together with the corresponding probabilities. The $\bar{\Lambda}$ and Λ distribution are compatible with the null hypothesis, while the K^0_S has a clear discrepancy, which will be discussed in the systematics paragraph § 4.5.3.

The extraction of the polarisation values has been done in bins of x_F and in bins of p_T separately, integrating out the other variable. This has been done in order to increase the statistics.

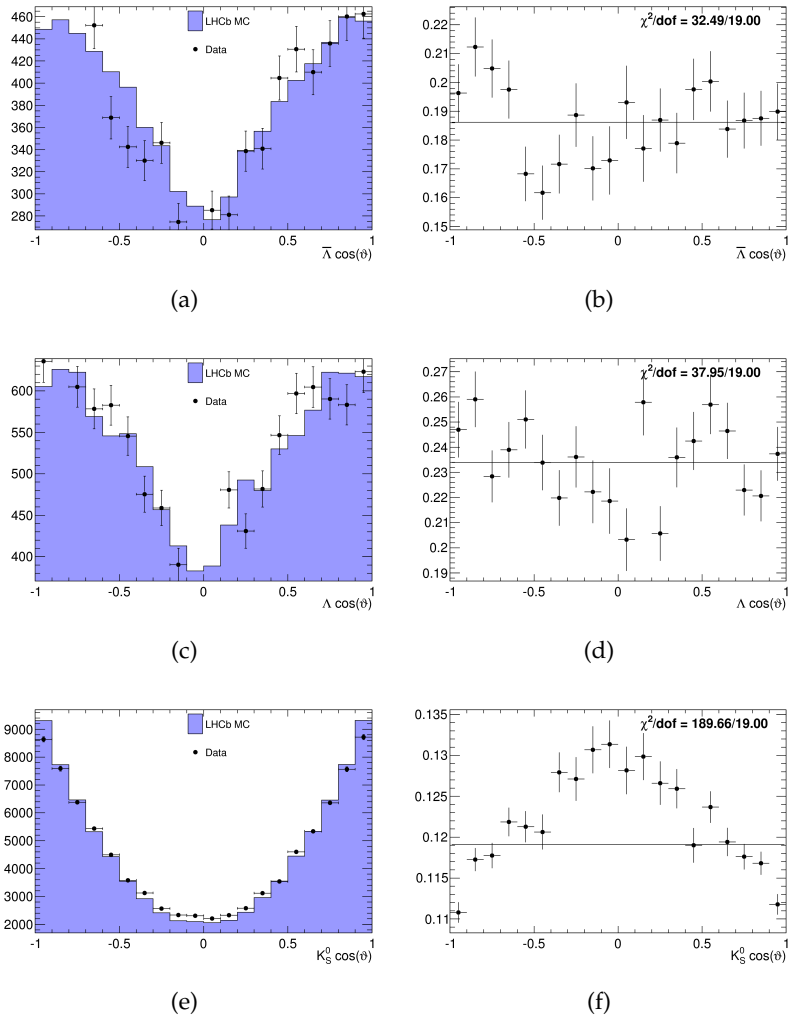

Figure 86.: Distribution of $\cos\vartheta$ for (top) $\bar{\Lambda}$, (middle) Λ and (bottom) K^0_S particles as obtained for pp collision data and MC samples at $\sqrt{s} = 0.9$ TeV. Distributions are sideband subtracted and normalised to the data one.

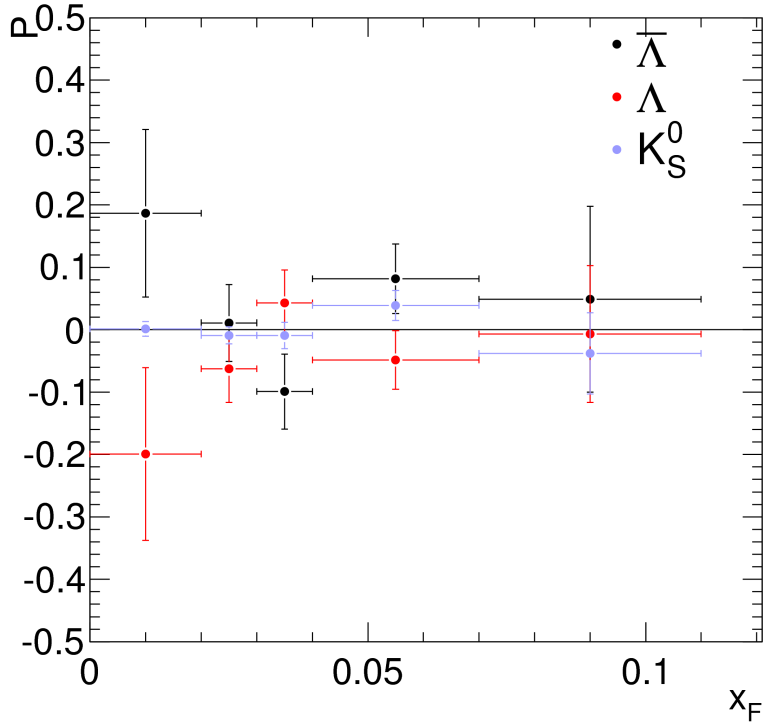

Figure 87.: Polarisation of Λ, $\bar{\Lambda}$ and K^0_S as a function of x_F as measured in pp collisions at $\sqrt{s} = 0.9$ TeV.

4.4 RESULTS

We present here and discuss our results on the $\bar{\Lambda}$ and Λ polarisation as obtained in pp collisions at $\sqrt{s} = 0.9$ TeV.

In Fig. 87 we show the values of the polarisation for Λ and $\bar{\Lambda}$ particles as a function of x_F; the numerical values are reported in Table 20. For comparison we show also the *polarisation* measured for the K^0_S decay the value of which are listed in Table 21.

All of the results appear consistent with no polarisation: some of the bins show values which are not consistent with zero within the errors, but none of them is farther than 1.5 σ.

In Fig. 88 we show instead the values of the polarisation for Λ and $\bar{\Lambda}$ particles as a function of p_T; the numerical values are reported in Table 22. For comparison we show also the corresponding *polarisation* measured for the K^0_S decay the value of which are listed in Table 23.

Also our measurement of the polarisation as a function of p_T seems to be limited by the statistics. However we can see some

Table 20.: Polarisation values for Λ and $\bar{\Lambda}$ as measured as a function of x_F in pp collisions at $\sqrt{s} = 0.9$ TeV

	P_Λ	$P_{\bar{\Lambda}}$
$0.00 < x_F < 0.02$	-0.199 ± 0.054	0.187 ± 0.062
$0.02 < x_F < 0.03$	-0.063 ± 0.053	0.011 ± 0.060
$0.03 < x_F < 0.04$	0.043 ± 0.047	-0.099 ± 0.056
$0.04 < x_F < 0.07$	-0.049 ± 0.110	0.082 ± 0.149
$0.07 < x_F < 0.11$	-0.007 ± 0.012	0.049 ± 0.139

Table 21.: Polarisation values for K^0_S as measured as a function of x_F in pp collisions at $\sqrt{s} = 0.9$ TeV

	$P_{K^0_S}$
$0.00 < x_F < 0.02$	0.002 ± 0.012
$0.02 < x_F < 0.03$	-0.009 ± 0.014
$0.03 < x_F < 0.04$	-0.009 ± 0.021
$0.04 < x_F < 0.07$	0.039 ± 0.024
$0.07 < x_F < 0.11$	-0.038 ± 0.065

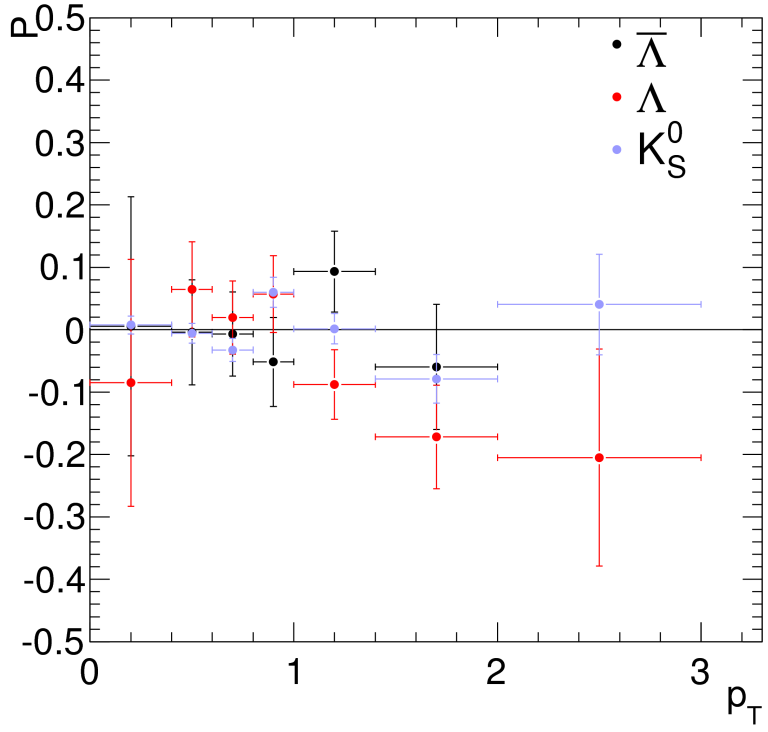

Figure 88.: Polarisation of Λ, $\bar{\Lambda}$ and K^0_S as a function of p_T as measured in pp collisions at $\sqrt{s} = 0.9$ TeV.

trend of the Λ polarisation to grow in absolute value as a function of p_T which would be consistent with the theoretical expectations.

In order to increase the statistics in the sensitive region of our measurement we have performed a measurement of the polarisation for V^0 particles with $x_F > 0.02$ and $p_T > 1$ GeV/c. In this way we exclude most of the statistics which is predicted to have no polarisation and we concentrate in the region where a sizable polarisation is expected. In Figure 89 we show the distributions of $\cos\vartheta$ for the different V^0 species after this selection. The ratio of the data to MC distributions is also shown with the fit for the measurement of the polarisation. The resulted polarisation values together with the χ^2 of the fits are summarised in Table 24. A non negligible polarisation can be observed in the Λ case, with a value $P = -0.104 \pm 0.044$ and a good χ^2 of the fit, conversely the $\bar{\Lambda}$ results not polarised. Since no significant slope can be seen in the K^0_S case we cannot attribute this Λ polarisation to acceptance effects.

Table 22.: Polarisation values for Λ and $\bar{\Lambda}$ as measured as a function of p_T in pp collisions at $\sqrt{s} = 0.9$ TeV

	P_Λ	$P_{\bar{\Lambda}}$
$0.00 < p_T < 0.40$	-0.085 ± 0.076	-0.006 ± 0.084
$0.40 < p_T < 0.60$	0.065 ± 0.059	0.004 ± 0.068
$0.60 < p_T < 0.80$	0.019 ± 0.061	0.007 ± 0.071
$0.80 < p_T < 1.00$	0.057 ± 0.056	0.052 ± 0.065
$1.00 < p_T < 1.39$	-0.088 ± 0.083	-0.093 ± 0.100
$1.39 < p_T < 2.00$	-0.172 ± 0.174	0.060 ± 0.238
$2.00 < p_T < 3.00$	-0.205 ± 0.014	-0.513 ± 0.198

Table 23.: Polarisation values for K^0_S as measured as a function of p_T in pp collisions at $\sqrt{s} = 0.9$ TeV

	$P_{K^0_S}$
$0.00 < p_T < 0.40$	0.008 ± 0.014
$0.40 < p_T < 0.60$	-0.006 ± 0.016
$0.60 < p_T < 0.80$	-0.032 ± 0.018
$0.80 < p_T < 1.00$	0.060 ± 0.024
$1.00 < p_T < 1.39$	0.002 ± 0.024
$1.39 < p_T < 2.00$	-0.079 ± 0.039
$2.00 < p_T < 3.00$	0.040 ± 0.081

Table 24.: Polarisation values for Λ, $\bar{\Lambda}$ and K^0_S as measured for in pp collisions at $\sqrt{s} = 0.9$ TeV for the V^0 particles with $x_F > 0.02$ and $p_T > 1$ GeV/c.

V^0	P	χ^2/dof
$\bar{\Lambda}$	0.039 ± 0.053	14.664/18.000
Λ	-0.104 ± 0.044	17.548/18.000
K^0_S	-0.020 ± 0.021	12.822/18.000

Summarising, our study of Λ and $\bar{\Lambda}$ polarisation shows no significant polarisation for neither of the two baryons when integrated over x_F or over p_T. A

Since the expected polarisation is low, more sensitive measurements are needed. In particular our measurements is still dominated by statistics. Since the current sample of data in pp collisions at $\sqrt{s} = 0.9$ TeV is likely to remain the full statistics at this energy, an improvement is possible only by considering looser selections. A further improvement is possible by considering different track types, *e.g.* downstream type, which are a considerable part of the Λ sample, due to its the large lifetime.

4.5 SYSTEMATIC UNCERTAINTIES

We consider in the following some possible systematic uncertainties which could affect the measurement of the Λ polarisation.

4.5.1 *Magnetic moment precession in the LHCb magnetic field*

An effect which could spoil our measurement is the precession of the Λ spin caused by the LHCb magnetic dipole field. This effectively change the direction of the spin from the one at the production to the one at the decay of the Λ. As already said the interesting measurement is the polarisation at the production, but this would be diluted by this rotation.

In order to understand if this can cause a problem for our measurement, we can calculate directly the angular difference for the spin of the Λ, due to the magnetic field.

The angular frequency (pulsation) for the precession of the spin of a Λ in a magnetic field B is given by:

$$\omega = -\frac{g_\Lambda \mu_N}{\hbar} B \tag{4.4}$$

where

$$\mu_N = e\hbar/2m_p = 5.05078324(13) \cdot 10^{-27} \quad [JT^{-1}] \tag{4.5}$$

is the nuclear magneton and

$$g_\Lambda = -0.613 \pm 0.004 \tag{4.6}$$

is the gyromagnetic factor for the Λ. [1]. Then the pulsation is

$$\omega = 2.936 \cdot 10^7 B \quad [Hz] \tag{4.7}$$

1 Both μ_N and g_Λ numerical values are taken from the PDG review of particle physics [64]

considering the B field to be measured in Tesla. For convenience we will call *specific pulsation* the pulsation for unit of magnetic field, given by:

$$\omega_b = \omega/B = 2.936 \cdot 10^7 \ \ [T^{-1}Hz] \quad . \tag{4.8}$$

The magnetic field of LHCb, directed parallel to the y axis of the lam frame, is at most 0.1 T within 2 m from the interaction point (cf. Fig. 20). If we substitute the upper value B=0.1 T in the pulsation formula we get:

$$\omega = 2.936 \cdot 10^6 [Hz] \tag{4.9}$$

this means that the period is

$$T = 2.14 \cdot 10^{-6} s \tag{4.10}$$

and the equivalent distance flying at the speed of light is:

$$s = 6.416 \cdot 10^2 m \tag{4.11}$$

which would be the distance to be covered for a Λ particle in order for its spin to precede of a whole turn in a constant B field of 0.1 T.

Now we can work out the equivalent error in the spin direction if ignoring the spin precession for a Λ particle in a B field of 0.1 T for one meter at the speed of light:

$$\sigma(\theta) = \frac{\omega \cdot 1m}{c} = 9.793 \cdot 10^{-3} \ [rad] \tag{4.12}$$

Even if we translate this in an equivalent error on the proton ϑ of the same amount, which is a conservative approach, this can be easily neglected for our measurement.

However if we consider the whole LHCb magnetic B field, which has an integrated bending power $\int B dl = 4Tm$ this would correspond to an angular error:

$$\sigma(\theta) = \omega_b \int B dl/c = 3.917 \cdot 10^{-1} \ [rad] \tag{4.13}$$

which would be a large error instead. However since we require *long* tracks for the Λ decay products, our Λ decay all in the VELO and hence are well within 2 metres from the interaction point, leading to an estimated total error on the spin angle of:

$$\sigma(\theta) = \frac{\omega \cdot 2m}{c} = 1.959 \cdot 10^{-2} \ [rad] \tag{4.14}$$

which can be safely ignored for our final estimates.

4.5.2 *Secondary Λ production*

As we have already seen in § 3.1 a non negligible portion of the Λ produced in proton-proton collisions come from higher mass hyperons decays. In particular we have seen that the percentage of the Λ are produced directly at the PV, of which we want to measure the polarisation, is only about 40%. Hence a relevant and unavoidable contribution to the ϑ distribution comes from secondary Λ. Note that, while within the V^0 production ratios analyses we considered as prompt the Λ from strong and electromagnetic decays of particles produced at the PV, in the polarisation analysis we would like to reject also this component.

No attempt has been done in this work to control this kind of decays by explicitly trying to reconstruct the full hyperon into Λ decays (e.g. $\Sigma^0 \to \Lambda\gamma$, $\Xi^- \to \Lambda\pi^-$, etc). First of all this is due to the complexity and inefficiency of this kind of analysis being the Λ companion in this decays particularly soft and hence difficult to detect, and secondly because we want to compare our results to similar data obtained in other experiments where this kind of rejection has never been achieved.

Hence in the following we will continue in studying the *effective polarisation* without specifying this "effectiveness".

4.5.3 K^0_S *helicity angle cross-check*

.

The measurement of the Λ polarisation can be modified, as we have seen, by various effects. A natural way to check the influence of any possible instrumental effect which could arise in this kind of measurement is the comparison with the very same analysis applied to the $K^0_S \to \pi^+\pi^-$ decay. The K^0_S is a pseudoscalar meson with spin 0 so that the *polarisation* concept is not even defined for this particle. The distribution of the decay product of the K^0_S must be just the one allowed by the available phase space, *i.e.* completely flat for the $\cos\vartheta$ of the pions.

Considering the sample of K^0_S used in Chapter 3 for the $\bar{\Lambda}/K^0_S$ production ratio we have analysed the distribution of the ϑ angle for $K^0_S \to \pi^+\pi^-$ events, using the positive pion in the place of the proton. The analysis procedure is exactly the same as the one depicted for Λ events, including efficiency correction and polarisation extraction.

The distribution for the K^0_S $\cos\vartheta$ was already shown in Fig. 86, and the *polarisation* values were calculated as a function of x_F

(Table 20) and as a function of p_T (Table 22). No significant slope was found, even if in some of the bins it is no compatible with zero. Moreover considering the corrected $\cos\vartheta$ distribution of K^0_S in 86 (f), we can see that the description of the acceptance given by MC events is not perfect and gives a non-flat distribution after correction.

A possible reason may be the different momentum spectra of K^0_S particles in MC and data as we have seen in Chapter 3. Once boosted to the center of mass frame, the different $\cos\vartheta$ bins correspond to different final state momenta. The efficiency for each bin therefore depends on the momentum distribution. We have calculated the $\cos\vartheta$ distribution for K^0_S particles after re-weighting the MC momentum distribution in an analogous way as described in § 3.6.1.1. The result of this procedure is shown in Fig. 90 before (a) and after (b) the reweighting. Apart from an overall normalisation which has not been restored for simplicity, it can be seen that the re-weighted distribution is more compatible with a flat distribution, with a χ^2/dof decreasing from 186.66/19 to 62.44/19. A discrepancy is still present, indicating that this effect is not the only one to modify the data distribution differently from MC expectations.

Further studies are needed in order to understand this disagreement. However the influence that this effect can bring to the measurement of the Λ polarisation is low. In fact the discrepancy is symmetric with respect to positive and negative $\cos\vartheta$ so that no odd parity contribution is added to corrected data distribution, that is no polarisation is artificially induced by acceptance correction as demonstrated by the measurement of *polarisation* for K^0_S particles.

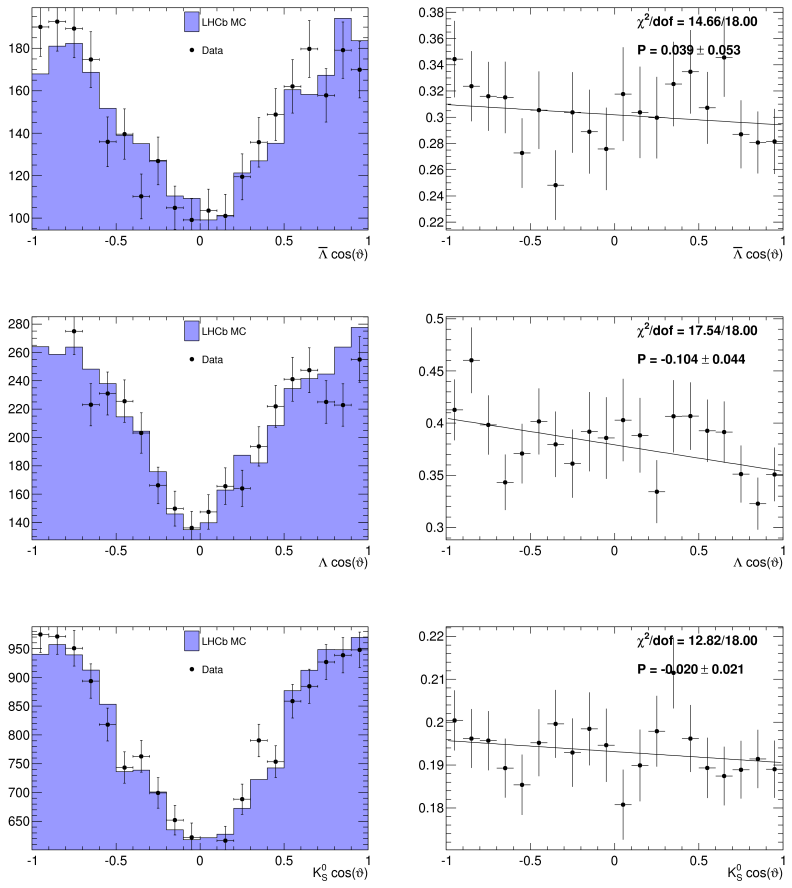

Figure 89.: Distribution of $\cos\vartheta$ for (top) $\bar{\Lambda}$, (middle) Λ and (bottom) K^0_S particles as obtained for pp collision data and MC samples at $\sqrt{s} = 0.9$ TeV for V^0 particles with $x_F > 0.02$ and $p_T > 1$ GeV/c. Distributions are sideband subtracted and normalised to the data one.

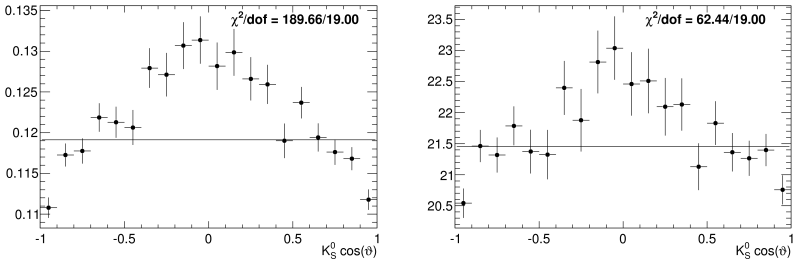

(a) (b)

Figure 90.: Corrected distribution of $\cos\vartheta$ for $K^0_S \to \pi^+\pi^-$ combinations before (a) and after (b) reweighting the MC momentum spectrum in order to match the data one. Distributions are not normalised.

5

SEARCH FOR $D^0 \to \mu^+\mu^-$ DECAY

5.1 MEASUREMENT STRATEGY

In this section we explain the strategy for the measurements of the $D^0 \to \mu^+\mu^-$ branching ratio or, in case of no signal observation, for an estimate of its upper limit. We give here a brief summary and next we will go into the details of the single steps.

For the search of $D^0 \to \mu^+\mu^-$ decays we have decided to use the so called *tagged analysis*, *i.e.* looking for $D^{*+} \to D^0(\to \mu^+\mu^-)\pi^+$ decay, the reasons for this will be described in §5.1.1. This analysis will be extended in the future using also the *untagged* analysis looking directly to $D^0 \to \mu^+\mu^-$.

The selection procedure has been divided in several steps, mainly for technical reasons:

- Trigger HLT2 (§5.1.3)
- Stripping (§5.1.4)
- Final selection based on multivariate methods. (§5.1.5)

Once the final selection has been applied we are left with the events with which to estimate our branching ratio. In order not to impose a bias in our analysis procedure we have decided to blind in data the region of the $\mu\mu$ invariant mass around the D^0 nominal mass until the end of the analysis and look at the events therein just after being confident of our method.

The background to our channel which we have to reject is mainly of two types:

- combinatorial background, composed of random combinations of two real muons;
- mis-identification background, due to D^0 hadronic two-body decays with both decay products mis-identified as muons.

While the first type of background, after been reduced as much as possible by selection cuts, can be subtracted by considering the invariant mass sideband regions, the mis-identification background is peaked in the signal mass-region so that it has to be

controlled with muon identification and precise measurement of the mis-ID probability (Cf. §5.1.2).

In order to estimate the signal properties for the final selection with real data we need a control channel very similar to our signal but with large branching ratio; we have chosen to use the $D^0 \to \pi^+\pi^-$ decay which has practically the same kinematics since the difference between muon and pion mass is small compared to the D^0 mass. Some comparison will also be made with the $D^0 \to K^-\pi^+$ decay which has a larger branching ratio.

The $D^0 \to \pi^+\pi^-$ channel will also be used as normalisation channel in the branching ration calculation.

5.1.1 *D* tag*

In order to search for the $D^0 \to \mu^+\mu^-$ decay, we have considered the possibility to find it using the $D^{*+} \to D^0\pi^+$ decay as source of D^0, *i.e.* looking for $D^{*+} \to D^0(\to \mu^+\mu^-)\pi^+$ decays. [1] This technique is often called D^* tag because is commonly used in order to label the flavour of the D^0 by the charge of the $D^{*\pm}$. With this choice we consider just a fraction of the total inclusive D^0 sample but we gain considerably in background rejection thanks to the additional information on the D^* decay.

In particular the fraction of D^0 considered when looking just at D^* decays is [71, 69]:

$$\frac{N(D^{*+} \to D^0)}{N(D^0)} = \frac{f(c \to D^{*+})\mathcal{BR}(D^{*+} \to D^0)}{f(c \to D^0)} \simeq 0.28 \quad (5.1)$$

where $f(c \to D^{*+})$ and $f(c \to D^0)$ are the inclusive probabilities of a c quark to hadronise into a D^* and D^0 respectively, and $\mathcal{BR}(D^{*+} \to D^0\pi^+)$ is the branching ratio of the considered decay. As it can be seen we consider in this way less than 1/3 of the events. This number has to be further multiplied by the pion reconstruction efficiency which is around 30% for long tracks and about 20% for upstream tracks.

The D^* tag, however, allow a much higher combinatorial background rejection, with respect to the inclusive search. In fact, if we introduce the mass difference

$$\Delta m = m_{D^*} - m_{D^0} = m_{\pi\mu\mu} - m_{\mu\mu} \quad , \quad (5.2)$$

we can prove that the resolution on Δm is much better of the one on the two masses separately. In fact the measurements of m_{D^0}

1 Here and in the following we always imply that we include also charge conjugated modes, unless otherwise specified.

and m_{D^*} are correlated one with each other being the result of the sum of the decay products four-vectors, two of which are in common; hence the only difference is due to the measurement of the pion momentum. Being the two positively correlated the errors on their subtraction partially cancel out when the full error propagation is taken into account. Naively this can be understood by the fact that the difference is just an indirect measurement of the mass of the pion.

In principle one would expect that a certain additional combinatorial background would come from all the possible $D^0\pi$ combinations composed by a given D^0 and the multitude of pions produced in high energy proton-proton collisions. This is indeed true, but a second effect helps us to reduce the background, *i.e.* the threshold effect. In fact the available phase space for the $D^{*+} \to D^0\pi^+$ decay is much reduced by the small difference between the mass of the pion and the nominal Δm, exactly [69]:

$$\begin{aligned} \Delta m_0 &= m_{D^{*\pm}(2010)} - m_{D^0} = 145.421 \pm 0.010 \text{ MeV} \\ m_\pi &= 139.57018 \pm 0.00035 \text{ MeV} \quad . \end{aligned}$$

This small difference cause that only D^* candidates are physically acceptable only if they have a minimum mass Δm corresponding to the pion mass. This reduced phase space due to the near threshold makes that the probability for a given $D^0\pi$ combination to be in the region next to the D^* smaller and smaller as the threshold approaches so that most of the possible fake D^* candidates will be concentrated at high Δm and easily rejected.

5.1.2 *Measurement of the mis-identification*

Apart from the combinatorial background, an irreducible limit on the search for the $D^0 \to \mu^+\mu^-$ decay could come from the mis-identification background. In fact the main two-body hadronic decays of the D^0, *i.e.* $D^0 \to K^-\pi^+$, $D^0 \to \pi^+\pi^-$ and $D^0 \to K^+K^-$, can mimic our signal channel if both the decay products are incorrectly identified as muons. The branching ratios of these decays are listed in Table 25. Even if the $D^0 \to K^-\pi^+$ decay has the larger branching fraction most of the background will come from the $D^0 \to \pi^+\pi^-$. In fact when a kaon gets mis-identified as a muon the large mass difference between the two particles cause a shift in the reconstructed D^0 which is large enough to move most of this events out of the D^0 signal mass window. Clearly, the $D^0 \to K^+K^-$ decay is subject to an even larger displacement and therefore does not represent a problem. On the contrary, this

Table 25.: Branching ratios of the main hadronic two-body decays of the D^0 meson [69].

Decay	Branching ratio
$D^0 \to K^-\pi^+$	$(3.89 \pm 0.05)\%$
$D^0 \to \pi^+\pi^-$	$(1.397 \pm 0.026) \cdot 10^{-3}$
$D^0 \to K^+K^-$	$(3.94 \pm 0.07) \cdot 10^{-3}$

reasoning does not apply to the $D^0 \to \pi^+\pi^-$ decay where the mass difference between the real D^0 peak and the mis-identified one is of order 10 MeV. Therefore the $\mu\mu$ invariant mass will present a peak due to the mis-identified $D^0 \to \pi^+\pi^-$ events which cannot be eliminated by simple side-band subtraction and requires a good knowledge of the mis-identification probability (mis-ID).

Within our experiment the muon identification is calibrated using the $J/\psi \to \mu^+\mu^-$ decay as a source of muons and the $\Lambda \to p\pi^-$ decay as a source of hadrons [72]. As we have seen in Chapter 3 a pure Λ sample can be selected without the need of particle ID so that it can be an unbiased source of pions and protons for the mis-ID calibration. Similarly, the $J/\psi \to \mu^+\mu^-$ decay can be selected by identifying with strong identification cuts one of the two muons leaving the second one, unbiased, to be used for the estimate of the muon identification.

In our study, however, we consider a second method to have a direct and precise estimate of our mis-identification background in the kinematic region in which we are interested; this method can also be used as a cross-check of the previously described one. We consider the $D^0 \to \pi^\pm\mu^\mp$ decay, which is forbidden in the Standard Model due to lepton number conservation and whatever New Physics scenario one considers it must be suppressed by many orders of magnitude. Therefore $D^0 \to \pi^\pm\mu^\mp$ candidates present in pp collision data must be due, apart from random combinations, to $D^0 \to \pi^+\pi^-$ decays with one of the two pions mis-identified as a muon. The single mis-identification probability then can be measured as:

$$p(\pi \to \mu) = \frac{N(D^0 \to \pi\mu)}{2 \cdot N(D^0 \to \pi\pi)} \tag{5.3}$$

where the number of events for each channel can be estimated from the invariant mass distributions and the factor 2 comes from

the fact that a $D^0 \to \pi^+\pi^-$ decay can be mis-identified once for each pion. The double mis-ID then is simply the square of (5.3) since no correlation is expected. [2]

The same strategy can be applied to the $D^0 \to K^-\pi^+$ decay, which can be mis-identified as a $D^0 \to K^-\mu^+$ decay. The use of this channel has the advantage of having a higher branching ratio and lower combinatorial background (if the kaon is selected using some identification cut) but presents the drawback that the kinematic region of the mis-identified pion is slightly different from the $D^0 \to \mu^+\mu^-$ one due to the the asymmetric $D^0 \to K^-\pi^+$ decay.

In this work we consider both channels since the $D^0 \to K^-\mu^+$ strategy is better suited when less statistics is available.

5.1.3 *Trigger HLT2*

As we have seen in §2.4.2 there is no possibility to record all the pp collisions data at high luminosities, so that a certain fraction must be rejected exploiting the L0 and HLT trigger. Being software based the HLT can be configured according to the physics analysis needs, and in particular the HLT2 contains already exclusive selections. Therefore we developed HLT2 lines to select our signal channel.

The HTL2 trigger has to cope with different requirements for its operation. The output rate of the HLT2 is fixed at the 2 kHz by the frequency with which events can be written on storage, therefore the decision must be taken as fast as possible. Both CPU and rejection requirements must be taken into account. For most physics channel triggers, the major source of CPU comes from the combination process in order to find the signal candidates. Within hadronic events the high number of tracks makes the number of possible two tracks combinations high and it is even worse for three or four body processes.

Therefore recently it has been decided by the collaboration to apply a cut of $p_T > 500$ MeV/c to all the tracks in the HLT2 processing. While this cut reduces the random combinatorial background by rejecting soft tracks, it prevents us to trigger on the full $D^{*+} \to D^0(\to \mu^+\mu^-)\pi^+$ channel since the pion from the D^* decay has low p_T. Hence we have developed our HLT2 trigger lines in order to select *untagged* $D^0 \to \mu^+\mu^-$ decay.

2 This wouldn't be true if we wanted to give a mis-ID as a function of the momentum since the two pions are clearly correlated in phase space; but here we consider just the average value.

The developing of our trigger lines has been based on the following guidelines:

1. obtain an higher as possible efficiency for the signal channel;
2. use exactly the same trigger cuts for signal and control samples;
3. if the background rejection is not enough for control channels (due to the presence of pions instead of muons), *prescale* the control channel lines;

The point number 2 is due to the fact that while, in principle, as far as the trigger efficiencies (ε_s for signal and ε_c for control channels) are known, their absolute value doesn't change the analysis, a smaller error in the final branching ratio measurement is obtained by making them as close as possible [3].

In order to have signal and control channels selected as similarly as possible the practical implementation of our HLT2 lines has been done by building a common template for $D^0 \to x^+y^-$ decays. The selection is based on cuts on the following variables and a summary of the applied cuts values is reported in Table 27:

- Muons track fit χ^2. Each track is fitted starting from the detector hits positions, a χ^2 of the goodness of fit is associated and helps to remove ghost tracks and have a more precise momentum measurement.
- Distance of closest approach between the two muons (DOCA). The minimum distance of the trajectories of two particles coming from a common decay should be zero or, because of experimental errors, very small; conversely random tracks combinations can have a DOCA of various millimetres and therefore we can reject them with this cut.
- D^0 Vertex fit χ^2. A common vertex is fitted starting from the two tracks and a χ^2 of the fit is calculated.
- $p_T(D^0)$ and $p_T(\mu)$. Since the $c\bar{c}$ quarks are produced in hard interactions, charmed particles usually have a large transverse momentum with respect to the mean of the particles produced in minimum bias interactions. For convenience we cut on the minimum and maximum p_T of the two muons separately.

3 A trivial demonstration of this is can be obtained in the case that the errors on the efficiencies are equal, by looking at the optimisation of $\sqrt{1/x^2 + 1/y^2}$.

- $\chi^2\mathrm{IP}(D^0)$. The χ^2 of the impact parameter of the π and of the D^0 with respect to the primary vertex position. This χ^2 is a measurement of the impact parameter which takes into account the errors on the determination of the primary vertex. In particular it is defined as the variation in the χ^2 per degree of freedom of the vertex fit done with and without the considered particle. Clearly, if the particles comes from the PV this variation of the reduced χ^2 should be small, while for secondarily produce particles this has to be large.

- $\mathrm{min}(\chi^2\mathrm{IP}(\mu))$ and $\mathrm{max}(\chi^2\mathrm{IP}(\mu))$. On the contrary since the two muons come from the D^0 decay vertex which is displaced with respect to the PV and since they have a certain transverse momentum with respect to the D^0 flight direction their impact parameter with respect to the PV must be sizable. Hence the two muons are required to have a large $\chi^2\mathrm{IP}$; the two cuts are for convenience applied separately to the minimum and to the maximum of the two $\chi^2\mathrm{IP}$, since, due to the p_T of the D^0 in the lab frame, one of the two muons will certainly have a smaller IP.

- χ^2_{FD} of the D^0. This variable is a measurement of the distance of the D^0 decay vertex from the PV, *i.e.* of the D^0 flight distance, which takes into account the errors of the two vertices positions. It is defined as:

$$\chi^2_{FD} = (\vec{r}_{DV} - \vec{r}_{PV})^T \Sigma^{-1} (\vec{r}_{DV} - \vec{r}_{PV}) \tag{5.4}$$

  where $\vec{r}_{DV}$ and $\vec{r}_{PV}$) are the fitted positions of the D^0 and primary vertices respectively and Σ^{-1} is the inverse of the covariance matrix for these measurements.

- Pointing angle, that is the angle between the D^0 candidate momentum and the line that joins the Primary and the D^0 decay vertex, in formulas:

$$\mathrm{Angle}(\vec{p}_{D^0}, \vec{r}_{PV} - \vec{r}_{DV}) \quad . \tag{5.5}$$

Despite the outlined selection reject most of random combinations, in a high energy hadronic environment the number of possible $K\pi$ and $\pi\pi$ combination is very high so that many events pass our selection because statistically one of the various combinations satisfies the requirements. Therefore we had to apply a prescale to some of our trigger lines in order to match the needed

Table 26.: Values of the prescale factors applied to the different channels. The value is reported as relative fraction, *i.e.* 1 means no prescale.

Channel	Prescale
$D^0 \to \mu^+\mu^-$	1
$D^0 \to K^-\pi^+$	0.02
$D^0 \to \pi^+\pi^-$	0.1
$D^0 \to K^-\mu^+$	0.2
$D^0 \to \pi^\pm\mu^\mp$	1

rejection. The prescale randomly select a certain fraction of the events before letting them pass through the trigger line. The net effect is that one has an unbiased output sample simply reduced by a known factor. The values of the prescales used for our HLT2 trigger lines are listed in Table 26.

5.1.4 *Stripping*

In parallel with the HLT2 we have also developed stripping lines in order to preselect the data samples to be analysed. In the Stripping procedure we could exploit all the possible tracks of one event since no stringent CPU requirements are present offline. Therefore we have developed stripping lines to selected $D^{*+} \to D^0(\to \mu^+\mu^-)\pi^+$ decays together with the corresponding control channels. These correspond to the *tagged* analysis previously described; moreover we have also foreseen to select inclusively $D^0 \to \mu^+\mu^-$ decays for the *untagged* analysis which however we will not describe here.

The summary of the cuts applied in the stripping pre-selection is reported in Table 28. As it can be seen these cuts trace the HLT2 ones as far as the $D^0 \to \mu^+\mu^-$ decay is concerned. Additional cuts include impact parameter and transverse momentum cuts on the pion and D^* and Δm regions.

5.1.5 *Final multivariate selection*

In order acquire the higher signal efficiency as possible while rejecting the background we have planned to use multi-variate methods for our final selection.

Table 27.: Summary of the selection cuts used in the HLT2 trigger for the $D^0 \to \mu^+\mu^-$ selection in 2010 data. Cuts referred to muons are also applied to kaons and pions for the $D^0 \to \pi^+\pi^-$ and $D^0 \to K^-\pi^+$ decays.

Variable	Cut value
DOCA	< 0.1 mm
$\min(p_T(\mu))$	> 750 MeV/c
$\max(p_T(\mu))$	> 1100 MeV/c
$\min(p(\mu))$	> 4000 MeV/c
Track fit χ^2	< 5
$\min(\chi^2\text{IP}(\mu))$ w.r.t. PV	> 3
$\max(\chi^2\text{IP}(\mu))$ w.r.t. PV	> 8
$\chi^2\text{IP}(D^0)$ w.r.t. PV	> 15
χ^2_{FD} of the D^0	> 20
$\cos(\text{Angle}(\vec{p}_{D^0}, \vec{r}_{PV} - \vec{r}_{DV}))$	> 0.9998
$p_T(D^0)$	> 1800 MeV/c
$\chi^2\text{IP}(D^0)$ w.r.t. PV	< 15
D^0 Vertex fit χ^2	< 10
D^0 Mass window	± 70 MeV/c^2

Table 28.: Summary of the selection cuts used in the stripping procedure for the $D^{*+} \to D^0(\to \mu^+\mu^-)\pi^+$ selection in 2010 data. Cuts referred to muons are also applied to kaons and pions for the $D^{*+} \to D^0(\to \pi^+\pi^-)\pi^+$ and $D^{*+} \to D^0(\to K^-\pi^+)\pi^+$ decays. The cuts which are labelled with π are referred to the *slow* pion coming from the D^* decay.

Variable	Cut value
$\min(p_T(\mu))$	> 750 MeV/c
$\max(p_T(\mu))$	> 1100 MeV/c
$\min(p(\mu))$	> 4000 MeV/c
Track fit $\chi^2(\mu)$	< 5
$\min(\chi^2\text{IP}(\mu))$ w.r.t. PV	> 3
$\max(\chi^2\text{IP}(\mu))$ w.r.t. PV	> 8
χ^2_{FD} of the D^0	> 20
$\cos(\text{Angle}(\vec{p}_{D^0}, \vec{r}_{PV} - \vec{r}_{DV}))$	> 0.9997
$p_T(D^0)$	> 1800 MeV/c
D^0 Vertex fit χ^2	< 10
$\chi^2\text{IP}(D^0)$ w.r.t. PV	< 15
Track fit $\chi^2(\pi)$	< 7
$p_T(\pi))$	> 110 MeV/c
$\chi^2\text{IP}(\pi)$ w.r.t. PV	< 10
D^0 Mass window	± 70 MeV/c^2
$D^{*\pm}$ Mass window	± 110 MeV/c^2
Δm	(145.421 ± 10) MeV/c^2

Unlike standard cuts, multivariate methods are able to exploit the full information contained in the used variables and in their correlations. In this section we explain briefly some of the multivariate methods used in the following, without any claim of completeness. In fact many possible different methods do exist as far as data mining is concerned [73, 66].

LIKELIHOOD For an event with n_{var} variables x_i, the likelihood defines the probability to belong to the k-category as:

$$\mathscr{L}^k = \prod_i^{n_{var}} p_i^k(x_i) \tag{5.6}$$

i.e. the product of the probabilities for each variable to come from an event in that category. These are calculated with probability distribution functions which in the experimental case are usually deduced by fitting histograms. As a discriminant variable is often used the ratio of the likelihoods for two given hypothesis and this ratio can be transformed in the difference of the likelihood logarithms, as done for the PID variable (Cf. §2.5.3.4).

FISHER DISCRIMINANT This is a method to select events with a convenient linear combination of variables [65] based on the search of an axes in the variables space where to project the events, in such a way that signal and background populations are as distant one from each other and as tight distributed as possible. Numerically the discriminant is built as:

$$y_{Fi} = \sum_{i=0}^{n} \lambda_i x_i \quad . \tag{5.7}$$

where x_i are the considered variables and λ_i the optimised coefficients.

NEURAL NETWORKS With (Artificial) Neural Networks (NN) are indicated simulations of artificial neurons connected one with each other; each neuron being able to give a particular output to a given input. The power of NN comes from the opportunity of requiring a non-linear response from a neuron, and hence from the whole network, that becomes able to solve complex problems.

Each neuron is connected to others with some weights w, and gives a single output for each input, applying the response function. As response function $\varphi(x)$ usually a sigmoid function $\frac{1}{1+e^{-x}}$ or a $\tanh(x)$ is chosen. If for simplicity we consider multilayer

NN where neurons are divided in layers and connections are allowed only between different layers, the output of the whole network would be:

$$y_{out} = \sum_{j=1}^{n_h} y_j^{(2)} w_{j1}^{(2)} = \sum_{j=1}^{n_h} \varphi\left(\sum_{i=1}^{n_{in}} x_i w_{ij}^{(1)}\right) w_{j1}^{(2)} \tag{5.8}$$

where n_{in} and n_h are the number of input and middle neurons, and w_{ij} is the weight between the i^{th} and j^{th} neurons of two layers.

DECISION TREES These are methods of selecting a signal from a background using a path of decisions considering one variable at a time; the path ends when a certain criterion is satisfied. Variable space is then subdivided in different regions belonging to signal or background.

This selection method is formally similar to the cut-based one, but while the latter is able to select just a region of variable space, Decision Trees are able to select many regions, allowing better performances.

After applying a preselection, for each method we consider the output variable as the only discriminant variable. This will be used in the final limit estimation as the sensitive variable together with the invariant mass information.

Each of these methods must be *trained* against the signal and background samples. In order to perform this training exploiting real data, we will consider the $D^0 \to \pi^+\pi^-$ sample as far as the kinematic is concerned. The muon identification instead will not be part of multivariate analysis.

5.1.6 *Branching ratio calculation and limit estimation*

Once the final analysis will be tuned on real data, the blinded invariant mass can be opened. If a significant number of signal events is present one can calculate the correspondent branching ratio, while if not a limit on its size can be put.

5.1.6.1 *Branching ratio calculation*

As anticipated, the calculation of the $D^0 \to \mu^+\mu^-$ branching ratio will be done by normalising to the $D^0 \to \pi^+\pi^-$ decay.

$$\mathcal{BR}(D^0 \to \mu^+\mu^-) = \frac{N_{D^0\to\mu^+\mu^-}}{N_{D^0\to\pi^+\pi^-}} \frac{\varepsilon_{\pi\pi}}{\varepsilon_{\mu\mu}} \mathcal{BR}(D^0 \to \pi^+\pi^-) \quad (5.9)$$

where the efficiency ratio $\varepsilon_{\pi\pi}/\varepsilon_{\mu\mu}$ takes into account for the different efficiencies that the two channels can have on the different analysis stages. In particular

$$\frac{\varepsilon_{\pi\pi}}{\varepsilon_{\mu\mu}} = \frac{\varepsilon_{trig}(\pi\pi)}{\varepsilon_{trig}(\mu\mu)} \times \frac{\varepsilon_{sel}(\pi\pi)}{\varepsilon_{sel}(\mu\mu)} \times \frac{1}{\varepsilon_{\mu ID}(\mu\mu)} \quad . \quad (5.10)$$

While the selection efficiency cancel out, by construction, for the way we developed the analysis, the trigger and identification efficiencies do not.

The trigger efficiency must be divided in several steps (Cf. §2.4). The HLT2 trigger, as we have seen, has been built for our signal and control channels such that the same selection is applied to both. This will make the HLT2 trigger efficiency ratio close to one, apart from, again, the identification efficiency, which however we will treat separately.

The rest of the trigger, Lo and HLT1, cannot be customised for each analysis so that we have to work out its efficiency from real data.

5.1.6.2 *Branching ratio limit estimation*

If no significant excess of events is found in the signal region, our analysis will be able to put an upper limit on the branching ratio, constraining in this way the phase space of new physics scenarios.

The naive way of estimating the upper limit would be by considering the fluctuation on the number of background events in the signal region, as the ultimate limit on the sensitivity. However, more complex techniques allow to improve the sensitivity for a given background level. Here we consider the work in Ref. [74]. The limit estimation technique there illustrated consists of a modified frequentist method which combines, through repeated simulation trials, the probabilities for an outcome correspondent with the given signal plus background found and gives as estimation of the suppression of the signal hypothesis for a given confidence level.

5.2 MONTE CARLO STUDIES

In order to assess the performances of the LHCb experiment for the search of the $D^0 \to \mu^+\mu^-$ decay we have performed sensitivity studies using Monte Carlo simulations.

5.2.1 *Monte Carlo samples*

These studies have been performed before the start of the LHCb data taking when it was foreseen that the center of mass energy of pp collisions in 2010 would have been $\sqrt{s} = 10TeV$, for this reason the MC samples that we have adopted are simulated at this energy. [4] The cross-sections for the production of charm and beauty quarks at this energy as implemented in PYTHIA are:

$$\sigma(c\bar{c}) \simeq 6.26 \text{ mb}$$
$$\sigma(b\bar{b}) \simeq 0.699 \text{ mb} \quad .$$

Different samples were used for this study. First of all a signal sample, composed by events with a $D^{*+} \to D^0(\to \mu^+\mu^-)\pi^+$ decay in the final state. This is achieved by selecting minimum bias events with at least one $D^* \to D^0\pi$ decay and forcing the D^0 to decay into two muons. The sample is further selected at generator level with the so-called *decay products cut*, *i.e.* the decay products are required to be in the geometric LHCb acceptance (*i.e.* with polar angle $10 < \theta < 300$ mrad).

As control and normalisation samples and in order to estimate the mis-ID, the $D^0 \to \pi^+\pi^-$ sample was used the generation of which is identical to the signal sample.

In order to estimate the combinatorial background various samples were analysed:

- *Minimum bias*, no requirements are imposed on this sample which represents all the possible (visible) pp collisions.
- *Minimum bias* $\to \mu\mu$, same as the previous sample but requiring that at least two muons are present in the final state inside the LHCb geometric acceptance.
- *Inclusive* $c\bar{c}$, a minimum bias sample with at least a $c\bar{c}$ pair produced in the interaction, no requirement on the acceptance are imposed.

4 For reference: technically these samples are referred to as MC09 samples.

Table 29.: Summary of the used samples statistics for the Monte Carlo samples. The number of events and the equivalent luminosity is indicated for each sample (not for the signal since we don't know its branching ratio). MCT and No MCT indicate the two minimum bias samples with and without the MC Truth stored.

Sample	N	Equiv. $\mathcal{L}_{int}(pb^{-1})$
$D^{*+} \to D^0(\to \mu^+\mu^-)\pi^+$	114 k	
$D^{*+} \to D^0(\to \pi^+\pi^-)\pi^+$	5 M	9.26
$b\bar{b} \to \mu^+\mu^-$	25 M	4.30
Inclusive $b\bar{b}$	52 M	0.17
Minimum bias (MCT)	10 M	$0.2 \cdot 10^{-3}$
Minimum bias (No MCT)	1 G	$25 \cdot 10^{-3}$
Minimum bias $\to \mu\mu$	23.7 M	1.79
Inclusive $c\bar{c}$	10M	$3.8 \cdot 10^{-3}$

- *Inclusive* $b\bar{b}$, same as the previous sample but requiring a $b\bar{b}$ pair to be produced.
- $b\bar{b} \to \mu^+\mu^-$, a selection of the inclusive $b\bar{b}$ sample with at least two muons in the final state, which are required to be inside the geometric LHCb acceptance.

A summary of the considered samples with the relative statistics and equivalent integrated luminosity is reported in Table 29. This table includes two different minimum bias samples: one of them contained information about the *Monte Carlo Truth* (MCT), *i.e.* about the particles which have been actually generated and simulated through the detector, while the second didn't. The reason for the need of two samples is that the MC Truth information requires a lot of storage space so that one of the minimum bias samples, in order to be able to have a large statistics, was recorded without storing this information.

5.2.2 *Preselection*

A first selection of the data samples was achieved through a pre-selection in order to reject part of the background and to deal with more manageable samples. This step correspond to the stripping procedure adopted currently with real data, but has different cut values for historical reasons.

Different variables were exploited; the cut values for each variable were chosen in order to have the largest efficiency for the signal while rejecting as much background as possible. In particular the following variables have been used, some of which have been already described, the cut values of which are summarised in Table 30:

- $\Delta\eta(D^0\pi)$, the difference in pseudo-rapidity between the D^0 and the π.
- $\Delta\phi(D^0\pi)$, the difference in the azimuthal angle ϕ between the D^0 and the π.
- $\Delta\eta(\mu\mu)$, the difference in pseudo-rapidity between the two muons.
- $\chi^2\text{IP}(\pi)$ and $\chi^2\text{IP}(D^0)$.
- $\mathrm{min}(\chi^2\text{IP}(\mu))$ and $\mathrm{max}(\chi^2\text{IP}(\mu))$.
- $p_T(D^0)$ and $p_T(\pi)$.
- Muons $\Delta\log\mathcal{L}(\mu,\pi)$ As explained in §2.5.3.4 a delta log-likelihood variable is built for particle identification purposes from the information of the various detectors. In order to identify the two muons and discard part of the mis-identification background we have applied a cut on the $\Delta\log\mathcal{L}(\mu,\pi)$ which compares the muon with the pion hypothesis.
- Pion $\Delta\log\mathcal{L}(e,\pi)$. In order to reduce the amount of $D^0\pi$ combinations we have required a loose cut on the identification of the pion with respect to the electron hypothesis.
- χ^2_{FD} of the D^0.
- Δm and D^0 mass. In order to polish the background sample from uninteresting events, preliminary mass window cuts were applied both to the D^0 mass and to the ΔM.

All of the variables presented in this list and the cuts summarised in Table 30 are applied to the signal as well as to all the background channels. For the $D^{*+} \to D^0(\to \pi^+\pi^-)\pi^+$ as a control channel the cuts referred to the muons have been applied to the two D^0 decay products pions with the exception of the muon identification variable, which has been applied separately in order to estimate $D^0 \to \pi^+\pi^-$ as as control and as a background channel.

Table 30.: Summary of the preselection cuts applied to the various samples for the MC analysis. Cuts are referred to the selection of $D^{*+} \to D^0(\to \mu^+\mu^-)\pi^+$. They have been applied equally to the $D^{*+} \to D^0(\to \pi^+\pi^-)\pi^+$ sample with the muon cuts applied to the pions, with the exception of the muon identification.

Variable	Cut value
$\Delta\eta(D^0\pi)$	< 0.2
$\Delta\phi(D^0\pi)$	< 0.2
$\Delta\eta(\mu\mu)$	< 1.3
$min(\chi^2\text{IP}(\mu))$ w.r.t PV	> 1
$max(\chi^2\text{IP}(\mu))$ w.r.t PV	> 10
$\chi^2\text{IP}(D^0)$ w.r.t PV	< 10
$\chi^2\text{IP}(\pi)$ w.r.t PV	< 10
$p_T(D^0)$	> 2 GeV
$p_T(\pi)$	> 0.15 GeV
χ^2_{FD} of the D^0	> 25
π: $\Delta \log \mathcal{L}(e, \pi)$	< 0
μ: $\Delta \log \mathcal{L}(\mu, \pi)$	> 0
$\Delta m(D^{*+} - D^0) - 145.5$	< 2.5
D^0 mass window	$\pm 30 MeV$

The results of the preselection as applied to the various Monte Carlo samples are reported in Table 31. The number of selected events and the equivalent efficiency is tabulated for each sample. We also list in this table the number of expected events in 100 pb^{-1} of integrated luminosity: this is the expected luminosity at the end of the first physics run of LHC and we consider this as a first step for the final result of this analysis.

Some of the background samples are very efficiently rejected by this preselection, hence in order to increase the statistics for these samples we have loosened the invariant mass window cut. This can be done since this samples are mostly source of combinatorial background so that their $\mu\mu$ invariant mass window distribution is flat and no correlation is expected (as a first approximation) with the rest of the preselection cuts. This method allowed us to compute the relevant numbers of Table 31 with more reliability. The samples for which it has been necessary to loosen the mass window are accompanied in this table by an $\mathcal{F}$ scale factor which takes into account the relative increase in statistics. In Table 31 some of the samples are analysed without requiring a muon-identification cut; this cut in fact would reject most events of these samples while here we want to understand their contribution to the combinatorial background.

We notice that after muon-identification cut has been applied the combinatorial background comes almost exclusively from the $b\bar{b} \to \mu^+\mu^-$ sample. In fact the inclusive $b\bar{b}$ sample is foreseen to have a contribution which is of the same order of the $b\bar{b} \to \mu^+\mu^-$ and this is a sub-sample (about 2% in cross-section) of the inclusive one. Also looking at minimum bias samples we notice that the number of inclusive minimum bias and events with two muons in the final state is pretty much the same after muon-ID cut.

Looking at the $D^{*+} \to D^0(\to \pi^+\pi^-)\pi^+$ sample we see that after applying the μ-ID cut still 86 events will be present, these events will be gaussian distributed in invariant mass and to statistical subtract them will be therefore necessary the mis-ID measurement already described.

In conclusion we confirm with these studies that two main backgrounds will be present for our signal channel: combinatorial background coming from $b\bar{b} \to \mu^+\mu^-$ events and mis-identification background from $D^0 \to \pi^+\pi^-$ decays.

Table 31.: Summary of the effect of the preselection on the various MC samples.

Sample	N_{sel}	ε_{tot}	$N_{sel}(100pb^{-1})$	$\mathcal{F}$	μ-ID cut
$D^{*+} \to D^0(\to \mu^+\mu^-)\pi^+$	5177	0.03	$1.8 \cdot 10^9 \times BR$		Yes
$D^{*+} \to D^0(\to \pi^+\pi^-)\pi^+$	4286	0.0086	$1.48 \cdot 10^6$		No
$D^{*+} \to D^0(\to \pi^+\pi^-)\pi^+$	8	$1.6 \cdot 10^{-6}$	86		Yes
$b\bar{b} \to \mu^+\mu^-$	542	$2.2 \cdot 10^{-5}$	1238	10	Yes
Inclusive $b\bar{b}$	32	$6 \cdot 10^{-7}$	1850	10	Yes
Minimum bias (MCT)	3	$3 \cdot 10^{-7}$	$1.14 \cdot 10^6$		No
Minimum bias (No MCT)	531	$5 \cdot 10^{-7}$	$2 \cdot 10^6$		No
Minimum bias (No MCT)	6	$6 \cdot 10^{-9}$	709	50	Yes
Minimum bias $\to \mu\mu$	127	$5.3 \cdot 10^{-6}$	707	10	Yes
Inclusive $c\bar{c}$	103	$1 \cdot 10^{-5}$	$2.6 \cdot 10^6$		No

5.2.3 *Multivariate methods*

The final analysis for these MC studies was done with multivariate methods, according to § 5.1.5.

The implementation, training and testing of the different multivariate methods was done exploiting the TMVA package [66, 67].

The variables used in the multivariate analysis were the following:

- Pointing angle.
- $\min(p_T(\mu))$
- $\Delta\phi(D^0, \pi)$
- $\Delta\eta(D^0, \pi)$
- $\chi^2 IP(D^0)$ w.r.t. PV
- $\min(\chi^2 IP(\mu))$ w.r.t. PV

We already described some of these variables previously; here we underline that even variables used in preselection, *i.e.* with already a cut applied on them, can be further exploited by multivariate selections. The distributions for the different variables are shown in Fig. 91, where background and signal samples are compared with common normalisation.

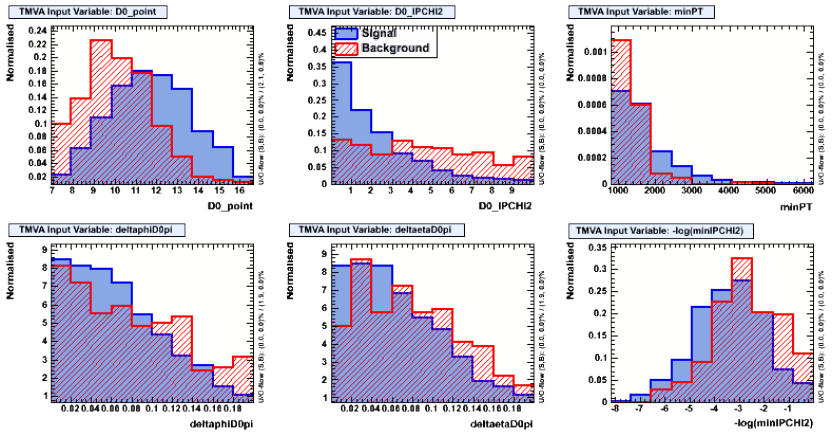

Figure 91.: Distribution of the variables used as input for the multivariate methods for $D^0 \to \mu^+\mu^-$ signal events and combinatorial background.

The MC signal and background samples were split into two halves in order to use independent samples for training and testing purposes.

The performances of the different methods were probed looking at the efficiency on the background as a function of the efficiency on the signal samples obtained by varying the cut on the considered method output variable. The results are shown in Fig 92, were in particular three different methods are compared: Likelihood, Fisher and Decision Trees (BDT).

The different methods were rated according to the final results, *i.e.* to the limit which could be set by the experiment, and the one with the best limit was chosen.

5.2.4 *Results*

Exploiting the method previously described we have computed the expected limit that, according to our studies on the MC simulations, the LHCb experiment will be able to set in 100 pb^{-1} of integrated luminosity. The resulted limit is:

$$\mathcal{BR}(D^0 \to \mu^+\mu^-) < 2.55 \cdot 10^{-8} \tag{5.11}$$

at 90% confidence level. Such a result would overcome the present results by about one order of magnitude. Some caveats must be underlined here; we remind that this analysis is performed considering a $\sqrt{s} = 10$ TeV center of mass energy, while LHC is currently running at $\sqrt{s} = 7$ TeV and the first 100 pb^{-1} of

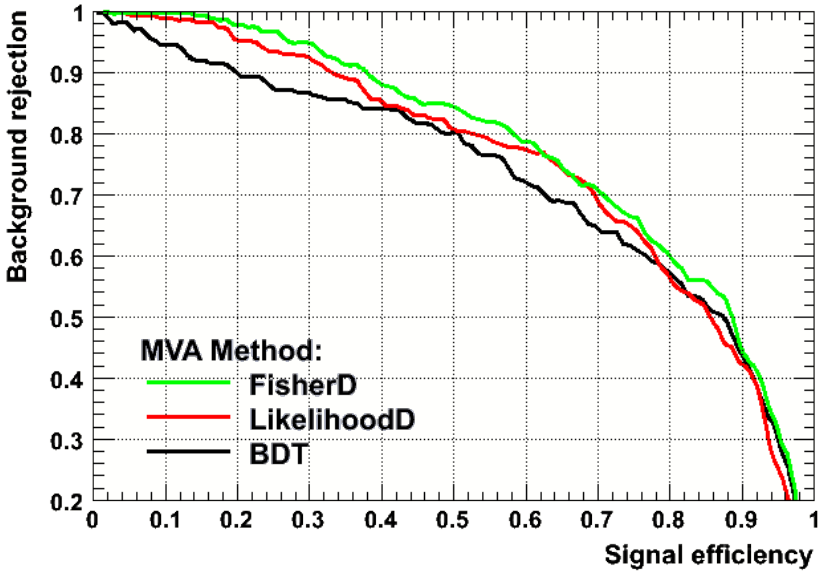

Figure 92.: Background efficiency as a function of signal efficiency for different multivariate methods for the selection of the $D^0 \to \mu^+\mu^-$ channel.

integrated will be collected certainly at this energy. At different energy in the centre of mass the total charm production cross-section is different and, according to PYTHIA predictions, would decrease from 6.3 at 10 TeV to about 4.6 ad 7 TeV. With a reduced cross-section the number of D^0 is clearly less by the same factor, however also the background is less so that the limit does not worsen by the same amount.

5.3 DATA ANALYSIS

As explained in the general analysis strategy, trigger and preselection (or stripping) are fundamental for this kind of search. HLT2 and stripping selections were developed, commissioned and used in 2010 data taking in order to acquire data for $D^0 \to \mu^+\mu^-$ and its control channels. In the following we describe the present status of the analysis on data events.

5.3.1 *Data and Monte Carlo samples*

Within the 2010 data taking, a total integrated luminosity of $\mathcal{L}_{Int} = 37.7\ pb^{-1}$ was recorded by the LHCb experiment in pp collisions at $\sqrt{s} = 7$ TeV. The data was acquired using the already described triggers and processed with the stripping selection algorithms; both included the lines we developed in order to select $D^0 \to \mu^+\mu^-$ and its control channels.

The analysis presented here do not include the whole acquired luminosity. In fact during the initial part of the data acquisition the trigger lines for $D^0 \to \mu^+\mu^-$ were not included yet. Moreover at the time of writing this work the stripping procedure is not completed for the whole data set. The data sample considered here corresponds therefore to an integrated luminosity of $\mathcal{L}_{Int} = 22\ pb^{-1}$.

In order to compare the properties of real data with simulations also different Monte Carlo samples were analysed with the same procedure. These samples reproduce pp collisions at the conditions of 2010 data taking. MC samples of signal and control channels has been considered.

Table 32.: Number of events as selected by the stripping algorithms for the different control channels of the $D^0 \to \mu^+\mu^-$ decay.

Channel	Events
$D^{*+} \to D^0(\to K^-\pi^+)\pi^+$	38189
$D^{*+} \to D^0(\to \pi^+\pi^-)\pi^+$	44719
$D^{*+} \to D^0(\to K^-\mu^+)\pi^+$	17485
$D^{*+} \to D^0(\to \pi^\pm\mu^\mp)\pi^+$	34067

5.3.2 *Efficiencies from MC simulations*

An important issue for this analysis is the comprehension of the reconstruction and selection efficiencies for the signal and control samples. These have been studied through Monte Carlo samples of pp collisions at $\sqrt{s} = 7$ TeV.

Here we present only the overall selection efficiencies for the $D^{*+} \to D^0(\to \mu^+\mu^-)\pi^+$ and $D^{*+} \to D^0(\to \pi^+\pi^-)\pi^+$ channels, which are:

$$\varepsilon(D^{*+} \to D^0(\to \mu^+\mu^-)\pi^+) = 0.0191 \pm 0.0004 \tag{5.12}$$

$$\varepsilon(D^{*+} \to D^0(\to \pi^+\pi^-)\pi^+) = 0.0025 \pm 0.0001 \tag{5.13}$$

respectively. Overall efficiencies comprehend trigger efficiency (both L0 and HLT2), reconstruction and selection (stripping) efficiencies. It can be seen that the two efficiencies are very different. This is mainly due to the difference in trigger which is the L0 Muon for the former and L0 Hadron for the latter.

Studies are ongoing in order to understand the trigger efficiencies directly from data events as well as from Monte Carlo simulations.

5.3.3 $D^0 \to \pi^+\pi^-$ *channel*

The $D^0 \to \pi^+\pi^-$ channel has been selected in the considered data samples by applying the stripping procedure both to data and MC. In Figure 93 we show the invariant mass distributions for the $D^{*+} \to D^0(\to \pi^+\pi^-)\pi^+$ channel as obtained in pp collision data. In particular we show the D^0 invariant ass in (a), the D^* invariant mass in (b) and the ΔM in (c).

In Figure 93 can be noticed a peak to the left of the D^0 nominal mass. It is due to $D^0 \to K^-\pi^+$ decays with the kaon misidentified as pion and could be safely removed by applying a cut on the $\Delta \log \mathcal{L}$ between the kaon an pion hypothesis.

The D^0 invariant mass is shown in Figure 94 (d) after requiring the Δm to be within 1.5 MeV/c^2 from the nominal value. The distribution is fitted with a gaussian to represent the signal plus a line to represent the background. By integrating the signal function we obtain a first estimate of the number of selected $\pi\pi$ events in real data, $N_{D^{*+} \to D^0(\to \pi^+\pi^-)\pi^+} = 2392 \pm 37$.

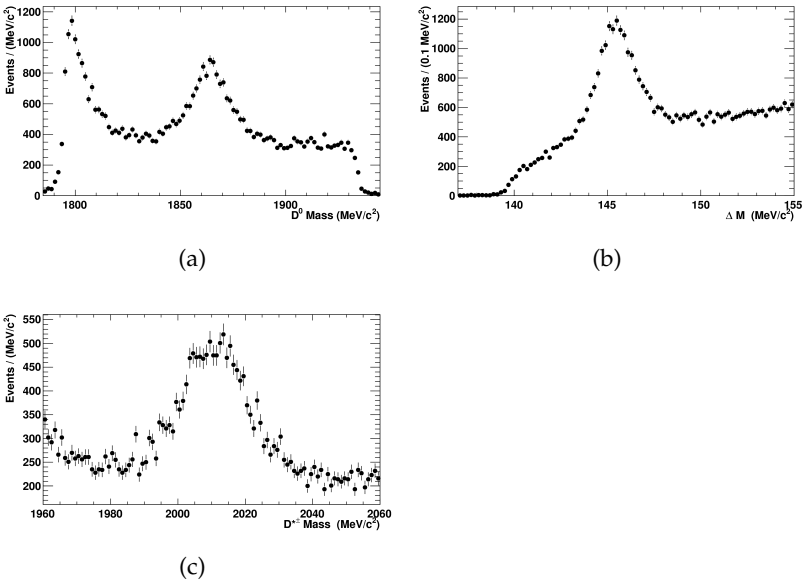

Figure 93.: Distribution of (a) the D^0 invariant mass, (b) the D^* invariant mass and (c) the ΔM for $D^{*+} \to D^0(\to \pi^+\pi^-)\pi^+$ events in data of pp collisions at $\sqrt{s} = 7$ TeV. Samples are considered after the stripping procedure without further selection.

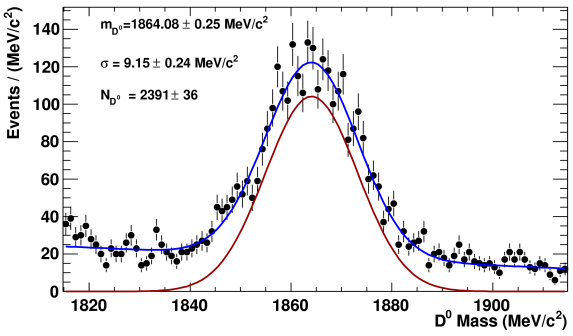

Figure 94.: Distribution of the D^0 invariant mass for $D^{*+} \to D^0(\to \pi^+\pi^-)\pi^+$ events in data of pp collisions at $\sqrt{s} = 7$ TeV after applying a further selection (see text).

We want to estimate if the number of selected $D^0 \to \pi^+\pi^-$ events in pp data is compatible with the expectations from MC events. This number can be obtained as

$$N^{exp}_{D^{*+}\to D^0(\to\pi^+\pi^-)\pi^+} = \mathcal{L}_{Int}\,\sigma(pp \to D^*)\,\mathcal{BR}_{D^*\to D^0}\mathcal{BR}_{D^0\to\pi\pi}\varepsilon \tag{5.14}$$

where ε is the overall efficiency and BR stands for the branching ratio of the two processes. The cross-section for the inclusive production of D^* in pp collisions at $\sqrt{s} = 7$ TeV has been recently measured by the LHCb experiment and is [75]:

$$\sigma_{LHCb}(pp \to D^*) = 676 \pm 137\mu b \quad . \tag{5.15}$$

The number of expected $D^{*+} \to D^0(\to \pi^+\pi^-)\pi^+$ events is then: 3170 ± 660. This number is of the same order of the selected combinations in real data even if not completely compatible. Apart from differences between efficiency in data and in MC, this can be due to the uncertainty in the considered luminosity and trigger efficiencies which are under study.

From the selected data sample we can also study the properties of the selected D^0 decays. This help us to understand the $D^0 \to \mu^+\mu^-$ channel which must be kinematically coincident apart from the pion muon mass difference. In Figure 95 we show the distribution for the momentum (a), the transverse momentum (b) and the rapidity (c) of the D^0 particle as obtained from data and compared with the analogous distribution obtained in MC. The distributions are obtained by statistically removing the background by means of sideband subtraction and are not efficiency corrected.

As can be seen, the Monte Carlo reproduces quite well the distributions of the data. However a certain difference in the p_T distribution can be seen in the lower part of the spectrum and can be due to incorrect simulations of the hardware trigger in MC simulations. In Figure 96 the distributions for the momentum (a) and p_T (b) for the pions from $D^0 \to \pi^+\pi^-$ decay are shown and compared to the MC simulations. While the momentum distribution for data is consistent with MC, the transverse momentum is significantly peaked at higher values, due probably to a propagation of the difference in D^0 p_T spectrum. In the (c) part of same figure we also show the impact parameter distribution for the pion.

These differences between MC and data have to be considered as systematic uncertainties on the efficiency estimation from MC.

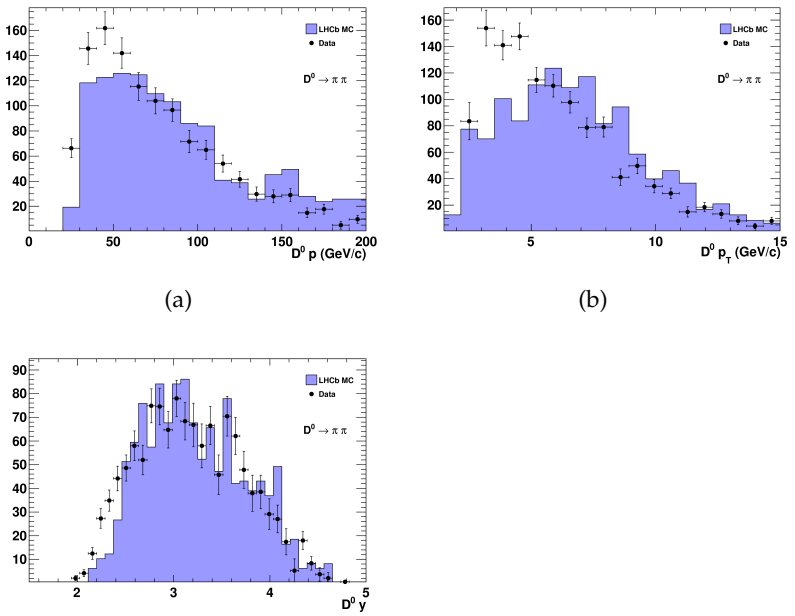

(a) (b)

(c)

Figure 95.: Distributions of D^0 properties as obtained from $D^{*+} \to D^0(\to \pi^+\pi^-)\pi^+$ events in pp collisions at $\sqrt{s} = 7$ TeV. Distributions are not efficiency corrected and are compared with MC simulations of the same channel.

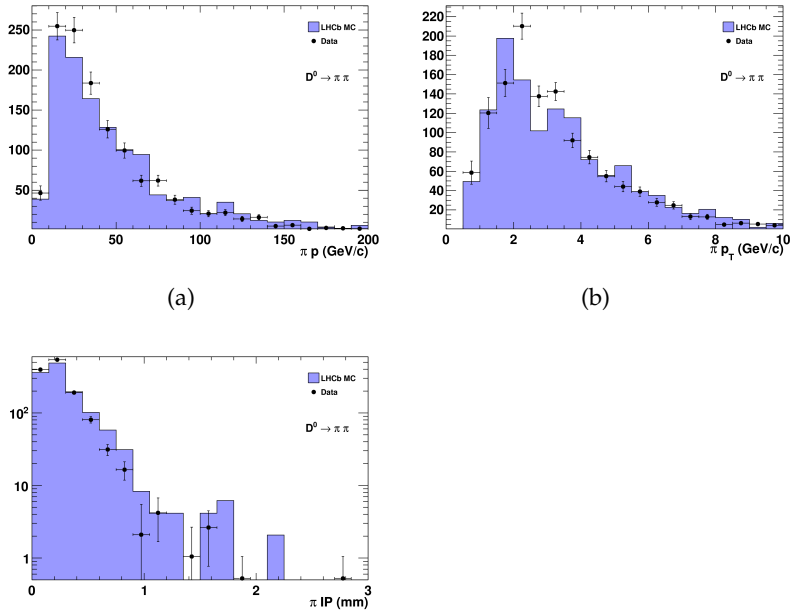

(a) (b)

(c)

Figure 96.: Distributions of π properties as obtained from $D^{*+} \to D^0(\to \pi^+\pi^-)\pi^+$ events in pp collisions at $\sqrt{s} = 7$ TeV. Distributions are not efficiency corrected and are compared with MC simulations of the same channel.

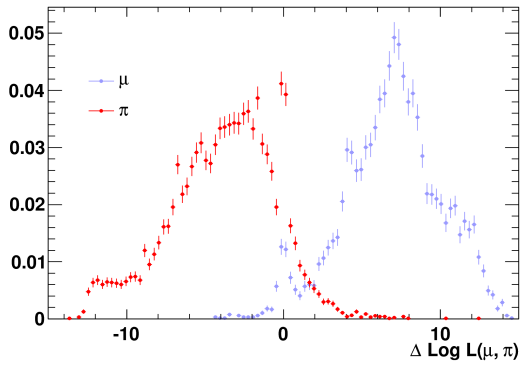

Figure 97.: Distribution of the $\Delta \log \mathcal{L}(\mu, \pi)$ for Monte Carlo particles: muons and pions are from $D^0 \to \mu^+\mu^-$ and $D^0 \to \pi^+\pi^-$ decays respectively.

5.3.4 *Muon identification*

The muon identification is based mainly on information from the Muon chambers, but exploits also information from the other detectors (*e.g.* a MIP signal in the calorimeter and the RICH information). A $\Delta \log \mathcal{L}$ function is built upon this information and can be used to discriminate muons from other particles, mainly pions and kaons. We studied the muon identification using MC simulations of the signal $D^0 \to \mu^+\mu^-$ channel and of the $D^0 \to \pi^+\pi^-$ control channel as a source of muons and pions respectively. Both have been processed with the already described procedure (obviously without applying any identification variable). The distribution of $\Delta \log \mathcal{L}(\mu, \pi)$ for the two samples is shown in Fig. 97 where it can be seen that a long tail of pions is present in the muon region. A sensible part of this contamination is due to the irreducible contribution of pion decays in flight which are clearly identified as muons by the muon chambers.

Apart from the $\Delta \log \mathcal{L}$ we have to consider the IsMuon variable which is used also in the online framework for its simplicity. It is built by extrapolating a track reconstructed in the tracking system to the MUON chambers. There hits are searched around the extrapolation within a defined Field Of Interest. If requirements which depends on the muon momentum and on the considered Muon station are satisfied the boolean value of IsMuon is set to true. This simple variable is specially useful in the online approach where a fast decision must be given, however contains clearly less information than the PID $\Delta \log \mathcal{L}$.

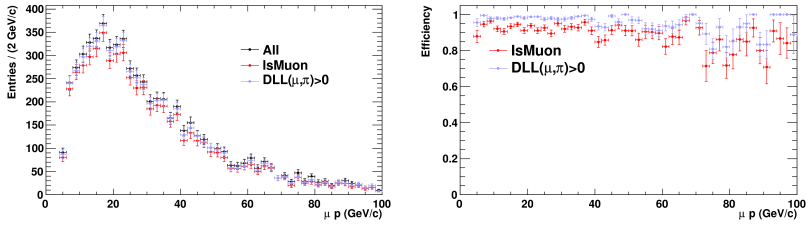

(a) (b)

Figure 98.: Distribution of (a) the muon momentum for Monte Carlo $D^0 \to \mu^+\mu^-$ events for all muons, muons with $\Delta \log \mathcal{L}(\mu, \pi) > 0$, muons with IsMuon true and with both requirements applied. In (b) the efficiencies as a function of the muon momentum for the mentioned variables are shown.

Table 33.: Muon identification efficiencies and pion mis-identification probabilities as obtained from MC studies for different identification requirements. The values are integrated over the full momentum spectrum and the errors are only statistical.

Cut	ε_μ	$\varepsilon_{\pi\to\mu}$
IsMuon	0.914 ± 0.004	0.006 ± 0.001
$\Delta \log \mathcal{L}(\mu, \pi) > 0$	0.971 ± 0.002	0.113 ± 0.003
$\Delta \log \mathcal{L}(\mu, \pi) > 0$ and IsMuon	0.909 ± 0.004	0.004 ± 0.001

In Figure 98 (a) we show the distribution of the momentum of muons from MC simulations of $D^0 \to \mu^+\mu^-$ decays after the stripping preselection. The distribution for all muons, muons with $\Delta \log \mathcal{L}(\mu, \pi) > 0$, muons with IsMuon true and with both cuts applied are shown. Through these distributions we calculated the efficiencies for the muon identification by means of the mentioned variables; the efficiencies as a function of the muon momentum are shown in Figure 98 (b). The integrated efficiency computed from these distributions are summarised in Table 33 where the errors are only statistical.

The distribution of pions from MC $D^0 \to \pi^+\pi^-$ decays is shown in Figure 99 (a) as a function of the momentum for all the pions, for pions with $\Delta \log \mathcal{L}(\mu, \pi) > 0$, pions with IsMuon true and with both requirements applied. Analogously we can calculate the efficiency for this identification variables applied to

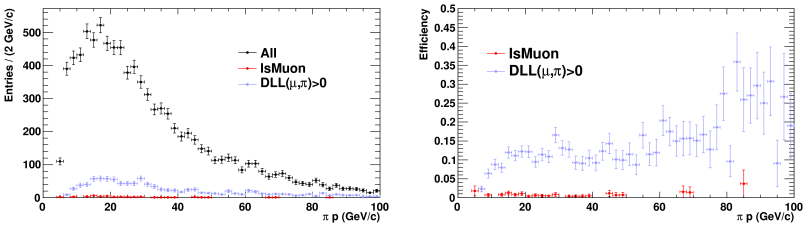

(a) (b)

Figure 99.: Distribution of (a) the muon momentum for Monte Carlo $D^0 \to \pi^+\pi^-$ events for all pions, pions with $\Delta \log \mathcal{L}(\mu, \pi) > 0$, pions with IsMuon true and with both requirements applied. In (b) the efficiencies as a function of the pion momentum for the mentioned variables are shown.

pions (*i.e.* mis-identification probabilities) and the results is shown in Fig. 99 (b) as a function of the pion momentum. The integrated misidentification probability for pions with the mentioned cuts are summarised in Table 33 where the errors are only statistical.

As previously stated we want to measure the misidentification probability directly in real data. We therefore consider the $D^0 \to K^-\mu^+$ and $D^0 \to \pi^\pm\mu^\mp$ channels as coming from misidentification of $D^0 \to K^-\pi^+$ and $D^0 \to \pi^+\pi^-$ respectively. We selected these channels with the mentioned trigger and stripping lines. In order to estimate the number of $D^0 \to K\pi, \pi\pi, K\mu, \pi\mu$ events, additionally we applied a cut on the Δm requiring it to be less than 1.5 MeV/c^2 distant from the nominal value. The resulting invariant mass distributions for the $D^0 \to K^-\mu^+$ and $D^0 \to \pi^\pm\mu^\mp$ decays are shown in Fig. 100 (a) and (c). A clear peak is visible in the $D^0 \to K^-\mu^+$ case while the $D^0 \to \pi^\pm\mu^\mp$ distribution is less clean. The peak position is shifted with respect to the nominal D^0 mass; this shift can be recovered by assigning to the muon of the two decays the correct pion mass: the results of this correction are shown in Fig. 100 (b) and (d), where it can be noticed that a cleaner peak is present also in the $D^0 \to \pi^\pm\mu^\mp$ case. These last distributions have been fit with a gaussian distribution plus a line to represent the signal and combinatorial background components respectively. By integrating the signal function we obtain the number of detected events for the two channels.

The integrated number of signal events, after being corrected for the prescales applied in the HLT2 (cf.Table 26) can be used, to-

Table 34.: Mis-identification probabilities as measured from $D^0 \to K^-\mu^+$ and $D^0 \to \pi^\pm\mu^\mp$ events. Values obtained applying the IsMuon requirement and adding the $\Delta \log \mathcal{L}(\mu, \pi) > 0$ cut are shown. Double mis-identification and number of expected misidentified $D^0 \to \pi^+\pi^-$ events in the considered sample are also listed.

	IsMuon	IsMuon and $\Delta \log \mathcal{L}(\mu, \pi) > 0$
$p(\pi \to \mu)_{D^0 \to K\mu}$	0.00554 ± 0.00009	0.00293 ± 0.00007
$p(\pi \to \mu)_{D^0 \to \pi\mu}$	0.00556 ± 0.00048	0.00282 ± 0.00034
$p(\pi\pi \to \mu\mu)$	$(3.1 \pm 0.1) \cdot 10^{-5}$	$(8.6 \pm 0.4) \cdot 10^{-6}$
$N_{D^0 \to \pi^+\pi^- \to \mu\mu}$	5.6 ± 0.2	1.56 ± 0.08

gether with the corresponding numbers for the $D^0 \to K^-\pi^+$ and $D^0 \to \pi^+\pi^-$ channels, in order to compute the mis-identification probability for a pion into a muon. The results of this procedure are shown in Table 34 for the IsMuon requirement and adding the $\Delta \log \mathcal{L}(\mu, \pi) > 0$ cut. The values for the $\Delta \log \mathcal{L}$ cut alone are not available since within the HLT2 and stripping procedure, in order to reduce the background, the IsMuon cut was already applied. The shown errors are only statistical. Agreement with the predicted values from MC simulations is present even if the errors on the latter are large.

Here we want to underline that even if MC agreement wasn't present the importance of these measurement is to have a direct estimate of the mis-identification contribution to the background in the $D^0 \to \mu^+\mu^-$ channel, using directly data information rather than MC.

With the hypothesis that the double mis-id probability is simply the square of the single one we can estimate the number of expected misidentified events in the considered integrated luminosity. These numbers are shown in Table 34. The expected number of mis-identified $D^0 \to \pi^+\pi^-$ events is 5.6 with IsMuon and 1.56 if also the $\Delta \log \mathcal{L}$ cut is applied, therefore being small if compared to the combinatorial background.

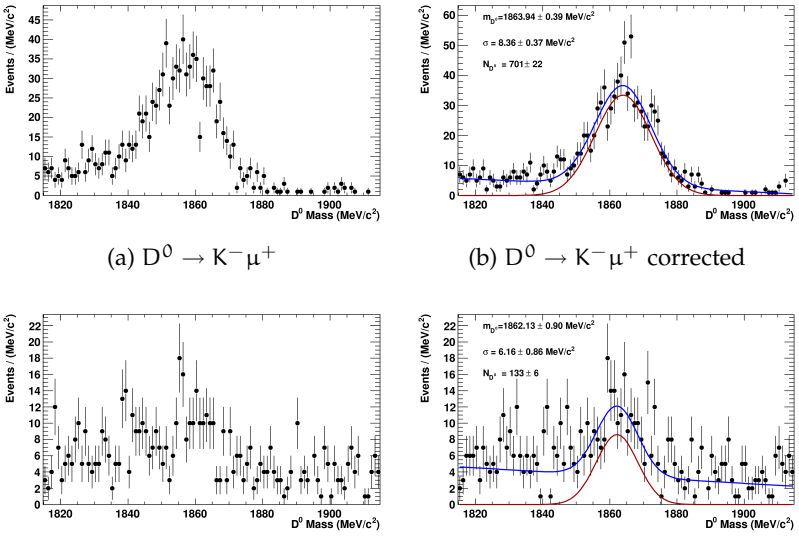

(a) $D^0 \to K^-\mu^+$ (b) $D^0 \to K^-\mu^+$ corrected

(c) $D^0 \to \pi^\pm\mu^\mp$ (d) $D^0 \to \pi^\pm\mu^\mp$ corrected

Figure 100.: Distribution of the invariant mass for $D^0 \to K^-\mu^+$ combinations (a) before and (b) after the correction restoring the pion mass. Figures (c) and (d) show the analogous distributions for $D^0 \to \pi^\pm\mu^\mp$ combinations. The samples are selected considering the IsMuon true requirement.

5.3.5 *Combinatorial background*

In order to study the properties of the combinatorial background directly in pp collision data, we have selected $D^{*+} \to D^0(\to \mu^+\mu^-)\pi^+$ combinations following the already outlined procedure. The signal region of the D^0 invariant mass, [1840, 1885] MeV/c^2, has been blinded for this study and will be opened only when the analysis will be complete and confidently ready for the final results.

The invariant mass distributions for the selected $D^{*+} \to D^0(\to \mu^+\mu^-)\pi^+$ combinations are shown in Fig. 101. The D^0 invariant mass (a), the Δm (b), and their bidimensional plot (c) are shown.

In order to estimate the number of residual background events in the signal region of the D^0 invariant mass we have applied a cut on the Δm, required to be within 1.5 MeV from the nominal value. The D^0 invariant mass distribution of this selected sample is shown in Fig. 101 (d) and has been fitted with a line. The integrated number of background events within 20 MeV from the D^0 nominal value is:

$$N_{bkg} = 97 \pm 10 \quad . \tag{5.16}$$

Assuming no further selection, we can compute the sensitivity for the $D^0 \to \mu^+\mu^-$ branching ratio as limited by the number of background events as:

$$\begin{aligned} \mathcal{BR}(D^0 \to \mu^+\mu^-) &< \frac{1.28\sqrt{N_{bkg}}}{\mathcal{L}_{Int}\, \varepsilon\, \sigma(pp \to D^*)\mathcal{BR}(D^* \to D^0)} \\ &= 6.6 \cdot 10^{-8} \end{aligned}$$

This estimate is not precise and is meant just to give the order of magnitude of the expected limit. It doesn't consider the studies which are still ongoing on some aspects of the present analysis and is referred only to the considered luminosity.

Moreover this background is still reducible by the use of multivariate methods as we have anticipated in the MC studies. In Figure 102 we show some of the variables which could be used in a multi-dimensional analysis. As it can be seen some rejection power is present in various variables.

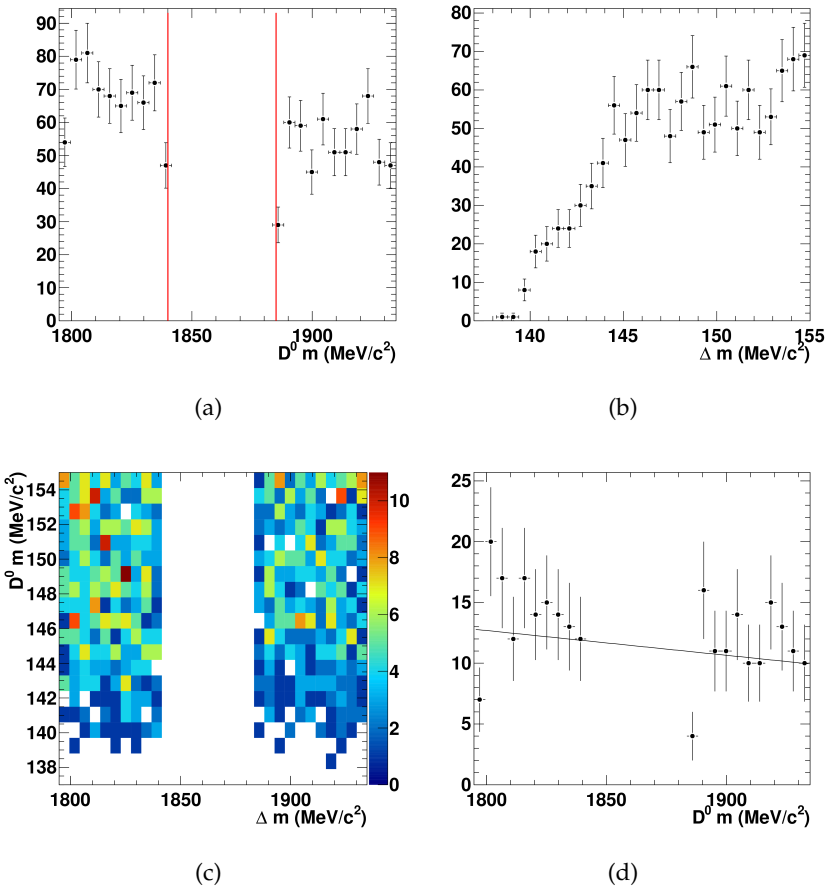

Figure 101.: Distribution of the invariant masses for $D^{*+} \to D^0(\to \mu^+\mu^-)\pi^+$ combinations in pp collisions at 7 TeV. D^0 invariant mass (a), ΔM and their correlation (c) are shown. Distributions are after the stripping preselection where the signal region of the D^0 invariant mass has been blinded.

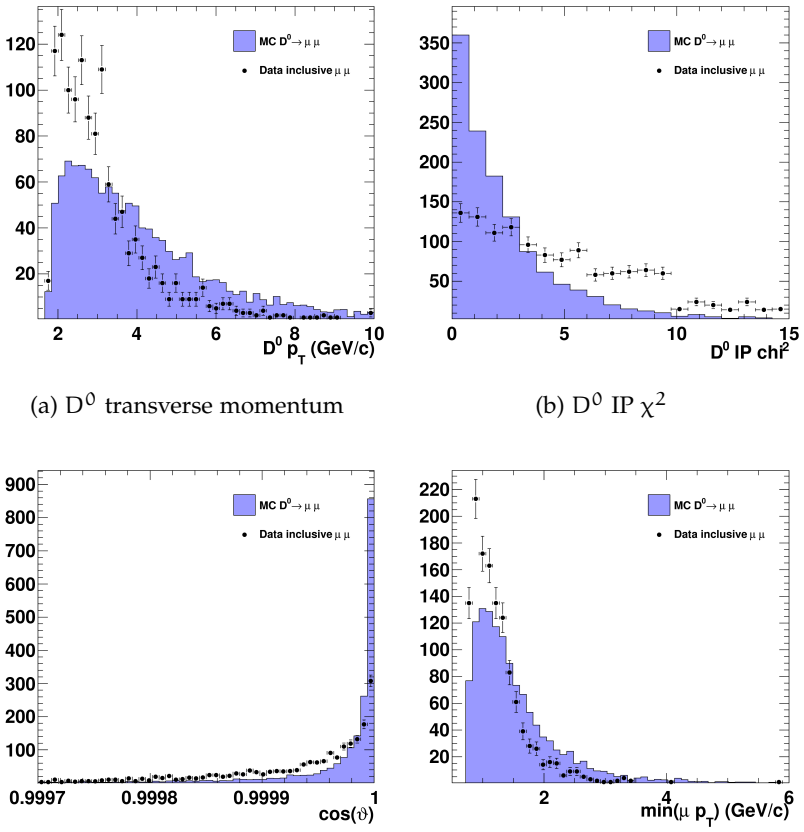

(a) D^0 transverse momentum

(b) D^0 IP χ^2

(c) D^0 pointing angle

(d) Minimum transverse momentum of the two muons

Figure 102.: Distributions of different variables which can be used in a multivariate analysis to reduce the background for the $D^0 \to \mu^+\mu^-$ search. Black points are combinatorial background events as taken from the D^0 invariant mass sidebands in pp collision data at $\sqrt{s} = 7$ TeV. Blue histogram is composed of MC simulated signal events.

5.4 FINAL REMARKS ON $D^0 \to \mu^+\mu^-$ ANALYSIS

We have presented a first analysis of the possibilities for the search of the rare decay $D^0 \to \mu^+\mu^-$ in LHCb and developed a full analysis strategy presented here as a work in progress.

Monte Carlo studies show that very good sensitivities can be reached by looking for the tagged $D^{*+} \to D^0(\to \mu^+\mu^-)\pi^+$ decay and exploiting the power of multivariate techniques for the final analysis. These studies must be repeated for the changed data taking conditions but we do not expect sensible worsening of the performances, besides the lost of statistics due to the lower production cross-section.

On the other side, studies have been started on real data pp collisions at $\sqrt{s} = 7$ TeV. Preliminary studies on the $D^{*+} \to D^0(\to \pi^+\pi^-)\pi^+$ decay show fare agreement with MC predictions as far as the kinematic properties of the final state are concerned. Muon-identification has been studied directly on real data and gives a double mis-identification probability of order 10^{-5} which yields to negligible mis-identification contribution on the final selected $D^0 \to \mu^+\mu^-$ events in the considered luminosity. Moreover the method has shown to be able to predict the mis-identification contribution in a sensitive way so that it will be exploited in order to subtract this background when the statistics will require it.

Even if the analysis is in progress and no final sensitivity can be quoted yet, preliminary studies on the combinatorial background show that it is at the level of 100 events in the signal region for the considered luminosity and is further reducible by exploiting multivariate techniques.

More studies are in progress in order to determine the efficiency ratios between the $D^0 \to \mu^+\mu^-$ and its control channel, $D^0 \to \pi^+\pi^-$, and the full 2010 statistics is yet to be analysed.

With these caveat in mind however, these studies allow us to foresee, in case of no signal observation, an expected limit on the $D^0 \to \mu^+\mu^-$ branching ratio of the order of 10^{-7} which would be already compatible or better than the current best value provided by the Belle experiment.

CONCLUSIONS

Proton-proton collisions at energies in the centre of mass of $\sqrt{s} = 0.9$ TeV and 7 TeV have been studied in this work within the LHCb experiment. This energy range, the TeV scale, is still to be studied in detail with proton collisions.

As a first step, we have studied the production of strange hadrons in these reactions at both the considered energies. The production ratio of $\bar{\Lambda}$ over Λ has been measured as a function of transverse momentum and rapidity of the considered hadrons. The results show that the $\bar{\Lambda}/\Lambda$ ratio decreases as function of rapidity and is independent of transverse momentum. The ratio increases as a function of the difference in rapidity between the baryons and the incoming proton beam showing that the suppression of anti-baryons is less important as the central part of the collision is gradually reached. Considering this ratio a measurement of the transport of the baryon number information from the initial to the final state of the $pp \to \Lambda(\bar{\Lambda})X$ reaction, the measurement of this observable leads to a comprehension of the mechanisms of quark production and hadronisation. The comparison with Monte Carlo simulations shows that the phenomenological models on which they are based, tuned on LEP and Tevatron data, are not able to reproduce the values of the $\bar{\Lambda}/\Lambda$ ratio in pp collisions at LHC.

The study of hadronisation in pp collisions has been done considering the $\bar{\Lambda}/K^0_S$ production ratio. The measurements performed at $\sqrt{s} = 0.9$ TeV and 7 TeV show that the suppression of the hadronisation into baryons with respect to mesons is almost independent of the rapidity while is a strong function of the transverse momentum. If we interpret this transverse momentum as composed mainly by the one of the produced strange quark, this suggests that the baryon suppression in hadronisation is less effective when a larger energy is available. This is predicted by the considered phenomenological models as a simple phase space effect which is smaller for the production of a diquark than for a quark, for simple kinematic reasons. However the comparison with MC simulations based on these models shows that agreement with data is not perfect, indicating that at LHC energies there is a possible discrimination for models which agree in other

energy ranges or different initial states.

The Λ and $\bar{\Lambda}$ produced at $\sqrt{s} = 0.9$ TeV have been also exploited in order to measure their polarisation which have been studied as a function of the baryon transverse momentum and Feynman's x, and integrated over the whole sample. No significant polarisation has been found, the measurement being limited by the small statistics of the sample. However a measurement in the most sensitive region with $p_T > 1$ GeV/c and $x_F > 0.02$ has shown a 2σ polarisation in the Λ sample, with a value $P = -0.104 \pm 0.044$, while no polarisation has been found for the anti-baryon. This result encourage us to deepen this study with a more efficient selection, including *downstream* tracks, presently discarded, in order to confirm this preliminary value by reducing the statistical error. This measurement will help the comprehension of spin effects in this high energy regime where such phenomena have not yet been measured.

The $D^0 \to \mu^+\mu^-$ decay has been studied as a promising process for the search of new physics phenomena. Studies performed with Monte Carlo simulations of pp collisions at $\sqrt{s} = 10$ TeV have shown that already with an integrated luminosity of 100 pb^{-1} upper limits on the $D^0 \to \mu^+\mu^-$ branching ratio can be put up to a level of order 10^{-7} or below. Moreover preliminary studies on real pp collisions data at $\sqrt{s} = 7$ TeV have shown that this limit is realistically reachable also at lower energy having under control the mis-identification and combinatorial background. This level of exclusion would be already lower than the present best limit. The possibility to measure the Standard Model branching ratio is clearly out of reach but a wide range of new physics scenarios can be possibly discovered or constraint through this measurement.

From these different measurements some common conclusions can be drawn. Proton-proton collisions at the TeV regime are a fundamental tool of discovery for new processes in particle physics. The high energies and luminosities reached at LHC will help in understanding the physics beyond the Standard Model. However the study of pp collisions shows that also very well known processes, as strange hadron production and polarisation, can shed new light on the fundamental laws in particle interactions.

Part III

APPENDIX

A

V^0 PRODUCTION RATIOS TABLES

We list in this Appendix some tables belonging to the V^0 ratios analysis. They are not essential for the comprehension of the analysis and are reported here for reference in order to make the reading of the analysis chapter more fluid.

Table 35.: Number of selected $\bar{\Lambda}$ in y and p_T bins, for field down events at $\sqrt{s} = 0.9$ TeV.

	$2.0 < y < 2.5$	$2.5 < y < 3.0$	$3.0 < y < 3.5$	$3.5 < y < 4.0$	$2.0 < y < 4.0$
$250 < p_T < 500$	2.20 ± 1.48	328.20 ± 18.12	181.40 ± 13.47	4.80 ± 2.19	516.60 ± 22.73
$500 < p_T < 650$	16.40 ± 4.05	288.40 ± 16.98	269.00 ± 16.40	20.60 ± 4.54	594.40 ± 24.38
$650 < p_T < 800$	20.60 ± 4.54	256.00 ± 16.00	349.20 ± 18.69	90.40 ± 9.51	716.20 ± 26.76
$800 < p_T < 1000$	34.20 ± 5.85	216.20 ± 14.70	428.60 ± 20.70	119.60 ± 10.94	798.60 ± 28.26
$1000 < p_T < 1200$	40.20 ± 6.34	135.00 ± 11.62	289.80 ± 17.02	80.40 ± 8.97	545.40 ± 23.35
$1200 < p_T < 2500$	128.40 ± 11.33	214.60 ± 14.65	408.00 ± 20.20	139.40 ± 11.81	890.40 ± 29.84
p_T integrated	242.00 ± 15.56	1438.40 ± 37.93	1926.00 ± 43.89	455.20 ± 21.34	

Table 36.: Number of selected Λ in y and p_T bins, for field down events at $\sqrt{s} = 0.9$ TeV.

	$2.0 < y < 2.5$	$2.5 < y < 3.0$	$3.0 < y < 3.5$	$3.5 < y < 4.0$	$2.0 < y < 4.0$
$250 < p_T < 500$	3.00 ± 1.73	298.40 ± 17.27	157.80 ± 12.56	2.40 ± 1.55	461.60 ± 21.48
$500 < p_T < 650$	10.80 ± 3.29	347.80 ± 18.65	368.20 ± 19.19	26.00 ± 5.10	752.80 ± 27.44
$650 < p_T < 800$	31.00 ± 5.57	325.20 ± 18.03	486.40 ± 22.05	78.00 ± 8.83	920.60 ± 30.34
$800 < p_T < 1000$	66.20 ± 8.14	293.20 ± 17.12	557.40 ± 23.61	149.00 ± 12.21	1065.80 ± 32.65
$1000 < p_T < 1200$	41.80 ± 6.47	170.60 ± 13.06	468.00 ± 21.63	189.80 ± 13.78	870.20 ± 29.50
$1200 < p_T < 2500$	138.80 ± 11.78	289.60 ± 17.02	582.00 ± 24.12	276.60 ± 16.63	1287.00 ± 35.87
p_T integrated	291.60 ± 17.08	1724.80 ± 41.53	2619.80 ± 51.18	721.80 ± 26.87	

Table 37.: Number of selected K^0_S in y and p_T bins, for field down events at $\sqrt{s} = 0.9$ TeV.

	$2.0 < y < 2.5$	$2.5 < y < 3.0$	$3.0 < y < 3.5$	$3.5 < y < 4.0$	$2.0 < y < 4.0$
$250 < p_T < 500$	152.50 ± 12.35	2254.50 ± 47.48	6146.25 ± 78.40	2960.50 ± 54.41	11513.75 ± 107.30
$500 < p_T < 650$	242.00 ± 15.56	1791.00 ± 42.32	3564.50 ± 59.70	2388.50 ± 48.87	7986.00 ± 89.36
$650 < p_T < 800$	296.75 ± 17.23	1740.50 ± 41.72	2674.00 ± 51.71	1896.50 ± 43.55	6607.75 ± 81.29
$800 < p_T < 1000$	426.75 ± 20.66	1733.50 ± 41.64	2310.75 ± 48.07	1820.25 ± 42.66	6291.25 ± 79.32
$1000 < p_T < 1200$	366.25 ± 19.14	1077.50 ± 32.83	1364.00 ± 36.93	1085.75 ± 32.95	3893.50 ± 62.40
$1200 < p_T < 2500$	700.25 ± 26.46	1587.25 ± 39.84	1868.25 ± 43.22	1314.00 ± 36.25	5469.75 ± 73.96
p_T integrated	2184.50 ± 46.74	10184.25 ± 100.92	17927.75 ± 133.89	11465.50 ± 107.08	

Table 38.: Number of selected $\bar{\Lambda}$ in y and p_T bins, for field up events at $\sqrt{s} = 0.9$ TeV.

	$2.0 < y < 2.5$	$2.5 < y < 3.0$	$3.0 < y < 3.5$	$3.5 < y < 4.0$	$2.0 < y < 4.0$
$250 < p_T < 500$	1.20 ± 1.10	227.40 ± 15.08	130.20 ± 11.41	-	358.80 ± 18.94
$500 < p_T < 650$	8.40 ± 2.90	227.40 ± 15.08	265.20 ± 16.28	26.20 ± 5.12	527.20 ± 22.96
$650 < p_T < 800$	21.00 ± 4.58	220.20 ± 14.84	305.40 ± 17.48	54.00 ± 7.35	600.60 ± 24.51
$800 < p_T < 1000$	48.60 ± 6.97	206.20 ± 14.36	346.00 ± 18.60	103.60 ± 10.18	704.40 ± 26.54
$1000 < p_T < 1200$	29.20 ± 5.40	119.80 ± 10.95	262.20 ± 16.19	80.40 ± 8.97	491.60 ± 22.17
$1200 < p_T < 2500$	88.00 ± 9.38	182.00 ± 13.49	350.80 ± 18.73	126.40 ± 11.24	747.20 ± 27.33
p_T integrated	196.40 ± 14.01	1183.00 ± 34.39	1659.80 ± 40.74	390.60 ± 19.76	

Table 39.: Number of selected Λ in y and p_T bins, for field up events at $\sqrt{s} = 0.9$ TeV.

	$2.0 < y < 2.5$	$2.5 < y < 3.0$	$3.0 < y < 3.5$	$3.5 < y < 4.0$	$2.0 < y < 4.0$
$250 < p_T < 500$	2.20 ± 1.48	239.80 ± 15.49	173.00 ± 13.15	1.20 ± 1.10	416.20 ± 20.40
$500 < p_T < 650$	5.80 ± 2.41	295.40 ± 17.19	368.00 ± 19.18	24.20 ± 4.92	693.40 ± 26.33
$650 < p_T < 800$	27.00 ± 5.20	323.80 ± 17.99	442.60 ± 21.04	65.60 ± 8.10	859.00 ± 29.31
$800 < p_T < 1000$	35.40 ± 5.95	286.40 ± 16.92	526.20 ± 22.94	178.40 ± 13.36	1026.40 ± 32.04
$1000 < p_T < 1200$	46.20 ± 6.80	161.40 ± 12.70	383.40 ± 19.58	140.40 ± 11.85	731.40 ± 27.04
$1200 < p_T < 2500$	121.00 ± 11.00	234.60 ± 15.32	508.80 ± 22.56	236.00 ± 15.36	1100.40 ± 33.17
p_T integrated	237.60 ± 15.41	1541.40 ± 39.26	2402.00 ± 49.01	645.80 ± 25.41	

Table 40.: Number of selected K^0_S in y and p_T bins, for field up events at $\sqrt{s} = 0.9$ TeV.

	$2.0 < y < 2.5$	$2.5 < y < 3.0$	$3.0 < y < 3.5$	$3.5 < y < 4.0$	$2.0 < y < 4.0$
$250 < p_T < 500$	136.75 ± 11.69	2079.00 ± 45.60	5464.25 ± 73.92	2666.75 ± 51.64	10346.75 ± 101.72
$500 < p_T < 650$	206.00 ± 14.35	1516.00 ± 38.94	3200.00 ± 56.57	2142.50 ± 46.29	7064.50 ± 84.05
$650 < p_T < 800$	258.00 ± 16.06	1591.50 ± 39.89	2402.25 ± 49.01	1745.50 ± 41.78	5997.25 ± 77.44
$800 < p_T < 1000$	367.00 ± 19.16	1530.75 ± 39.12	2136.00 ± 46.22	1537.50 ± 39.21	5571.25 ± 74.64
$1000 < p_T < 1200$	315.75 ± 17.77	1004.50 ± 31.69	1278.75 ± 35.76	915.25 ± 30.25	3514.25 ± 59.28
$1200 < p_T < 2500$	613.00 ± 24.76	1438.50 ± 37.93	1663.25 ± 40.78	1133.50 ± 33.67	4848.25 ± 69.63
p_T integrated	1896.50 ± 43.55	9160.25 ± 95.71	16144.50 ± 127.06	10141.00 ± 100.70	

Table 41.: Number of selected $\bar{\Lambda}$ in y and p_T bins, for field down events at $\sqrt{s} = 7$ TeV.

	$2.0 < y < 2.5$	$2.5 < y < 3.0$	$3.0 < y < 3.5$	$3.5 < y < 4.0$	$4.0 < y < 4.5$	$2.0 < y < 4.5$
$150 < p_T < 250$	-	673.00 ± 25.94	1226.40 ± 35.02	50.40 ± 7.10	14.40 ± 3.79	1964.20 ± 44.32
$250 < p_T < 500$	-	5550.00 ± 74.50	9153.80 ± 95.68	3738.80 ± 61.15	110.80 ± 10.53	18553.40 ± 136.21
$500 < p_T < 650$	46.60 ± 6.83	4544.60 ± 67.41	7917.20 ± 88.98	4239.00 ± 65.11	748.20 ± 27.35	17495.60 ± 132.27
$650 < p_T < 800$	290.80 ± 17.05	3879.20 ± 62.28	8582.60 ± 92.64	4458.40 ± 66.77	1193.20 ± 34.54	18404.20 ± 135.66
$800 < p_T < 1000$	769.60 ± 27.74	4201.60 ± 64.82	9933.20 ± 99.67	5675.60 ± 75.34	1690.80 ± 41.12	22270.80 ± 149.23
$1000 < p_T < 1200$	954.40 ± 30.89	3417.80 ± 58.46	6937.20 ± 83.29	4929.00 ± 70.21	1337.60 ± 36.57	17576.00 ± 132.57
$1200 < p_T < 2500$	3325.60 ± 57.67	8435.20 ± 91.84	11448.20 ± 107.00	10106.00 ± 100.53	2467.80 ± 49.68	35782.80 ± 189.16
p_T integrated	5387.00 ± 73.40	30701.40 ± 175.22	55198.60 ± 234.94	33197.20 ± 182.20	7562.80 ± 86.96	

Table 42.: Number of selected Λ in y and p_T bins, for field down events at $\sqrt{s} = 7$ TeV.

	$2.0 < y < 2.5$	$2.5 < y < 3.0$	$3.0 < y < 3.5$	$3.5 < y < 4.0$	$4.0 < y < 4.5$	$2.0 < y < 4.5$
$150 < p_T < 250$	-	525.20 ± 22.92	1171.00 ± 34.22	64.40 ± 8.02	8.20 ± 2.86	1768.80 ± 42.06
$250 < p_T < 500$	-	5677.00 ± 75.35	9746.80 ± 98.73	3718.60 ± 60.98	72.00 ± 8.49	19214.40 ± 138.62
$500 < p_T < 650$	104.20 ± 10.21	4790.60 ± 69.21	8435.60 ± 91.85	4581.00 ± 67.68	639.80 ± 25.29	18551.20 ± 136.20
$650 < p_T < 800$	294.00 ± 17.15	4011.40 ± 63.34	9167.00 ± 95.74	4760.00 ± 68.99	1246.20 ± 35.30	19478.60 ± 139.57
$800 < p_T < 1000$	774.00 ± 27.82	4389.60 ± 66.25	10889.60 ± 104.35	6055.60 ± 77.82	2018.20 ± 44.92	24127.00 ± 155.33
$1000 < p_T < 1200$	1057.00 ± 32.51	3425.40 ± 58.53	7561.40 ± 86.96	5396.80 ± 73.46	1548.20 ± 39.35	18988.80 ± 137.80
$1200 < p_T < 2500$	3571.60 ± 59.76	8740.20 ± 93.49	12452.00 ± 111.59	11200.20 ± 105.83	3281.40 ± 57.28	39245.40 ± 198.10
p_T integrated	5800.80 ± 76.16	31559.40 ± 177.65	59423.40 ± 243.77	35776.60 ± 189.15	8814.00 ± 93.88	

Table 43.: Number of selected K^0_S in y and p_T bins, for field down events at $\sqrt{s} = 7$ TeV.

	$2.0 < y < 2.5$	$2.5 < y < 3.0$	$3.0 < y < 3.5$	$3.5 < y < 4.0$	$4.0 < y < 4.5$	$2.0 < y < 4.5$
$150 < p_T < 250$	341.50 ± 18.48	16054.00 ± 126.70	50862.75 ± 225.53	43571.75 ± 208.74	12682.50 ± 112.62	123512.50 ± 351.44
$250 < p_T < 500$	3873.50 ± 62.24	58841.25 ± 242.57	155685.00 ± 394.57	153423.25 ± 391.69	63814.50 ± 252.62	435637.50 ± 660.03
$500 < p_T < 650$	5167.50 ± 71.89	43393.00 ± 208.31	75422.75 ± 274.63	83042.50 ± 288.17	35846.00 ± 189.33	242871.75 ± 492.82
$650 < p_T < 800$	6388.25 ± 79.93	39926.75 ± 199.82	56072.00 ± 236.80	62706.00 ± 250.41	26164.00 ± 161.75	191257.00 ± 437.33
$800 < p_T < 1000$	8948.50 ± 94.60	41411.75 ± 203.50	49868.50 ± 223.31	57449.00 ± 239.69	22149.25 ± 148.83	179827.00 ± 424.06
$1000 < p_T < 1200$	7942.75 ± 89.12	28551.00 ± 168.97	30602.00 ± 174.93	35516.75 ± 188.46	13184.25 ± 114.82	115796.75 ± 340.29
$1200 < p_T < 2500$	21114.00 ± 145.31	51585.75 ± 227.12	45886.25 ± 214.21	52978.25 ± 230.17	19229.50 ± 138.67	190793.75 ± 436.80
p_T integrated	53776.00 ± 231.90	279763.50 ± 528.93	464399.25 ± 681.47	488687.50 ± 699.06	193070.00 ± 439.40	

Table 44.: Number of selected $\bar{\Lambda}$ in y and p_T bins, for field up events at $\sqrt{s} = 7$ TeV.

	$2.0 < y < 2.5$	$2.5 < y < 3.0$	$3.0 < y < 3.5$	$3.5 < y < 4.0$	$4.0 < y < 4.5$	$2.0 < y < 4.5$
$150 < p_T < 250$	-	1130.80 ± 33.63	2042.60 ± 45.20	103.00 ± 10.15	12.20 ± 3.49	3288.60 ± 57.35
$250 < p_T < 500$	-	10511.80 ± 102.53	17620.80 ± 132.74	7023.20 ± 83.80	197.20 ± 14.04	35353.00 ± 188.02
$500 < p_T < 650$	113.80 ± 10.67	8657.20 ± 93.04	15286.60 ± 123.64	8147.20 ± 90.26	1380.80 ± 37.16	33585.60 ± 183.26
$650 < p_T < 800$	570.40 ± 23.88	7183.80 ± 84.76	16698.80 ± 129.22	8613.00 ± 92.81	2464.00 ± 49.64	35530.00 ± 188.49
$800 < p_T < 1000$	1512.00 ± 38.88	8064.20 ± 89.80	19386.20 ± 139.23	11139.20 ± 105.54	3434.60 ± 58.61	43536.20 ± 208.65
$1000 < p_T < 1200$	2000.20 ± 44.72	6406.20 ± 80.04	14066.00 ± 118.60	9647.20 ± 98.22	2669.40 ± 51.67	34789.00 ± 186.52
$1200 < p_T < 2500$	6682.60 ± 81.75	16470.00 ± 128.34	23051.40 ± 151.83	19840.80 ± 140.86	5202.00 ± 72.12	71246.80 ± 266.92
p_T integrated	10879.00 ± 104.30	58424.00 ± 241.71	108152.40 ± 328.87	64513.60 ± 254.00	15360.20 ± 123.94	

Table 45.: Number of selected Λ in y and p_T bins, for field up events at $\sqrt{s} = 7$ TeV.

	$2.0 < y < 2.5$	$2.5 < y < 3.0$	$3.0 < y < 3.5$	$3.5 < y < 4.0$	$4.0 < y < 4.5$	$2.0 < y < 4.5$
$150 < p_T < 250$	-	1408.60 ± 37.53	2636.00 ± 51.34	190.80 ± 13.81	35.40 ± 5.95	4270.80 ± 65.35
$250 < p_T < 500$	-	12264.60 ± 110.75	20059.60 ± 141.63	7987.20 ± 89.37	182.80 ± 13.52	40494.20 ± 201.23
$500 < p_T < 650$	148.20 ± 12.17	9779.60 ± 98.89	17622.20 ± 132.75	9539.60 ± 97.67	1448.40 ± 38.06	38538.00 ± 196.31
$650 < p_T < 800$	772.60 ± 27.80	8283.40 ± 91.01	18733.20 ± 136.87	9918.60 ± 99.59	2750.40 ± 52.44	40458.20 ± 201.14
$800 < p_T < 1000$	1863.80 ± 43.17	9068.00 ± 95.23	21983.80 ± 148.27	12714.20 ± 112.76	3969.00 ± 63.00	49598.80 ± 222.71
$1000 < p_T < 1200$	2153.80 ± 46.41	7542.60 ± 86.85	15588.00 ± 124.85	10998.60 ± 104.87	3146.80 ± 56.10	39429.80 ± 198.57
$1200 < p_T < 2500$	7148.00 ± 84.55	18208.20 ± 134.94	25300.60 ± 159.06	22563.20 ± 150.21	6060.40 ± 77.85	79280.40 ± 281.57
p_T integrated	12086.40 ± 109.94	66555.00 ± 257.98	121923.40 ± 349.18	73912.20 ± 271.87	17593.20 ± 132.64	

Table 46.: Number of selected K^0_S in y and p_T bins, for field up events at $\sqrt{s} = 7$ TeV.

	$2.0 < y < 2.5$	$2.5 < y < 3.0$	$3.0 < y < 3.5$	$3.5 < y < 4.0$	$4.0 < y < 4.5$	$2.0 < y < 4.5$
$150 < p_T < 250$	626.25 ± 25.02	31408.75 ± 177.23	101598.00 ± 318.74	88197.75 ± 296.98	24915.25 ± 157.85	246746.00 ± 496.74
$250 < p_T < 500$	7666.25 ± 87.56	118198.25 ± 343.80	311274.00 ± 557.92	307747.25 ± 554.75	127343.50 ± 356.85	872229.25 ± 933.93
$500 < p_T < 650$	10252.50 ± 101.25	86668.25 ± 294.39	151664.25 ± 389.44	164743.50 ± 405.89	72679.50 ± 269.59	486008.00 ± 697.14
$650 < p_T < 800$	12852.75 ± 113.37	79723.75 ± 282.35	112807.50 ± 335.87	126374.50 ± 355.49	51972.25 ± 227.97	383730.75 ± 619.46
$800 < p_T < 1000$	18038.00 ± 134.31	82908.75 ± 287.94	99692.50 ± 315.74	114788.50 ± 338.80	44123.75 ± 210.06	359551.50 ± 599.63
$1000 < p_T < 1200$	16301.50 ± 127.68	56870.00 ± 238.47	61126.25 ± 247.24	71689.50 ± 267.75	26490.00 ± 162.76	232477.25 ± 482.16
$1200 < p_T < 2500$	42126.25 ± 205.25	104137.25 ± 322.70	92417.25 ± 304.00	106480.75 ± 326.31	38401.25 ± 195.96	383562.75 ± 619.32
p_T integrated	107863.50 ± 328.43	559915.00 ± 748.27	930579.75 ± 964.67	980021.75 ± 989.96	385925.50 ± 621.23	

Table 47.: Efficiency for $\bar{\Lambda}$ in y and p_T bins, for field down events at $\sqrt{s} = 0.9$ TeV. Values are shown in percent.

	$2.0 < y < 2.5$	$2.5 < y < 3.0$	$3.0 < y < 3.5$	$3.5 < y < 4.0$	$2.0 < y < 4.0$
$250 < p_T < 500$	0.01 ± 0.01	1.05 ± 0.06	0.71 ± 0.05	0.02 ± 0.01	0.49 ± 0.02
$500 < p_T < 650$	0.08 ± 0.03	1.80 ± 0.11	2.29 ± 0.13	0.27 ± 0.05	1.19 ± 0.05
$650 < p_T < 800$	0.17 ± 0.04	1.82 ± 0.12	3.18 ± 0.17	0.73 ± 0.09	1.52 ± 0.06
$800 < p_T < 1000$	0.35 ± 0.05	1.81 ± 0.12	3.72 ± 0.19	1.49 ± 0.14	1.80 ± 0.07
$1000 < p_T < 1200$	0.59 ± 0.08	1.66 ± 0.14	4.14 ± 0.25	1.78 ± 0.20	1.92 ± 0.08
$1200 < p_T < 2500$	0.66 ± 0.07	1.45 ± 0.11	3.53 ± 0.20	2.44 ± 0.21	1.77 ± 0.07
p_T integrated	0.26 ± 0.02	1.50 ± 0.04	2.35 ± 0.06	0.67 ± 0.03	

Table 48.: Efficiency for Λ in y and p_T bins, for field down events at $\sqrt{s} = 0.9$ TeV. Values are shown in percent.

	$2.0 < y < 2.5$	$2.5 < y < 3.0$	$3.0 < y < 3.5$	$3.5 < y < 4.0$	$2.0 < y < 4.0$
$250 < p_T < 500$	0.05 ± 0.01	0.88 ± 0.05	0.56 ± 0.04	0.00 ± 0.00	0.39 ± 0.02
$500 < p_T < 650$	0.14 ± 0.03	1.66 ± 0.10	2.22 ± 0.12	0.12 ± 0.03	1.08 ± 0.04
$650 < p_T < 800$	0.21 ± 0.04	1.94 ± 0.12	2.89 ± 0.15	0.59 ± 0.07	1.45 ± 0.05
$800 < p_T < 1000$	0.30 ± 0.05	1.88 ± 0.12	4.22 ± 0.19	1.30 ± 0.11	1.91 ± 0.06
$1000 < p_T < 1200$	0.51 ± 0.08	1.61 ± 0.13	4.50 ± 0.24	1.76 ± 0.17	1.99 ± 0.08
$1200 < p_T < 2500$	0.72 ± 0.07	1.26 ± 0.09	3.78 ± 0.19	2.35 ± 0.18	1.83 ± 0.06
p_T integrated	0.29 ± 0.02	1.42 ± 0.04	2.40 ± 0.05	0.61 ± 0.03	

Table 49.: Efficiency for K^0_S in y and p_T bins, for field down events at $\sqrt{s} = 0.9$ TeV. Values are shown in percent.

	$2.0 < y < 2.5$	$2.5 < y < 3.0$	$3.0 < y < 3.5$	$3.5 < y < 4.0$	$2.0 < y < 4.0$
$250 < p_T < 500$	0.16 ± 0.01	1.59 ± 0.03	4.79 ± 0.06	2.53 ± 0.05	2.43 ± 0.02
$500 < p_T < 650$	0.44 ± 0.03	2.68 ± 0.06	6.06 ± 0.10	4.69 ± 0.09	3.60 ± 0.04
$650 < p_T < 800$	0.70 ± 0.04	3.73 ± 0.09	6.64 ± 0.12	5.66 ± 0.12	4.26 ± 0.05
$800 < p_T < 1000$	1.16 ± 0.06	4.33 ± 0.10	6.93 ± 0.14	6.46 ± 0.15	4.69 ± 0.06
$1000 < p_T < 1200$	1.53 ± 0.09	4.77 ± 0.15	6.84 ± 0.19	6.83 ± 0.22	4.85 ± 0.08
$1200 < p_T < 2500$	1.87 ± 0.09	4.32 ± 0.13	6.06 ± 0.17	6.30 ± 0.20	4.42 ± 0.07
p_T integrated	0.68 ± 0.03	2.83 ± 0.08	5.74 ± 0.12	4.24 ± 0.11	

Table 50.: Efficiency for $\bar{\Lambda}$ in y and p_T bins, for field up events at $\sqrt{s} = 0.9$ TeV. Values are shown in percent.

	$2.0 < y < 2.5$	$2.5 < y < 3.0$	$3.0 < y < 3.5$	$3.5 < y < 4.0$	$2.0 < y < 4.0$
$250 < p_T < 500$	0.04 ± 0.02	1.08 ± 0.07	0.69 ± 0.06	-	0.52 ± 0.03
$500 < p_T < 650$	0.10 ± 0.03	1.75 ± 0.12	2.22 ± 0.13	0.23 ± 0.05	1.19 ± 0.05
$650 < p_T < 800$	0.16 ± 0.04	1.88 ± 0.13	3.00 ± 0.17	0.92 ± 0.11	1.55 ± 0.06
$800 < p_T < 1000$	0.30 ± 0.05	1.70 ± 0.12	3.69 ± 0.19	1.41 ± 0.15	1.75 ± 0.07
$1000 < p_T < 1200$	0.42 ± 0.07	1.55 ± 0.14	3.93 ± 0.25	2.40 ± 0.25	1.87 ± 0.08
$1200 < p_T < 2500$	0.63 ± 0.07	1.34 ± 0.11	3.07 ± 0.19	2.02 ± 0.21	1.56 ± 0.06
p_T integrated	0.27 ± 0.02	1.50 ± 0.05	2.35 ± 0.06	0.80 ± 0.04	

Table 51.: Efficiency for Λ in y and p_T bins, for field up events at $\sqrt{s} = 0.9$ TeV. Values are shown in percent.

	$2.0 < y < 2.5$	$2.5 < y < 3.0$	$3.0 < y < 3.5$	$3.5 < y < 4.0$	$2.0 < y < 4.0$
$250 < p_T < 500$	0.02 ± 0.01	1.01 ± 0.07	0.58 ± 0.05	-	0.45 ± 0.02
$500 < p_T < 650$	0.10 ± 0.03	1.74 ± 0.11	2.15 ± 0.12	0.21 ± 0.04	1.14 ± 0.05
$650 < p_T < 800$	0.16 ± 0.04	1.91 ± 0.13	3.20 ± 0.16	0.58 ± 0.08	1.54 ± 0.06
$800 < p_T < 1000$	0.31 ± 0.05	1.75 ± 0.12	3.72 ± 0.18	1.34 ± 0.13	1.78 ± 0.06
$1000 < p_T < 1200$	0.43 ± 0.07	1.65 ± 0.14	3.96 ± 0.24	2.09 ± 0.21	1.91 ± 0.08
$1200 < p_T < 2500$	0.63 ± 0.07	1.17 ± 0.09	3.72 ± 0.19	2.37 ± 0.19	1.76 ± 0.06
p_T integrated	0.27 ± 0.02	1.48 ± 0.04	2.44 ± 0.06	0.76 ± 0.04	

Table 52.: Efficiency for K^0_S in y and p_T bins, for field up events at $\sqrt{s} = 0.9$ TeV. Values are shown in percent.

	$2.0 < y < 2.5$	$2.5 < y < 3.0$	$3.0 < y < 3.5$	$3.5 < y < 4.0$	$2.0 < y < 4.0$
$250 < p_T < 500$	0.17 ± 0.02	1.57 ± 0.04	4.68 ± 0.06	2.50 ± 0.05	2.45 ± 0.02
$500 < p_T < 650$	0.47 ± 0.03	2.78 ± 0.07	5.99 ± 0.10	4.58 ± 0.09	3.67 ± 0.04
$650 < p_T < 800$	0.72 ± 0.05	3.69 ± 0.09	6.51 ± 0.13	5.54 ± 0.13	4.27 ± 0.05
$800 < p_T < 1000$	1.14 ± 0.07	4.48 ± 0.11	6.67 ± 0.14	6.15 ± 0.15	4.66 ± 0.06
$1000 < p_T < 1200$	1.47 ± 0.09	4.61 ± 0.15	7.04 ± 0.20	6.54 ± 0.22	4.83 ± 0.08
$1200 < p_T < 2500$	1.97 ± 0.09	4.54 ± 0.13	6.18 ± 0.17	5.92 ± 0.20	4.49 ± 0.07
p_T integrated	0.73 ± 0.03	2.88 ± 0.09	5.65 ± 0.13	4.13 ± 0.12	

Table 53.: Efficiency for $\bar{\Lambda}$ in y and p_T bins, for field down events at $\sqrt{s} = 7$ TeV. Values are shown in percent.

	$2.0 < y < 2.5$	$2.5 < y < 3.0$	$3.0 < y < 3.5$	$3.5 < y < 4.0$	$4.0 < y < 4.5$	$2.0 < y < 4.5$
$150 < p_T < 250$	-	0.65 ± 0.36	1.63 ± 0.58	0.19 ± 0.21	0.01 ± 0.06	0.55 ± 0.16
$250 < p_T < 500$	-	2.23 ± 0.34	3.95 ± 0.46	1.65 ± 0.32	0.05 ± 0.06	1.71 ± 0.14
$500 < p_T < 650$	0.12 ± 0.11	2.71 ± 0.46	4.95 ± 0.64	3.37 ± 0.57	0.62 ± 0.26	2.47 ± 0.21
$650 < p_T < 800$	0.19 ± 0.14	2.52 ± 0.47	6.55 ± 0.78	3.59 ± 0.63	1.25 ± 0.40	2.91 ± 0.25
$800 < p_T < 1000$	0.41 ± 0.20	2.33 ± 0.44	6.62 ± 0.76	4.67 ± 0.71	1.43 ± 0.43	3.13 ± 0.25
$1000 < p_T < 1200$	0.81 ± 0.32	2.67 ± 0.56	6.36 ± 0.89	5.55 ± 0.91	1.47 ± 0.52	3.40 ± 0.31
$1200 < p_T < 2500$	1.04 ± 0.23	2.74 ± 0.37	4.80 ± 0.52	4.51 ± 0.56	1.50 ± 0.37	2.90 ± 0.19
p_T integrated	0.44 ± 0.08	2.41 ± 0.17	5.05 ± 0.26	3.41 ± 0.23	0.87 ± 0.12	

Table 54.: Efficiency for Λ in y and p_T bins, for field down events at $\sqrt{s} = 7$ TeV. Values are shown in percent.

	$2.0 < y < 2.5$	$2.5 < y < 3.0$	$3.0 < y < 3.5$	$3.5 < y < 4.0$	$4.0 < y < 4.5$	$2.0 < y < 4.5$
$150 < p_T < 250$	-	1.21 ± 0.48	1.18 ± 0.48	0.09 ± 0.15	-	0.56 ± 0.16
$250 < p_T < 500$	-	2.20 ± 0.33	4.06 ± 0.46	1.60 ± 0.31	-	1.71 ± 0.14
$500 < p_T < 650$	0.09 ± 0.09	3.02 ± 0.48	5.26 ± 0.65	2.97 ± 0.53	0.46 ± 0.22	2.50 ± 0.21
$650 < p_T < 800$	0.28 ± 0.17	2.58 ± 0.48	5.90 ± 0.74	4.32 ± 0.69	0.99 ± 0.35	2.89 ± 0.24
$800 < p_T < 1000$	0.48 ± 0.22	2.39 ± 0.45	6.17 ± 0.74	4.52 ± 0.69	1.33 ± 0.41	3.04 ± 0.24
$1000 < p_T < 1200$	0.77 ± 0.31	2.71 ± 0.56	6.14 ± 0.86	4.78 ± 0.85	1.48 ± 0.51	3.21 ± 0.29
$1200 < p_T < 2500$	1.07 ± 0.23	2.77 ± 0.37	4.28 ± 0.49	4.80 ± 0.56	1.70 ± 0.38	2.90 ± 0.18
p_T integrated	0.46 ± 0.08	2.51 ± 0.17	4.81 ± 0.25	3.40 ± 0.23	0.83 ± 0.12	

Table 55.: Efficiency for K^0_S in y and p_T bins, for field down events at $\sqrt{s} = 7$ TeV. Values are shown in percent.

	$2.0 < y < 2.5$	$2.5 < y < 3.0$	$3.0 < y < 3.5$	$3.5 < y < 4.0$	$4.0 < y < 4.5$	$2.0 < y < 4.5$
$150 < p_T < 250$	0.10 ± 0.03	3.27 ± 0.18	11.74 ± 0.34	10.83 ± 0.35	3.15 ± 0.20	5.72 ± 0.11
$250 < p_T < 500$	0.28 ± 0.03	3.93 ± 0.12	11.80 ± 0.20	13.06 ± 0.22	5.54 ± 0.15	6.75 ± 0.07
$500 < p_T < 650$	0.77 ± 0.08	6.03 ± 0.20	11.55 ± 0.28	14.13 ± 0.33	6.88 ± 0.24	7.68 ± 0.11
$650 < p_T < 800$	1.25 ± 0.11	7.04 ± 0.25	11.21 ± 0.32	14.14 ± 0.38	6.31 ± 0.27	7.79 ± 0.12
$800 < p_T < 1000$	1.84 ± 0.14	7.92 ± 0.28	10.61 ± 0.33	14.00 ± 0.40	6.26 ± 0.29	7.94 ± 0.13
$1000 < p_T < 1200$	2.47 ± 0.20	8.36 ± 0.35	9.96 ± 0.40	13.54 ± 0.50	5.94 ± 0.36	7.88 ± 0.16
$1200 < p_T < 2500$	3.22 ± 0.16	7.94 ± 0.24	7.79 ± 0.26	11.04 ± 0.33	4.83 ± 0.24	6.83 ± 0.11
p_T integrated	1.21 ± 0.12	5.83 ± 0.15	10.91 ± 0.27	13.00 ± 0.33	5.60 ± 0.24	

Table 56.: Efficiency for $\bar{\Lambda}$ in y and p_T bins, for field up events at $\sqrt{s} = 7$ TeV. Values are shown in percent.

	$2.0 < y < 2.5$	$2.5 < y < 3.0$	$3.0 < y < 3.5$	$3.5 < y < 4.0$	$4.0 < y < 4.5$	$2.0 < y < 4.5$
$150 < p_T < 250$	-	0.90 ± 0.32	1.30 ± 0.38	0.09 ± 0.11	-	0.56 ± 0.12
$250 < p_T < 500$	-	2.25 ± 0.25	3.95 ± 0.32	1.57 ± 0.22	0.05 ± 0.05	1.81 ± 0.11
$500 < p_T < 650$	0.09 ± 0.07	2.50 ± 0.32	5.01 ± 0.44	3.32 ± 0.39	0.44 ± 0.16	2.51 ± 0.15
$650 < p_T < 800$	0.32 ± 0.14	2.87 ± 0.36	5.94 ± 0.51	3.30 ± 0.41	1.14 ± 0.28	2.93 ± 0.17
$800 < p_T < 1000$	0.58 ± 0.17	2.17 ± 0.30	6.27 ± 0.51	3.78 ± 0.43	1.66 ± 0.33	3.02 ± 0.17
$1000 < p_T < 1200$	0.60 ± 0.20	2.72 ± 0.40	5.46 ± 0.57	4.50 ± 0.56	1.83 ± 0.42	3.10 ± 0.20
$1200 < p_T < 2500$	1.23 ± 0.18	2.93 ± 0.27	4.30 ± 0.35	4.20 ± 0.38	1.76 ± 0.29	2.91 ± 0.13
p_T integrated	0.54 ± 0.06	2.49 ± 0.12	4.76 ± 0.17	3.11 ± 0.15	0.98 ± 0.10	

Table 57.: Efficiency for Λ in y and p_T bins, for field up events at $\sqrt{s} = 7$ TeV. Values are shown in percent.

	$2.0 < y < 2.5$	$2.5 < y < 3.0$	$3.0 < y < 3.5$	$3.5 < y < 4.0$	$4.0 < y < 4.5$	$2.0 < y < 4.5$
$150 < p_T < 250$	-	0.80 ± 0.30	1.77 ± 0.44	0.09 ± 0.11	-	0.65 ± 0.13
$250 < p_T < 500$	-	2.39 ± 0.26	4.29 ± 0.33	1.72 ± 0.23	0.04 ± 0.04	1.96 ± 0.11
$500 < p_T < 650$	0.11 ± 0.08	2.78 ± 0.33	5.58 ± 0.46	3.55 ± 0.40	0.46 ± 0.16	2.76 ± 0.16
$650 < p_T < 800$	0.31 ± 0.13	2.56 ± 0.33	5.89 ± 0.50	3.81 ± 0.44	1.25 ± 0.29	2.97 ± 0.17
$800 < p_T < 1000$	0.61 ± 0.17	2.47 ± 0.32	6.65 ± 0.52	4.48 ± 0.47	1.36 ± 0.29	3.28 ± 0.18
$1000 < p_T < 1200$	0.69 ± 0.21	2.49 ± 0.37	5.89 ± 0.58	5.41 ± 0.60	1.32 ± 0.34	3.26 ± 0.21
$1200 < p_T < 2500$	1.20 ± 0.18	2.92 ± 0.27	4.52 ± 0.35	4.69 ± 0.39	1.54 ± 0.26	3.02 ± 0.13
p_T integrated	0.55 ± 0.06	2.53 ± 0.12	5.08 ± 0.18	3.54 ± 0.16	0.87 ± 0.09	

Table 58.: Efficiency for K^0_S in y and p_T bins, for field up events at $\sqrt{s} = 7$ TeV. Values are shown in percent.

	$2.0 < y < 2.5$	$2.5 < y < 3.0$	$3.0 < y < 3.5$	$3.5 < y < 4.0$	$4.0 < y < 4.5$	$2.0 < y < 4.5$
$150 < p_T < 250$	0.09 ± 0.03	3.19 ± 0.16	11.45 ± 0.31	10.89 ± 0.31	3.29 ± 0.18	5.72 ± 0.10
$250 < p_T < 500$	0.26 ± 0.03	4.09 ± 0.11	11.99 ± 0.18	12.87 ± 0.20	5.68 ± 0.14	6.85 ± 0.06
$500 < p_T < 650$	0.71 ± 0.07	6.06 ± 0.18	11.50 ± 0.25	14.16 ± 0.29	6.79 ± 0.22	7.68 ± 0.10
$650 < p_T < 800$	1.23 ± 0.10	7.08 ± 0.23	11.14 ± 0.29	13.70 ± 0.33	6.40 ± 0.24	7.78 ± 0.11
$800 < p_T < 1000$	1.91 ± 0.13	8.12 ± 0.25	10.75 ± 0.30	13.63 ± 0.35	6.18 ± 0.26	7.97 ± 0.12
$1000 < p_T < 1200$	2.50 ± 0.18	8.57 ± 0.32	10.03 ± 0.36	12.69 ± 0.43	5.73 ± 0.32	7.77 ± 0.15
$1200 < p_T < 2500$	3.21 ± 0.14	8.00 ± 0.22	7.79 ± 0.23	10.27 ± 0.28	4.43 ± 0.21	6.68 ± 0.10
p_T integrated	1.21 ± 0.11	5.93 ± 0.13	10.93 ± 0.24	12.70 ± 0.30	5.59 ± 0.21	

Table 59.: Corrected production yields for $\bar{\Lambda}$ in y and p_T bins, for field down events at $\sqrt{s} = 0.9$ TeV.

	$2.0 < y < 2.5$	$2.5 < y < 3.0$	$3.0 < y < 3.5$	$3.5 < y < 4.0$	$2.0 < y < 4.0$
$250 < p_T < 500$	16890 ± 15077	31275 ± 2456	25536 ± 2657	26816 ± 17596	105139 ± 6550
$500 < p_T < 650$	20909 ± 8577	16027 ± 1334	11729 ± 973	7623 ± 2140	49909 ± 2841
$650 < p_T < 800$	12051 ± 3898	14054 ± 1271	10994 ± 832	12340 ± 1986	46984 ± 2533
$800 < p_T < 1000$	9865 ± 2300	11975 ± 1131	11516 ± 809	8023 ± 1041	44271 ± 2237
$1000 < p_T < 1200$	6791 ± 1441	8151 ± 981	7001 ± 591	4516 ± 711	28356 ± 1722
$1200 < p_T < 2500$	19602 ± 2722	14770 ± 1484	11550 ± 864	5703 ± 693	50188 ± 2520
p_T integrated	91490 ± 8685	96070 ± 3634	81911 ± 2713	67937 ± 4580	

Table 60.: Corrected production yields for Λ in y and p_T bins, for field down events at $\sqrt{s} = 0.9$ TeV.

	$2.0 < y < 2.5$	$2.5 < y < 3.0$	$3.0 < y < 3.5$	$3.5 < y < 4.0$	$2.0 < y < 4.0$
$250 < p_T < 500$	6270 ± 4082	33872 ± 2822	28222 ± 3163	63575 ± 71325	117907 ± 7812
$500 < p_T < 650$	7505 ± 2900	20987 ± 1689	16573 ± 1254	21451 ± 6508	69713 ± 3747
$650 < p_T < 800$	14747 ± 4051	16750 ± 1379	16857 ± 1182	13238 ± 2195	63431 ± 3175
$800 < p_T < 1000$	21949 ± 4531	15620 ± 1336	13215 ± 817	11446 ± 1362	55900 ± 2524
$1000 < p_T < 1200$	8252 ± 1769	10616 ± 1192	10402 ± 741	10757 ± 1309	43629 ± 2280
$1200 < p_T < 2500$	19208 ± 2476	22987 ± 2185	15382 ± 994	11765 ± 1135	70464 ± 3103
p_T integrated	100013 ± 8738	121736 ± 4407	108979 ± 3252	119171 ± 6969	

Table 61.: Corrected production yields for K^0_S in y and p_T bins, for field down events at $\sqrt{s} = 0.9$ TeV.

	$2.0 < y < 2.5$	$2.5 < y < 3.0$	$3.0 < y < 3.5$	$3.5 < y < 4.0$	$2.0 < y < 4.0$
$250 < p_T < 500$	98365 ± 11459	142201 ± 4273	128375 ± 2274	117005 ± 3017	474205 ± 6205
$500 < p_T < 650$	54985 ± 5170	66829 ± 2227	58783 ± 1353	50966 ± 1438	221967 ± 3451
$650 < p_T < 800$	42270 ± 3612	46676 ± 1566	40286 ± 1067	33508 ± 1055	155191 ± 2644
$800 < p_T < 1000$	36679 ± 2611	40054 ± 1362	33334 ± 960	28172 ± 926	134100 ± 2379
$1000 < p_T < 1200$	23954 ± 1898	22584 ± 981	19943 ± 773	15893 ± 701	80335 ± 1862
$1200 < p_T < 2500$	37465 ± 2282	36773 ± 1424	30818 ± 1104	20850 ± 880	123727 ± 2598
p_T integrated	323341 ± 14672	360051 ± 10267	312344 ± 7068	270687 ± 7713	

Table 62.: Corrected production yields for $\bar{\Lambda}$ in y and p_T bins, for field up events at $\sqrt{s} = 0.9$ TeV.

	$2.0 < y < 2.5$	$2.5 < y < 3.0$	$3.0 < y < 3.5$	$3.5 < y < 4.0$	$2.0 < y < 4.0$
$250 < p_T < 500$	2733 ± 2717	21093 ± 2008	18817 ± 2277	-	68558 ± 5094
$500 < p_T < 650$	8574 ± 3965	12999 ± 1219	11962 ± 1021	11188 ± 3319	44188 ± 2707
$650 < p_T < 800$	12811 ± 4186	11707 ± 1122	10181 ± 816	5900 ± 1088	38797 ± 2230
$800 < p_T < 1000$	16454 ± 3693	12115 ± 1204	9388 ± 698	7371 ± 1057	40284 ± 2152
$1000 < p_T < 1200$	7033 ± 1772	7723 ± 996	6675 ± 591	3354 ± 515	26239 ± 1676
$1200 < p_T < 2500$	13935 ± 2128	13632 ± 1488	11438 ± 926	6245 ± 852	47775 ± 2619
p_T integrated	72846 ± 7474	78881 ± 3305	70729 ± 2494	48989 ± 3597	

Table 63.: Corrected production yields for Λ in y and p_T bins, for field up events at $\sqrt{s} = 0.9$ TeV.

	$2.0 < y < 2.5$	$2.5 < y < 3.0$	$3.0 < y < 3.5$	$3.5 < y < 4.0$	$2.0 < y < 4.0$
$250 < p_T < 500$	10402 ± 9114	23678 ± 2236	30069 ± 3485	-	92467 ± 6744
$500 < p_T < 650$	5678 ± 2891	16939 ± 1478	17091 ± 1333	11313 ± 3302	60597 ± 3436
$650 < p_T < 800$	17077 ± 5274	16913 ± 1454	13823 ± 968	11371 ± 2120	55789 ± 2873
$800 < p_T < 1000$	11256 ± 2637	16364 ± 1470	14135 ± 924	13298 ± 1609	57801 ± 2745
$1000 < p_T < 1200$	10750 ± 2365	9788 ± 1135	9690 ± 760	6718 ± 872	38347 ± 2159
$1200 < p_T < 2500$	19222 ± 2670	19974 ± 2071	13684 ± 919	9978 ± 1046	62664 ± 2935
p_T integrated	87101 ± 8405	104311 ± 4061	98382 ± 3068	84708 ± 5292	

Table 64.: Corrected production yields for K^0_S in y and p_T bins, for field up events at $\sqrt{s} = 0.9$ TeV.

	$2.0 < y < 2.5$	$2.5 < y < 3.0$	$3.0 < y < 3.5$	$3.5 < y < 4.0$	$2.0 < y < 4.0$
$250 < p_T < 500$	80099 ± 9918	132251 ± 4178	116874 ± 2195	106581 ± 2890	422121 ± 5832
$500 < p_T < 650$	44013 ± 4489	54616 ± 1937	53446 ± 1300	46743 ± 1393	192421 ± 3168
$650 < p_T < 800$	35874 ± 3314	43114 ± 1525	36876 ± 1033	31528 ± 1041	140494 ± 2525
$800 < p_T < 1000$	32188 ± 2489	34190 ± 1218	32028 ± 970	25019 ± 888	119607 ± 2250
$1000 < p_T < 1200$	21514 ± 1844	21783 ± 989	18157 ± 721	13998 ± 659	72700 ± 1763
$1200 < p_T < 2500$	31053 ± 1918	31688 ± 1235	26910 ± 985	19154 ± 850	108078 ± 2322
p_T integrated	259947 ± 12718	317767 ± 9988	285498 ± 7138	245501 ± 7646	

Table 65.: Corrected production yields for $\bar{\Lambda}$ in y and p_T bins, for field down events at $\sqrt{s} = 7$ TeV.

	$2.0 < y < 2.5$	$2.5 < y < 3.0$	$3.0 < y < 3.5$	$3.5 < y < 4.0$	$4.0 < y < 4.5$	$2.0 < y < 4.5$
$150 < p_T < 250$	-	103496 ± 56792	75440 ± 26938	26664 ± 30337	105609 ± 458973	358917 ± 104002
$250 < p_T < 500$	-	248432 ± 37596	231872 ± 26945	226256 ± 44144	209843 ± 241784	1081935 ± 90515
$500 < p_T < 650$	39619 ± 36358	167724 ± 28577	159809 ± 20649	125851 ± 21468	121257 ± 52008	708344 ± 61290
$650 < p_T < 800$	150134 ± 111266	154177 ± 29128	130938 ± 15679	124029 ± 21878	95816 ± 31040	633148 ± 53751
$800 < p_T < 1000$	185449 ± 89220	180221 ± 34066	149945 ± 17339	121561 ± 18561	118399 ± 35731	711619 ± 56586
$1000 < p_T < 1200$	118276 ± 47600	128219 ± 26889	109017 ± 15268	88872 ± 14567	91121 ± 32626	517016 ± 46611
$1200 < p_T < 2500$	320109 ± 72046	308236 ± 41873	238722 ± 25998	224114 ± 28080	164330 ± 40649	1232029 ± 80144
p_T integrated	1227532 ± 214195	1273495 ± 89130	1093155 ± 56084	974174 ± 65635	873030 ± 123708	

Table 66.: Corrected production yields for Λ in y and p_T bins, for field down events at $\sqrt{s} = 7$ TeV.

	$2.0 < y < 2.5$	$2.5 < y < 3.0$	$3.0 < y < 3.5$	$3.5 < y < 4.0$	$4.0 < y < 4.5$	$2.0 < y < 4.5$
$150 < p_T < 250$	-	43528 ± 17447	99215 ± 40779	68745 ± 109590	-	313962 ± 88872
$250 < p_T < 500$	-	258124 ± 39254	240233 ± 27312	232651 ± 45887	-	1125877 ± 93727
$500 < p_T < 650$	119132 ± 125827	158747 ± 25426	160410 ± 20009	154098 ± 27819	138052 ± 67098	742390 ± 63422
$650 < p_T < 800$	105271 ± 64662	155774 ± 28976	155431 ± 19462	110285 ± 17646	126505 ± 45624	673687 ± 56963
$800 < p_T < 1000$	160502 ± 72206	183668 ± 34568	176532 ± 21126	133993 ± 20503	152069 ± 47259	794479 ± 64088
$1000 < p_T < 1200$	137732 ± 56638	126282 ± 26023	123101 ± 17294	112970 ± 20237	104961 ± 36327	592035 ± 54494
$1200 < p_T < 2500$	332654 ± 72968	315752 ± 42031	290697 ± 33273	233247 ± 27442	193222 ± 43699	1355192 ± 86837
p_T integrated	1261292 ± 214019	1258106 ± 85910	1234482 ± 64212	1052234 ± 70218	1066587 ± 152228	

Table 67.: Corrected production yields for K^0_S in y and p_T bins, for field down events at $\sqrt{s} = 7$ TeV.

	$2.0 < y < 2.5$	$2.5 < y < 3.0$	$3.0 < y < 3.5$	$3.5 < y < 4.0$	$4.0 < y < 4.5$	$2.0 < y < 4.5$
$150 < p_T < 250$	351616 ± 122906	490878 ± 27650	433222 ± 12861	402380 ± 13245	402649 ± 25447	2157426 ± 42920
$250 < p_T < 500$	1370614 ± 161228	1498131 ± 44482	1319627 ± 22691	1174490 ± 20163	1152041 ± 31724	6449734 ± 68168
$500 < p_T < 650$	673779 ± 67214	720090 ± 24180	653150 ± 16067	587808 ± 13701	520953 ± 18310	3163363 ± 44183
$650 < p_T < 800$	510657 ± 45525	567439 ± 20182	500051 ± 14484	443463 ± 12039	414792 ± 17853	2454721 ± 39339
$800 < p_T < 1000$	487484 ± 37160	522759 ± 18336	469911 ± 14804	410477 ± 11794	353824 ± 16467	2265673 ± 37877
$1000 < p_T < 1200$	322211 ± 26332	341626 ± 14481	307397 ± 12617	262243 ± 9750	222103 ± 13627	1469611 ± 31027
$1200 < p_T < 2500$	656515 ± 32066	649339 ± 20021	589014 ± 19729	479701 ± 14522	397910 ± 20268	2793202 ± 45351
p_T integrated	4439575 ± 432122	4801782 ± 120105	4256672 ± 105820	3760446 ± 96815	3450589 ± 146530	

Table 68.: Corrected production yields for $\bar{\Lambda}$ in y and p_T bins, for field up events at $\sqrt{s} = 7$ TeV.

	$2.0 < y < 2.5$	$2.5 < y < 3.0$	$3.0 < y < 3.5$	$3.5 < y < 4.0$	$4.0 < y < 4.5$	$2.0 < y < 4.5$
$150 < p_T < 250$	-	125378 ± 45105	156567 ± 45230	110107 ± 129796	-	584040 ± 129568
$250 < p_T < 500$	-	467540 ± 52266	446548 ± 36827	446693 ± 63540	379475 ± 338953	1948804 ± 117655
$500 < p_T < 650$	121424 ± 94794	346804 ± 44169	305153 ± 27133	245325 ± 29071	316019 ± 117373	1339232 ± 82321
$650 < p_T < 800$	176031 ± 74305	250673 ± 31538	281326 ± 24127	260933 ± 32832	216154 ± 53607	1212733 ± 72441
$800 < p_T < 1000$	261735 ± 77624	372474 ± 51817	309233 ± 25252	294772 ± 33771	206444 ± 41489	1441566 ± 81947
$1000 < p_T < 1200$	332414 ± 110688	235730 ± 34393	257622 ± 26749	214418 ± 26844	146172 ± 33429	1121346 ± 74068
$1200 < p_T < 2500$	543108 ± 80789	562012 ± 51984	536220 ± 43362	472522 ± 42509	295247 ± 48067	2452110 ± 112669
p_T integrated	2011233 ± 237388	2348472 ± 116394	2271226 ± 83434	2076276 ± 101419	1561463 ± 153313	

Table 69.: Corrected production yields for Λ in y and p_T bins, for field up events at $\sqrt{s} = 7$ TeV.

	$2.0 < y < 2.5$	$2.5 < y < 3.0$	$3.0 < y < 3.5$	$3.5 < y < 4.0$	$4.0 < y < 4.5$	$2.0 < y < 4.5$
$150 < p_T < 250$	-	176849 ± 67516	148920 ± 36858	215434 ± 260640	-	653565 ± 134296
$250 < p_T < 500$	-	513039 ± 55229	467329 ± 36511	464882 ± 62568	513656 ± 547760	2068746 ± 119019
$500 < p_T < 650$	139840 ± 101089	352375 ± 42334	315878 ± 26231	268658 ± 30182	315144 ± 113196	1396447 ± 80810
$650 < p_T < 800$	248623 ± 107008	322946 ± 42230	318044 ± 27062	259992 ± 30265	220015 ± 51289	1361493 ± 79928
$800 < p_T < 1000$	303230 ± 86413	367258 ± 48025	330560 ± 25756	283723 ± 29550	290818 ± 62858	1511131 ± 81530
$1000 < p_T < 1200$	312360 ± 96633	303495 ± 45673	264701 ± 26270	203338 ± 22686	238894 ± 62656	1210917 ± 76983
$1200 < p_T < 2500$	593257 ± 88786	623228 ± 56971	560168 ± 43109	481362 ± 39809	393962 ± 66789	2626855 ± 116255
p_T integrated	2207944 ± 257308	2628057 ± 128062	2398041 ± 84270	2087192 ± 94411	2015624 ± 206076	

Table 70.: Corrected production yields for K^0_S in y and p_T bins, for field up events at $\sqrt{s} = 7$ TeV.

	$2.0 < y < 2.5$	$2.5 < y < 3.0$	$3.0 < y < 3.5$	$3.5 < y < 4.0$	$4.0 < y < 4.5$	$2.0 < y < 4.5$
$150 < p_T < 250$	676374 ± 217238	986143 ± 50824	886983 ± 23981	809902 ± 23564	757530 ± 42315	4317130 ± 77184
$250 < p_T < 500$	3003003 ± 332879	2890871 ± 76194	2596214 ± 39609	2390377 ± 36668	2243634 ± 54926	12724910 ± 119709
$500 < p_T < 650$	1443696 ± 134105	1431294 ± 43287	1319339 ± 29205	1163275 ± 24059	1070859 ± 34249	6332024 ± 79419
$650 < p_T < 800$	1045682 ± 84608	1125280 ± 36078	1012277 ± 26177	922138 ± 22538	811778 ± 31197	4934880 ± 70936
$800 < p_T < 1000$	943517 ± 62979	1021570 ± 31875	927213 ± 25845	842005 ± 21778	713853 ± 29989	4512013 ± 67301
$1000 < p_T < 1200$	652170 ± 47150	663273 ± 24975	609168 ± 22238	564745 ± 19445	462164 ± 26088	2991907 ± 57020
$1200 < p_T < 2500$	1310521 ± 57186	1301199 ± 35735	1187039 ± 35142	1036651 ± 28717	867819 ± 41415	5744287 ± 83947
p_T integrated	8948420 ± 786418	9439126 ± 210051	8513689 ± 190045	7716536 ± 181685	6909757 ± 263322	

Table 71.: $\bar{\Lambda}/\Lambda$ ratio in y and p_T bins, for field down events at $\sqrt{s} = 0.9$ TeV.

	$2.0 < y < 2.5$	$2.5 < y < 3.0$	$3.0 < y < 3.5$	$3.5 < y < 4.0$	$2.0 < y < 4.0$
$250 < p_T < 500$	$2.69 \pm 2.98 \pm 0.05$	$0.92 \pm 0.11 \pm 0.02$	$0.90 \pm 0.14 \pm 0.02$	$0.42 \pm 0.55 \pm 0.01$	$0.89 \pm 0.08 \pm 0.02$
$500 < p_T < 650$	$2.79 \pm 1.57 \pm 0.05$	$0.76 \pm 0.09 \pm 0.01$	$0.71 \pm 0.08 \pm 0.01$	$0.36 \pm 0.15 \pm 0.01$	$0.72 \pm 0.06 \pm 0.01$
$650 < p_T < 800$	$0.82 \pm 0.35 \pm 0.01$	$0.84 \pm 0.10 \pm 0.02$	$0.65 \pm 0.07 \pm 0.01$	$0.93 \pm 0.22 \pm 0.02$	$0.74 \pm 0.05 \pm 0.01$
$800 < p_T < 1000$	$0.45 \pm 0.14 \pm 0.01$	$0.77 \pm 0.10 \pm 0.01$	$0.87 \pm 0.08 \pm 0.02$	$0.70 \pm 0.12 \pm 0.01$	$0.79 \pm 0.05 \pm 0.01$
$1000 < p_T < 1200$	$0.82 \pm 0.25 \pm 0.01$	$0.77 \pm 0.13 \pm 0.01$	$0.67 \pm 0.07 \pm 0.01$	$0.42 \pm 0.08 \pm 0.01$	$0.65 \pm 0.05 \pm 0.01$
$1200 < p_T < 2500$	$1.02 \pm 0.19 \pm 0.02$	$0.64 \pm 0.09 \pm 0.01$	$0.75 \pm 0.07 \pm 0.01$	$0.48 \pm 0.08 \pm 0.01$	$0.71 \pm 0.05 \pm 0.01$
p_T integrated	$0.91 \pm 0.12 \pm 0.02$	$0.79 \pm 0.04 \pm 0.01$	$0.75 \pm 0.03 \pm 0.01$	$0.57 \pm 0.05 \pm 0.01$	

Table 72.: $\bar{\Lambda}/\Lambda$ ratio in y and p_T bins, for field up events at $\sqrt{s} = 0.9$ TeV.

	$2.0 < y < 2.5$	$2.5 < y < 3.0$	$3.0 < y < 3.5$	$3.5 < y < 4.0$	$2.0 < y < 4.0$
$250 < p_T < 500$	$0.26 \pm 0.35 \pm 0.01$	$0.89 \pm 0.12 \pm 0.03$	$0.63 \pm 0.10 \pm 0.02$	-	$0.74 \pm 0.08 \pm 0.02$
$500 < p_T < 650$	$1.51 \pm 1.04 \pm 0.05$	$0.77 \pm 0.10 \pm 0.02$	$0.70 \pm 0.08 \pm 0.02$	$0.99 \pm 0.41 \pm 0.03$	$0.73 \pm 0.06 \pm 0.02$
$650 < p_T < 800$	$0.75 \pm 0.34 \pm 0.02$	$0.69 \pm 0.09 \pm 0.02$	$0.74 \pm 0.08 \pm 0.02$	$0.52 \pm 0.14 \pm 0.02$	$0.70 \pm 0.05 \pm 0.02$
$800 < p_T < 1000$	$1.46 \pm 0.47 \pm 0.04$	$0.74 \pm 0.10 \pm 0.02$	$0.66 \pm 0.07 \pm 0.02$	$0.55 \pm 0.10 \pm 0.02$	$0.70 \pm 0.05 \pm 0.02$
$1000 < p_T < 1200$	$0.65 \pm 0.22 \pm 0.02$	$0.79 \pm 0.14 \pm 0.02$	$0.69 \pm 0.08 \pm 0.02$	$0.50 \pm 0.10 \pm 0.01$	$0.68 \pm 0.06 \pm 0.02$
$1200 < p_T < 2500$	$0.72 \pm 0.15 \pm 0.02$	$0.68 \pm 0.10 \pm 0.02$	$0.84 \pm 0.09 \pm 0.03$	$0.63 \pm 0.11 \pm 0.02$	$0.76 \pm 0.05 \pm 0.02$
p_T integrated	$0.84 \pm 0.12 \pm 0.03$	$0.76 \pm 0.04 \pm 0.02$	$0.72 \pm 0.03 \pm 0.02$	$0.58 \pm 0.06 \pm 0.02$	

Table 73.: $\bar{\Lambda}/\Lambda$ ratio in y and p_T bins, for field down events at $\sqrt{s} = 7$ TeV.

	$2.0 < y < 2.5$	$2.5 < y < 3.0$	$3.0 < y < 3.5$	$3.5 < y < 4.0$	$4.0 < y < 4.5$	$2.0 < y < 4.5$
$150 < p_T < 250$	-	$2.38 \pm 1.62 \pm 0.04$	$0.76 \pm 0.41 \pm 0.01$	$0.39 \pm 0.76 \pm 0.01$	-	$1.14 \pm 0.46 \pm 0.02$
$250 < p_T < 500$	-	$0.96 \pm 0.21 \pm 0.02$	$0.97 \pm 0.16 \pm 0.02$	$0.97 \pm 0.27 \pm 0.02$	-	$0.96 \pm 0.11 \pm 0.02$
$500 < p_T < 650$	$0.33 \pm 0.47 \pm 0.01$	$1.06 \pm 0.25 \pm 0.02$	$1.00 \pm 0.18 \pm 0.02$	$0.82 \pm 0.20 \pm 0.01$	$0.88 \pm 0.57 \pm 0.01$	$0.95 \pm 0.12 \pm 0.02$
$650 < p_T < 800$	$1.43 \pm 1.37 \pm 0.02$	$0.99 \pm 0.26 \pm 0.02$	$0.84 \pm 0.15 \pm 0.01$	$1.12 \pm 0.27 \pm 0.02$	$0.76 \pm 0.37 \pm 0.01$	$0.94 \pm 0.11 \pm 0.02$
$800 < p_T < 1000$	$1.16 \pm 0.76 \pm 0.02$	$0.98 \pm 0.26 \pm 0.02$	$0.85 \pm 0.14 \pm 0.01$	$0.91 \pm 0.20 \pm 0.02$	$0.78 \pm 0.34 \pm 0.01$	$0.90 \pm 0.10 \pm 0.02$
$1000 < p_T < 1200$	$0.86 \pm 0.49 \pm 0.01$	$1.02 \pm 0.30 \pm 0.02$	$0.89 \pm 0.18 \pm 0.02$	$0.79 \pm 0.19 \pm 0.01$	$0.87 \pm 0.43 \pm 0.01$	$0.87 \pm 0.11 \pm 0.01$
$1200 < p_T < 2500$	$0.96 \pm 0.30 \pm 0.02$	$0.98 \pm 0.19 \pm 0.02$	$0.82 \pm 0.13 \pm 0.01$	$0.96 \pm 0.17 \pm 0.02$	$0.85 \pm 0.29 \pm 0.01$	$0.91 \pm 0.08 \pm 0.02$
p_T integrated	$0.97 \pm 0.24 \pm 0.02$	$1.01 \pm 0.10 \pm 0.02$	$0.89 \pm 0.06 \pm 0.02$	$0.93 \pm 0.09 \pm 0.02$	$0.82 \pm 0.16 \pm 0.01$	

Table 74.: $\bar{\Lambda}/\Lambda$ ratio in y and p_T bins, for field up events at $\sqrt{s} = 7$ TeV.

	$2.0 < y < 2.5$	$2.5 < y < 3.0$	$3.0 < y < 3.5$	$3.5 < y < 4.0$	$4.0 < y < 4.5$	$2.0 < y < 4.5$
$150 < p_T < 250$	-	$0.71 \pm 0.37 \pm 0.01$	$1.05 \pm 0.40 \pm 0.02$	$0.51 \pm 0.86 \pm 0.01$	-	$0.89 \pm 0.27 \pm 0.02$
$250 < p_T < 500$	-	$0.91 \pm 0.14 \pm 0.02$	$0.96 \pm 0.11 \pm 0.02$	$0.96 \pm 0.19 \pm 0.02$	$0.74 \pm 1.03 \pm 0.01$	$0.94 \pm 0.08 \pm 0.02$
$500 < p_T < 650$	$0.87 \pm 0.92 \pm 0.02$	$0.98 \pm 0.17 \pm 0.02$	$0.97 \pm 0.12 \pm 0.02$	$0.91 \pm 0.15 \pm 0.02$	$1.00 \pm 0.52 \pm 0.02$	$0.96 \pm 0.08 \pm 0.02$
$650 < p_T < 800$	$0.71 \pm 0.43 \pm 0.01$	$0.78 \pm 0.14 \pm 0.01$	$0.88 \pm 0.11 \pm 0.02$	$1.00 \pm 0.17 \pm 0.02$	$0.98 \pm 0.33 \pm 0.02$	$0.89 \pm 0.07 \pm 0.02$
$800 < p_T < 1000$	$0.86 \pm 0.36 \pm 0.02$	$1.01 \pm 0.19 \pm 0.02$	$0.94 \pm 0.11 \pm 0.02$	$1.04 \pm 0.16 \pm 0.02$	$0.71 \pm 0.21 \pm 0.01$	$0.95 \pm 0.07 \pm 0.02$
$1000 < p_T < 1200$	$1.06 \pm 0.48 \pm 0.02$	$0.78 \pm 0.16 \pm 0.01$	$0.97 \pm 0.14 \pm 0.02$	$1.05 \pm 0.18 \pm 0.02$	$0.61 \pm 0.21 \pm 0.01$	$0.93 \pm 0.08 \pm 0.02$
$1200 < p_T < 2500$	$0.92 \pm 0.19 \pm 0.02$	$0.90 \pm 0.12 \pm 0.02$	$0.96 \pm 0.11 \pm 0.02$	$0.98 \pm 0.12 \pm 0.02$	$0.75 \pm 0.18 \pm 0.01$	$0.93 \pm 0.06 \pm 0.02$
p_T integrated	$0.91 \pm 0.15 \pm 0.02$	$0.89 \pm 0.06 \pm 0.02$	$0.95 \pm 0.05 \pm 0.02$	$0.99 \pm 0.07 \pm 0.02$	$0.77 \pm 0.11 \pm 0.01$	

Table 75.: $\bar{\Lambda}/K^0_S$ ratio in y and p_T bins, for field down events at $\sqrt{s} = 0.9$ TeV.

	$2.0 < y < 2.5$	$2.5 < y < 3.0$	$3.0 < y < 3.5$	$3.5 < y < 4.0$	$2.0 < y < 4.0$
$250 < p_T < 500$	$0.17 \pm 0.15 \pm 0.01$	$0.22 \pm 0.02 \pm 0.01$	$0.20 \pm 0.02 \pm 0.01$	$0.23 \pm 0.15 \pm 0.01$	$0.22 \pm 0.01 \pm 0.01$
$500 < p_T < 650$	$0.38 \pm 0.16 \pm 0.01$	$0.24 \pm 0.02 \pm 0.01$	$0.20 \pm 0.02 \pm 0.01$	$0.15 \pm 0.04 \pm 0.00$	$0.22 \pm 0.01 \pm 0.01$
$650 < p_T < 800$	$0.29 \pm 0.10 \pm 0.01$	$0.30 \pm 0.03 \pm 0.01$	$0.27 \pm 0.02 \pm 0.01$	$0.37 \pm 0.06 \pm 0.01$	$0.30 \pm 0.02 \pm 0.01$
$800 < p_T < 1000$	$0.27 \pm 0.07 \pm 0.01$	$0.30 \pm 0.03 \pm 0.01$	$0.35 \pm 0.03 \pm 0.01$	$0.28 \pm 0.04 \pm 0.01$	$0.33 \pm 0.02 \pm 0.01$
$1000 < p_T < 1200$	$0.28 \pm 0.06 \pm 0.01$	$0.36 \pm 0.05 \pm 0.01$	$0.35 \pm 0.03 \pm 0.01$	$0.28 \pm 0.05 \pm 0.01$	$0.35 \pm 0.02 \pm 0.01$
$1200 < p_T < 2500$	$0.52 \pm 0.08 \pm 0.02$	$0.40 \pm 0.04 \pm 0.01$	$0.37 \pm 0.03 \pm 0.01$	$0.27 \pm 0.04 \pm 0.01$	$0.41 \pm 0.02 \pm 0.01$
p_T integrated	$0.28 \pm 0.03 \pm 0.01$	$0.27 \pm 0.01 \pm 0.01$	$0.26 \pm 0.01 \pm 0.01$	$0.25 \pm 0.02 \pm 0.01$	

Table 76.: $\bar{\Lambda}/K^0_S$ ratio in y and p_T bins, for field up events at $\sqrt{s} = 0.9$ TeV.

	$2.0 < y < 2.5$	$2.5 < y < 3.0$	$3.0 < y < 3.5$	$3.5 < y < 4.0$	$2.0 < y < 4.0$
$250 < p_T < 500$	$0.03 \pm 0.03 \pm 0.00$	$0.16 \pm 0.02 \pm 0.01$	$0.16 \pm 0.02 \pm 0.01$	-	$0.16 \pm 0.01 \pm 0.01$
$500 < p_T < 650$	$0.19 \pm 0.09 \pm 0.01$	$0.24 \pm 0.02 \pm 0.01$	$0.22 \pm 0.02 \pm 0.01$	$0.24 \pm 0.07 \pm 0.01$	$0.23 \pm 0.01 \pm 0.01$
$650 < p_T < 800$	$0.36 \pm 0.12 \pm 0.01$	$0.27 \pm 0.03 \pm 0.01$	$0.28 \pm 0.02 \pm 0.01$	$0.19 \pm 0.04 \pm 0.01$	$0.28 \pm 0.02 \pm 0.01$
$800 < p_T < 1000$	$0.51 \pm 0.12 \pm 0.02$	$0.35 \pm 0.04 \pm 0.01$	$0.29 \pm 0.02 \pm 0.01$	$0.29 \pm 0.04 \pm 0.01$	$0.34 \pm 0.02 \pm 0.01$
$1000 < p_T < 1200$	$0.33 \pm 0.09 \pm 0.01$	$0.35 \pm 0.05 \pm 0.01$	$0.37 \pm 0.04 \pm 0.01$	$0.24 \pm 0.04 \pm 0.01$	$0.36 \pm 0.02 \pm 0.01$
$1200 < p_T < 2500$	$0.45 \pm 0.07 \pm 0.02$	$0.43 \pm 0.05 \pm 0.02$	$0.43 \pm 0.04 \pm 0.02$	$0.33 \pm 0.05 \pm 0.01$	$0.44 \pm 0.03 \pm 0.02$
p_T integrated	$0.28 \pm 0.03 \pm 0.01$	$0.25 \pm 0.01 \pm 0.01$	$0.25 \pm 0.01 \pm 0.01$	$0.20 \pm 0.02 \pm 0.01$	

Table 77.: $\bar{\Lambda}/K^0_S$ ratio in y and p_T bins, for field down events at $\sqrt{s} = 7$ TeV.

	$2.0 < y < 2.5$	$2.5 < y < 3.0$	$3.0 < y < 3.5$	$3.5 < y < 4.0$	$4.0 < y < 4.5$	$2.0 < y < 4.5$
$150 < p_T < 250$	-	$0.21 \pm 0.12 \pm 0.01$	$0.17 \pm 0.06 \pm 0.01$	$0.07 \pm 0.08 \pm 0.00$	$0.26 \pm 1.14 \pm 0.01$	$0.17 \pm 0.05 \pm 0.00$
$250 < p_T < 500$	-	$0.17 \pm 0.03 \pm 0.00$	$0.18 \pm 0.02 \pm 0.01$	$0.19 \pm 0.04 \pm 0.01$	$0.18 \pm 0.21 \pm 0.01$	$0.17 \pm 0.01 \pm 0.01$
$500 < p_T < 650$	$0.06 \pm 0.05 \pm 0.00$	$0.23 \pm 0.04 \pm 0.01$	$0.24 \pm 0.03 \pm 0.01$	$0.21 \pm 0.04 \pm 0.01$	$0.23 \pm 0.10 \pm 0.01$	$0.22 \pm 0.02 \pm 0.01$
$650 < p_T < 800$	$0.29 \pm 0.22 \pm 0.01$	$0.27 \pm 0.05 \pm 0.01$	$0.26 \pm 0.03 \pm 0.01$	$0.28 \pm 0.05 \pm 0.01$	$0.23 \pm 0.08 \pm 0.01$	$0.26 \pm 0.02 \pm 0.01$
$800 < p_T < 1000$	$0.38 \pm 0.19 \pm 0.01$	$0.34 \pm 0.07 \pm 0.01$	$0.32 \pm 0.04 \pm 0.01$	$0.30 \pm 0.05 \pm 0.01$	$0.33 \pm 0.10 \pm 0.01$	$0.31 \pm 0.03 \pm 0.01$
$1000 < p_T < 1200$	$0.37 \pm 0.15 \pm 0.01$	$0.38 \pm 0.08 \pm 0.01$	$0.35 \pm 0.05 \pm 0.01$	$0.34 \pm 0.06 \pm 0.01$	$0.41 \pm 0.15 \pm 0.01$	$0.35 \pm 0.03 \pm 0.01$
$1200 < p_T < 2500$	$0.49 \pm 0.11 \pm 0.01$	$0.47 \pm 0.07 \pm 0.01$	$0.41 \pm 0.05 \pm 0.01$	$0.47 \pm 0.06 \pm 0.01$	$0.41 \pm 0.10 \pm 0.01$	$0.44 \pm 0.03 \pm 0.01$
p_T integrated	$0.28 \pm 0.06 \pm 0.01$	$0.27 \pm 0.02 \pm 0.01$	$0.26 \pm 0.01 \pm 0.01$	$0.26 \pm 0.02 \pm 0.01$	$0.25 \pm 0.04 \pm 0.01$	

Table 78.: $\bar{\Lambda}/K^0_S$ ratio in y and p_T bins, for field up events at $\sqrt{s} = 7$ TeV.

	$2.0 < y < 2.5$	$2.5 < y < 3.0$	$3.0 < y < 3.5$	$3.5 < y < 4.0$	$4.0 < y < 4.5$	$2.0 < y < 4.5$
$150 < p_T < 250$	-	$0.13 \pm 0.05 \pm 0.00$	$0.18 \pm 0.05 \pm 0.01$	$0.14 \pm 0.16 \pm 0.00$	-	$0.14 \pm 0.03 \pm 0.00$
$250 < p_T < 500$	-	$0.16 \pm 0.02 \pm 0.00$	$0.17 \pm 0.01 \pm 0.01$	$0.19 \pm 0.03 \pm 0.01$	$0.17 \pm 0.15 \pm 0.01$	$0.15 \pm 0.01 \pm 0.00$
$500 < p_T < 650$	$0.08 \pm 0.07 \pm 0.00$	$0.24 \pm 0.03 \pm 0.01$	$0.23 \pm 0.02 \pm 0.01$	$0.21 \pm 0.03 \pm 0.01$	$0.30 \pm 0.11 \pm 0.01$	$0.21 \pm 0.01 \pm 0.01$
$650 < p_T < 800$	$0.17 \pm 0.07 \pm 0.01$	$0.22 \pm 0.03 \pm 0.01$	$0.28 \pm 0.02 \pm 0.01$	$0.28 \pm 0.04 \pm 0.01$	$0.27 \pm 0.07 \pm 0.01$	$0.25 \pm 0.02 \pm 0.01$
$800 < p_T < 1000$	$0.28 \pm 0.08 \pm 0.01$	$0.36 \pm 0.05 \pm 0.01$	$0.33 \pm 0.03 \pm 0.01$	$0.35 \pm 0.04 \pm 0.01$	$0.29 \pm 0.06 \pm 0.01$	$0.32 \pm 0.02 \pm 0.01$
$1000 < p_T < 1200$	$0.51 \pm 0.17 \pm 0.02$	$0.36 \pm 0.05 \pm 0.01$	$0.42 \pm 0.05 \pm 0.01$	$0.38 \pm 0.05 \pm 0.01$	$0.32 \pm 0.07 \pm 0.01$	$0.37 \pm 0.03 \pm 0.01$
$1200 < p_T < 2500$	$0.41 \pm 0.06 \pm 0.01$	$0.43 \pm 0.04 \pm 0.01$	$0.45 \pm 0.04 \pm 0.01$	$0.46 \pm 0.04 \pm 0.01$	$0.34 \pm 0.06 \pm 0.01$	$0.43 \pm 0.02 \pm 0.01$
p_T integrated	$0.22 \pm 0.03 \pm 0.01$	$0.25 \pm 0.01 \pm 0.01$	$0.27 \pm 0.01 \pm 0.01$	$0.27 \pm 0.01 \pm 0.01$	$0.23 \pm 0.02 \pm 0.01$	

B

PRINCIPLES FOR THE MEASUREMENT OF THE Λ POLARISATION

The measurements of the Λ polarisation starts from the "self-analysing" $\Lambda \to p\pi^-$ decay. It is called self-analysing because, being mediated by the weak interaction, exhibit parity violation. The violation of parity permits the transport of the spin information from the Λ to the angular distribution in the final states which can be used in order to measure the Λ polarisation.

As already said strong interactions give rise to transversely polarised Λ particles. Considering the Λ rest-frame and taking as z axis the spin direction, the angular distribution of the decay particles can be easily expressed in terms of the ϑ and ϕ of the so specified spherical coordinate system.

The angular distribution will depend on the angular momentum between the pion and the proton. Now, since the Λ has spin $J_\Lambda = \frac{1}{2}$, we can have two possibilities:

- $l = 0$, which corresponds to Λ and proton spins parallel, leading to an s-wave;
- $l = 1$, with spins anti-parallel, leading to a p-wave.

In general we expect a combination of the two for the final state. Considering $J_z = +\frac{1}{2}$, if m_1 and m_2 are the z projections of the proton spin and of the orbital angular momentum respectively, the s-wave component is given by $m_2 = 0$ and $m_1 = \frac{1}{2}$ and consequently build up of the spherical harmonic Y_0^0 and of the spin of the proton in the up direction (χ^+):

$$\psi_s = a_s Y_0^0 \chi^+ \tag{B.1}$$

where a_s is the amplitude of this component. The p-wave component instead is due to two contribution: $m_2 = 0$ and $m_1 = \frac{1}{2}$ or $m_2 = 1$ and $m_1 = -\frac{1}{2}$, so that:

$$\psi_p = a_p \left[\sqrt{\frac{2}{3}} Y_1^1 \chi^- - \sqrt{\frac{1}{3}} Y_1^0 \chi^+ \right] \tag{B.2}$$

where the two contributions have been summed using Clebsh-Gordan coefficients for the sum of a $J = 1$ to a $J = \frac{1}{2}$ state. Being

the total amplitude the sum of the s-wave and of the p-wave, $\psi = \psi_s + \psi_p$, the probability distribution for the final state is given by:

$$\psi\psi^* = (a_s Y_0^0 - a_p \sqrt{\frac{1}{3}} Y_1^0)(a_s Y_0^0 - a_p^* \sqrt{\frac{1}{3}} Y_1^0) + a_p^2 (\sqrt{\frac{2}{3}} Y_1^1)^2 \quad \text{(B.3)}$$

where the orthogonality of χ^+ and χ^- has been used and a_s has been taken as real in order to fix the arbitrary phase. Using the explicit expression of the spherical harmonics one finally obtains:

$$f(\vartheta) = \psi\psi^* = |a_s|^2 + |a_p|^2 - 2a_s \Re(a_p^*) \cos\vartheta \quad \text{(B.4)}$$

which can be re-written as:

$$f(\vartheta) = 1 - \alpha \cos\vartheta \quad \text{(B.5)}$$

with

$$\alpha = \frac{2\Re(a_p^*)}{|a_s|^2 + |a_p|^2} \quad \text{(B.6)}$$

usually referred to as the Λ asymmetry parameter, because of the obvious interpretation as the source of the asymmetry in the distribution, but is also known as *analysing power* because the possibility to analyse the polarisation of the Λ is proportional to α.

The description of the $\bar{\Lambda} \to \bar{p}\pi^+$ decay is completely the same. In particular, from simple symmetry constraints, the following relation must hold:

$$\alpha_\Lambda = -\alpha_{\bar{\Lambda}} \quad \text{(B.7)}$$

which however is valid only if CP symmetry is not broken in the Λ sector. Indeed this relation can be used as a measurement of the direct CP violation in the Λ.

As already said, on the experimental side one usually cannot identify the spin axis event-by-event, so that the z axis is usually identified as the orthogonal to the production plane ($z \parallel p_{beam} \wedge p_\Lambda$); in this case the proton distribution is modified by the amount of Λ polarisation P with respect to that axis:

$$f(\vartheta) = 1 - \alpha P \cos\vartheta \quad \text{(B.8)}$$

and obviously coincides with Eq. (B.5) just for full polarisation ($P = 1$).

Note that if the weak interaction didn't violate parity conservation ($\alpha = 0$) the Λ polarisation would not be experimentally observable from this measurement.

BIBLIOGRAPHY

[1] G. Altarelli, "Status of the Standard Model at the LHC start", *Nuovo Cimento B Serie* 123 (2008) 257–269, arXiv:0804.4147. (Cited on page vii.)

[2] N. A. Bahcall, J. P. Ostriker, S. Perlmutter, and P. J. Steinhardt, "The Cosmic Triangle: Revealing the State of the Universe", *Science* 284 (1999) 1481–+, arXiv:astro-ph/. (Cited on page vii.)

[3] W. Bonivento, F. Dettori, and N. Serra, "LHCb sensitivity to the $B_s^0 \to \mu^{\pm}\mu^{\mp}\gamma$ decay", Tech. Rep. LHCb-PUB-2010-008. CERN-LHCb-PUB-2010-008, CERN, Geneva, Mar 2010. (Cited on page viii.)

[4] J. C. Collins, D. E. Soper, and G. F. Sterman, "Factorization of Hard Processes in QCD", *Adv. Ser. Direct. High Energy Phys.* 5 (1988) 1–91, hep-ph/0409313. (Cited on page 7.)

[5] B.-Q. Ma, I. Schmidt, and J.-J. Yang, "Particle antiparticle asymmetries of Λ production in hadron nucleon collisions", *Phys. Lett.* B598 (2004) 211–217, hep-ph/0408022. (Cited on pages 7, 8, and 13.)

[6] J.-J. Yang, "Resolving flavor structure of λ fragmentation functions via asymmetry in production", *Physics Letters B* 526 (2002), no. 1-2, 50 – 54. http://www.sciencedirect.com/science/article/B6TVN-44T524R-4/2/f799c467d91fe2acefd6c65d2e297a16. (Cited on page 8.)

[7] B. Andersson, G. Gustafson, and C. Peterson, "A Semiclassical Model for Quark Jet Fragmentation", *Zeit. Phys.* C1 (1979) 105. (Cited on page 8.)

[8] B. Andersson, G. Gustafson, G. Ingelman, and T. Sjostrand, "Parton Fragmentation and String Dynamics", *Phys. Rept.* 97 (1983) 31–145. (Cited on pages 8 and 9.)

[9] B. R. Webber, "A QCD Model for Jet Fragmentation Including Soft Gluon Interference", *Nucl. Phys.* B238 (1984) 492. (Cited on pages 8 and 10.)

[10] B. Andersson, G. Gustafson, and T. Sjostrand, "A Model for Baryon Production in Quark and Gluon Jets", *Nucl. Phys.* B197 (1982) 45. (Cited on page 9.)

[11] B. Andersson, G. Gustafson, and T. Sjostrand, "Baryon production in jet fragmentation and Υ decay", *Phys. Scripta* 32 (1985) 574. (Cited on page 10.)

[12] G. A. Alves *et al.*, "Asymmetries in the production of Λ^0 in 250 GeV/c π, K and p-nucleon interactions", *Physics Letters B* 559 (2003), no. 3-4, 179 – 186. http://www.sciencedirect.com/science/article/B6TVN-486432M-9/2/5050d467ab6ca2dac79935b63245dd38. (Cited on page 13.)

[13] P. Koch, "Strong interacting probes for quark gluon plasma", *Zeitschrift fÃijr Physik C Particles and Fields* 38 (1988) 269–272, 10.1007/BF01574548. http://dx.doi.org/10.1007/BF01574548. (Cited on page 14.)

[14] G. C. Rossi and G. Veneziano, "A possible description of baryon dynamics in dual and gauge theories", *Nuclear Physics B* 123 (1977), no. 3, 507 – 545. http://www.sciencedirect.com/science/article/B6TVC-4718XVF-1FS/2/fea739b766049c480493900b4167c6a8. (Cited on page 14.)

[15] A. Capella, U. Sukhatme, C. I. Tan, and J. T. T. Van, "Dual parton model", *Physics Reports* 236 (1994), no. 4-5, 225 – 329. http://www.sciencedirect.com/science/article/B6TVP-46SPH2B-1W/2/be33c9f9725efef9672bd993cb807de7. (Cited on page 14.)

[16] X. Artru, "String model with baryons: Topology; classical motion", *Nuclear Physics B* 85 (1975), no. 2, 442 – 460. http://www.sciencedirect.com/science/article/B6TVC-471XKYR-HW/2/1af0e0915692dda5c952bd33a6867521. (Cited on page 14.)

[17] B. Kopeliovich and B. Povh, "Baryon stopping at hera: evidence for gluonic mechanism", *Physics Letters B* 446 (1999), no. 3-4, 321 – 325. http://www.sciencedirect.com/science/article/B6TVN-3VPBMNC-P/2/ebb4d9376908daa3ce3bd3068ea2b25d. (Cited on page 14.)

[18] G. H. Arakelyan, C. Merino, C. Pajares, and Y. M. Shabelski, "Midrapidity Production of Secondaries in pp Collisions at RHIC and LHC Energies in the Quark-Gluon String Model", *Eur. Phys. J.* C54 (2008) 577–581, arXiv:0709.3174. (Cited on page 14.)

[19] C. Merino, M. M. Ryzhinskiy, and Y. M. Shabelski, "Odderon Effects in pp Collisions: Predictions for LHC Energies", *ArXiv e-prints*, 2009 arXiv:0906.2659. (Cited on page 14.)

[20] D. Kharzeev, "Can gluons trace baryon number?", *Physics Letters B* 378 (1996) 238–246, arXiv:nucl-th/9. (Cited on pages 14 and 15.)

[21] STAR Collaboration, A. R. Timmins, "The centrality dependence of strange baryon and meson production at RHIC", *J. Phys.* G35 (2008) 044062. (Cited on page 16.)

[22] T. "Sjostrand, "Monte Carlo Tools", *ArXiv e-prints*, 2009 arXiv:0911.5286. (Cited on page 16.)

[23] T. Sjostrand, S. Mrenna, and P. Z. Skands, "PYTHIA 6.4 Physics and Manual", *JHEP* 05 (2006) 026, hep-ph/0603175. (Cited on pages 16 and 81.)

[24] P. Bartalini, (ed.) *et al.*, "Proceedings of the First International Workshop on Multiple Partonic Interactions at the LHC (MPI08)", arXiv:1003.4220. (Cited on pages 16, 110, 111, 113, 114, 115, 116, and 118.)

[25] P. Z. Skands, "Tuning Monte Carlo Generators: The Perugia Tunes", *Phys. Rev.* D82 (2010) 074018, arXiv:1005.3457. (Cited on pages 16, 81, 110, 111, 113, 114, 115, 116, and 118.)

[26] P. Skands, "Personal web-page". http://home.fnal.gov/skands/leshouches-plots/. (Cited on pages 17 and 18.)

[27] A. D. Panagiotou, "Λ^0 polarization in hadron-nucleon, hadron-nucleus and nucleus-nucleus interactions", *Int. J. Mod. Phys.* A5 (1990) 1197. (Cited on page 19.)

[28] G. L. Kane, J. Pumplin, and W. Repko, "Transverse quark polarization in large-p_T reactions, e^+e^- jets, and leptoproduction: A test of quantum chromodynamics", *Phys. Rev. Lett.* 41 Dec (1978) 1689–1692. (Cited on pages 19 and 23.)

[29] K. J. Heller, "Inclusive hyperon polarization: a review", *J. Phys. Coll. (France)* 46 (1985) 121–129. (Cited on page 20.)

[30] B. Andersson, G. Gustafson, and G. Ingelman, "A semiclassical model for the polarization on inclusively produced Λ^0-particles at high energies", *Physics Letters B* 85 (1979), no. 4, 417 – 420. http://www.sciencedirect.com/science/article/B6TVN-472K5S4-36M/2/3b8f2d8da9525ad1d159aa6c46ff0556. (Cited on pages 21 and 23.)

[31] S. Erhan *et al.*, "LAMBDAo POLARIZATION IN PROTON PROTON INTERACTIONS AT s**(1/2) = 53-GeV and 62-GeV", *Phys. Lett.* B82 (1979) 301. (Cited on page 23.)

[32] M. Anselmino, D. Boer, U. D'Alesio, and F. Murgia, "Λ polarization from unpolarized quark fragmentation", *Phys. Rev. D* 63 Feb (2001) 054029. (Cited on pages 22, 23, and 24.)

[33] D. Boer, "Transverse Lambda polarization at high energy colliders", in "Proceedings of the XVIIIth International Workshop on Deep-Inelastic Scattering and Related Subjects. April 19 -23, 2010. Convitto della Calza, Firenze, Italy. Published online at http://pos.sissa.it/cgi-bin/reader/conf.cgi?confid=106, id.215". 2010. arXiv:1007.3145. (Cited on pages 22, 23, and 24.)

[34] P. J. Mulders and R. D. Tangerman, "The complete tree-level result up to order 1/q for polarized deep-inelastic leptoproduction", *Nuclear Physics B* 461 (1996), no. 1-2, 197 – 237. http://www.sciencedirect.com/science/article/B6TVC-3VSPKYC-1F/2/a7ee095d31ec7e19f76e03a3b8069f76. (Cited on page 23.)

[35] D. Boer, "Transverse Lambda Polarization at LHC", *ArXiv e-prints*, 2009 arXiv:0907.1610. (Cited on pages 23 and 24.)

[36] A. M. Smith, R. Bonino, A. Castellina, S. Erhan, N. Medinnis, P. E. Schlein, P. Sherwood, S. Vernetto, J. G. Zweizig, J. Alitti, J. B. Cheze, A. Montag, J. Zsembery, L. Meritet, and F. Vazeille, "Λ^0 polarization in proton-proton interactions from $\sqrt{s}$ = 31 to 62 GeV", *Physics Letters B* 185 (1987), no. 1-2, 209 – 212. http://www.sciencedirect.com/science/article/

B6TVN-46XYJW8-1F/2/6e0ae68c4239c388d66ee6593cae0faf. (Cited on pages 23 and 24.)

[37] D. Boer, C. Bomhof, D. Hwang, and P. Mulders, "Spin asymmetries in jet-hyperon production at lhc", *Physics Letters B* 659 (2008), no. 1-2, 127 – 136. http://www.sciencedirect.com/science/article/B6TVN-4R29FH6-5/2/8cd0078b8007ad0501fe8ad1d09dd002. (Cited on page 24.)

[38] D. Boer and A. Dumitru, "Polarized hyperons from pA scattering in the gluon saturation regime", *Physics Letters B* 556 (2003), no. 1-2, 33 – 40. http://www.sciencedirect.com/science/article/B6TVN-47SV3GW-3/2/e67a8aa605fc6acb0f8f378c965dbbd6. (Cited on pages 24 and 25.)

[39] D. Boer, A. Utermann, and E. Wessels, "The saturation scale and its x-dependence from Λ polarization studies", *Physics Letters B* 671 (2009), no. 1, 91 – 98. http://www.sciencedirect.com/science/article/B6TVN-4V3HF7Y-1/2/b0d246c0d112b9e6823f10db4732aecf. (Cited on page 24.)

[40] J. Felix, "On theoretical studies of Λ^0 polarization", *Mod. Phys. Lett.* A14 (1999) 827–842. (Cited on page 25.)

[41] J. Soffer, "Is the riddle of the hyperon polarizations solved?", hep-ph/9911373. (Cited on page 25.)

[42] T. A. DeGrand and H. I. Miettinen, "Quark dynamics of polarization in inclusive hadron production", *Phys. Rev. D* 23 Mar (1981) 1227–1230. (Cited on page 25.)

[43] T. A. DeGrand, J. Markkanen, and H. I. Miettinen, "Hyperon polarization asymmetry: Polarized beams and ω^- production", *Phys. Rev. D* 32 Nov (1985) 2445–2448. (Cited on page 25.)

[44] L. Zuo-tang and C. Boros, "Hyperon polarization and single spin left-right asymmetry in inclusive production processes at high energies", *Phys. Rev. Lett.* 79 Nov (1997) 3608–3611. (Cited on page 26.)

[45] K. Heller, P. T. Cox, J. Dworkin, O. E. Overseth, P. Skubic, L. Schachinger, T. Devlin, B. Edelman, R. T. Edwards,

G. Bunce, R. Handler, R. March, P. Martin, L. Pondrom, and M. Sheaff, "Polarization of Λ's and $\bar{\Lambda}$'s produced by 400-GeV protons", *Phys. Rev. Lett.* 41 Aug (1978) 607–611. (Cited on page 26.)

[46] R. Barni, G. Preparata, and P. G. Ratcliffe, "A simple explanation of hyperon polarization at high pt", *Physics Letters B* 296 (1992), no. 1-2, 251 – 255. http://www.sciencedirect.com/science/article/B6TVN-46YST6W-220/2/b6a403079622cd867d2d5221c631ebef. (Cited on page 26.)

[47] J. Soffer and N. A. Törnqvist, "Origin of the polarization for inclusive Λ production in pp collisions", *Phys. Rev. Lett.* 68 Feb (1992) 907–910. (Cited on page 26.)

[48] Belle Collaboration, M. Petric *et al.*, "Search for leptonic decays of Do mesons", *Phys. Rev.* D81 (2010) 091102, arXiv:1003.2345. (Cited on page 27.)

[49] G. Buchalla, A. J. Buras, and M. E. Lautenbacher, "Weak decays beyond leading logarithms", *Rev. Mod. Phys.* 68 (1996) 1125–1144, hep-ph/9512380. (Cited on pages 29 and 30.)

[50] E. Golowich, J. Hewett, S. Pakvasa, and A. A. Petrov, "Relating Do-anti-Do Mixing and Do -> l+l- with New Physics", *Phys. Rev.* D79 (2009) 114030, arXiv:0903.2830. (Cited on pages 31, 32, and 33.)

[51] G. Burdman, E. Golowich, J. L. Hewett, and S. Pakvasa, "Rare Charm Decays in the Standard Model and Beyond", *Phys. Rev.* D66 (2002) 014009, hep-ph/0112235. (Cited on page 32.)

[52] G. Burdman and I. Shipsey, "D^0 - $\bar{D}^0$ mixing and rare charm decays", *Ann. Rev. Nucl. Part. Sci.* 53 (2003) 431–499, hep-ph/0310076. (Cited on page 32.)

[53] LHCb Collaboration, A. A. Alves *et al.*, "The LHCb Detector at the LHC", *JINST* 3 (2008) S08005. (Cited on page 35.)

[54] L. Evans, (ed.) and P. Bryant, (ed.), "LHC Machine", *JINST* 3 (2008) S08001. (Cited on page 35.)

[55] M. Needham and T. Ruf, "Estimation of the material budget of the lhcb detector", Tech. Rep. LHCb-2007-025.

CERN-LHCb-2007-025, CERN, Geneva, Mar 2007. (Cited on page 36.)

[56] LHCb Collaboration, "Lhcb velo (vertex locator): Technical design report", CERN, Geneva, 2001. http://cdsweb.cern.ch/search.py?recid=504321&ln=en. (Cited on page 37.)

[57] LHCb Collaboration, "Lhcb reoptimized detector design and performance: Technical design report", CERN, Geneva, 2003. http://cdsweb.cern.ch/search.py?recid=630827&ln=en. (Cited on page 40.)

[58] LHCb Collaboration, "Lhcb inner tracker: Technical design report", CERN, Geneva, 2002. http://cdsweb.cern.ch/search.py?recid=582793&ln=en. (Cited on page 40.)

[59] LHCb Collaboration, "Lhcb outer tracker: Technical design report", CERN, Geneva, 2001. http://cdsweb.cern.ch/search.py?recid=519146&ln=en. (Cited on page 43.)

[60] LHCb Collaboration, "Lhcb magnet: Technical design report", CERN, Geneva, 1999. http://cdsweb.cern.ch/search.py?recid=424338&ln=en. (Cited on page 44.)

[61] LHCb Collaboration, "Lhcb rich: Technical design report", CERN, Geneva, 2000. http://cdsweb.cern.ch/search.py?recid=494263&ln=en. (Cited on page 46.)

[62] F. Dettori, "LHCb commissioning", in "Incontri di Fisica delle Alte Energie - IFAE 2009", pp. 113–117. Nuovo Cimento C **032**, 2009. (Cited on page 61.)

[63] M. Anelli *et al.*, "Performance of the LHCb muon system with cosmic rays", *JINST* 5 (2010) P10003. (Cited on page 62.)

[64] C. Amsler *et al.*, "Review of particle physics", *Physics Letters B* 667 (2008), no. 1-5, 1 – 6, Review of Particle Physics. http://www.sciencedirect.com/science/article/B6TVN-4T4VKPY-2/2/2fe3ceb40a4d144f48321db99160ecb2. (Cited on pages 76, 77, and 153.)

[65] A. R. Fisher, "The use of multiple measurements in taxonomic problems", *Annals of Eugenics* 7 (1936) 179–188. (Cited on pages 83 and 169.)

[66] A. Hoecker, P. Speckmayer, J. Stelzer, J. Therhaag, E. von Toerne, H. Voss, M. Backes, T. Carli, O. Cohen, A. Christov, D. Dannheim, K. Danielowski, S. Henrot-Versille, M. Jachowski, K. Kraszewski, A. Krasznahorkay, Jr., M. Kruk, Y. Mahalalel, R. Ospanov, X. Prudent, A. Robert, D. Schouten, F. Tegenfeldt, A. Voigt, K. Voss, M. Wolter, and A. Zemla, "TMVA - Toolkit for Multivariate Data Analysis", *ArXiv Physics e-prints*, 2007 arXiv:physics/0. (Cited on pages 83, 169, and 177.)

[67] A. Hocker, P. Speckmayer, J. Stelzer, F. Tegenfeldt, H. Voss, and K. Voss, "TMVA". Software available online at http://tmva.sourceforge.net/. (Cited on pages 83 and 177.)

[68] J. Podolanski and R. Armenteros, "Analysis of v-events", *Philosophical Magazine Series* 7, 1953. (Cited on page 85.)

[69] Particle Data Group Collaboration, K. Nakamura, "Review of particle physics", *J. Phys.* G37 (2010) 075021. (Cited on pages 93, 94, 123, 143, 160, 161, and 162.)

[70] STAR Collaboration, B. I. Abelev *et al.*, "Strange particle production in p + p collisions at $\sqrt{s} = 200$-GeV", *Phys. Rev.* C75 (2007) 064901, nucl-ex/0607033. (Cited on pages 112 and 115.)

[71] ALEPH Collaboration, R. Barate, and et al., "Study of charm production in Z decays", *European Physical Journal C* 16 (2000) 597–611, arXiv:hep-ex/99. (Cited on page 160.)

[72] A. Sarti, S. Furcas, G. Lanfranchi, and M. Palutan, "Calibration strategy and efficiency measurement of the muon identification procedure at lhcb", Tech. Rep. LHCb-PUB-2010-002. CERN-LHCb-PUB-2010-002, CERN, Geneva, Jan 2010. (Cited on page 162.)

[73] F. Dettori, "Application of multivariate methods to rare events selection in LHCb [ITA]", Master's thesis, Universitá Degli Studi di Cagliari, Cagliari, Italy, 2007. (Cited on page 169.)

[74] T. Junk, "Confidence level computation for combining searches with small statistics", *Nuclear Instruments and*

Methods in Physics Research Section A: Accelerators, Spectrometers, Detectors and Associated Equipment 434 (1999), no. 2-3, 435 – 443. http://www.sciencedirect.com/science/article/B6TJM-3YN3H63-S/2/20fc279c270826d9fdf33fd5629c7c9d. (Cited on page 171.)

[75] "LHCb" Collaboration, "Prompt charm production in pp collisions at $\sqrt{s} = 7$ TeV", 2010, "LHCb-CONF-2010-013". (Cited on page 183.)

[76] F. Dettori, "First minimum bias physics results at LHCb", in "Proceedings of the 15th International QCD Conference (QCD 10 - 25th anniversary), 28th June - 3rd July 2010 Montpellier (France)". to appear in Nuc. Phys (Proc. Supp.), 2010.

[77] LHCb Collaboration, "Roadmap for selected key measurements of LHCb", *ArXiv e-prints*, 2009 arXiv:0912.4179.

[78] F. Dettori, "Production measurements at LHCb with the first data", in "Proceedings of Meeting of the Division of Particles and Fields of the American Physical Society (DPF 2009), Detroit, Michigan, 26-31 Jul 2009.". arXiv:0909.5596.

[79] LHCb Collaboration, "LHCb: Technical Proposal", CERN, Geneva, 1998. http://cdsweb.cern.ch/search.py?recid=622031&ln=en.

[80] LHCb Collaboration, "Lhcb calorimeters: Technical design report", CERN, Geneva, 2000. http://cdsweb.cern.ch/search.py?recid=494264&ln=en.

[81] LHCb Collaboration, "Lhcb muon system: Technical design report", CERN, Geneva, 2001. http://cdsweb.cern.ch/search.py?recid=504326&ln=en.

[82] LHCb Collaboration, "Lhcb muon system: addendum to the technical design report", CERN, Geneva, 2003. http://cdsweb.cern.ch/record/577415?ln=en.

[83] LHCb Collaboration, "Lhcb muon system: second addendum to the tdr", CERN, Geneva, 2005. http://cdsweb.cern.ch/record/831955?ln=en.

[84] LHCb Collaboration, "Lhcb online system, data acquisition and experiment control: Technical design report", CERN, Geneva, 2001. http://cdsweb.cern.ch/search.py?recid=545306&ln=en.

[85] LHCb Collaboration, "Lhcb trigger system: Technical design report", CERN, Geneva, 2003. http://cdsweb.cern.ch/search.py?recid=630828&ln=en.

[86] LHCb Collaboration, "Lhcb computing: Technical design report", CERN, Geneva, 2005. http://cdsweb.cern.ch/search.py?recid=835156&ln=en.

[87] S. M. Troshin and N. E. Tyurin, "On Λ polarization asymmetry in the $pp \to \Lambda X$ process", *Sov. J. Nucl. Phys.* 38 (1983) 639.

[88] S. M. Troshin and N. E. Tyurin, "Hyperon Polarization in the Constituent Quark Model", *Phys. Rev.* D55 (1997) 1265–1272, hep-ph/9602392.

[89] K. J. Heller, "Hyperon polarization at high energy: a tool to investigate the strong interaction", *J. Phys. Colloq.* 51 (1990) 163–173.

[90] GEANT4 Collaboration, S. Agostinelli *et al.*, "GEANT4: A simulation toolkit", *Nucl. Instrum. Meth.* A506 (2003) 250–303.

[91] M. Gyulassy, V. Topor Pop, and S. E. Vance, "Baryon number transport in high-energy nuclear collisions", *Heavy Ion Phys.* 5 (1997) 299, nucl-th/9706048.

[92] K. Jedamzik and G. M. Fuller, "Baryon number transport in a cosmic QCD phase transition", *Nucl. Phys.* B441 (1995) 215–233, astro-ph/9408081.

[93] ALICE Collaboration, P. Christakoglou, "Baryon number transport at LHC energies with the ALICE experiment", *PoS* EPS-HEP2009 (2009) 405.

[94] G. Bocquet *et al.*, "Inclusive production of strange particles in collisions at with ua1", *Physics Letters B* 366 (1996), no. 1-4, 441 – 446. http://www.sciencedirect.com/science/article/B6TVN-3VS8GS2-3H/2/30761a3498926439b5568f4f9d86ea5a.

[95] The CDF Collaboration and T. Aaltonen, "Updated Search for the Flavor-Changing Neutral-Current Decay $D^0 \to \mu^+\mu^-$", *ArXiv e-prints*, 2010 arXiv:1008.5077.